



UNIVERSITÀ
DEGLI STUDI
DI PADOVA

Sede Amministrativa: Università degli Studi di Padova

Dipartimento di Tecnica e Gestione dei Sistemi Industriali

SCUOLA DI DOTTORATO DI RICERCA IN:
INGEGNERIA MECCATRONICA E DELL'INNOVAZIONE
MECCANICA DEL PRODOTTO
XXVII° CICLO

OPTIMIZATION OF INDUSTRIAL PROCESSES FOR FORGING OF CARBON AND STAINLESS STEELS

Direttore della Scuola: Ch.mo Prof. Alessandro Persona

Supervisore: Ch.mo Prof. Paolo Ferro

Dottorando: Fabio Bassan

31 GENNAIO 2015

to my family and to my grandfather

*"Considerate la vostra semenza:
fatti non foste a viver come bruti,
ma per seguir virtute e canoscenza"*

(Dante Alighieri, La Divina commedia, L'inferno, Canto XXVI, vv. 118-120)

TABLE OF CONTENTS

PREFACE	5
SUMMARY	7
SOMMARIO	9
AIM OF THE WORK	11
<u>PART 1: METAL FORMING PROCESSES IN MANUFACTURING</u>	13
1. General introduction	14
1.1. Cold and warm forging	16
2. Cold and warm forging as operation system	17
2.1. Steels for cold and warm forging	18
2.1.1. Low-carbon steels	19
2.1.2. Stainless steels	22
2.1.2.1. Austenitic stainless steels	23
2.1.2.2. Duplex stainless steels	27
2.2. Equipment	30
2.3. Conditions at the tool-material interface	31
2.3.1. Lubrication in cold forging of steel parts	32
2.3.2. Alternative lubricants in cold forging of steel parts	34
2.3.3. Lubrication in warm forging of steel parts	37
2.3.4. Experimental procedure	37
2.4. Tooling	38
<u>PART 2: PROCESS MODELLING</u>	43
1. General introduction	44
2. Process modelling input	44
2.1. Geometric parameters	45
2.2. Process parameters	45
2.3. Material parameters	46
2.4. Friction models	47
2.4.1. Experimental friction test methods in cold and warm forging	49
3. Process modelling output	51
3.1. Metal flow	51

3.2. Distribution and history of state variables	51
3.3. Equipment response.....	52
4. Inverse FE analysis theoretical bases for determination of flow stress and friction condition.....	52
4.1. Procedure for parameters identification	55
5. Experimental procedures.....	56
5.1. Material rheology characterization.....	56
5.1.1. Experimental apparatus	56
5.1.2. Results and discussion.....	58
5.2. Evaluation of friction conditions	59
5.2.1. Experimental apparatus	60
5.2.2. Results and discussion.....	61
6. Numerical models calibration.....	62
6.1. Material constitutive equation	62
6.1.1. Numerical simulation of tensile test.....	62
6.2. FE model of T-shape compression.....	63
6.2.1. Numerical simulation of T-shape test.....	63
7. Industrial case studies	64
7.1. The multi-stage cold forging process of an heat pipe fitting.....	65
7.2. The single-stage forging process of an hex-head plug fitting.....	66

PART 3: MICROSTRUCTURAL CHARACTERIZATION OF FORGED

PARTS.....	69
1. Defects in cold and the warm forging	70
1.1. State of the art	70
1.2. Forging defects	70
2. Plastic deformation structures	73
2.1. Recrystallization and grain-growth structures	74
2.2. Conventional dynamic recrystallization (DRX)	75
3. Electron backscatter diffraction (EBSD) technique.....	78
3.1. Plastic strain	78
3.1.1. Image quality (IQ) approach.....	79
3.1.2. Local misorientation approach	80

3.1.3. Statistical correlation of EBSD strain indicators with crystal orientation	83
3.2. Grain boundary	84
3.3. Special boundaries	84
4. Grain refinement on stainless steels	85
4.1. Heavy plastic deformation.....	85
5. Industrial case studies	86
5.1. Evaluation of defects in the multi-stage cold forged heat pipe fitting...	87
5.2. Dimensional inspection and microstructural characterization of the single-stage forged hex-head plug fitting	87
CONCLUSIONS.....	91
REFERENCES	93
ACKNOWLEDGEMENTS	101
<u>PAPERS</u>	103
ADVANCED MICROSTRUCTURAL CHARACTERIZATION OF TOOL STEELS AND COATINGS FOR COLD FORGING OF STEELS	105
PREDICTION OF DEFECTS IN MULTI-STAGE COLD FORGING BY USING FINITE ELEMENT METHOD	117
SIMULATING MULTI-STAGE COLD FORGING TO REDUCE TIME-TO-MARKET AND PRODUCTION COSTS.....	125
NUMERICAL PROCESS SIMULATION AND MICROSTRUCTURAL EVOLUTION OF CARBON AND STAINLESS STEEL FORGED COMPONENTS	135
MICROSTRUCTURAL AND LOCAL PLASTIC STRAIN EVOLUTION IN COLD-WARM FORGED COMPONENTS STUDIED BY MEANS OF EBSD TECHNIQUE	155

<u>OTHER ACTIVITIES</u>	177
INNOVATIVE RHEOCASTING PROCESSES IN MG FOUNDRY	179
MICROSTRUCTURAL AND MECHANICAL CHARACTERIZATION OF AM60B ALLOY CAST BY RSF PROCESS	189

PREFACE

The work described in this doctoral thesis has been carried out during three years full-time research and studies at the University of Padua from January 2012 to December 2014. The experimental work was carried out at the Department of Management and Engineering (DTG) in Vicenza (Italy), under the main supervision of Professor Paolo Ferro and Professor Franco Bonollo. The cold and warm forging tests presented in the discussion were performed at Zoppelletto S.p.A. (Torri di Quartesolo, Vicenza, Italy) in collaboration with Eng. Luca Zoppelletto.

The thesis is divided in two parts:

- 1) An introduction, which gives to the reader a literature and historical background on forging processes (i.e. definition, process parameters and wrought steels for forming) and on their modelling using Finite Element Analysis and advanced techniques to characterize forged microstructures;
- 2) The second section presents a discussion of the work (with the main industrial case studies and conclusions) and also the following papers, referred in the text by their roman numerals:

Article I

"ADVANCED MICROSTRUCTURAL CHARACTERIZATION OF TOOL STEELS AND COATINGS FOR COLD FORGING OF STEELS"

F. Bassan, P. Ferro, F. Bonollo

Proc. "24th AIM National Conference on Heat Treatments", 2013, Piacenza (IT)

Article II

"PREDICTION OF DEFECTS IN MULTI-STAGE COLD FORGING BY USING FINITE ELEMENT METHOD"

F. Bassan, P. Ferro, F. Bonollo

Published in Key Engineering Materials, 2014, vols. 622-623, pp. 659-663

Proc. "15th International Conference Metalforming 2014", Palermo (IT)

Article III

"SIMULATING MULTI-STAGE COLD FORGING TO REDUCE TIME-TO-MARKET AND PRODUCTION COSTS"

F. Bassan, L. Zoppelletto, M. Gabrielli

Published in "Forging", September/October 2014, pp. 18-22

Article IV

"NUMERICAL PROCESS SIMULATION AND MICROSTRUCTURAL EVOLUTION OF CARBON AND STAINLESS STEEL FORGED COMPONENTS"

F. Bassan, P. Ferro, F. Bonollo

Proc. "35th AIM National Conference", 2014, Roma (IT)

Accepted for publication in "La Metallurgia Italiana", 2015

Article V

"MICROSTRUCTURAL AND LOCAL PLASTIC STRAIN EVOLUTION IN COLD-WARM FORGED COMPONENTS STUDIED BY MEANS OF EBSD TECHNIQUE"

F. Bassan, P. Ferro, F. Bonollo

Submitted to "Materials Characterization", 2015

OTHER PAPERS

The final part of the thesis contains other studies not mentioned above, but which have been elaborated during the PhD work:

Article VI

"INNOVATIVE RHEOCASTING PROCESSES IN MG FOUNDRY"

F. Bassan, G. Timelli, F. Bonollo

Published in Interall S.r.l., 2013, pp. 58-67

Proc. "8th International World Congress Aluminium Two Thousand", 2013, Milano (IT)

Article VII

"MICROSTRUCTURAL AND MECHANICAL CHARACTERIZATION OF AM60B ALLOY CAST BY RSF PROCESS"

F. Bassan, G. Timelli

Published in "Materials Science Forum", 2013, vol. 765, pp. 296-300

Proc. "6th International Light Metals Technology Conference (LMT) 2013", Old Windsor, London (UK)

OTHER ACTIVITIES NOT INCLUDED IN THE THESIS

In addition to the papers included in the thesis, further activities are listed below:

1) *"PROCESS ANALYSIS AND INVESTIGATION OF DEFECTS IN MULTI-STAGE COLD FORGING BY USING FINITE ELEMENT METHOD"*

F. Bassan, P. Ferro, F. Bonollo

Presented in the oral session at "29th International CAE Conference 2013", Lazise (IT)

2) *"PROCESS SIMULATION OF MULTI-STAGE COLD FORGING HELPS TO REDUCE TIME-TO-MARKET AND COSTS FOR A STEEL HEATING PIPE FITTING"*

F. Bassan, L. Zoppelletto, M. Gabrielli

Published in "Newsletter Enginsoft S.p.A.", 2014, year 11, pp. 24-27.

3) *"PROCESS ANALYSIS AND INVESTIGATION OF DEFECTS IN MULTI-STAGE COLD FORGING BY USING FINITE ELEMENT METHOD"*

F. Bassan, L. Zoppelletto

Presented in the oral session at "FORGE[®] International Users Meeting 2014", Cannes (FR)

4) *"MICROSTRUCTURAL ANALYSIS OF COLD FORGED DUPLEX STAINLESS STEEL USING EBSD AND TEM TECHNIQUES"*

A. Fabrizi, F. Bassan, F. Bonollo

Presented in the poster session at "18th International Microscopy Congress", 2014, Prague (CZ)

In addition, the following thesis has been supervised:

M. Veller, *Caratterizzazione microstrutturale e meccanica di acciai da deformazione plastica a freddo*, supervisor: P. Ferro, F. Bassan, A.A. 2013-2014.

SUMMARY

The possibility to produce stainless steel components at limited cost and characterized by elevated mechanical properties, has gained more importance in the last years. Nowadays, the cold and warm forging processes of carbon steels are widely used to form industrial parts due to their economic advantages, but there is still lack of extensive research on industrial process design and evaluation of the microstructural properties of cold-warm forged stainless steel parts.

In the last few decades, the environment concerning the recent forging industry has been rapidly changed. Now, near-net-shape or net-shape manufacturing processes are becoming a useful practice in metal forming, resulting in saving material and energy.

Many parts produced with machining can be manufactured at lower cost by cold and warm forging. Traditionally, forging design is carried out using mainly empirical guidelines, experience, and trial-and-error, which results in a long process development time and high production costs.

In order to avoid this, in recent years, computer-aided simulation approaches have proved to be powerful tools to predict and analyze material deformation during a metal forming operation. There are now many commercial finite-element (FE) packages to simulate forging and bulk metalworking processes. To date, most have focussed on predicting the shape of the final product after simple or complex single- or multi-stage forming operations. On the other hand, other aspects are being included in these numerical models, such as an improved understanding of the constitutive material behaviour, friction and lubrication conditions, and the properties of the final product, in order to predict more complicated phenomena such as tool life prediction, ductile fracture and microstructure evaluation.

The focus of this PhD thesis is the development of an innovative approach based on the design of integrated experimental procedures and modelling tools, in order to accurately re-design a range of industrial single-stage cold-warm forming processes to form stainless steel components and investigate the microstructural evolution of forged parts obtained at different forging temperatures. In addition, the design of a multi-stage cold forging process of a low-carbon steel and the prediction of surface defects that occur in each stage of the forming-sequence have been carried out.

To this aim, a series of tensile tests were conducted to evaluate the influence of temperature and strain rate on the materials elasto-plastic properties.

Furthermore, an innovative experimental setup was used to reproduce the realistic friction conditions at the tool-workpiece interface, in order to accurately predict metal flow during forging cycles.

Experimental data were subsequently validated and implemented in a commercial 3D-FE software and accurately calibrated to perform fully coupled numerical simulations for the reference processes.

Finally, the forged parts obtained were characterized by macro- and microstructural inspections in order to evaluate the presence of underfilling problems and surface defects, which were consistent with the numerical FE results coming from both simulated processes (i.e. single- and multi-stage forging), and to analyze the microstructural evolution of α and γ -phase during single-stage tests both at room temperature and from 400 to 700 °C.

The materials investigated in this work are low-carbon AISI 1005 ferritic-pearlitic steel (Wr. N. 1.0303), AISI 304L austenitic (Wr. N. 1.4307) and commercially named Duplex 2205 ferritic-austenitic stainless steel (Wr. N. 1.4462). The developed experimental tests

are suitable to proper evaluation of steels behaviour in terms of mechanical properties, and to precisely calibrate coupled numerical models when they are applied to conventional and re-design forging processes.

The techniques used in this work include: tensile tests, T-shape compression tests, visual inspections (i.e. supported by vernier calliper and micrometer measurements), hardness and micro-hardness tests, LOM (Light Optical Microscopy), FEG-ESEM (Field-Emission Gun Environmental Scanning Electron Microscope), EDS (Energy Dispersive X-ray Spectroscopy), EBSD (Electron Back Scattering Diffraction) and numerical models carried out with FORGE2011[®]-3D.

SOMMARIO

La possibilità di produrre componenti in acciaio inossidabile a costo limitato e caratterizzati da elevate proprietà meccaniche, ha assunto notevole importanza negli ultimi anni. Al giorno d'oggi, i processi di stampaggio a freddo e a semicaldo di acciai al carbonio sono ampiamente usati per produrre componenti industriali, grazie ai loro vantaggi economici, ma è ancora assente in letteratura un'ampia ricerca di nuovi metodi di progettazione industriale di processi di deformazione plastica a freddo e a semicaldo di prodotti in acciaio inossidabile, con la successiva valutazione delle proprietà microstrutturali.

Negli ultimi decenni, l'industria dei processi di stampaggio è cambiata rapidamente. Ora i processi produttivi near-net-shape o net-shape stanno diventando una pratica utile nella formatura dei metalli, garantendo notevoli risparmi di materiale ed energetici. Molti componenti, ottenuti con lavorazioni per asportazione di truciolo, possono essere prodotti a basso costo mediante stampaggio a freddo o a semicaldo. Tradizionalmente, la progettazione dei processi di forgiatura avviene utilizzando linee guida empiriche, basate sull'esperienza e su tentativi trail-and-error da parte dei progettisti, che si traducono poi in tempi di sviluppo dei processi e costi di produzione elevati.

Per evitare ciò, negli ultimi anni, gli approcci di simulazione numerica si sono dimostrati strumenti potenti per prevedere e analizzare la deformazione del materiale mediante processo di formatura. Attualmente sul mercato sono presenti molti pacchetti commerciali adatti a simulare i processi di forgiatura dei metalli e la maggior parte di essi sono concentrati sulla previsione della forma del prodotto finale dopo operazioni di formatura semplici o complesse, mono- o multi-stadio. Altri aspetti vengono inclusi in questi modelli numerici, quali una migliore comprensione del comportamento del materiale, delle condizioni di attrito e lubrificazione e delle proprietà del prodotto finale, per poter prevedere fenomeni più complicati come la stima della vita dell'utensile, delle condizioni di frattura duttile e la valutazione della microstruttura.

Lo scopo della presente tesi di dottorato è lo sviluppo di un approccio innovativo basato sulla progettazione di procedure sperimentali integrate con strumenti di modellazione numerica, per riprogettare accuratamente una serie di processi di forgiatura industriali mono-stadio adatti alla produzione di componenti in acciaio inossidabile a diverse temperature.

Inoltre è stata effettuata la riprogettazione di un processo di formatura multi-stadio a freddo di un acciaio a basso tenore di carbonio, con la successiva previsione dei difetti superficiali che si verificano in ogni fase della sequenza di formatura.

A tale scopo sono stati condotti una serie di test di trazione, per valutare l'influenza della temperatura e della velocità di deformazione sulle proprietà elasto-plastiche dei materiali considerati. Inoltre è stato realizzato un innovativo apparato sperimentale per riprodurre le condizioni di attrito reali all'interfaccia tra lo spezzone e l'utensile, al fine di prevedere con precisione il flusso del metallo in fase di deformazione plastica.

I dati sperimentali sono stati validati e implementati in un software commerciale agli elementi finiti 3D-FE e successivamente calibrati con precisione, per effettuare accurate simulazioni numeriche dei processi di riferimento.

I componenti forgiati ottenuti sono stati oggetto di indagini macro e microstrutturali, per valutare l'eventuale presenza di difetti superficiali, e analizzare l'evoluzione microstrutturale della fase α e γ a diverse temperature di forgiatura (i.e. 20, 400, 500, 600, 700 °C). I risultati sperimentali sono stati successivamente validati mediante simulazione numerica.

I materiali studiati in questo lavoro sono: acciaio ferritico-perlitico AISI 1005 a basso tenore di carbonio (Wr. N. 1.0303), AISI 304L austenitico (Wr. N. 1.4307) e ferritico-austenitico Duplex 2205 (Wr. N. 1.4462). Le prove sperimentali sviluppate sono adatte ad una corretta valutazione del comportamento degli acciai in termini di proprietà meccaniche, calibrando con precisione i modelli numerici se applicate a processi industriali di forgiatura tradizionali e riprogettati.

Le tecniche utilizzate in questo lavoro prevedono: test di trazione, test di compressione T-shape, controlli visivi (mediante calibro cinquantiesimale e micrometro), misure di durezza e microdurezza, microscopia ottica (LOM), microscopia elettronica a scansione ad emissione di campo (FEG-ESEM), spettroscopia a dispersione di energia (EDS), diffrazione da retrodiffusione elettronica (EBSD) e modelli numerici sviluppati in FORGE2011[®]-3D.

AIM OF THE WORK

Aim of the present work is to develop an innovative approach based on the design of integrated experimental procedures and modelling tools, in order to accurately re-design and optimize an industrial single-stage cold forging process applied to stainless steels and investigate its impact on the microstructural and mechanical properties of the forged components obtained. The same procedure has been carried out for the design of a multi-stage cold forging process of a low-carbon steel and the prediction of underfillings and surface defects formation. The numerical models, describing the different material flow behaviour of the steels considered, has been developed in the commercial FORGE2011®-3D software. The reference materials for most of the work have been the AISI 1005 (Wr. N. 1.0303) steel, the AISI 304L (Wr. N. 1.4307) and Duplex 2205 grade (Wr. N. 1.4462) stainless steel.

The following diagram represents the "leading thread" of the PhD thesis. It describes the relationships between the industrial case histories (i.e. the forging processes), numerical FE models and final forged components obtained (Fig. 1).

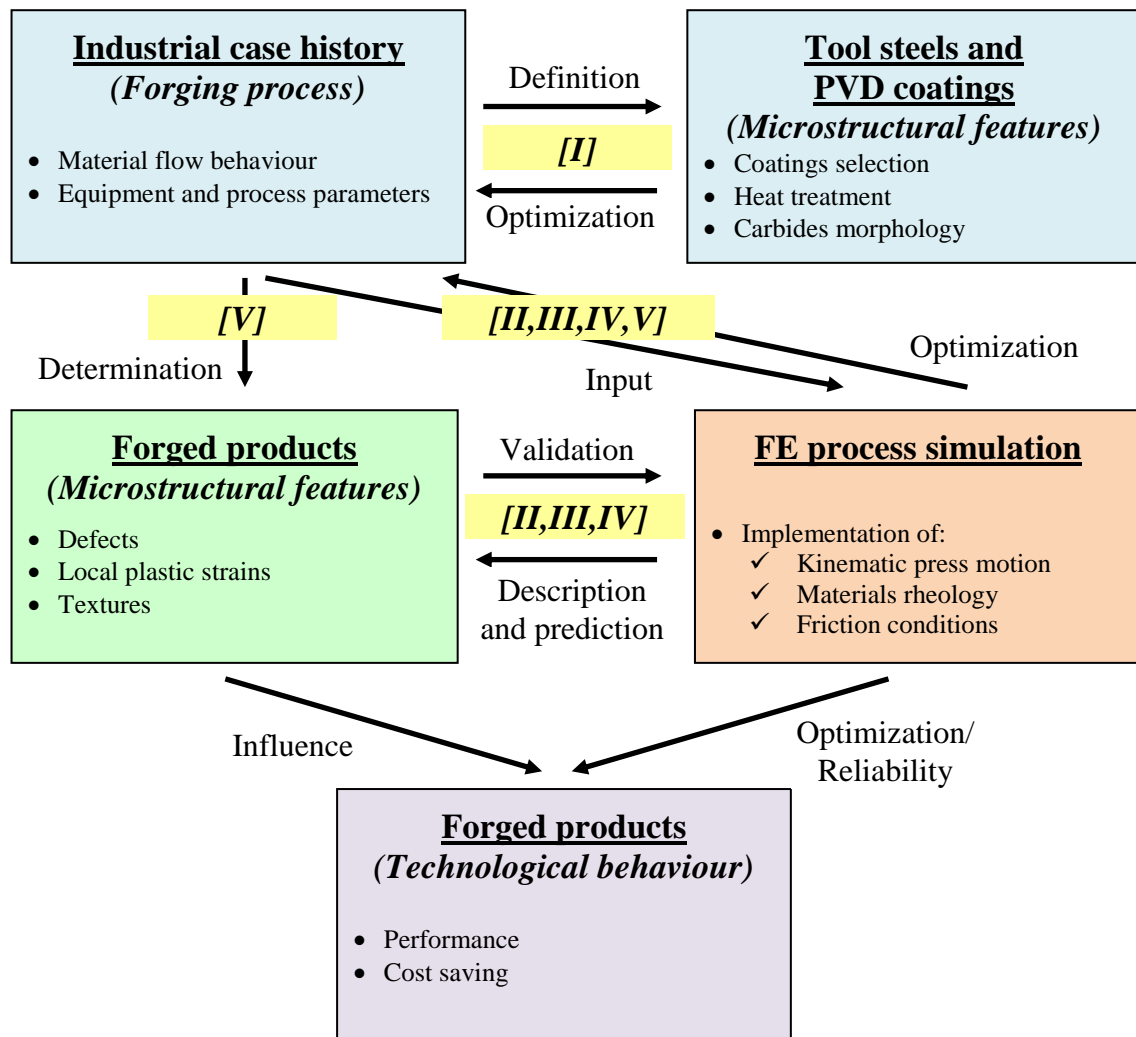


Fig. 1. PhD scheme of the thesis.

With reference to Fig. 1, the starting point is the type of process analyzed (i.e. how the forged component will be obtained), which requires the definition of specific parameters. At the same time, the FE models carried out for the design of the part need to be accurately calibrated, to perform fully coupled numerical simulations by using experimental tests (i.e. for the evaluation of material rheology behaviour and friction conditions). In addition, computer-aided simulation techniques in metal forming may reduce the long process development time and high production costs of a trial-and-error re-design of an existed industrial forging process (e.g. for testing a new wrought material). Moreover, the results of the FE models are finally compared with those obtained from the real forging process and a good agreement is observed (e.g. a systematic approach to predict underfilling and surface defects shows good agreement between numerical and experimental observations). The papers presented in this thesis go deeper into the various aspects illustrated in the previous diagram:

- The selection and the microstructural characterization of a series of tool steels and surface Physical Vapor Deposition (PVD) coatings used on cold forging processes;
- The simulating multi-stage cold forging process to reduce time-to-market and production costs, optimize the production-sequence design and predict the formation mechanisms of surface defects with good agreement between virtual and real defects observed;
- The FE re-design of an industrial single-stage process to form stainless steel forged components and the investigation of their microstructural grain evolution at different forging temperatures. This helps to reduce time-to-market, production costs and improve product quality of the new component.

In detail, the issues discussed in this thesis can be summarized as follows:

- Evaluation of heat treatment conditions on the microstructural characterization of different types of carbides on tool steels (i.e. conventional and powder metallurgy high-speed steels). Selection and microstructural investigation of different single and multi-layer Physical Vapor Deposition (PVD) coatings feasible to coat cold work tools (*Article I*);
- Forging-sequence re-design, carried out on a cold forging process by using computer-aided simulation techniques, in order to obtain a shorter development lead-time, lower production costs, savings in tool materials costs and the development of higher precision parts (*Article II and III*). Moreover, the formation mechanisms of surface defects in the optimized process-sequence analyzed have been studied through FEM simulations (*Article II and III*);
- Study of the feasibility of a single-stage cold forging process to form forged stainless steel components (*Article IV*) and subsequent re-design to create a warm forging cycle. A microstructural characterization of cold-forged stainless steels components, in order to evaluate the preferred orientation of α and γ -phase, has also been made (*Article IV*). In addition, the differences in the deformation behaviour of the two phases on an AISI 1005 low-carbon steel, AISI 304L and Duplex 2205 stainless steel are described qualitatively and quantitatively. The strain heterogeneities and microstructural evolution on γ -phase in stainless steels during warm forging process are also investigated. Finally, the strain hardening behaviour of the steels at cold and warm working conditions is analyzed (*Article V*).

PART 1

**METAL FORMING PROCESSES IN
MANUFACTURING**

1. General introduction

The manufacture of metal parts and assemblies can be classified, in a simplified manner, into five general areas: *primary shaping, metal forming, metal cutting, metal treatment and joining processes.*

Among all manufacturing processes, metal forming technology has a special place because it helps to produce parts of superior mechanical properties with minimum waste of material.

The term *metal forming* refers to a group of manufacturing methods by which the given material, usually shapeless or of a simple geometry, is transformed into a useful part without change in the mass or composition of the material. This part usually has a complex geometry with well-defined shape, size, accuracy and tolerances, appearance and properties.

In metal forming the material, a billet or a blanked sheet, is plastically deformed between tools (or dies) in one or more operations to obtain a product of relatively complex configuration. Forming to near-net or to net-shape dimensions drastically reduces metal removal requirements, resulting in significant material and energy savings.

Metal forming processes are usually classified according to two broad categories: *bulk, or massive, forming operations* (such as forging, extrusion, rolling, and drawing) and *sheet forming operations* (such as brake forming, deep drawing, and stretch forming).

In both types of process, the surfaces of the deforming metal and the tools are in contact, and friction between them may have a major influence on material flow. In *bulk forming*, the input material is in billet, rod, or slab form, and the surface-to-volume ratio in the formed part increases considerably under the action of largely compressive loading. In *sheet forming*, on the other hand, a piece of sheet metal is plastically deformed by tensile loads into a three-dimensional shape, often without changes in sheet thickness or surface characteristic.

Processes that fall under the category of *bulk forming* have the following distinguishing features [1]:

- The deforming material, or workpiece, undergoes large plastic (permanent) deformation, resulting in an appreciable change in shape or cross section;
- The portion of the workpiece undergoing plastic deformation is generally much larger than the portion undergoing elastic deformation and, therefore, elastic recovery after deformation is negligible.

Bulk forming processes are frequently used together with other manufacturing processes, in order to complete the transformation from the raw material to the finished and assembly-ready part. Desirable material properties for forming include low yield strength and high ductility. These properties are affected by temperature and rate of deformation (i.e. strain rate). When the work temperature is raised, ductility is increased and yield strength is decreased.

In relation to melting temperature (T_m), the effect of temperature gives rise to distinctions among [2]:

- *Cold forming* (workpiece initially at room temperature, i.e. $<0.25T_m$)
- *Warm forming* (workpiece heated above room temperature, but below the recrystallization temperature of the workpiece material, i.e. $0.25-0.65T_m$)
- *Hot forming* (workpiece heated above the recrystallization temperature, i.e. $>0.65T_m$).

Usually, the yield stress of a metal increases with increasing strain (or deformation) during cold forming and with increasing strain rate (or deformation rate) during hot forming.

Fig. 1 reports the iron-carbon phase diagrams, which enable to identify the range of working temperatures for cold and warm forging.

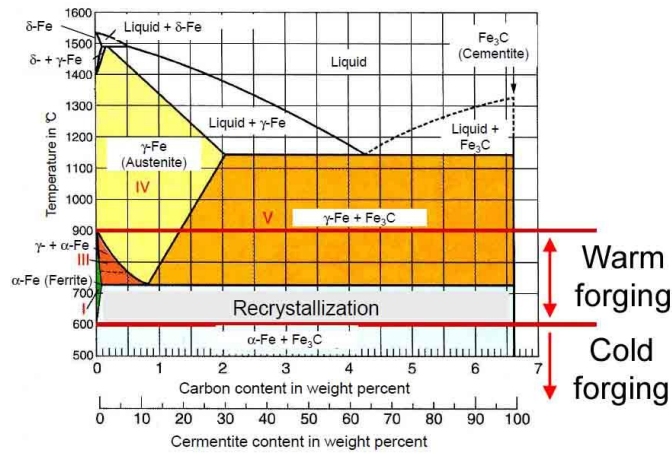


Fig. 1. The iron-carbon phase diagrams for steel forged metal.

The design, analysis, and optimization of forming processes require knowledge regarding metal flow, stresses, and heat transfer as well as technological information related to lubrication, heating and cooling techniques, material handling, die design and manufacture and forming equipment. A considerable amount of information on the general aspects of metal forming is available in the literature [1-7].

The following list outlines some of the important areas of application of workpieces produced by metal forming [4]:

- Components for automobiles and machine tools as well as for industrial plants;
- Hand tools, such as hammers, pliers, screwdrivers, and surgical instruments;
- Fasteners, such as screws, nuts, bolts, and rivets;
- Containers, such as metal boxes, cans, and canisters;
- Construction elements used in tunneling, mining, and quarrying (i.e. roofing and walling elements, pit props, etc.);
- Fittings used in the building industry, such as for doors and windows.

Examples of specific bulk forming processes are listed in Table 1.

Forging	Rolling	Extrusion	Drawing
Closed-die forging with flash	Sheet rolling	Nonlubricated hot extrusion	Drawing
Closed-die forging without flash	Shape rolling	Lubricated direct hot extrusion	Drawing with rolls
Coining	Tube rolling	Hydrostatic extrusion	Ironing
Electro-upsetting	Ring rolling		Tube sinking
Forward extrusion forging	Rotary tube piercing		
Backward extrusion forging	Gear rolling		
Hobbing	Roll forging		
Isothermal forging	Cross rolling		
Nosing	Surface rolling		
Open-die forging	Shear forming		
Rotary (orbital) forging	Tube reducing		
Precision forging			
Metal powder forging			
Radial forging			
Upsetting			

Tab. 1. Classification of bulk (massive) forming processes [1].

1.1. Cold and warm forging

Cold forging is defined as forming of a bulk material at room temperature with no initial heating of the preform or intermediate stages (i.e. $<0.25T_m$, cf. §1 of "Part 1"). *Cold extrusion* is a special type of forging process wherein the cold metal flows plastically under compressive forces into a variety of shapes. These shapes are usually axisymmetric with relatively small nonsymmetrical features. The terms *cold forging* and *cold extrusion* are often used interchangeably and refer to well-known forming operations such as extrusion, upsetting or heading and coining [8-12]. Generally, several forming steps are used to produce a final part of relatively complex geometry, starting with a slug or billet of simple shape. Some basic techniques of cold forging are illustrated in Fig. 2 [13]. Through a combination of these processes, a very large number of parts can be produced.

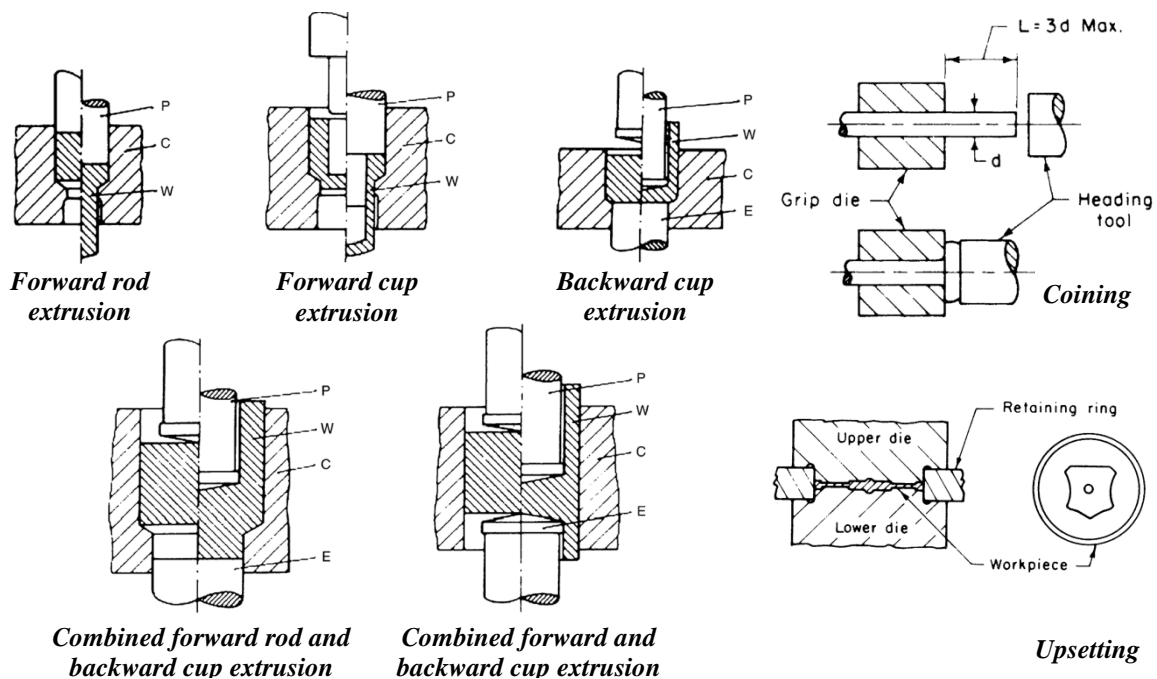


Fig. 2. Various cold forging techniques (P, Punch; C, Container; W, Workpiece; E, Ejector).

Some of the advantages provided by the cold forging process are:

- High production rates;
- Excellent dimensional tolerances and surface finish for forged parts;
- Savings in material and machining;
- Higher tensile strengths in the forged parts than in the original materials;
- Favorable grain flow to improve strength.

In cold forging of parts with relatively complex geometries, forging pressures are extremely high and the ductility of the material is low. As a result, short tool life and defects formed during forging limit the economic use of the cold forging processes. Consequently *warm forging* (i.e. forging at temperatures below recrystallization temperature, cf. §1 of "Part 1") is commonly used [1].

This forging process may be interpreted as thermomechanical processing at elevated temperature to achieve the following advantages:

- A reduction in flow stress, strain hardening, tooling loads and forging press loads;
- Greater ductility and toughness of the forged parts;
- Improved accuracy as compared to hot forging;
- Enhanced product properties through grain refinement.

Warm forging requires determination of the optimum forging temperature. On the other hand this technology is still undergoing development, particularly in aspects of surface treatment, lubrication and tooling.

By far the largest area of application of cold and warm forging is the automotive. However, cold forged parts are also used in manufacturing bicycles, motorcycles, farm machinery, off-highway equipment, nuts and bolts.

2. Cold and warm forging as operation system

A cold-warm forging system, as shown in Fig. 3, reports all the input variables such as the billet or blank (i.e. geometry and material), the tooling (i.e. geometry and material), the condition at the tool/material interface, the mechanism of plastic deformation, the equipment used, the characteristics of the final product and, finally, the plant environment where the process is being conducted [14].

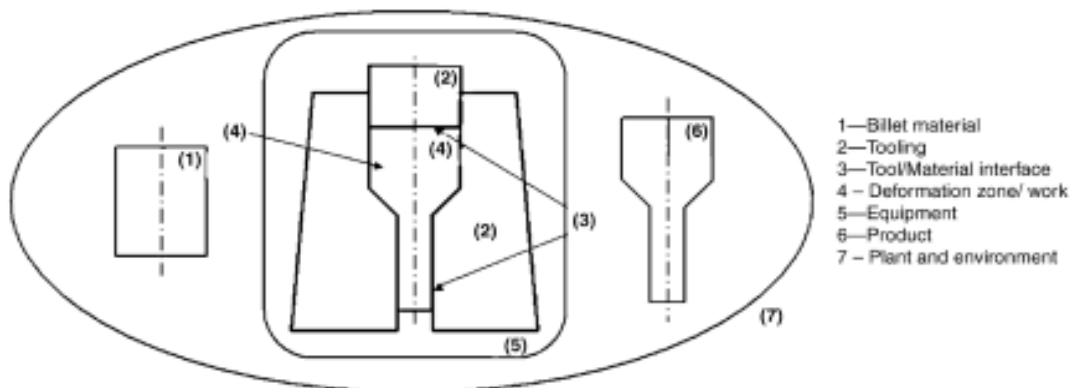


Fig. 3. Cold and warm forging as a system [14].

In a cold-warm forging process, a simple part geometry is transformed into a complex one, whereby the tools "store" the desired geometry and impart pressure on the deforming material through the tool/material interface. Forging processes usually produce little or no scrap and generate the final part geometry in a very short time. As a result, cold and warm forging offers potential savings in energy and material. In addition, for a given weight, parts produced by forging exhibit better mechanical, metallurgical properties and reliability than those manufactured by casting or machining [15].

Forging is an experience-oriented technology. Throughout the years, a great deal of know-how and experience has been accumulated in this field, largely by trial-and-error methods. The physical phenomena describing a forging operation are difficult to express with quantitative relationships. The metal flow, the friction at the tool/material interface, the heat generation during plastic flow, and the relationships between microstructure and process conditions are difficult to predict and analyze.

Often in producing discrete parts, several forging operations (i.e. preformings) are required. For a given operation (i.e. preforming or finish forging), such design essentially

consists of: a) establishing the kinematic relationships between the deformed and undeformed part (i.e. predicting metal flow), b) establishing the limits of formability (i.e. determining whether it is possible to form the part without surface or internal failure) and c) predicting the forces and stresses necessary to execute the forging operation so that tooling and equipment can be designed or selected.

In Fig. 3 the "systems approach" in cold-warm forging allows study of the input/output relationships and the effect of process variables on product quality and process economics. The key to a successful metal forming operation (i.e. to obtaining the desired shape and properties), is the understanding and control of metal flow. The local metal flow is in turn influenced by the following input variables:

Billet material

- Geometry and initial conditions (i.e. size, temperature, history/pre-strain);
- Flow stress and forgeability;
- Thermal and physical properties;

Tooling

- Tool geometry and material;
- Surface lubrication;

Conditions at the tool/material interface

- Lubricant type, temperature, application and removal;
- Lubricity and frictional shear stress;

Equipment

- Speed/production rate;
- Force/energy capabilities;

Deformation Zone

- The mechanics of deformation (e.g. model used for analysis);
- Metal flow, strain, strain rate (i.e. kinematics);
- Stresses (i.e. variation during deformation);
- Temperatures (i.e. heat generation and transfer);

Product

- Dimensional accuracy/tolerances;
- Surface finish;
- Microstructural and mechanical properties;

Environment

- Available manpower;
- Plant and production facilities and control.

2.1. Steels for cold and warm forging

Selection of a steel for a forged component is an integral part of the design process. A thorough understanding of the end use of the finished part will serve to define the required mechanical properties, surface finish requirements, tolerance to non-metallic inclusions, and the attendant inspection methods and criteria.

Steels can be classified by a variety of different systems. The classification depending on the chemical composition is the most widely used.

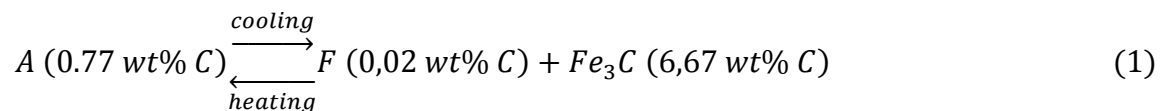
Out of this classification, steels may be categorized into several main classes:

- Low-carbon steels contain up to 0,30% C. The largest category of this class of steel is usually in the cold-rolled and annealed condition. The C content for these high-formability steels is very low, less than 0,10%, with up to 0,40% Mn.
- Medium-carbon steels are similar to low-carbon steels except that C ranges from 0,30 to 0,60% and the Mn from 0,60 to 1,65%. Increasing C content to approximately 0,50% with an accompanying increase in Mn allows medium-carbon steels to be used in the quenched and tempered condition.
- High-carbon steels contain from 0,60 to 1,00% C with Mn contents ranging from 0,30 to 0,90%.
- Ultrahigh-carbon steels are experimental alloys containing approximately 1,25 to 2,00% C.

All steels that exhibit ductility at room temperature and below recrystallization temperature can be respectively cold and warm forged. Stainless steels usually are not easily forged. Especially, cold forging of austenitic or austenitic-ferritic steels require high forces and tool pressures. Furthermore, these materials are difficult to lubricate. Cold forging of stainless steel is sometimes limited due to lack of information on the behaviour of the material [16]. Steels for cold forging are supplied as rolled or drawn rod or wire as well as in the form of sheared or sawed-off billets.

2.1.1. Low-carbon steels

Generally, C content is kept low in steels that require high ductility and high toughness. Low-carbon steels (<0,30% C) are characterized by a ferritic-pearlitic structure at as-received conditions. Pearlite is the name given to the microstructure produced from austenite (A) during cooling of a steel by the following solid-state reaction (Eq. (1)):



In the case of low-carbon steels, the ferrite (F) and cementite (Fe_3C) form as roughly parallel lamellae to produce a composite lamellar two-phase structure named pearlite [17].

Forgeability and extrudability

Forgeability is the relative ability of a steel to flow under compressive loading without fracturing. Except for resulfurized and rephosphorized grades, most carbon and low-alloy steels are usually considered to have good forgeability. Carbon and alloy steels are by far the most commonly forged materials, and are readily forged into a wide variety of shapes using cold-warm forging processes and standard equipment.

Extrusion ratio (R) is determined by dividing the original area (A_0) undergoing deformation by the final deformed area (A_f) of the workpiece (Eq. (2)):

$$R = \frac{A_0}{A_f} \quad (2)$$

Because volume remains constant during extrusion, the extrusion ratio can also be estimated by increase in length. An extrusion ratio of 4 to 1 indicates that the length has increased by approximately a factor of four.

The *extrudability* of steel decreases with increasing C or alloy content. It is also adversely affected by greater hardness. In addition, free-machining additives (i.e. S or Pb) and non-metallic inclusions are detrimental to extrudability.

Carbon content

Fig. 4 shows the effects of carbon content, type of annealed structure, and R on the ram pressure required to forward extrude a specific shape from carbon steels. Most carbon and alloy steels that are extruded contain up to 0.25% C. These data show that ram pressures are essentially the same for steels containing 0.19 and 0.26% C, regardless of the other variables, but that ram pressure is markedly increased as carbon content reaches 0.34 and 0.38%. Fig. 5 illustrates the effect of tensile strength on extrudability in terms of ram pressure for both the backward and forward extrusion of low-carbon and medium-carbon steels at different extrusion ratios. Because an increase in R results in a corresponding increase in the amount of cold deformation, the effects of work hardening will normally vary directly with R .

Alloy content

For a given carbon content, most alloy steels are harder than plain carbon steels and are therefore more difficult to extrude. Most alloy steels also work harden more rapidly than their carbon steel counterparts; therefore, they sometimes require intermediate annealing.

Hardness

Steels that have been spheroidize annealed are in their softest condition and are therefore preferred for extrusion. Fig. 4 shows that spheroidized steels are extruded at lower ram pressures than hot-rolled or mill-annealed steels, regardless of other variables. The data in Fig. 5 show that ram pressure must be increased as tensile strength increases for steels of low-to-medium carbon content at three extrusion ratios.

Non-metallic inclusions

Silicate inclusions have been found to be the most harmful. Therefore, some steels have been deoxidized with Al rather than Si in an attempt to keep the number of silicate inclusions at a minimum. The Al-killed steels have better extrudability in severe applications.

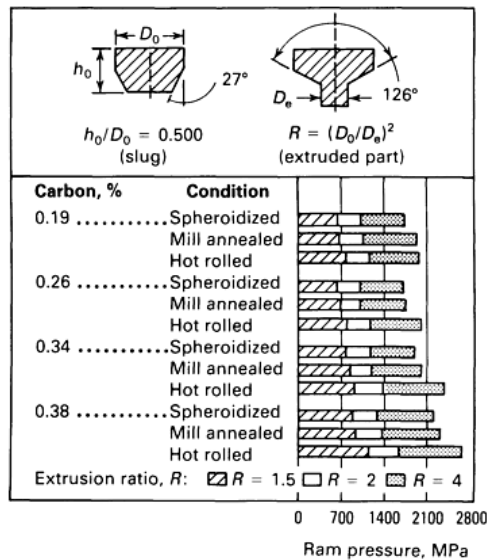


Fig. 4. Effect of C content, annealing treatment, and extrusion ratio (R) on maximum ram pressure in the forward extrusion of the carbon steel part from the preformed slug [3].

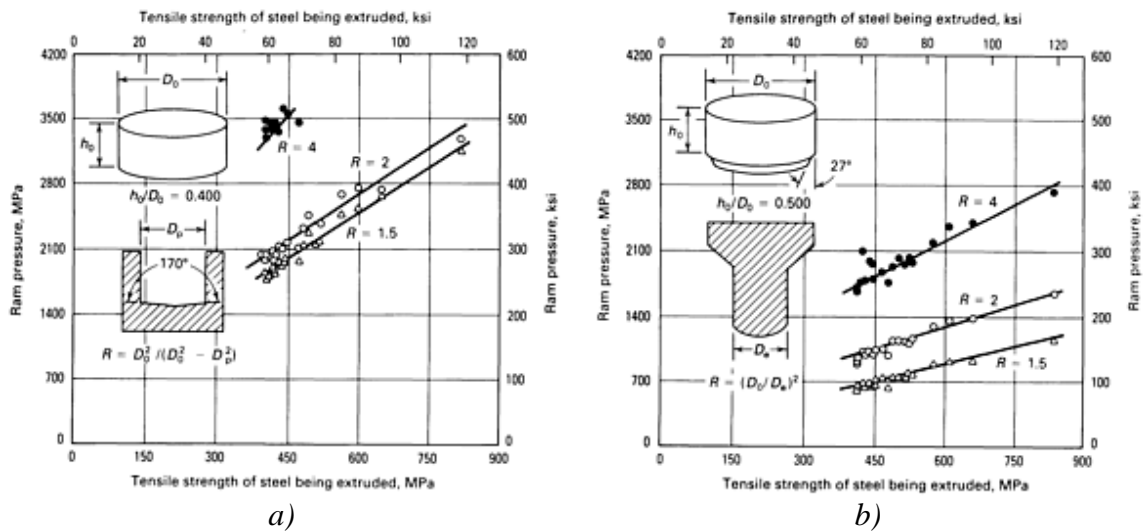


Fig. 5. Effect of tensile strength on ram pressure required for a) backward and b) forward extrusion of low and medium-carbon steels at different extrusion ratios. Data are for AISI 1000, 1100, and 1500 series steels containing 0.13 to 0.44% C [3].

Cost

The cost of steel as a percentage of the total manufacturing cost of forgings is shown in Fig. 6. These curves are based on an average of many actual forgings that are different in number of forging and heat-treating operations required, cost of steel, quantity, and setup cost. It should not be inferred from these data that an average 14 kg stainless steel forging will cost 34% more than an average carbon steel forging of the same weight.

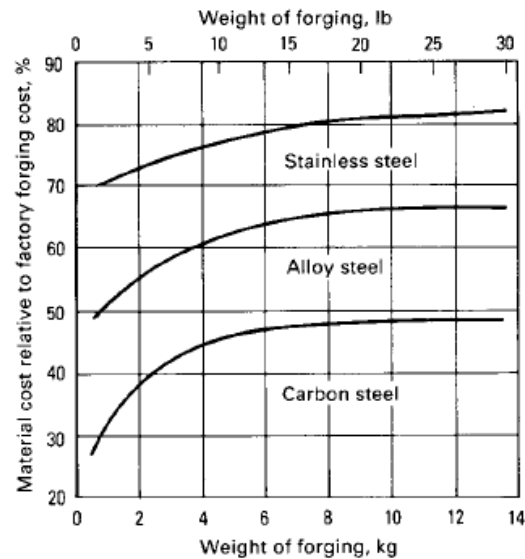


Fig. 6. Cost of steel as a percentage of total cost of forgings [3].

2.1.2. Stainless steels

The importance of stainless steels is shown in the plenitude of applications that rely on their use [17]. In order to impart "stainlessness" to steels, Cr must be added to at least about 11 wt%. At this Cr level, an adherent, self-healing Cr oxide can form on the steel surface in relatively benign environments. However, to guard against pitting and rusting in more hostile environments or in the presence of elements like C, higher Cr contents must be added.

Stainless steels may be categorised into several main classes [18,19]. These are ferritic, austenitic, martensitic, duplex, precipitation hardening and Mn-N substituted austenitic stainless steels. The different properties of the various stainless steels have been studied extensively for a very long period and thus are very well documented in the literature. An early handbook on stainless steels is a very good source on this topic [20].

The fundamental criterion in the selection of a stainless steel is generally that it can survive with virtually no corrosion in the environment in which it is to be used. The choice among the stainless steels that can be used in that environment is then based on the alloy from which the component can be produced at the lowest cost, including maintenance, over the intended service life. The less-expensive martensitic grades are used instead of austenitic when high strength and hardness are better achieved by heat treating rather than by cold work, and mechanical properties are more important than corrosion resistance. Duplex grades match austenitic grades in corrosion resistance and have higher strength in the annealed condition but present the designer with challenges with regard to embrittling phases that can form with prolonged exposure to elevated temperatures and only moderate ductility like the ferritic alloys.

Global production and consumption

The importance of stainless steels may be appreciated by looking at the tonnages of their production and consumption in some of the major continents since the year 2000. Table 2 clearly shows that the tonnages of production of stainless steels and heat resisting steels are constantly on the rise. It shows that Asia accounts for a large portion of stainless steels produced worldwide. Among Asian countries, China is the world's leading producer of stainless steels [21,22], with per capita consumption reaching over 4,6 kg in 2006 [23].

	Year						
	2001	2002	2003	2004	2005	2006	2007
Western Europe/Africa	8210	8628	9043	9422	8823	9972	9700
Central and Eastern Europe	285	279	322	318	310	363	400
The Americas	2289	2735	2830	2933	2688	2951	2850
Asia	8403	9048	10645	11897	12498	15074	16850
World	19187	20690	22840	24570	24319	28359	29800

Tab. 2. Tonnes of stainless and heat resisting crude steel produced in major continents from 2001 to 2007 (in 000 metric tonnes) [22].

2.1.2.1. Austenitic stainless steels

The austenitic stainless steel is the most commonly used grade, because it provide very predictable levels of corrosion resistance with excellent mechanical properties. Austenitic stainless steels have a face-centered cubic (fcc) structure. This structure is attained through the liberal use of austenitizing elements such as Ni, Mn, and N. These steels are essentially non-magnetic in the annealed condition and can be hardened only by cold working. They usually possess excellent cryogenic properties and good high-temperature strength. Cr content generally varies from 16 to 26%, Ni up to about 35% and Mn up to 15%. The 2xx series steels contain N, 4 to 15,5% Mn, and up to 7% Ni. The 3xx types contain larger amounts of Ni and up to 2% Mn. Mo, Cu, Al, Ti and Nb may be added to confer certain characteristics such as halide pitting resistance or oxidation resistance. S or Se may be added to certain grades to improve machinability.

Austenitic alloys are generally classified into three groups:

- Lean alloys, such as 201 and 301, are generally used when high strength or high formability is the main objective since the lower, yet tailorable, austenite stability of these alloys gives a great range of work-hardening rates and great ductility. Richer alloys, such as 305, with minimal work hardening are the high-alloy, lowest work-hardening rate grade for this purpose. The general-purpose alloy 304 is within this group.
- Cr-Ni alloys when the objective is high temperature oxidation resistance. This can be enhanced by Si and rare earth (RE) elements. If the application requires high-temperature strength, C, Ni, Nb and Mo can be added. 302B, 309, 310, 347, and various proprietary alloys are found in this group.
- Cr, Mo, Ni and N alloys when corrosion resistance is the main objective. Alloys such as Si and Cu are added for resistance to specific environments. This group includes 316L, 317L, 904L, and many proprietary grades.

Lean alloys

Lean austenitic alloys constitute the largest portion of all stainless steel produced. Alloys with less than 20% Cr and 14% Ni fall into this unofficial category.

These grades are easily formable and can be given many attractive and useful surface finishes, so they are general purpose alloys. Table 3 lists some typical compositions of the most commonly used lean austenitic alloys. The main difference among the lean austenitic alloys lies in their work-hardening rate: the leaner the alloy, the lower the austenite stability. As unstable alloys are deformed, they transform from austenite to the much harder martensite. This increases the work-hardening rate and enhances ductility since it

delays the onset of necking since greater localized deformation is more than offset by greater localized strain hardening.

AISI Designation	C	N	Cr	Ni	Mo	Mn	Si	Others		
201	0.08	0.07	16.3	4.5	0.2	7.1	0.45	0.001 S	0.03 P	0.2 Cu
201LN	0.02	0.13	16.3	4.5	0.2	7.1	0.45	0.001 S	0.03 P	0.5 Cu
301	0.08	0.4	16.6	6.8	0.2	1.0	0.45	0.001 S	0.03 P	0.3 Cu
304	0.05	0.05	18.3	8.1	0.3	1.8	0.45	0.001 S	0.03 P	0.3 Cu
304L	0.02	0.09	18.3	8.1	0.3	1.8	0.45	0.013 s	0.030 P	0.4 Cu
305	0.05	0.02	18.8	12.1	0.2	0.8	0.60	0.001 S	0.02 P	0.2 Cu
321	0.05	0.01	17.7	9.1	0.03	1.0	0.45	0.001 S	0.03 P	0.4 Ti
316L	0.02	0.0	16.4	10.5	2.1	1.8	0.50	0.010 S	0.03 P	0.4 Cu

Tab. 3. Typical compositions of the most commonly used lean austenitic alloys [20].

Effects of Composition

Chromium

The film is first observed at about 10.5% Cr, but it is rather weak at this composition and affords only mild atmospheric protection. Increasing the Cr content to 17-20%, typical of the austenitic stainless steels, or to 26-29%, as possible in the newer ferritic stainless steels, greatly increases the stability of the passive film. However, higher Cr may adversely affect mechanical properties. Therefore, it is often more efficient to improve corrosion resistance by altering other elements, with or without some increase in Cr.

Nickel

In sufficient quantities, Ni will stabilize the austenitic structure; this greatly enhances mechanical properties. Ni is effective in promoting repassivation, especially in reducing environments. Increasing Ni content to about 8 to 10% decreases resistance to stress-corrosion cracking (SCC), but further increases begin to restore SCC in most service environments is achieved at about 30% Ni. In the newer ferritic grades, in which the Ni addition is less than that required to destabilize the ferritic phase, there are still substantial effects. In this range, Ni increases yield strength, toughness and resistance to reducing acids, but makes the ferritic grades susceptible to SCC in concentrated magnesium chloride (MgCl₂) solutions [24-26]. All austenitic stainless steels are susceptible to chloride cracking (Fig. 7).

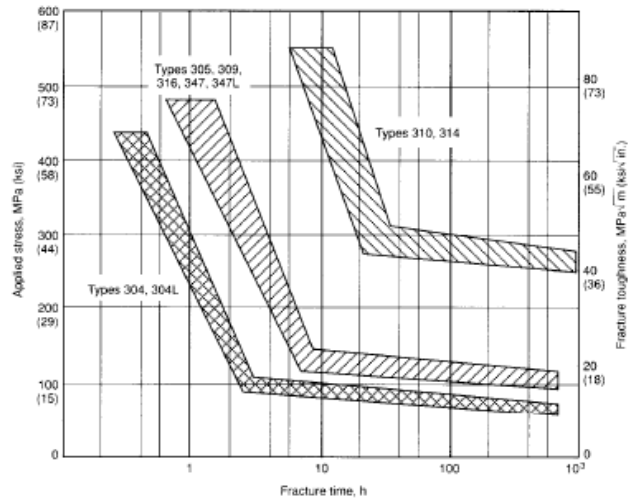


Fig. 7. Relative SCC behaviour of austenitic stainless steels in boiling magnesium chloride [27].

Manganese

In moderate quantities and in association with Ni additions, Mn will perform many of the functions attributed to Ni. However total replacement of Ni by Mn is not practical. High Mn steels have some unusual and useful mechanical properties, such as resistance to galling. Mn interacts with S in stainless steels to form MnS sulfides, which can have substantial effects on corrosion resistance.

Molybdenum

In combination with Cr, Mo is very effective in terms of stabilizing the passive film in the presence of chlorides. Mo is especially effective in increasing resistance to the initiation of pitting and crevice corrosion.

Carbon

C is useful to the extent that it provides strength in the high-temperature applications of stainless steels. In all other applications, C is detrimental to corrosion resistance through its reaction with Cr.

Nitrogen

N is beneficial to austenitic stainless steels in that it enhances pitting resistance, retards the formation of the Cr-Mo σ (sigma) phase and strengthens the steel.

Forgeability and extrudability

In cold and warm forging applications, a lower rate of work hardening is usually preferable and can be obtained in the austenitic alloys that have higher Ni contents, notably, grades 304, 304L, and 305.

In general, the austenitic alloys are more difficult to form as the Ni content or both the Ni and the Cr contents are lowered, as in grade 301. Such alloys show increased work-hardening rates and are less suitable for cold and warm extrusion or multiple forming operations. The presence of the stabilizing elements Nb, Ti and Ta, as well as higher C contents, also exerts an adverse effect on the forming characteristics of the austenitic stainless steels. Therefore, the forming properties of grades 321 and 347 stainless steel are less favorable than those of grades 302, 304, and 305.

The curves for 1008 low-carbon steel are included in Fig. 8 as a reference for the evaluation of stainless steels. Fig. 8 shows that cold work does not increase the strength of degree 1008 as rapidly as it does that of type 301 and the ferritic alloys.

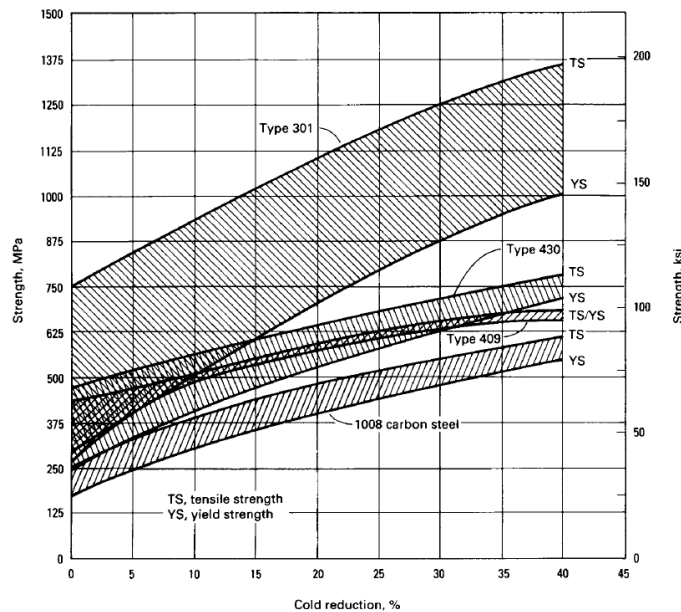


Fig. 8. A comparison of work-hardening qualities of degree 301 austenitic stainless steel, degrees 409 and 430 ferritic stainless steels, and 1008 low-carbon steel [3].

Based on forging pressure and load requirements, austenitic stainless steels are considerably more difficult to forge than carbon or low-alloy steels. Forging load requirements and forgeability vary widely among different types of austenitic stainless steels and compositions.

The relative forging characteristics of austenitic stainless steels can be most easily depicted through examples of closed-die forgings. The forgeability trends these examples establish can be interpreted in light of the grade, type of part and forging method to be used.

Stainless steels of the 300 series can be forged into any of the hypothetical parts illustrated in Fig. 9. However, the forging of stainless steel into shapes equivalent in severity to part 3 may be prohibited by shortened die life (20 to 35% of that obtained in forging such a shape from carbon or low-alloy steel) and by the resulting high cost. For a given shape, die life is shorter in forging stainless steel than in forging carbon or low-alloy steel.

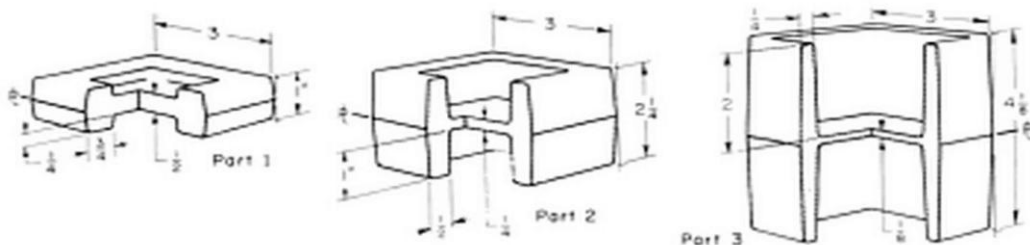


Fig. 9. Three degrees of forging severity. Dimensions given in inches [3].

Forgings of mild severity, such as part 1 in Fig. 9, can be produced economically from any stainless steel with a single heating and about five blows. Forgings approximating the severity of part 2 can be produced from any stainless steel with a single heating and about

ten blows. For any type of stainless steel, die life in the forging of part 1 will be about twice that in the forging of part 2.

Part 3 represents the maximum severity for forging all stainless steels and especially those with high strength at elevated temperature, namely types 309, 310, 314, 316, 317, 321 and 347. Austenitic stainless steels are more difficult to forge than the straight-chromium types, but are less susceptible to surface defects. Equally important restrictions in forging the austenitic stainless steels apply to the finishing temperatures. The stabilized or extra low-carbon austenitic stainless steels, which are resistant to sensitization, are sometimes strain hardened by small reductions at temperatures well below the forging temperature. Strain hardening is usually accomplished at 535 to 650 °C (referred to as warm working). When minimum hardness is required, the forgings are solution annealed.

A forgeability comparison, as defined by dynamic hot hardness, is provided in Fig. 10.

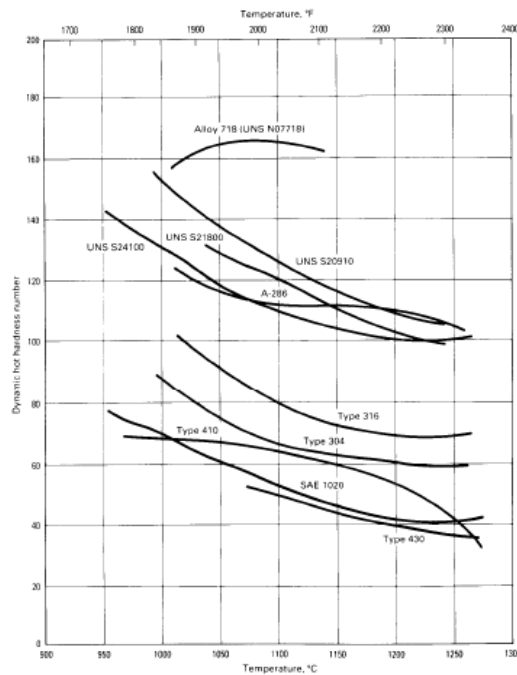


Fig. 10. Comparative dynamic hot hardness versus temperature (forgeability) for various ferrous alloys [3].

2.1.2.2. Duplex stainless steels

Duplex stainless steels (DSS) are a particular category of stainless steels characterized by a biphasic microstructure with about equal proportions of austenite and ferrite.

The mixed ferrite/austenite microstructure leads to different advantages if compared with the unique structure of the austenitic and ferritic stainless steels. In fact, DSS show more toughness than most ferritic grades, improved chloride stress-corrosion-cracking (SCC) resistance than most austenitic grades, and higher strength than most grades of either type. DSS are also less expensive than austenitic stainless steels with similar corrosion resistance, due to a lower Ni content.

Nowadays duplex stainless steels comprise almost 1% of all stainless steels production, however their sector is continuously growing. Some statistics reported the trend of DSS market during the last years. Research from the ISSF reveals that production increased and, in 2008, reached 22.000 metric tonnes a month [28]. Even Gagnepain revealed the growth in DSS market, especially concerning with new grade DSS, as reported in Fig. 11 [29].

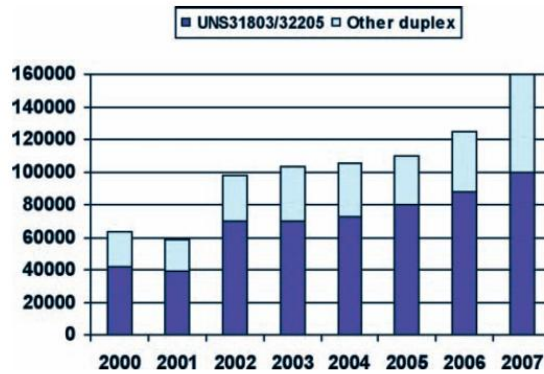


Fig. 11. Crude productions of duplex stainless steel according to global markets [29].

Today the most common duplex grade is UNS S31803/S32205 (EN 1.4462) or commercially named 2205, characterized by a nominal chemical composition of 22% Cr, 5% Ni, 3% Mo, and 0.16% N. This steel is used for a wide area of applications. The DSSs of the previous generation showed quite good resistance to general corrosion and chloride stress-corrosion cracking.

The 2205 DSS provides corrosion resistance superior to that of AISI Type 304, 316 and 317 austenitic stainless steels in various media. 2205 DSS is commonly used as welded pipe and welded sheet product as well as tubular components for applications in environments where resistance to general corrosion and SCC are important. Moreover 2205 DSS has higher mechanical properties than austenitic stainless steels. However the cost of 2205 DSS still remained quite high.

Recently some new duplex grades have been introduced in the market following the aim to reduce alloying elements than 2205 grade and to maintain comparable corrosion resistance of the 304 and 316 austenitic stainless steels. For applications in more aggressive environments Mo, Cu and W alloying elements are added.

The duplex family is now an industrial success and represents about 1% of the total stainless steel market. An annual growth of more than 10% is expected [30].

Duplex stainless steels are generally classified into four groups:

- Lean duplex (such as 2304 or as 2101, with 0.05-0.6 wt% of Mo);
- 2205, the most common grade which covers more than 80% of duplex use;
- 25Cr duplex (such as 255 and DP-3);
- Superduplex, with 25-26 Cr and increased Mo and N compared with the 25 Cr grades, including grades such as 2507, Zeron 100, UR52N, and DP-3W.

Table 4 shows the chemical composition of the modern wrought duplex stainless steels.

Grade	UNS	C	Cr	Ni	Mo	Mn	N	Cu	W
2304	S32304	0.03	21.5-24.5	3.0-5.5	0.0-0.6	2.5	0.05-0.20	-	-
2205	S31803	0.03	21.0-23.0	4.5-6.5	2.5-3.5	2.0	0.08-0.20	-	-
DP-3	S31260	0.03	24.0-26.0	5.5-7.5	5.5-7.5	1.0	0.10-0.30	0.20-0.80	0.10-0.5
UR52N	S32520	0.03	24.0-26.0	5.5-8.0	3.0-5.0	1.5	0.20-0.35	0.50-3.00	-
255	S32550	0.04	24.0-27.0	4.5-6.5	2.9-3.9	1.5	0.10-0.25	1.50-2.50	-
DP-3W	S39274	0.03	24.0-26.0	6.8-8.0	2.5-3.5	1.0	0.24-0.32	0.20-0.80	1.50-2.5
2507	S32750	0.03	24.0-26.0	6.0-8.0	3.0-5.0	1.2-2.0	0.24-0.32	0.50	-
Zeron 100	S32760	0.03	24.0-26.1	6.0-8.1	3.0-4.0	1.0	0.20-0.30	0.50-1.00	0.50-1.0

Tab. 4. Chemical composition in wt.% of wrought duplex stainless steel grades with the corresponding Unified Numbering System (UNS) [31].

Forgeability and extrudability

Duplex stainless steels have about twice the yield strength of most austenitic stainless steels. Their elongation, toughness and work-hardening rates are generally intermediate to those of the usual austenitic and ferritic grades. Duplex stainless steels can be cold formed and expanded. Their higher strength relative to their austenitic counterparts necessitates greater loads in cold-forming operations. Because elongation is lower, they should be formed to more generous radii than fully austenitic materials. Heavily cold-formed sections (>25%) should be fully annealed and quenched. Full annealing is conducted in the temperature range of 1010 to 1100 °C followed by a rapid cooling.

Mechanical properties

Many authors have studied the relation between mechanical properties and microstructure in DSS [32-35].

The yield strength of DSS is two-three times that of AISI 304 austenitic stainless steel. The higher strength properties are related to the presence of ferrite which is, for the same interstitial content, stronger than austenite. However ferrite has also lower ductility. In the DSS the presence of ferrite is not the only reason for high strength properties. It has been found that DSS has stronger ferrite than those of common ferritic stainless steels. This is due to the smaller grain size in DSS that contributes to enhance the strength, according to Hall-Petch relation. The effect of both the volume fraction of ferrite and grain size was extensively analyzed by Floreen and Hayden [33].

Finally it was found that yield strength, tensile strength and hardness are improved after cold rolling, with a slight loss in elongation [36]. The fatigue strength of DSSs is directly related to the yield strength [34]. Hayden and Floreen [33] assessed the relation between grain size and fatigue strength, stating that better fatigue properties were reached with duplex structure than with single phase. Grain boundaries act as obstacle to cracks propagation [36]. Low fatigue resistance can be enhanced both by N additions thus increasing austenite volume fraction, which avoid brittle fracture [37]. In high cycle fatigue tests the failure mechanism was mainly governed by ferritic phase [38]. Cold deformation seems to have slight effects on toughness at low temperatures [36], as shown by Fig. 12.

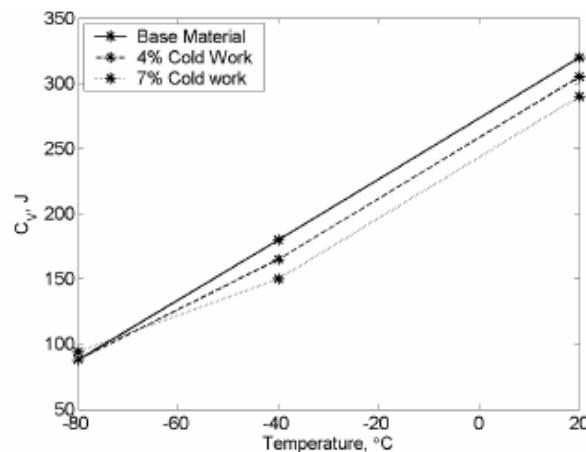


Fig. 12. Effect of cold working on toughness properties in DSS [36].

Applications

The typical sectors where DSS find application are mainly oil production, petrochemicals and desalination plants. DSS are used in oil production industry thanks to their resistance in conditions of SCC and localized corrosion [39-41]. In general in petrochemical industry applications corrosion environments are less aggressive than the ones observed in oil refineries [39]. However the production of organic acids can cause corrosion problems, so duplex and superduplex, especially DSS S32803/S32205 and S32750 were found to be suitable materials for such applications. Since 2006 the application area covered by DSS became larger. Recent statistic data states that traditional applications as oil and gas, offshore and petrochemical declines from 27% to 7%. While segments with increased market share include (waste) water (9% to 18%), construction and civil engineering (6% to 12%) and power generation (1% to 7%) [42]. DSSs are of great interest also in lightweight automotive design. This is due to the advantageous combination of many properties as corrosion resistance, surface quality, high strength and formability. Moreover high energy absorption in crash situation enhances the safe use this class of steels [43].

2.2. Equipment

The selection of a press machine for a given process is influenced by the time, accuracy, and load/energy characteristics of it. Optimal equipment selection requires consideration of the entire forging system, including lot size, conditions at the plant, environmental effects, and maintenance requirements, as well as the requirements of the specific part and process under consideration.

There are basically three types of presses used for cold and warm forging: hydraulic, screw and mechanical presses.

Hydraulic presses are essentially load-restricted machines and their capability for carrying out a forming operation is limited mainly by the maximum available load [44-46].

The screw press uses a friction, gear, electric or hydraulic drive to accelerate the flywheel and the screw assembly. It converts the angular kinetic energy into the linear energy of the slide or ram [47].

Finally mechanical presses employ flywheel energy, which is transferred to the workpiece by a network of gears, cranks, eccentrics or levers. The ability of mechanical presses to deform the workpiece material is determined by the length of the press stroke and the available force at various stroke positions.

Two major groups of mechanical presses are with a) crank drive or b) cam drive. Crank presses may have either simple or extended crank drives. Conventional crank (i.e. the total stroke cannot be varied) and eccentric (i.e. the total stroke is variable) presses, belong to the simple drives. If either a knuckle or a lever is used to extend the crank drive, the design are called knuckle-joint or link-drive presses. For a long time, eccentric or crank drive systems were the only type of drive mechanisms used in mechanical presses.

In this PhD thesis only modified drives (i.e. knuckle-joint) are involved in the forging processes considered. The typical sinusoidal slide displacement of an eccentric press, compared with those of a knuckle-joint and a linkage-driven press, is shown in Fig. 13.

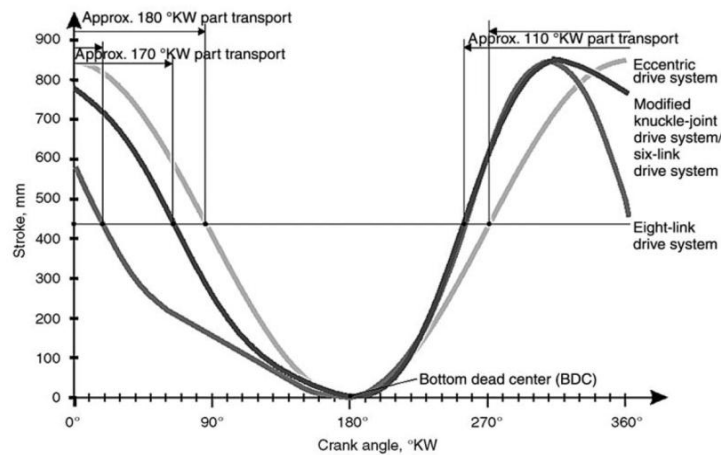


Fig. 13. Displacement-time diagram. A comparison of the slide motion performed by an eccentric, a knuckle-joint and a link-drive press [48].

The knuckle-joint drive system is capable of generating high forces with a relatively small crank drive. In the knuckle-joint drive, the ram velocity slows down much more rapidly toward the bottom dead center (BDC) than in the regular crank drive. This machine is successfully used for cold forming and coining applications [48].

In addition, considering the industrial case studies analyzed in this work, some forging tools are floating. They are connected with the accumulator-driven hydraulic circuit of the mechanical press considered and driven by the contact stresses exerted on the die/material interface during forging process. This forging mechanism employs an oil emulsion as the working medium and use air-loaded accumulators to keep the medium under pressure. Consequently, the rate of penetration (i.e. the ram speed under load), is not directly dependent on the pump characteristics and can vary depending on the pressure in the accumulator, the compressibility of the pressure medium and the resistance of the workpiece to deformation. Toward the end of the forming stroke, as deformation progresses, the working medium expands, the force required to form the material increases and the speed of penetration and the load available at the ram decrease. As the pressure builds up and the working medium is compressed, a certain slow down in penetration rate occurs.

2.3. Conditions at the tool-material interface

Lubricants carry out numerous tasks within the tribological system of metal forming technology (Fig. 14). In cold and warm working technologies, the range of suitable lubricants is far more diverse. In addition, the lubrication system used for steel may be very different from those used for other alloys [49].

In cold forging, for example, a combination of several lubricants is used to form one lubricating system. After the workpieces (i.e. counterbodies) have been degreased and undergone subsequent chemical (pickling) pretreatment, a coating of zinc phosphate or iron oxalate is applied to them. The applied coatings separate the surface of the base body and counterbody (i.e. tool and workpiece) and thus avoid adhesive wear (i.e. fretting). This wear can be suppressed with conventional lubrication by adding suitable extreme pressure additives, which lead to formation of a reaction layer.

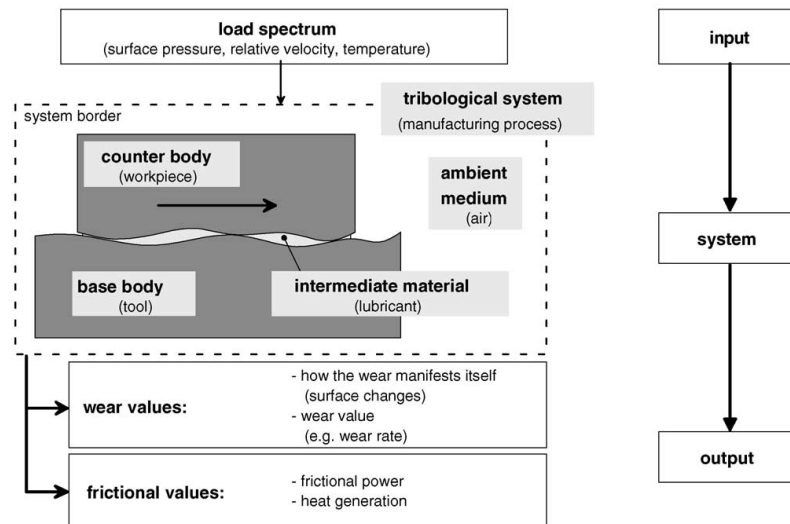


Fig. 14. Constitution of tribological systems.

Efficient lubricants prevent metal to metal contact between tool and workpiece, with the reduction of extrusion loads and wear, avoid galling (i.e. breakdown of lubricant film) and improve products quality and tools life. However, they are not sufficient to ensure the lubrication of all regions of the forming billet [50] in cold forging systems. It means that high temperatures of several hundred degrees centigrade may occur in the forming zone, where workpiece and tool come into strong contact, which may impair or even completely nullify the effect of normal lubricants. The large surface expansion (i.e. $\sim 3000\%$) and high normal pressure (i.e. ~ 2500 MPa) combined with elevated contact temperature between workpiece and tool cause the necessity of an high performance lubrication system [49,51-57]. In the approach outlined in this PhD thesis, the separation of the surfaces is achieved through coating the forging tools, while the sole purpose of lubricant is to reduce friction.

2.3.1. Lubrication in cold forging of steel parts

Because of the severe deformation conditions typical of many cold forging operations, the most widely used lubrication system to prevent the tool wear and the increase of extrusion load in the cold forging of low-carbon steels is a conversion coating of zinc phosphate chemically bonded to the metal substrate. It improves the friction conditions at the tool-workpiece interface and severe sequences of cold extrusion are also possible [58-60].

Zinc phosphate is a chemical conversion coating extensively used in cold forging processes in which high level deformation is produced [61-65]. Even though the coatings can prevent metal-to-metal contact between the tool and the workpiece surfaces in the early stage of deformation, they do not have efficient intrinsic low-friction properties due to their friability [62]. Thus, the coated part is provided with a lubricant by dipping into a hot bath of alkaline soap (typically sodium stearate) that reacts with the zinc phosphate to form zinc stearate, which is eventually covered with excessive sodium soap [66,67]. The crystalline layer of zinc phosphate partly acts as a chemical agent binding the soap to the surface and partly as physical carrier for the soap (Fig. 15).

The treatment sequence to obtain this lubrication system on carbon steel billets for cold forging operations is shown in Table 5 [49].

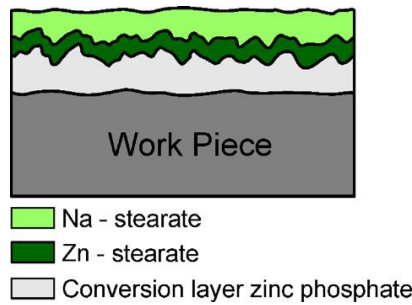


Fig. 15. Conventional lubricant film of phosphate coating reacted with sodium soap [49].

Type of operation	Operation	Time [min]	Temperature [°C]
Cleaning	Alcalin grease removing	5	90
Acid pickling	HCl + inhibitor	20	30
Rinsing	Water	2	20
Phosphating	Zinc phosphate + accelerator	10	80
Rinsing	Water	2	20
Soaping	Sodium stearate	3	80

Tab. 5. Phosphating and soaping procedure.

The coating procedure has several environmental drawbacks [68-72]: a) sludge of heavy metal phosphates, which need to be reclaimed or buried, b) large water requirement in the rinse baths, c) periodic replacement of baths for degreasing, neutralizing, pickling and lubrication required and d) large amounts of waste water, typically containing grease and tramp oils, acid and soap. In addition to these environmental concerns, the phosphating process requires prolonged treatment time and high bath temperature (i.e. 80-90 °C) [67,70].

Within this conventional chemical treatment much progress has been made in the last decades to reduce the consumption of chemicals and the amount of waste water. This so-called "iron-free" phosphating process results in huge amounts of sludge of iron and heavy metal phosphates, which has to be disposed by burying. By introducing new phosphating agents without the accelerating compounds of nitrite and chlorate, the consumption of phosphating agents can be reduced by one-third and the amount of sludge by 80-90%. Recent developments have led to new, advanced aqueous dispersions both of polymer lubricants and MoS₂. The improved adhesion and increased forming capability allow a reduction of the number of complete chemical pre-treatment steps (e.g. lubrication without phosphating).

For less demanding cold forging operations (i.e. bolt and nut production, etc.), the soap is replaced by a mineral oil film. Table 6 presents an overview of their major content [70,73]. The effects of S- and P-based extreme pressure additives were intensively studied in the period 1986-1991 by Komatsuzaki et al. [74,75] and Ohmori et al. [76,77]. As shown in Fig. 16 phosphate compounds assist lubrication at lower temperatures, S compounds in a somewhat higher range, but none of them is effective in the intermediate range from 200 to 300 °C.

Adding phosphate compounds like alkyl acid phosphate to a lubricant formulated with S additives feasible for high temperatures makes it possible to obtain stable lubrication in this medium temperature range [70,73]. Attempts to add metallic compounds of Ca and Zn have also occurred, and a variety of non-chlorinated cold forging oils are commercially available [78-80].

Ingredient	Main compounds
Base oil	Mineral oil, fat and oil, synthetic ester
Extreme pressure additives	Phosphorus, chlorine and sulphur
Oiliness improving agent	Fatty acid, higher alcohols
Solid lubricant	Graphite, MoS ₂ , PTFE, metal soap, etc.

Tab. 6. Oil lubricants for cold forging [73].

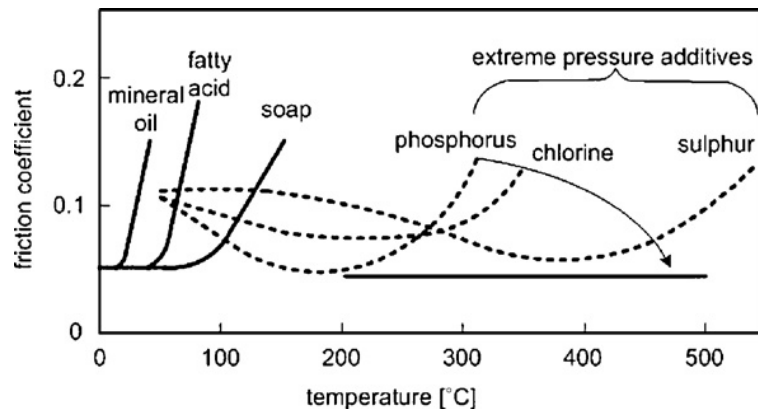


Fig. 16. Applicable temperature range of extreme pressure additives [49,73].

2.3.2. Alternative lubricants in cold forging of steel parts

For cold forging of stainless steels and other steels containing more than 5% Cr, an oxalate coating is used in place of the phosphate coating. This is done because it is difficult to phosphate these materials [49].

As alternatives to zinc phosphate or iron oxalate, a number of lubrication systems have been developed. They may be summarized into the following groups:

- New conversion coatings
 - Electrolytic phosphate coating
 - Microporous coating
- Lubrication without conversion coating
 - Dual bath system
 - Single bath system

Electrolytic phosphating

Many of the drawbacks associated with zinc phosphates are eliminated by electrolytic phosphating [81-83]. The main advantages are that a sludge free phosphating bath is obtained, the use of acid for pickling may be avoided by electrochemical pickling, the treatment time is considerably shortened, the working environment is improved and the electrochemical procedure makes it possible to phosphate high-alloyed steels and stainless steel, as reported by Bjerrum et al. [84,85].

Fig. 17 shows SEM micrographs of chemical and electrolytic phosphate coating, which ensure a much more uniform and finer crystalline coating with smaller film thickness. The phosphating time is 4 s for the electrochemical procedure. Coating thickness can furthermore be much better controlled, since it is linearly related to current density and treatment time [86]. Application of an electrolytical coating combined with zinc stearate as lubricant has demonstrated feasibility of severe cold forging operations such as backward can extrusion in AISI 304 stainless steel [87].

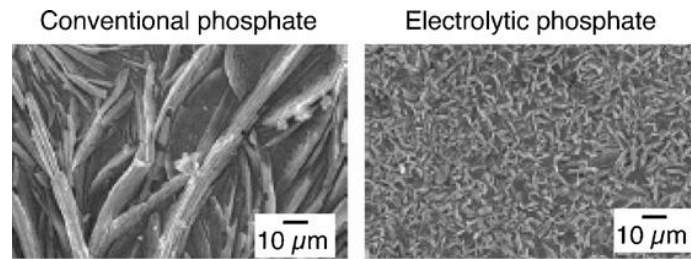


Fig. 17. SEM micrographs of conventional and electrolytic phosphate coatings [86].

Nittel [83] reports substitution of chemical zinc or zinc-calcium phosphating with electrolytic calcium phosphating carried out at 25 °C bath temperature. The process has the same advantages as electrolytic zinc phosphating, i.e. heavy metal sludge in the phosphating bath is avoided. It may be applied to highly alloyed steel and stainless steel. Due to energy savings and in disposal of chemicals, the new conversion coating system also should have economic advantages. Furthermore the problems of tramp oil (i.e. mixture of the process lubricant with the lubricating oil for the machinery) are avoided.

Microporous coating

Utsunomiya et al. [88] have developed a technique to produce porous surfaces in steel slugs or billets by artificial oxidation at 600 °C in air, followed by subsequent reduction of the oxides in a hydrogen atmosphere at the same temperature. By this second treatment the oxide layer is transformed into a porous surface layer with an average pore diameter of ~300 nm. The thickness of this layer is about 1 mm. The porous structure is beneficial for entrapment of liquid lubricants.

Tang et al. [89,90] have also developed a porous coating that serves as an efficient lubricant carrier. A two-phase alloy of Sn and Zn is electrochemically deposited on the workpiece surface after which one of the two metals is selectively etched leaving a micro- or nanoporous layer of the remaining metal on the workpiece surface (Fig. 18). The layer thickness is typically 5 μm. When a lubricant subsequently is applied to the porous coating, it will be trapped in the pores acting as numerous small lubricant reservoirs and will be entrained in even the most demanding applications.

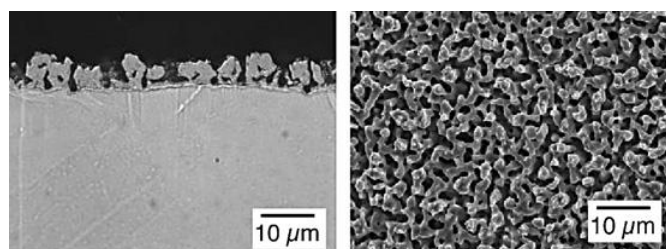


Fig. 18. Cross-section and top view of new porous coating [89,90].

Dual bath systems

Nakamura et al. [91,92] have tested a number of alternatives including single as well as dual bath systems. The dual bath systems form a base coating adhering to the slug or billet surface and an over-coating to further reduce friction. Two types of lubricants were investigated, a white lubricant consisting of wax and metal soap, and a black one consisting of MoS₂ and graphite. Based on laboratory cold forging tests, these systems

were selected for industrial testing in a multi-stage cold extrusion operation. Both systems showed good performance with no sign of pick-up on the forging tools.

Single bath systems

In the case of more demanding cold forging operations, alternative single bath lubrication systems have been developed, especially in Japan. After descaling/shot blasting and hot water rinsing, the slugs or billets are dipped in an aqueous bath containing inorganic salt and an organic lubricant and subsequently dried, after which they are ready for cold forging. The whole procedure takes about 2 min implying that in-process lubrication is attainable in many cold forging lines [93,94].

Development of such lubricants was initiated by Toyota Motor Corp., together with MEC Int. Initial investigations were directed towards a series of different water-based compounds with fatty acid, phosphates, polymer-based dispersant and Zn- and Mo-compounds [95-97]. During cold forging the heat developed by deformation and friction results in a chemical reaction between the steel slug or billet surface and the lubricant film containing a chelating agent. The reaction generates iron sulphide and forms a boundary lubricating film with Zn and S components [94,98].

Ngale et al. [99] describe the systematic development of new, environmentally friendly metal forming lubricants for steel based on co-polymer emulsions containing acrylic and methacrylic monomers. The polymer forms strong ionic bonds to the metal substrate. The procedure for coating includes alkaline cleaning, sulphuric acid pickling, conditioning, polymer coating with intermediate water between the operations and final drying in hot air. The conditioning provides the steel billets with an inorganic layer primarily consisting of iron phosphate and iron oxide. This layer ensures a greater quantity of polymer coating to be bonded in the subsequent step. Compared to conventional zinc phosphate coating and soap lubrication the treatment time and water consumption are reduced by 25% and 75% respectively.

Comparison of the new coating with conventional phosphate coating and soap lubrication in backward can extrusion measuring the backstroke force has shown seizure occurring at larger can height with the new lubricant. Production trials show it to be applicable in almost the same range as phosphate coating and soap lubrication as seen in Fig. 19. The new, single bath lubricants are now applied in numerous cold forging operations at Toyota and under trial in the most complex ones. Substituting zinc phosphate coating plus soap with the new lubrication system has reduced the waste from former 360 tons to a present 45 tons, corresponding to 88% less waste.

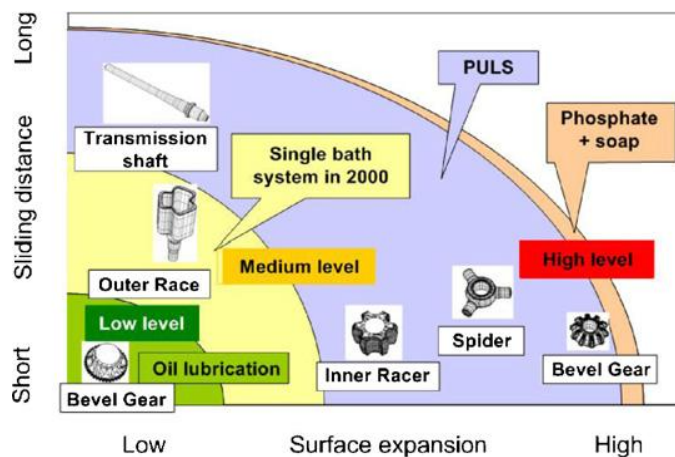


Fig. 19. Range of applicability of different cold forging lubricants [100].

2.3.3. Lubrication in warm forging of steel parts

Lubrication in warm forging of steel is very difficult, since neither the lubricants for cold forging nor those for hot forging are fully effective. Table 7 shows guidelines for lubrication in warm forging over different temperature ranges [101]. Efforts to find alternatives to graphite-based lubricants have been driven by: a) bad working environment, b) earth leakage (i.e. electric conductivity of oil), c) pipe corrosion due to electric conductivity and d) low recovery rate due to poor oil separation [102].

Temp. [°C]	Surface Treatment	Lubricant	Application
200-400	Phosphate coating	Graphite, MoS ₂	Workpiece
400-700	Phosphate coating	Graphite, Graphite dispersed in water	Workpiece or tool
700-850	None	Graphite (rapid heating) Graphite dispersed in water	Workpiece and tool

Tab. 7. Guidelines on lubricants for warm forging of steel [101].

Hibi [103] gives a good overview of possible water soluble high molecular weight polymers for warm forging. The main element in the polymer base is alkyl maleate. The carvone base oils are essential oils such as volatile or ethereal oils from plants. The main content of these lubricants are carboxylic acids such as fumaric acid and isophthalic acid. The liquid glass base lubricants are Si-glass containing colloidal silica. However, while a water soluble white lubricant improves the working conditions compared to a graphite lubricant in general, it continuously dissolves in water, and produces a high environmental burden associated with difficulties in waste liquid disposal.

Therefore, separation of such oil content and sludge and improvement in the disposability of waste liquid are the keys to improving environmental performance [104].

2.3.4. Experimental procedure

Conversion coatings are popular lubricant films for cold forging. However they have environmental risks, because a lot of sludge and waste fluid are generated during the coating process (cf. §2.3.1 of "Part 1").

In this PhD thesis, in order to replace the conversion coatings and reduce the environmental risks, a single bath lubrication system was developed to coat the surface of the cylindrical billets for subsequent cold forging tests (i.e. single-stage, multi-stage and friction tests).

The development of such lubrication process was carried out by Henkel Italy S.p.A., together with Zoppelletto S.p.A. and the Department of Management and Engineering (DTG). The tests were performed at Zoppelletto S.p.A.

For major details on the cylindrical billet geometries tested see §1 and §2 of "Part 2". The reference materials for most of the work and experimental tests conducted have been a low-carbon AISI 1005 steel, AISI 304L and Duplex 2205 stainless steel.

After sandblasting and hot water rising, the billets were dipped in an aqueous bath containing 70% of Bonderlube FL 744 lubricant (Fig. 20), and subsequently dried in a muffle furnace.

The treatment sequence (i.e. times and bath temperatures) to obtain this lubrication system on low-carbon and stainless steel billets for cold forging operations is shown in Table 8. The cleaning operations were designed to remove fine scale and grease from the billet

surface. The sandblasting even provided a porous structure on it that is beneficial for entrapment of liquid lubricant.

The Bonderlube FL 744 lubricant was a water-based compound, which generic chemical composition were: sodium nitrite 0.1-1%, dipotassium tetraborate tetrahydrate 5-10% and water 89-94.9%.

Type of operation	Operation	Time [min]	Temperature [°C]
Cleaning	Sandblasting	10	-
Rinsing	Water	10	50
Lubrication	Bonderlube FL 744	10	55
Air drying	Muffle furnace	15	150

Tab. 8. Bonderlube FL 744 treatment sequence of steel billets.

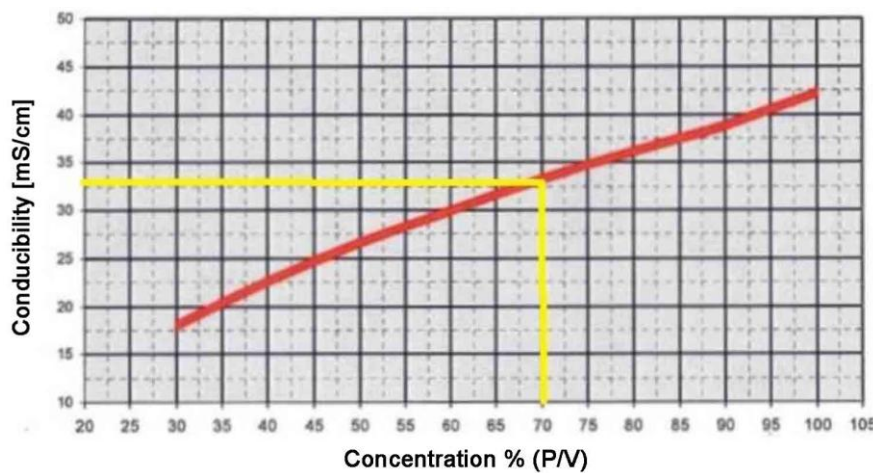


Fig. 20. Concentration of Bonderlube FL 744 lubricant as a function of the measured electrical conductivity of the bath.

On the other hand, the warm forging tests on stainless steels were conducted without applying any type of lubricant on the initial billets.

2.4. Tooling

The choice of a tool material is a very difficult task for designers and process engineers. The life of a tool and its suitability for production depend on many factors which often have opposing consequences. The design and manufacture of tools and the selection of the tool materials are very important in the production of discrete parts by forging.

The design of tools is also affected by many forging parameters, such as the flow stress of the workpiece material, the type of the process, the geometry of the die and the slug or preform and lubrication conditions.

In this PhD thesis, each stage of the forging cycles considered presented punches, workpiece ejectors and dies. The punch is the portion of the tool assembly that forms the internal surface of the workpiece and the die contains the part and forms the external surface. Moreover, the die inserts are prestressed with one shrink rings so that they can withstand the high stresses present in the die cavity. Tools for cold and warm forging can be of different configurations, depending on the design preferences or operational requirements.

Tools manufacture

Forging tools (i.e. punches and dies) for most of the work reported in this thesis are machined from solid blocks or forged die steels. The information flow and processing steps used in tool manufacturing are divided into die design, heat treatment, tool path generation, rough machining (of die block and/or electrical discharge machining electrode), finish machining (including semi-finishing where necessary), manual finishing, or benching (including manual polishing) and tryout.

Tools materials for cold and warm forging

The material used to produce each tool component can be selected once the dimensions of the tool have been fixed. Tools for cold and warm forging processes are in sliding contact with solid metal parts for a portion of their working time and may be subject to high stresses for short periods of time during operation. Conventional cold-warm work tool steels (i.e. oil-hardening, air-hardening, high-carbon, high-chromium and high-speed steels) contain additions of Cr, W, V and Mo to provide deep hardening characteristics, high wear and high abrasion resistance [105-107].

The AISI classification system arranges these steels into groups that are based on prominent characteristics (i.e. alloying, application or heat-treatment) and identifies them with letter symbols [108-110]:

- Oil-hardening steels ("O");
- Air-hardening steels ("A");
- High-carbon, high-chromium steels ("D");
- Tungsten high-speed steels ("T");
- Molybdenum high-speed steels ("M").

Moreover high-speed steels (HSS) are denoted with the letters "HS" and the percents of alloy elements in the order W-Mo-V, according to DIN EN 10027a.

Table 9 lists some typical chemical compositions of the most commonly used conventional cold and warm work tool steels.

International steel No.		Chemical composition						
AISI System	Unified Numbering System (UNS No.)	C	Mn	Si	Cr	V	W	Mo
O1	T31501	0.9	1.0	-	0.5	-	0.5	-
A2	T30102	1.0	-	-	5.0	-	-	1.0
D2	T30402	1.5	-	-	12.0	1.0	-	1.0
D3	T30403	2.3	-	-	12.0	-	-	-
M2	T11302	1.0	-	-	4.0	2.0	6.0	5.0

Tab. 9. Common cold and warm work tool steels listed in the AISI system [111].

Not only is tempered high-carbon martensite an important component of the microstructure for these steels, but large volume fractions of alloy carbides also play an important role in achieving high hardness and wear resistance, especially in high-speed steels [112-114].

Enhanced demand for high-quality tool steels at the present time results in the necessity to produce steels with higher amounts of carbon, as well as of other alloying elements. However, increasing the concentration of the alloying elements generally promotes segregation effects and coarsening of carbides, and hence a considerable reduction of the

toughness. One way how to suppress segregation and coarsening is the application of powder metallurgy (PM) processes. Recently, powder metallurgy (PM) techniques are becoming increasingly widespread for manufacturing high-speed steels. In addition to the typical advantages of PM (i.e. raw material saving, low-energy costs), PM HSSs present better microstructural features than conventional (wrought) steels, such as homogeneity of carbide distribution in the matrix and smaller grain and fine carbide sizes, among others [115,116]. These advantages result in an enhancement of the wear resistance, toughness and hardness compared with the conventional cold and warm work tool steels.

In order to achieve the desired properties of a particular steel, an appropriate procedure of thermal treatment should be used [117]. Generally, it includes hardening and tempering and, after it, the cold-warm work tool steels should be characterized by hardness in a range of 50-65 HRC (considerably higher than that of the forged product), good hardenability, high tensile strength, high impact strength and low abrasibility.

The quenching rate from the austenitizing temperature is of great importance for achieving the optimum mechanical properties of a tool steel. It is necessary to bypass the proeutectoid and perlite nose in the kinetic diagram and to ensure that the alloying elements remain dissolved in the matrix to the maximum extent. In the case of high-quality high-speed steels fast cooling is generally performed by gas (nitrogen) in vacuum furnaces [118].

As mentioned before, the properties of any tool steel are determined by the type, distribution and morphology of the carbides present in the microstructure. Depending on the chemical composition of a high-speed steel and on the cooling rate, the following types of primary carbide appear in the alloyed steels after solidification: M_7C_3 , M_2C and M_6C . Other carbides are of a minor importance [118]. The M_2C carbides decompose into the M_6C and M_7C_3 ones during the high temperature annealing [119]. The M_7C_3 carbides dissolve during austenitisation only to a very limited extent due to their high thermal stability [120]. In recent years, powder metallurgical nitrogen alloyed cold-warm work tool steel with excellent anti galling properties [121,122]. N increases the stability of V-nitride and the size of the hard phases become very small in the final tool material. Fig. 21 shows a comparison of the microstructure of this type of steel with conventional cold-warm work tool steels. Traditional tool steel has large carbides and uneven distribution. The nitrogen alloyed PM tool steel has a high fraction of more densely distributed MN phase consisting mainly of $V(N,C)$ (black phase in Fig. 21) and furthermore a small fraction of Mo-rich carbides.

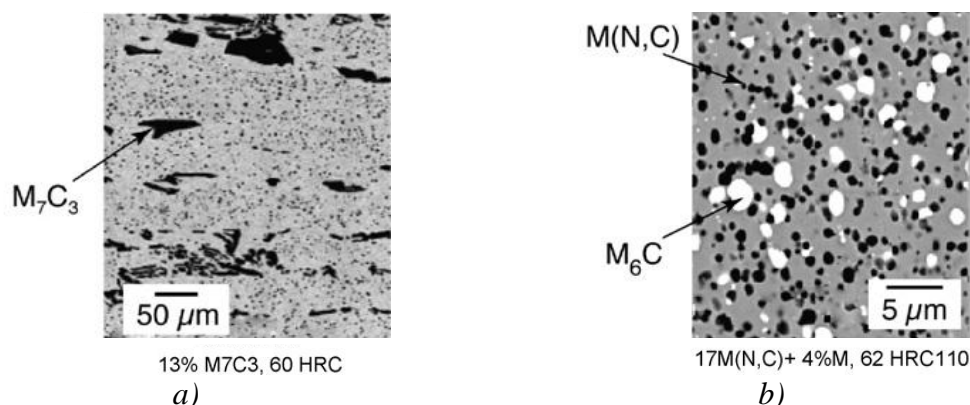


Fig. 21. Microstructure, hardness and amount of hard phase in a) conventional and b) PM tool steel. Note the scaling is 50 and 5 μm for the conventional and PM steel, respectively [109].

In this thesis, the effects of heat treatments on microstructure of a conventional and a PM HSS tool steel have been studied in this work (*Article I*) and the results found could be summarized as:

- PM HSS steel shows fine-dispersed and homogeneous-distributed carbides into the matrix. The presence of W-Mo and V-W-Mo rich carbides, and Mn-sulphides are revealed.
- Fine Mn-sulphides and large and unevenly distributed V-rich and V-Cr rich carbides are detected in conventional tool steel.

PVD coatings

By optimising forging processes, it is possible to reduce the use of lubricants, but it cannot be completely avoid. Coating processes deposit an overlayer on the tool surface. Under cold-warm forging conditions, thin-film coatings deposited by physical vapour deposition (PVD) or chemical vapor deposition (CVD) are likely to crack or even delaminate. However, a PVD or CVD coating can be used for forging tools when deposited over another coating, or on top of a surface modified underlayer. In this instance, customized PVD coating system provide a powerful tool in this field and the underlying coating or surface modification process provides support for the overlay coating [123,124].

Many PVD coatings are single-layers. On the other hand, one of the problems in applying PVD coatings for cold and warm forging tools is the high hardness and Young's modulus compared to the base tool material leading to risk of coating fracture. Due to the fact that these tools have relatively low bulk hardness (i.e. 50-65 HRC), it is supposed that such soft substrates could not efficiently serve as a basis for a physical vapour deposited (PVD) coating, which is only a few micrometers thick. For this reason multi-layer coatings, that combine the properties of the component layers, are becoming increasingly popular. In recent years, several multi-layer PVD coatings have recently emerged and an interlayer is sometimes deposited between a PVD coating and the substrate to enhance adhesion.

Some common PVD coatings are listed in Table 10.

Coating	Typical coating thickness [μm]	Hardness [HV]
TiN	1-5	2300-2900
AlCrN	1-5	3000-3200
TiCN	1-5	3000-3500
DLC	1-10	1000-5000
MoS ₂ /Ti	2-5	1500-2100

Tab. 10. Some common PVD coatings [110].

In this thesis the composition and surface morphology of different single- and multi-layer PVD coatings, applied on cold-warm forging tools, have been studied in this work (*Article D*), using ESEM-FEG microscopy equipped with an energy dispersive x-ray spectroscopy (EDS). The analysis included a single-layer TiN and a double-layer TiN/AlCrN PVD coating deposition on different tool steel substrates. In addition a combined process, as so called duplex treatment, consisting of ion nitriding and subsequent multi-layer TiAlCN PVD deposition technology is also investigated. The decisive advantage of these multi-layer coatings are that the surface and the subsurface of the substrate are first modified to produce a deep hardened case, which can be up to a few ten micrometers thick, in order to enhance coating adhesion.

PART 2

PROCESS MODELLING

1. General introduction

The environment concerning the recent forging industry has been rapidly changed. Decreasing experienced designer and making higher quality product within shorter development time are important issue recently. Therefore, the importance of Computer Aided Engineering (CAE) in forging process design has been raised remarkably to overcome the difficulties in the new design environment.

The finite-element method (FEM) is one of the numerical techniques used for solving differential equations governing engineering problems. Development of FE process simulation in forging started in the late 1970s [125-127]. Nowadays commercial FE simulation softwares are gaining wide acceptance in the forging industry and are becoming an integral part of the forging process design [128-131].

The main objectives of the numerical process design in forging are [132]:

- To develop adequate tool design and establish process parameters by:
 - Process simulation to assure die fill and prevent flow-induced defects;
 - Predicting processing limits and temperatures (i.e. friction conditions and tool wear can be controlled);
- To improve part quality and complexity while reducing manufacturing costs by:
 - Predicting and improving grain flow and microstructure;
 - Reducing tool tryouts and lead times;
- To predict forging load and energy as well as tool stresses so that:
 - Premature tool failure can be avoided;
 - The appropriate forging machines can be selected for a given application.

In its earlier application, process modelling of closed-die cold and warm forging using FE modelling helped tool design engineers to foresee the metal flow and possible defect formation in a forging [133,134]. After the forging simulation is done, the contours of state variables, such as effective strain, effective strain rate and temperature at any instant of time during forging, can be generated. Integrated with the process modelling, microstructure modelling allows the right-the-first-time optimum metallurgical features of the forging to be foreseen on the computer, such as grain size [135,136].

The numerical models developed in this PhD thesis were thermo-mechanical models carried out with the FORGE2011[®]-3D commercial software (Transvalor, Mougins, France). This FE code enables coupled modelling of deformation and friction conditions evolution for the simulation of cold and warm forging operations and its main features are briefly described. The minimum work rate principle is used for accurate calculation of metal flow, thus the velocity distributions which predicts the lowest work is the best approximation of the actual velocity distribution. The manner in which the problem is divided into little subproblems that are easier to formulate is a process called meshing and represents the principle of FEM theory. Bodies are divided in several elements representing a portion of material.

2. Process modelling input

It is well known that the quality of the simulations based on the FE analysis results is highly related with the use of reliable process input-data of the simulated processes and the material properties. A guide of validation of FE simulations in the bulk metal forming processes has been reported by Tekkaya [137]. The validations of numerical simulations are virtually based on the comparisons of modelling results with those of the forming

processes. Once the model is validated, it becomes a very powerful tool, not only in the designing stage of forming process but also in the identification of the operating faulty designs. Process modelling input is discussed in terms of geometric parameters, process parameters, tool and workpiece material properties, interface conditions (i.e. friction) and material parameters [138]. Information flow in process modelling of closed-die cold and warm forging is shown schematically in Fig. 22 [139]. The modelling is then performed to provide information on the metal flow and thermo-mechanical history, the distribution of the state variables at any stage and the equipment response of the forging. The histories of the state variables are then input to the microstructure model for microstructural feature prediction.

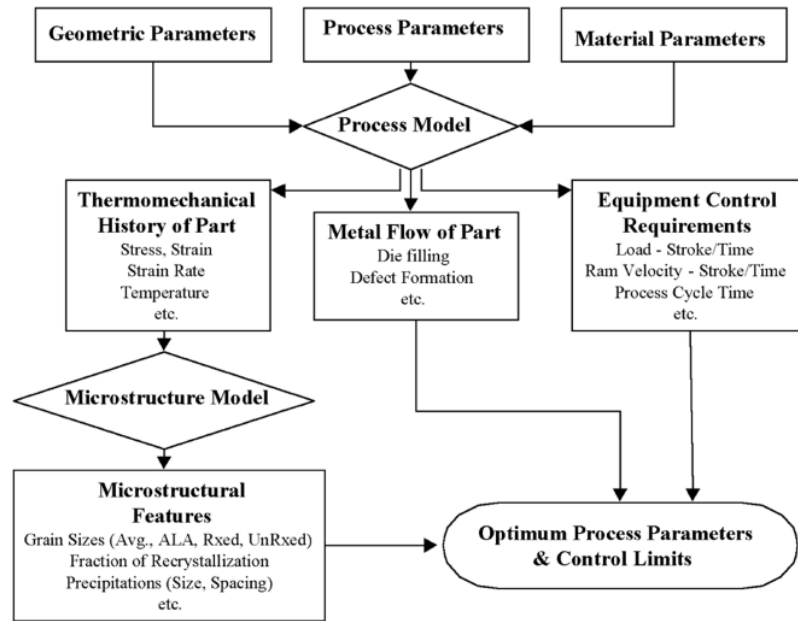


Fig. 22. Flow chart of modelling of closed-die cold and warm forging processes [139].

2.1. Geometric parameters

The starting two or three-dimensional workpiece and tools CAD geometries need to be defined in a closed-die forging modelling. Boundary conditions on specific segments of the workpiece and tools that relate to deformation need to be defined. In this case, FORGE2011[®]-3D software has an automatic remeshing capabilities, which is important in the simulation of metal forming operations with large material deformations and displacements. The 2D elements use triangular elements, whereas 3D parts (i.e. cylindrical billets and forging tools) consider tetrahedral elements for meshing and automatic remeshing [140].

2.2. Process parameters

The typical process parameters considered in a close-die cold and warm forging include [138]:

- The environment and workpiece temperature;
- The press kinematic;
- The heat-transfer coefficients (HTC);
- The friction coefficients at the tool-workpiece interface.

Moreover, the tools (i.e. punches and dies) velocity is a very important parameter to be defined in the modelling of a closed-die forging [138].

2.3. Material parameters

In order to accurately predict the metal flow and forming loads, it is necessary to use reliable input data. The yield stress of a metal under uniaxial conditions can also be considered as the "flow stress". The metal starts flowing or deforming plastically when the applied stress reaches the value of the yield stress or flow stress. The flow stress of a metal is influenced by many factors such as chemical composition, metallurgical structure, phases, grain size, segregation, temperature of deformation, strain and strain rate. For a given microstructure, the flow stress σ is expressed as a function of strain ε , strain rate $\dot{\varepsilon}$ and temperature T (Eq. (3)):

$$\sigma = f(\varepsilon, \dot{\varepsilon}, T) \quad (3)$$

To formulate the constitutive equation (Eq. (6)) and be useful in metal forming processes, it is necessary to conduct experimental tests, such as tensile tests.

Rheological models describe the during-deformation aspect of the material response in terms of the current value of the flow stress [139]. In the empirical-analytical models, the flow stress is calculated as a function of the current process parameters by using an empirically derived equation [141]. The following expression represents the oldest formulation of this kind of model, where the flow stress is determined as a function of a single variable, respectively the equivalent strain or strain rate in cold and hot conditions (Eq. (4)) [142,143]:

$$\sigma = k\varepsilon^n \quad (4)$$

where σ is the equivalent stress, ε is the equivalent strain and k is a constant material coefficient.

The simultaneous dependence on equivalent strain ε , equivalent strain rate $\dot{\varepsilon}$ and temperature T is expressed by the Norton-Hoff constitutive law (Eq. (5)):

$$\sigma = k\varepsilon^n \dot{\varepsilon}^m e^{\frac{\beta}{T}} \quad (5)$$

where k indicates the material consistency, n is the strain hardening coefficient and m represents the material strain rate dependency. The influence of the absolute temperature T is described through the exponential term of Eq. (5) where β is a constant material coefficient. To improve the fitting of this model the n and m coefficients can be described as functions of the temperature T .

The most accurate representation of the flow curve in cold and hot deformation conditions for FE simulations is the Hansell-Spittel constitutive law (Eq. (6)):

$$\sigma_f = A \cdot e^{m_1 T} \cdot \varepsilon^{m_2} \cdot \dot{\varepsilon}^{m_3} \cdot e^{m_4/\varepsilon} \cdot (1 + \varepsilon)^{m_5 T} \cdot e^{m_7 \varepsilon} \cdot \dot{\varepsilon}^{m_8 T} \cdot T^{m_9} \quad (6)$$

where σ is the stress tensor, ε the strain tensor, $\dot{\varepsilon}$ the strain rate tensor and T the temperature.

These models generally provide excellent mapping of the experimental σ - ε curves. They are more used than other types, because they make it easy to identify the constitutive material coefficients, which can be easily implemented in FE codes.

In this thesis the material rheological behaviour in FORGE2011[®]-3D software was described by the Hansel-Spittel law. In order to assure the repeatability of the results and perform reliable thermo-mechanical coupled simulations, the mean values of typical mechanical properties (i.e. Yield and Ultimate strength) in evolution with temperature were implemented in the FE models developed [144]. Moreover, forging tools were considered as rigid bodies, thus their deformations and stresses were neglected.

2.4. Friction models

A friction model is another of the key input boundary conditions in FE simulations. The importance of tribological considerations in bulk metal forming has been generally recognized as affecting output results predicted: tool and tool life, metal flow during forming, workpiece integrity and surface finish, the relationship of lubricant to machine elements and energy conservation [145-149]. However, how to exactly express a friction model in bulk metal forming is, at times, rather controversial [147]. In commercial FEM packages (e.g. FORGE2011[®]-3D), Amontons-Coulomb, constant and general friction models are normally applied.

Amontons-Coulomb friction model

Friction is most commonly characterized by using constant coefficient of friction model, variously attributed to Amontons, Coulomb or Da Vinci (Eq. (7)) [146,150]:

$$\tau = \mu \cdot p \quad (7)$$

where τ is the friction stress, μ is the coefficient of friction and p is the normal pressure. Dry slipping occurs over the whole tool-workpiece interface. Friction stress τ is directly proportional to local normal pressure p (Fig. 23a). This model is used for most applications due to its simplicity.

Constant friction model

This model was proposed by Orowan in 1943. Model assumes that friction stress is proportional to interface pressure, as in Amontons-Coulomb model, until a critical value of interface pressure is reached. Above the critical pressure, which is associated with real area of contact becoming equal to the apparent area, the friction stress is constant and equal to yield stress in pure shear stress conditions (Fig. 23b). It is one of most popular model due to its simplicity. However it is not accurate, since friction does not depend on the current state of stress at the tool-workpiece interface, but simply on material property (Eq. (8)) [146,151]:

$$\tau = m \cdot k \quad (8)$$

where k is the shear flow stress and m is the friction factor.

General friction model

Friction models, mentioned up to here, are relatively insufficient to model bulk metal forming operations, since those are simply depend on either material property or normal pressure value.

In an earlier study Wanheim [152] stated that Amontons-Coulomb's friction law should not be applied when the normal pressure is higher than approximately yield stress of the material. It was also put forward the necessity of considering the frictional stress as a function of normal pressure, surface topography, length of sliding, viscosity and compressibility of the lubricant. With this aim Wanheim, Bay and Petersen developed a general friction model [153]. The model can be considered as an updated model of constant friction (Eq. (9)) [152-154]:

$$\tau = f \cdot \alpha \cdot k \quad (9)$$

where k is the shear flow stress, f is the friction factor expressing the friction in real contact ($0 \leq f \leq 1$) and α is the ratio of real to the apparent contact area. The real contact ratio α and friction stress τ are determined as functions of the nominal normal pressure q/σ_0 and friction factor (Fig. 23c).

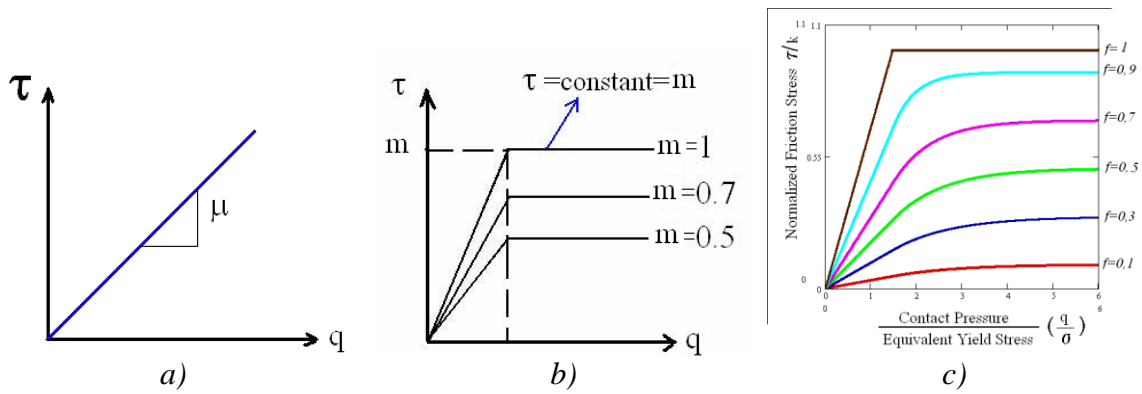


Fig. 23. a) Amontons-Coulomb friction model, b) constant friction model and c) normalized friction stress as a function of nominal normal pressure and friction factor for the general friction model.

The model assumes that the friction to be proportional to the normal stress at low normal pressure (i.e. $q/\sigma_0 < 1.5$), but going towards a constant value at high normal pressure (i.e. $q/\sigma_0 > 3$). These two ranges are being combined by the intermediate transition region as shown in Fig. 23b. It is found that friction conditions at high normal pressures differ greatly from friction conditions at low normal pressures. Amontons-Coulomb's law is valid only until ($q/\sigma_0 > 1.3$), irrespective of friction factor value. Starting from this point, coefficient of friction would become pressure dependent. In metal working processes, normal pressure is often considerably greater than the yield stress of the material and, consequently, in Amontons-Coulomb's law friction stress becomes greater than yield stress of the material in pure shear. However Amontons-Coulomb's law in the case of small f values ($f < 0.2$) is nearly correct at high pressures [153].

Evaluation of friction models

The models mentioned above are the eminent ones in bulk metal forming. One can say that with the new models taking into account the non-linear frictional forces and asperity deformation during the process have advantages in analyzing friction. For example, researches showed that using general friction model better estimation of the material flow than Amontons-Coulomb's law were obtained [153]. Even though the validity of the general friction model had verified experimentally, its implementation in FE software for metal forming has so far been limited. Therefore this model also must be verified with other bulk metal forming operations.

A comprehensive research made by Tan [155] investigating differences between five friction models (including Amontons-Coulomb's, constant and general friction models, and two others) in obtaining calibration curves. The most important conclusion for friction models was that it was difficult to establish a friction model that valid for all kind of metalworking processes for different conditions. With the better understanding and analyzing of friction it will be possible to understand the metal flow, the forming loads inside a die accurately and it leads to reduce the number of tool design trial-and-error processes.

Conventional FE programs, such as FORGE2011[®]-3D software used in this thesis, adopt either Amontons-Coulomb friction model or constant friction model to describe friction between the workpiece and the tools in metal forming processes by simple relationships. In cold and warm forging processes, the Eq. (8) describes the friction conditions better than the Coulomb friction law (i.e. Eq (9)) especially to the high pressure conditions [156].

2.4.1. Experimental friction test methods in cold and warm forging

In the experimental determination of friction in metal forming, direct and indirect methods are distinguished. These tests differ in their aspects of the complexity of the setup and their aptness to simulate the exact production conditions.

In direct testing methods, the friction stresses are acquired by using measurement pins locally in the tool-workpiece interface, whereas friction is determined via a deduced quantity such as force or deformation in indirect experiments.

For the characterization of lubricants, usually indirect methods are used because in indirect measurements the friction stress is averaged on the entire tool-workpiece interface and thus local inhomogeneities are compensated.

Indirect tests, in which friction is determined from force or torque measurements, allow a more detailed investigation of the tribological interactions in the tool-workpiece interface.

Hansen and Bay performed backward-can-extrusion followed by a rotation of the container, where the torque transferred from the cup to the punch is measured (Fig. 24a) [157]. Groche and Kappes used a sliding-upsetting test, in which at first a cylindrical specimen is compressed with a special tool in order to obtain an homogenous surface expansion on the bottom side of the specimen and then the lower tool is moved and the sliding force is measured (Fig. 24b) [158]. Doege et al. developed a model experiment to determine friction and heat transfer in backward-can-extrusion by means of a lower punch equipped with strain gauges and thermocouples (Fig. 24c) [159]. Lately, two different research teams evaluated lubricants by performing a sliding-upsetting test where relative motion is applied on an indenter penetrating a cylindrical billet (Fig. 24d) [160,161].

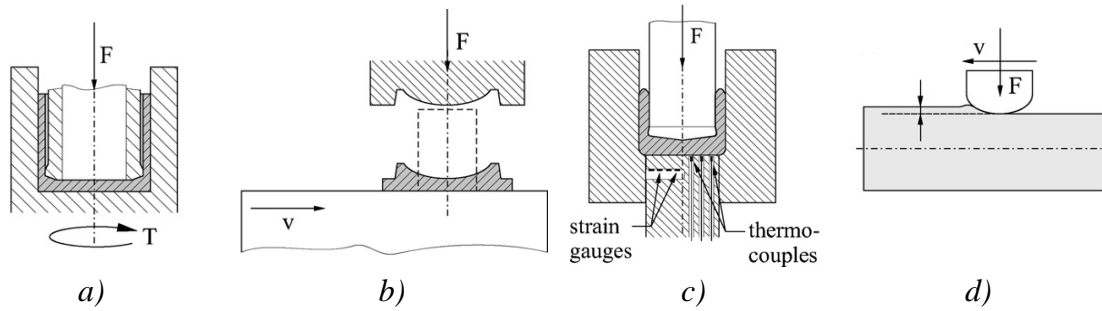


Fig. 24. Indirect friction tests, where friction is determined from force (or torque) measurements (the specimens are marked gray): a) backward can extrusion test [157], b) sliding-upsetting test [158], c) backward can extrusion test [159] and d) upsetting-sliding test [160,161].

Indirect testing methods, where friction is determined from specimen deformation, are very popular in industrial practice. These tests are easy to perform and represent the real process very well. The most popular and simplest friction test in this category is the ring-compression test, initially proposed by Kunogi [162] and then developed by Male and Cockcroft [163] (Fig. 25a). The concept of the test is the increasing or decreasing of inner diameter of a short ring specimen when it is compressed between two flat, parallel platens. It provides a particular knowledge about the friction factor at the tool-workpiece interface. If the friction is low (i.e. good lubrication), the internal diameter increases; while if the friction is high (i.e. poor lubrication), the internal diameter decreases. Calibration curves are formed to ring geometries and each geometry has its own specific set of curves [164]. Once the percentage of reduction in internal diameter and height are known, one can determine coefficient of the friction using the appropriate chart.

This test is widely recognized as one of the best methods for evaluating friction by virtue of the advantages of there being no need for force measurement during the test, nor a knowledge of the yield strength of the material [165-168]. However, this test induces a very simple deformation path and relative small new surface expansion ratio, which is nearly equals to 20%.

Fig. 25b shows the double-cup-extrusion (DCE) test initially explored by Geiger [169] and then developed by Bunschhausen et al. [170], Arentoft et al. [171] and Kim et al. [172]. This test combines the single-cup forward and backward extrusion which reflects the real process conditions more accurately. Fig. 25b shows the principle of test where h_1 is the upper cup height and h_2 is the lower cup height. The cups were generated by the action of the upper punch, which moves down with the press ram while the lower punch and container are stationary. The output of DCE test are the cup heights and these are used to determine the cup height ratio as the ratio between h_1 and h_2 .

Fundamental knowledge about DCE test is that cup height ratio increases with the increasing of the friction coefficient. If the friction is very low, the two cups will have the same height, while in severe friction conditions the forward extrusion cup will be prevented. On the other hand, some researchers stated that this test is strongly influenced by the loads required for the double cup extrusion, that are lower than the ones needed for single forward and backward extrusion [173]. In addition other authors found that the maximum contact pressure between specimen and container is rather small (i.e. <700 MPa for low-carbon steel) [174].

In Fig. 25c the spike test utilized for lubricant characterization is presented [175]. This test combines an extrusion and an upsetting operation. It can be used to determine friction, because the load and spike height increase with friction. The spike test requires a top die

with a sharp-corned tapered orifice of circular cross-section and a flat-bottom die. A circular billet squeezed between the dies flows both sideways and into the orifice. Higher friction restricts sideways flow and therefore a longer spike is extruded. This test eliminates the difficulty faced in extracting the tested specimen, such as in DCE test. However, like in ring compression test, the cylindrical surface of specimens are not in contact with the tools of the test and contact conditions can be different with the ones on end surfaces.

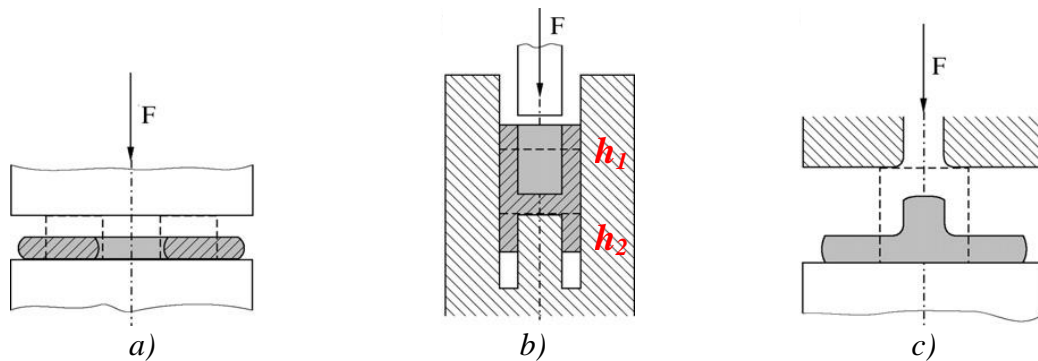


Fig. 25. Indirect friction tests, where friction is determined from the change of the specimen's shape (the specimens are marked gray): a) ring-compression test performed [162,163], b) double-cup-extrusion test [170,172] and c) spike test [175].

In this thesis, to overcome the limits of the spike test, a new T-shape compression method to measure the interfacial friction during forging processes is validated by means of numerical simulations and experiments. To evaluate the selected lubricants and measure their corresponding friction factors, the experimental tests have been coupled with FE simulations. This test validated the numerical studies and provided the friction factor m and coefficient μ for different lubrication conditions (cf. §5.2 of "Part 2").

3. Process modelling output

The output of process modelling can be discussed in terms of the metal flow, the distribution and history of state variables and the equipment response during forging.

3.1. Metal flow

The information on metal flow is very important for tool design. Improper metal flow produces defects in the forging. The advantage of computer simulation for forging is that the entire forging process is stored in a database file and can be tracked. Whether there is a defect formed and how it is formed can be previewed before the actual forging (Article II, and III).

3.2. Distribution and history of state variables

The distribution of the state variables on each stage of a closed-die cold-warm forging, can be plotted from the database file saved for the forging simulation. The history plot of state variables provides valuable informations on the thermo-mechanical history of the forging that determines its mechanical properties.

3.3. Equipment response

Process modelling also provides the information regarding the response of the equipments (e.g. forging loads on tools). During a closed-die forging operation the workpiece rises its contact area with the tools, which increases the forging load.

4. Inverse FE analysis theoretical bases for determination of flow stress and friction conditions

As mentioned before, the FE analysis (FEA) based simulation of metal forming processes has been widely used to predict metal flow and to optimize the manufacturing operations. By using user-friendly commercial FE software, the assign input parameters in the flow stress equation, friction factor and anisotropy coefficients of a material are usually obtained from the appropriate tests. The results of process simulation are extremely sensitive to the accuracy of flow stress and interface friction that are input to FEM programs. Therefore, it is essential that these input values are determined using reliable material tests and accurate evaluation methods. A test used to determine material properties should replicate processing conditions that exist in practical applications.

In this thesis, an inverse analysis technique will be used to determine material parameters in the flow stress model and the friction at the tool-workpiece interface. Therefore its theoretical bases are briefly introduced for the accurate determination of the input data for FEM process simulations.

A physical system can be described through a mathematical model able to express the system response M^C taking into account the boundary conditions. This direct model can be given as (Eq. (11)):

$$M^C = S(x) \quad (10)$$

where x represents the parameters describing the system under study and S is called forward operator.

On the contrary, the inverse analysis consists in determining the condition x leading a physical system to describe the experimental value M^{exp} , and can be expressed as the determination of (Eq. (12)):

$$x = S^{-1}(M^C) \quad \text{so that} \quad M^C = M^{exp} \quad (11)$$

The complexity of most direct models commonly adopted is sometime so elaborate that a simple inversion of the model results impossible; therefore regression methods are instead used, in order to predict an experimental state M^{exp} closer as possible to the predicted value M^C [176]. Only in the last years a systematic study for a general formulation and resolution of inverse problems has been performed involving several fields such as electronic [177], structural analysis [178], heat engineering [179], geometrical optimization [180] and rheological parameters identification [181].

A FE analysis of a generic metal forming process, as illustrated in Fig. 26a, is regarded as direct problem.

In the direct problem FEA predicts the metal flow, forming load and energy by simulating the forming operation assuming that the flow stress and friction values are known. Compared with the direct problem, in the inverse problem the authors determine one or more of input data of the direct problem, leading to the best fit between experimental measurements and FEM prediction. With experimental data provided to the inverse

problem, the input parameters are identified or calibrated (Fig. 26b). Therefore, an inverse problem is regarded as a parameter identification problem that can be formulated further as an optimization problem where the difference between measurement and FEM prediction is minimized by adjusting the input parameters.

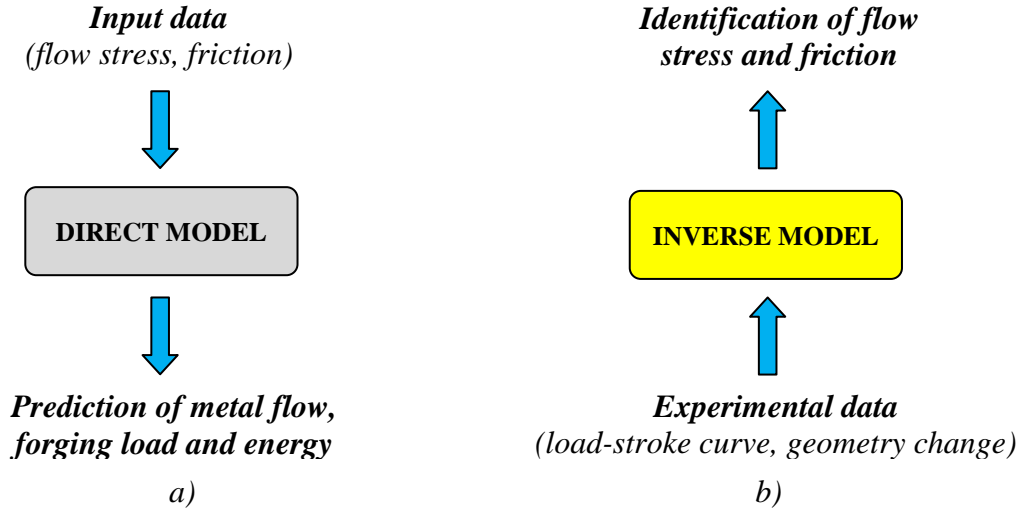


Fig. 26. Comparison between a) direct and b) inverse models.

The inverse problem finds the model parameters given the observable values of the forward problem and it can be well conditioned if the following conditions are satisfied:

- For any M in the experimental space a solution exists;
- The solution is unique in the model parameters space;
- The inverse mapping $M \rightarrow x$ is continuous.

Otherwise the existence, unicity and continuity of a solution are not all verified in bad-conditioned problems. Metal forming problems are generally bad-conditioned considering the model complexity and the typical number of variables.

The parameters identification method is based on the determination of the set of parameters P , in order to minimize the difference between calculated values M^C of the observables and experimental values M^{exp} , which are given by the equation (Eq. (13)):

$$M_i^{exp} = M_i^C + \lambda_i \quad \text{with } i = 1, 2, \dots, s \quad (12)$$

where λ_i represents the gap between correspondent calculation and measurement including numerical approximation, measurement uncertainty and errors due to model assumptions and simplifications of the real process. The minimization of this difference basically consists of minimizing the gap λ_i by means of the cost function defined by (Eq. (14)):

$$Q(M^C(P), M^{exp}) = \sum_{i=1}^s \lambda_i^2 = \sum_{i=1}^s (M_i^{exp} - M_i^C)^2 \quad (13)$$

Eq. (14) is often expressed as the adimensional form (Eq. (15)):

$$Q = \sum_{i=1}^s \beta_i (M_i^{exp} - M_i^C)^2 \quad (14)$$

where β_i are called weight coefficients and the following conditions have to be assured:

- Q must be semipositive defined (supposing $\beta_i > 0$);
- $Q = 0 \leftrightarrow M^C = M^{exp}$.

When the optimization is based on multiple objectives it is necessary to define a multi-criteria cost function (Eq. (16)):

$$Q = \sum_{k=1}^{nobs} \sum_{i=1}^s \beta_i (M_i^{k^{exp}} - M_i^{k^C})^2 \quad (15)$$

where $nobs$ is the number of observable quantities taken into account and $M_i^{k^{exp}}$ refers to the i -th experimental values of the k -th observable quantities. Eq. (16) permits to consider, during deformation, the influence of different optimizing parameters on different experimental values.

A more general form of the cost function employs a statistical approach, where the optimization problem is led to the determination of the parameters which maximize the prediction probability of the experimentally evaluated measures. For a Gaussian distribution, the cost function depends on the mean values of the experimental measures $\bar{m}(M_i^{k^{exp}})$, which are supposed to be equal to the calculated ones $M_i^{k^C}$ and the quadratic deviation of measurement errors $\sigma_i^{k^2}$.

The cost function can be expressed as (Eq. (17)):

$$Q = \sum_{k=1}^{nobs} \sum_{i=1}^s \lambda_i^k [\bar{m}_i - M_i^{k^C}]^2 + \sum_{j=1}^r \gamma_j [P_j - \bar{P}_j]^2 \quad (16)$$

where $\lambda_i^k = 1/\sigma_i^{k^2}$ with $k=1, 2, \dots, nobs$ and $\gamma_j = 1/\sigma_{pj}^2$.

Several methods can be used for the minimization problem [182] and the Gauss-Newton method, used in this investigation, will be described more in detail. The Gauss-Newton method introduces a linearization of the non-linear expression in terms of representing the computed M_i^C neglecting the second-order derivative. This method is based on the first-order Taylor series expansion of Q in the quadratic form (Eq. (18)):

$$\frac{dQ}{dP}(P + \Delta P) = \frac{dQ}{dP}(P) + \frac{d^2Q}{dP^2}(P) \cdot \Delta P + \theta(\Delta P^2) \quad (17)$$

An extreme of the Q function is obtained imposing (Eq. (19)):

$$\frac{dQ}{dP}(P + \Delta P) = 0 \quad (18)$$

and neglecting terms greater than first-order, Eq. (19) can be expressed as a linear system (Eq. (20)):

$$\begin{cases} A \cdot \Delta P + B = 0 \\ A = \frac{d^2 Q}{dP^2}(P) \\ B = \frac{dQ}{dP}(P) \end{cases} \quad (19)$$

where (Eq. (21), (22), (23)):

$$B_k = \frac{dQ(P)}{dP_k} = 2 \sum_{i=1}^s \beta_i (M_i^C - M_i^{exp}) S_{ik} \quad (20)$$

$$A_{jk} = \frac{d^2 Q(P)}{dP_j dP_k} = 2 \sum_{i=1}^s \beta_i (M_i^C - M_i^{exp}) \frac{d^2 M_i^C}{dP_j dP_k} + 2 \sum_{i=1}^s \beta_i \frac{dM_i^C}{dP_j} S_{jk} \quad (21)$$

$$S_{jk} = \frac{dM_i^C}{dP_k} \quad (22)$$

and S is called sensibility matrix.

The peculiarity of this method consists in neglecting the second-order derivatives of the calculated variables of the direct model in Eq. (22), which becomes (Eq. (24)):

$$A_{jk} = \frac{d^2 Q(P)}{dP_j dP_k} \cong 2 \sum_{i=1}^s \beta_i \frac{dM_i^C}{dP_j} S_{ik} \quad (23)$$

Thus, the solution of the linear system (Eq. (20)) leads to the determination of the components of the S matrix.

The sensitivity matrix allows to determine the A matrix and the B gradient of the linear system (Eq. (20)). It is therefore necessary to calculate the derivatives of M^C respect to each parameter to be determined and the sensitivity analysis may be performed [183]:

- by finite differences;
- by means of analytic direct calculation;
- with the formulation of a conjugate problem;
- with a semi-analytical evaluation.

4.1. Procedure for parameters identification

The basic concept of an inverse analysis consists of a set of unknown parameters defined in flow stress equation and friction conditions. First, a FE simulation of the selected material test with the assumed parameters of the flow stress equation and friction conditions are conducted and the computed load-stroke curve is compared with the experimentally measured curve. Then, the assumed parameters of the flow stress equation are adjusted in such a way that the difference in the calculated and measured load-stroke curves is reduced in the next comparison. This procedure is repeated until the difference between experimental measurements and computed data disappear. The result of inverse analysis is a set of the identified material parameters, which represents material properties and the real conditions of the forging process.

The procedure used to identify the material parameters includes:

- 1) Guess the material parameters in experimentally measured curves;
- 2) Start FEM simulation of the selected material test with given experimental data;
- 3) Compare the computed forming load with experimentally measured one;
- 4) Obtain the amount of adjustments in material parameters by minimizing the difference between the computed and measured loads;
- 5) Improve the material parameters until the difference becomes within a desired tolerance.

Generally, the unknown parameters are determined by minimizing a least-square function consisting of experimental and FEM simulated data. The FEM is used to analyze the material flow behaviour during the test, whereas the optimization technique allows for automatic adjustment of parameters until the calculated response matches the measured one within a specified tolerance.

5. Experimental procedures

FE simulations are even more important in the optimization of the cold and warm forging processes analyzed and the precise calibration of the numerical models is a strong requirement to obtain reliable results. Nevertheless, accurate data about the material flow behaviour and friction conditions at the tool-workpiece interface can be hardly found in the literature.

Therefore, some investigations have been carried out to overcome this lack and the inverse analysis theoretical bases for determination of flow stress and friction conditions are previously described.

In this thesis, two experimental apparatus, developed to study the rheological and friction properties in the same thermo-mechanical conditions of the industrial processes tested, and the experimental results regarding the flow curves at different forging temperatures and the evaluation of friction conditions are presented in §5.1 and §5.2 of "Part 2" respectively.

5.1. Material rheology characterization

Data about the elasto-plastic properties of the bulk metal as function of strain rate and temperature can be hardly found in the literature, as well as the influence of applied stress and strain on the materials flow behaviour. To overcome this lack, an experimental apparatus was developed at the Department of Management and Engineering (DTG) at the University of Padua, in order to evaluate the mechanical properties of the materials at different strain rates and temperatures.

5.1.1. Experimental apparatus

A series of tensile tests were performed to study the rheological behaviour of bulk steels at different strain rates and temperatures, in a controlled experimental environment. This was made in order to reproduce the limits of the thermo-mechanical working conditions of the cold and warm forging processes analyzed. The apparatus consisted of a 250 kN MTS 810 hydraulic tensile testing machine, equipped with an inductive heating system used for warm tensile tests (Fig. 27).

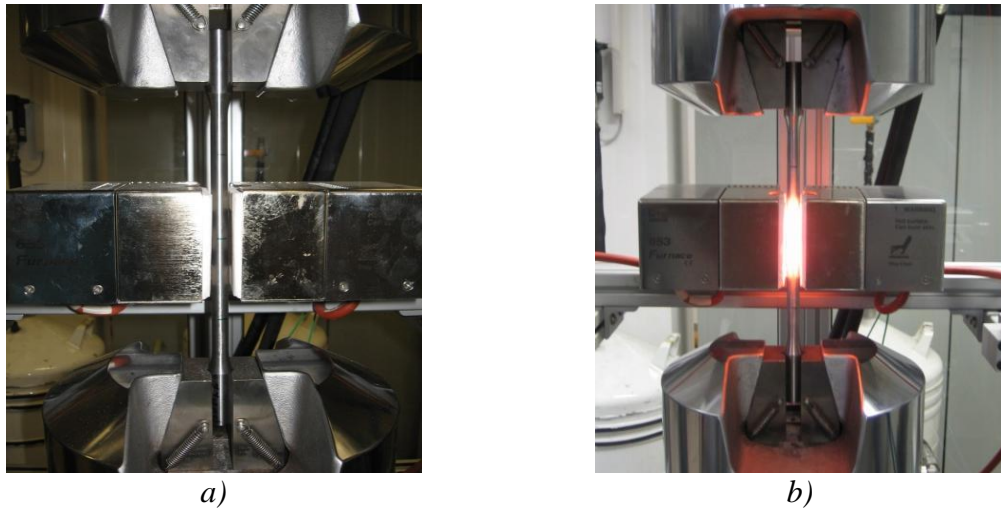


Fig. 27. The experimental apparatus developed at the Department of Management and Engineering (DTG) for a) cold and b) warm tensile tests.

The frontal inductor, which shape was previously optimized through an infrared analysis in order to obtain a uniform thermal distribution in the gauge length, could heat the round tensile specimen up to 1000 °C. The temperature evolution was measured by means of a K-type thermocouple spot-welded in the centre of the specimen.

This equipment also adjusted the vertical position of the inductor during the deformation phase, to maintain the heated zone of the tensile specimen centered with respect to the thermocouple position and to guarantee a constant and uniform thermal profile in the area of interest.

Fig. 28 illustrates the tensile test specimen dimensions in accordance with ASTM E8M-04 standard.

At least three specimens were tested for each steel and test condition (i.e. strain rate and temperature), in an attempt to assure the repeatability of the results. The specimens were directly machined from the same hot rolled bars used for cold and warm forging tests.

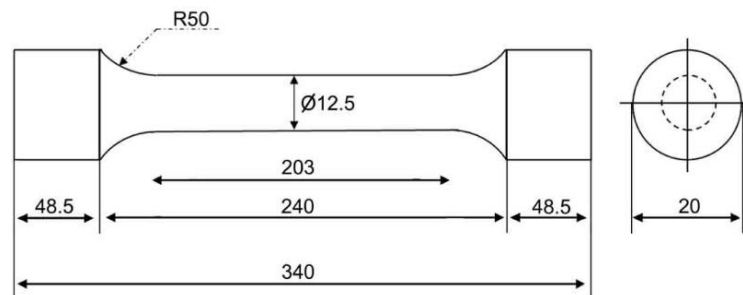


Fig. 28. Tensile test specimen geometry. All dimensions are in mm.

Samples were loaded at two different constant strain rate $\dot{\epsilon}$ of 2 min^{-1} (0.03 s^{-1}) and 3000 min^{-1} (50 s^{-1}) and at three different temperature T (i.e. 20, 400 and 700 °C). The stroke speed of the testing machine was set in order to obtain the desired average strain rate in tensile tests and it was kept as a constant value during all the deformation phase.

During the tests a PC-based data acquisition system, *TestWare-SX*, was used to record and store loads and displacements. Meanwhile, to measure accurately Young's modulus E and Yield strength YS , a raster extensometer was adopted during the elastic period in all tests. The same thermal cycles that stainless steels (i.e. AISI 304L and Duplex 2205) underwent before forging operations, were reproduced for tensile tests at elevated temperatures (i.e.

400 and 700 °C). In this case, the gauge lengths of the specimens were heated at 400 and 700 °C for 10 min respectively and when the desired temperature was reached, isothermal tensile tests were performed at different strain rates.

5.1.2. Results and discussion

Fig. 29 plots the average experimental engineering stress-strain curves of the three steels at each strain rate and temperature analyzed.

As usual, the engineering stress σ_{nom} is defined as F/A_0 , where F is the axial load and A_0 is the initial transversal area, while the engineering strain or elongation l is computed as $(L - L_0)/L_0$, with L and L_0 being the current and initial gauge lengths, respectively.

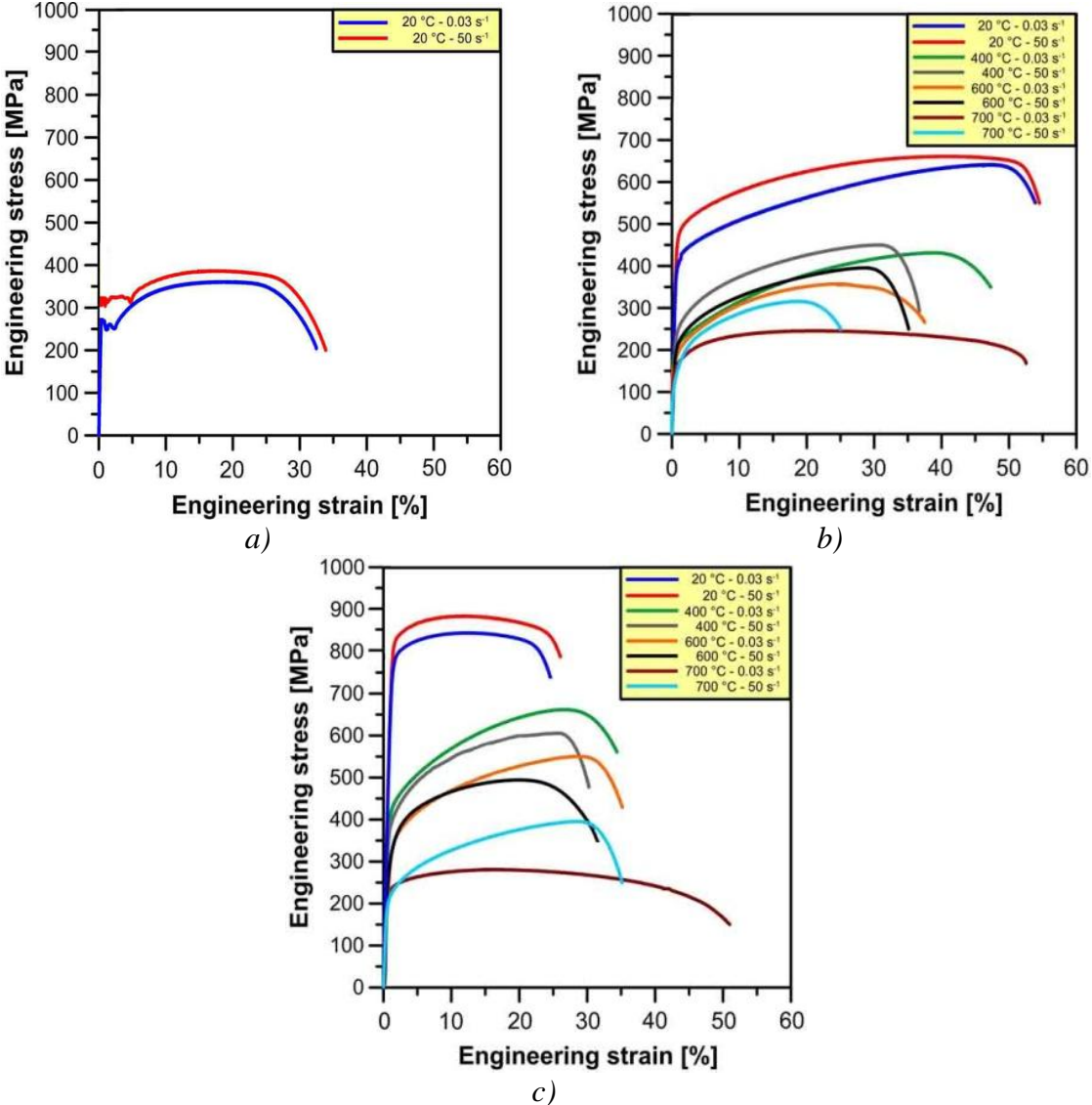


Fig. 29. Average experimental engineering stress-engineering strain curves with respect to strain rate and temperature obtained by the tensile tests: a) AISI 1005, b) AISI 304L and Duplex 2205.

The average true stress and strain curves can be derived from the engineering stress and engineering strain measurements and were calculated using the following formulas (Eq. (24), (25)):

$$\varepsilon_{true} = \ln(1 + l) \quad (24)$$

$$\sigma_{true} = \sigma_{nom} \times (1 + l) \quad (25)$$

Tables 10, 11 and 12 report the mean values of typical mechanical properties of AISI 1005, AISI 304L and Duplex 2205, take at different strain rates and temperatures for the investigation. The testing temperature has a strong influence on the elastic properties of the materials, which drastically decrease with enhancing forging temperature.

Temperature, T [°C]	20	
Strain rate, s^{-1}	0.03	50
Yield strength, $YS_{0,2\%}$ [MPa]	256 (5)	322 (4)
Ultimate strength, UTS [MPa]	361 (3)	490 (5)

Tab. 10. Average mechanical properties of AISI 1005 (standard deviation in parenthesis).

Temperature, T [°C]	20		400		700	
Strain rate, s^{-1}	0.03	50	0.03	50	0.03	50
Yield strength, $YS_{0,2\%}$ [MPa]	439 (1)	501 (1)	199 (2)	203 (4)	141 (3)	120 (3)
Ultimate strength, UTS [MPa]	643 (1)	661 (2)	431 (2)	445 (2)	230 (2)	322 (5)

Tab. 11. Average mechanical properties of AISI 304L (standard deviation in parenthesis).

Temperature, T [°C]	20		400		700	
Strain rate, s^{-1}	0.03	50	0.03	50	0.03	50
Yield strength, $YS_{0,2\%}$ [MPa]	775 (3)	830 (1)	376 (2)	321 (3)	210 (2)	235 (4)
Ultimate strength, UTS [MPa]	835 (4)	882 (2)	660 (3)	597 (2)	279 (2)	483 (2)

Tab. 12. Average mechanical properties of Duplex 2205 (standard deviation in parenthesis).

5.2. Evaluation of friction conditions

Similarly to material rheology characterization, data about the friction properties for the industrial processes considered are hardly found in the literature. To overcome this lack, a new experimental apparatus was developed to evaluate friction conditions in different metal forming processes.

5.2.1. Experimental apparatus

An experimental setup was designed with the aim to reproduce the thermo-mechanical friction conditions established at the tool-workpiece interface on the industrial forging processes analyzed, in order to study the friction behaviour of bulk steels. The experimental procedure to identify the friction factor m and coefficient μ , depending on the local contact parameters. As shown in Fig. 30, the new method to determine friction based on the T-shape compression (cf. §2.4.1 of "Part 2") includes three parts: punch, cylindrical specimens and die with a V-groove. The sectional shape of a formed part is "T-shaped", hence the test is named T-shape compression.

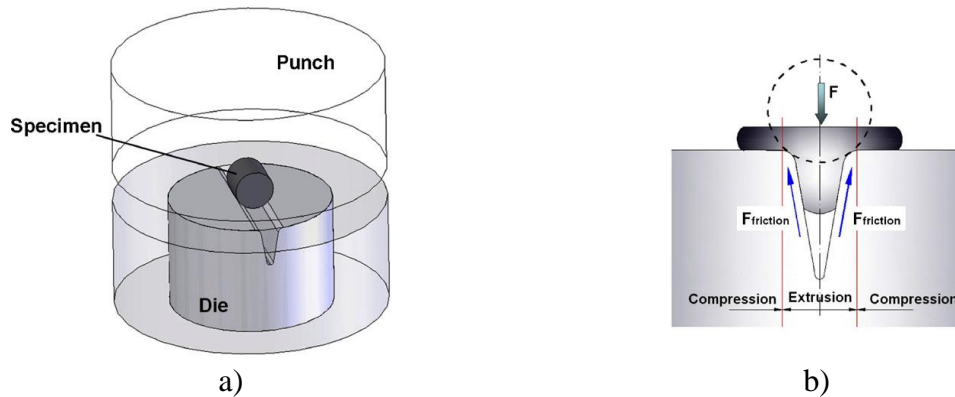


Fig. 30. The principle of T-shape compression test.

In this test, the specimen is first located in the V-groove as shown in Fig. 30a. During deformation by the top punch, some metal is extruded into the groove and some is upset and moved sideways between the flat surfaces (Fig. 30b). The friction force, generated along the wall of groove, restricted metal flow into it, so the height of extruded part changes with different friction conditions and materials. Furthermore, the forming load is influenced by the friction along the dies surface, especially the groove wall friction, as the direction of a large component of its force is opposite to that of forming load. In addition, this test is well to evaluate the ability of the lubricant and the material flow behaviour by combined a compression and an extrusion operation, which is widely used in cold and warm forging processes considered. One essential point is that the contact conditions of the workpiece and the tools used in the test must be identical to the tool, with which the simulated process will be performed later on in practice. For this reason the tool material was an high-speed steel, commercially named *HPS*, coated by a multilayer coating composed of a first TiN layer and a second AlCrN thin film. The total thickness of the multilayer was 7-9 μm thick, which was deposited on steel substrate by a PVD technique and chosen for its high strength and hardness. The experimental die reported in Fig. 34 was then inserted in a steel shrink ring. The corner radius R was 1 mm and V-groove angle β was 20° . The total depth of groove, neglecting the final radius, was 10 mm. Then, a series of three tests were performed on the steels considered for each lubrication condition and a MTS 810 hydraulic compression testing machine, 250 kN in capacity, was used. The loading speed of testing was 2 min^{-1} ($0,03 \text{ min}^{-1}$) and the maximum stroke was 4,5 mm. Experimental T-shape apparatus and a formed specimen obtain are shown in Fig. 31. Cylindrical specimens (i.e. 6.85 mm diameter and 7 mm long) were used performing the T-shape compression tests. As for tensile specimens, they were directly machined from the same hot rolled bars used for the cold and warm forging tests.

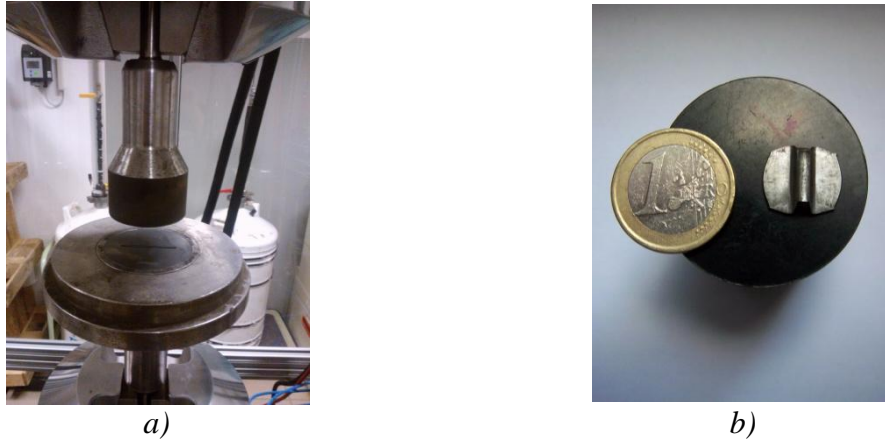


Fig. 31. a) The experimental apparatus and b) an example of formed specimen.

Then steel specimens were coated by a single-layer-type solid lubricant film, subsequently applied on a series of cylindrical billet used to perform the industrial forging process tests on the three steels considered (§2.3.4 of "Part 1"). For all these steps, similar process conditions were used, mainly the ageing of lubricant baths and the lubricating time. For solid lubrication condition, the cylindrical surface of the specimen was coated, contacted with die and punch directly. For the oil lubrication condition test, the V-groove was filled with the lubricant, so the billet surface was easily lubricated during the test. The two lubrication conditions in tests are shown in Table 13.

Lubrication condition	Lubricant
Solid lubrication	Single-layer Bonderlube FL 744
Solid + oil lubrication	Single-layer Bonderlube FL 744 + Mobilgear 600 XP 220 (viscosity $\eta = 220 \text{ mm}^2/\text{s}$, at 40°C)

Tab. 13. Lubrication conditions.

5.2.2. Results and discussion

Fig. 32 shows the typical process-sequence of specimen deformation.

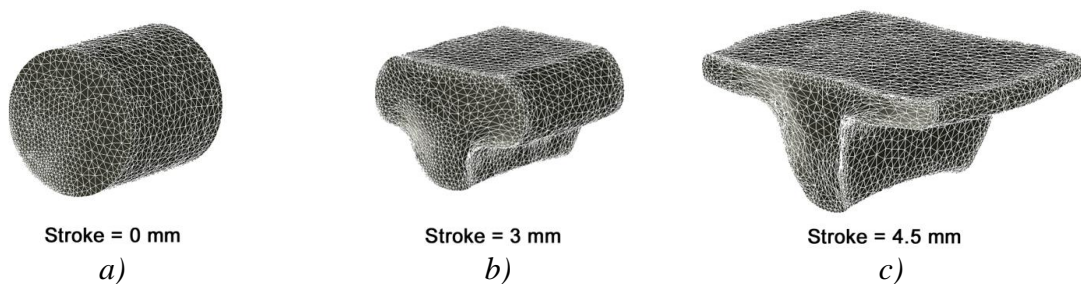


Fig. 32. Specimen deformation process for AISI 1005 steel.

The whole T-shape compression test includes two stages. In the first stage, the metal is pushed into the die groove and no lateral expansion appears between the punch and flat-top surface of die, due to small contact area between specimen and punch. Also it can be observed that the load changes almost linearly with punch stroke when the ratio of punch stroke to billet diameter increases from 0.1 to 0.35 (Fig. 33). In the second stage, the

contact region of specimen/punch becomes larger, then the compression of metal occurs between the flat surfaces of the tools, so load will increase shapely.

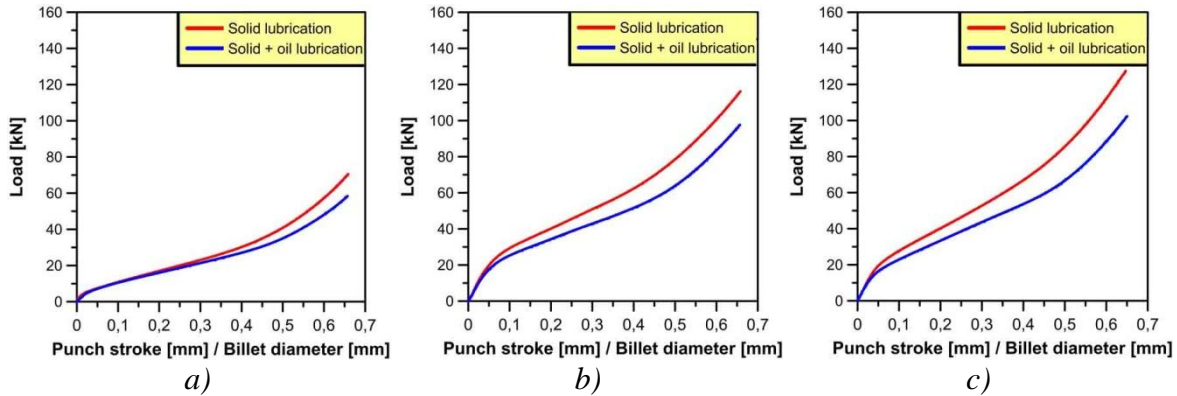


Fig. 33. Average experimental load curves under different lubrication conditions: a) AISI 1005 steel, b) AISI 304L and c) Duplex 2205 stainless steel.

6. Numerical models calibration

The accurate calibration of the numerical models previously described is a strong requirement to improve the quality and reliability of numerical simulations of the cold and warm forging processes analyzed. Such models were therefore calibrated through both material testing experiments, to determine the rheological and friction parameters, and inverse analysis method to get a feasible description of the real processes considered.

6.1. Material constitutive equation

The material rheological characterization is essential for a proper FE model calibration. Therefore the experimental device described in §5.1.1 of "Part 2" was used to carry out tensile tests at room and elevated temperature and thus generate reliable data as function of strain rate and temperature. The rheological behaviour of the material was described on FEM code FORGE2011[®]-3D by means of the Hansell-Spittel's law given in Eq. (6). This constitutive equation of AISI 1005, AISI 304L and Duplex 2205 was obtained by fitting experimental data into Eq. (6). It is clear that for only room temperature testings performed, the temperature related terms of Eq. (6) were ignored.

The Hansell-Spittel coefficients for the steels analyzed were obtained by fitting average $\sigma_{true}-\epsilon_{true}$ experimental curves by means of the inverse FE analysis approach introduced in §4.1 of "Part 2". As direct model of simulation, a FE model of experimental tensile test was used. The least square function was chosen as cost function. The minimization algorithm was a Gauss-Newton method with sensitivity matrix evaluated through finite differences, jointed to a linear search algorithm inspired to the golden section linear search method.

6.1.1. Numerical simulation of tensile test

The commercial implicit FE software FORGE2011[®]-3D was used to simulate the experimental tensile tests. Because the operation has two planes of symmetry, only one quarter of tensile specimen was modelled by 5976 four node tetrahedron elements and an elastic-plastic material model was assigned to specimen (Fig. 34), in order to significantly reduce the computation time.



Fig. 34. 2D FE model of the tensile specimen.

These material models (i.e. the average engineering stress - engineering strain curves reported in a matrix form as function of strain rates and temperatures) and the average mechanical properties of each steel reported in Tables 10, 11 and 12 were used as the material input data of the FE models presented in this thesis.

6.2 FE model of T-shape compression

It is well known that, as an essential input parameter for the FE simulation, a realistic friction condition must be specified at the die-workpiece interface in order to accurately predict metal flow in the industrial forging processes analyzed. In order to estimate the real values of the friction factor m and coefficient μ , the average of experimental load curves obtained for the two different lubricant conditions on each steel considered (cf. Fig. 37) were coupled with FE simulation. The analytical procedure to identify the friction factor m and coefficient μ for each steel analyzed were obtained by fitting average experimental load curves by means of the inverse analysis approach introduced in §4.1 of "Part 2".

6.2.1. Numerical simulation of T-shape test

The commercial implicit FE software FORGE2011[®]-3D was used to simulate the experimental T-shape compression tests. The 3D specimen geometry was modelled by 8910 four node tetrahedron elements and an elastic-plastic material model was assigned to specimen. In order to assure the reliability of the results, the simulated flow stress-strain data carried out from the average experimental σ - ϵ curves were used as the material input data of the FE models and several points on the average load-punch stroke/billet diameter curves were chosen to put into the FE code.

In order to calculate the values of the friction factor m and coefficient μ , the average experimental and simulated load curves are plotted in Fig. 35. The difference between the curves is less than $\pm 2\%$ on each steel considered. This suggests that simulated and experimental results are in good agreement.

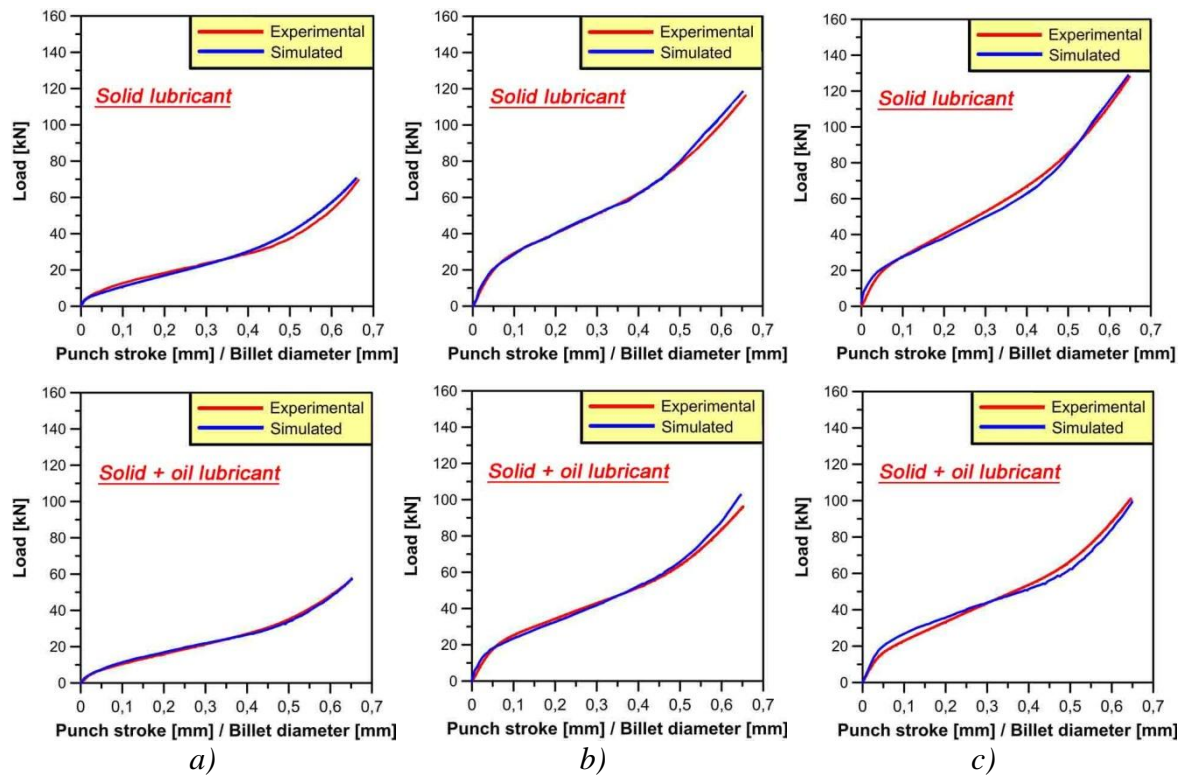


Fig. 35. Comparison between the average experimental and simulated load curves at different lubrication conditions: a) AISI 1005, b) AISI 304L and c) Duplex 2205.

The estimated values of the friction factor m and coefficient μ for the two different lubrication conditions on each steel analyzed are given in Table 14.

Steels	Solid lubrication		Solid + oil lubrication	
	μ	m	μ	m
AISI 1005	0.11	0.83	0.14	0.79
AISI 304L	0.03	0.86	0.07	0.80
Duplex 2205	0.05	0.91	0.09	0.86

Tab. 14. Friction factors m and Amontons-Coulomb coefficients μ values under different lubrication conditions estimated by using FE simulations.

7. Industrial case studies

In this PhD thesis, thermo-mechanical coupled 3D FE simulations modelling deformation and friction conditions on a series of industrial forging processes were performed by using the commercial FE code FORGE2011[®]-3D. As industrial case studies, savings on process design costs and the prediction of surface defects in a multi-stage cold forging process of an heat pipe fitting were analyzed. Moreover the design of integrated experimental procedures and modelling tools to re-design a single-stage cold forming cycle of an AISI 1005 plug fitting in the attempt to form stainless steel components was developed by using FE methods.

7.1. The multi-stage cold forging process of an heat pipe fitting

In this industrial case study, a re-design of the deformation process-sequence and a systematic approach to predict surface defects, based on numerical simulation, has been proposed (cf. [Article II and III](#)). The results found could be summarized as:

- Using FE methods as tools result in reducing time-to-market, reducing tool development costs, predicting the influence of process parameters, reducing production costs, increasing product quality, improving the understanding of material behaviour and reducing material waste.
- Such modelling efforts can be very valuable in identifying inhomogeneous deformations that could not easily be detected through regular visual inspection;
- The simulation-enabled approach shifts the design paradigm from experience-based trial-and-error to scientific-based calculation and analysis, reducing the time required to set up new forging cycles at about 40%.

Process description and modelling

The material used for the workpiece was a low-carbon AISI 1005 steel. The initial cylindrical billet (24 mm diameter, 91.4 mm height and 324 g weight) was modelled by 25,958 four node tetrahedron elements. The rheological parameters reported in §6.1.1 of "Part 2" at different strain rates and room temperature were implemented in the FE model. Forging tools were assumed to be rigid with an infinite elasticity modulus and a constant temperature of 20 °C. In addition, the tool-workpiece interface was characterized by friction parameters (i.e. m and μ) presented in Table 17 for solid lubrication condition. Finally, the physical constants and properties of the AISI 1005 steel were chosen among those present in the software database, as well as the heat-transfer coefficients (HTC) between the workpiece and the tool.

For major details on process-sequence description and modelling see [Article II](#) and [Article III](#).

Process sequence optimization

As shown in the load-forming time relationships reported in [Article II](#) the elimination of the third operation is suggested. This process-sequence optimization gives a shorter process development lead-time, lower production costs, savings in tool material costs and the development of higher precision parts.

Underfilling and surface defects prediction

Underfilling problems are limited by the use of multiple forming stages. The reduction of underfilling areas at the die corners obtained by FE analysis is consistent with the experimental observation (cf. [Article II and III](#)).

Defects occur in each stage of the optimized forming sequence (cf. [Article III](#)). Based on simulated flow behaviour of material, several types of surface defects are identified and attributed to plastic instability of the work-material, inappropriate axial/radial flow ratio, excessive forming-pressure and uncorrect tooling design (cf. [Article III](#)). For major details on the formation mechanisms of surface defects studied through FE models see [Article III](#).

Benefits of FE method

FEM simulation provides also deeper insights into the forging processes. Focusing on a generic new product development chain of a company's multi-stage cold forged component, Zoppelletto S.p.A. estimates to reduce time-to-market expected (cf. [Article II](#)). Completely removing the trial-and-error iterations of it saves the costs of trial tool production, so the time to recover the entire software and training investment decrease dramatically to some months, depending on how widely the approach is adopted (cf. [Article II](#)).

7.2. The single-stage forging process of an hex-head plug fitting

Traditional cold forging set-up

In another case study, a 3D FE model of a cold forging operation of an hex-head plug fitting was developed. The initial cylindrical billet (22 mm diameter, 18 mm height and 51 g weight) was discretised with 167,235 four node tetrahedron elements to ensure sufficient accuracy and convergences. Then, the rheological parameters calculated at different strain rates and room temperature (cf. §6.1.1 of "Part 2") and the friction parameters m and μ established in solid lubrication condition (cf. Table 14) were implemented in the FE models of each steel considered. Moreover forging tools were considered to be rigid bodies at a constant temperature of 20 °C. Furthermore, the physical constants and properties of each steel were chosen among those present in the software database, as well as the heat-transfer coefficients (HTC) between the workpiece and the tool.

For major details on process description and modelling see [Article IV](#).

FE analysis provides detailed information on the forming panorama, forming load and metal flow, which can be incorporated into the traditional process extended to cold forging of stainless steels. These informations have been reported in this work ([Article IV](#)) and the results found could be summarized as:

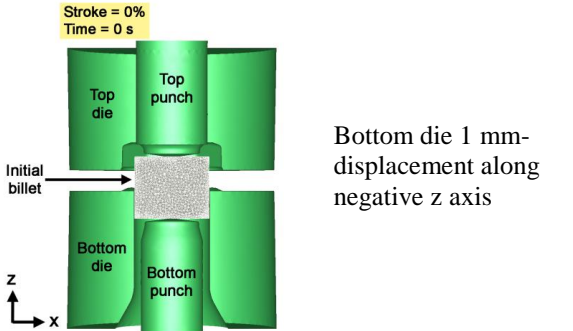
- The traditional cold forging cycle of AISI 1005 hex-head plug fitting seems to be non-adaptable to different material categories, such as stainless steels. This can be highlighted by some underfilling areas that occur at the die corners in AISI 304L and Duplex 2205 components. Moreover, due to the higher forging loads reached by the punches during the whole forging operation, the re-design and calibration of the process is suggested.

Optimized cold forging set-up

The re-design of the traditional single-stage operation for cold forging of stainless steels has been performed by using FE methods (cf. [Article IV](#)).

Starting from the FE model of the above conventional process, the workpiece was optimized through many trial-and-error simulations in terms of the die filling and the forming load requirements and reductions. Subsequently, the deformation mechanism of the optimized cold forging operation was thoroughly revealed by analyzing the forming panorama and effective strains in detail.

In Table 15 the optimization of the initial billet and process parameters were obtain by means of the inverse FE analysis approach introduce in §4.1 of "Part 2".

Billet dimensions		Tools set-up	
Traditional process	Optimized process	Optimized process	
<u>Diameter:</u> 22 mm <u>Height:</u> 18 mm <u>Weight:</u> 51 g	<u>Diameter:</u> 22 mm <u>Height:</u> 18.3 mm <u>Weight:</u> 55 g		

Tab. 15. Variation of traditional billet geometry and process parameters.

The optimized billet geometry has a significant influence on the die filling. Moreover forming load requirements are important for accurate tools design and proper determination of process specification.

Major informations about the optimized cold forging set-up have been reported in [Article IV](#) and the results found through numerical simulations could be summarized as:

- The optimized single-stage forging processes to form the stainless steel hex-head plug fittings (i.e. AISI 304L and Duplex 2205) assure a better filling of the die-cavities and a lower forming load requirements as compared to the traditional ones (cf. [Article IV](#)).
- The lowest forging loads reached by the punches during the optimized forging cycle are mainly associated to the new dimensions of the billet geometry and the re-design bottom die displacement. On the other hand a non-perfect filling of die-cavity could easily be detected through virtual inspection of the optimized cold forged stainless steel components (cf. [Article IV](#)).

Optimized warm forging set-up

The optimized single-stage forging process was subsequently adapted to warm forge stainless steel hex-head plug fittings to ensure a better die filling and the respect of forging drawing tolerances established by Zoppelletto S.p.A. for the traditional AISI 1005 cold forged parts. Based on the above optimized FE models, the AISI 304L and Duplex 2205 virtual billets were set at 700 °C for the first simulations cycle. This temperature was below the recrystallization temperatures of the workpiece materials, i.e. $0.25-0.65T_m$ (cf. 1 of "Part 1"). In the subsequent numerical models, temperature was set at 600, 500 and 400 °C respectively, in the attempt to establish the lowest forging temperature to form near-net-shape and tolerances-respected forged components made of stainless steel. Thus, in order to guarantee energetical and economical benefits to the company.

Starting from the optimized billet geometry (cf. 7.2 of "Part 2"), the rheological parameters estimated at different strain rates and temperatures (cf. §6.1.1 of "Part 2") and the friction parameters stated for solid lubrication condition were the key materials input data of the FE models for both stainless steels considered.

As on previous numerical models, the physical constants and properties of each material were chosen among those present in the software database, as well as the heat-transfer coefficients (HTC) between the workpiece and the tool.

Analyzing the FE results for both stainless steels, it is clearly highlighted the total absence of underfilling red areas already at the minimum forging temperature of 400 °C, as shown in Fig. 36. This temperature was selected after several trial tests by using the FORGE2011®-3D code.

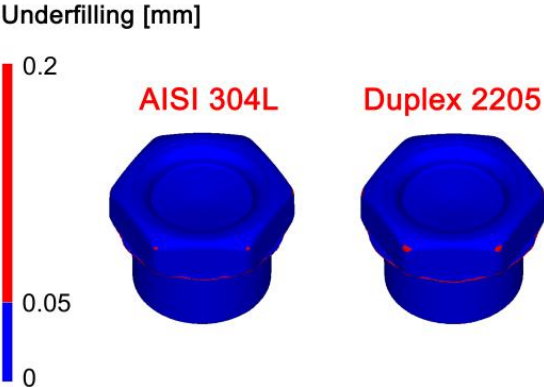


Fig. 36. Underfilling red areas on virtual optimized warm forged parts at 400 °C.

PART 3

**MICROSTRUCTURAL CHARACTERIZATION
OF FORGED PARTS**

1. Defects in cold and warm forging

1.1. State of the art

The competitiveness of cold and warm forging processes in relation to other manufacturing processes is good. To remain competitive, cold forging processes have to produce defect free products. Therefore, it is essential to detect and prevent defects during the production process.

As mentioned before, cold and warm forging are governed by many factors such as friction, part geometry, die shape, and temperature setting of the die and workpieces. Hence, they have an high tendency to form defects.

In the past, few researches were focused on defect issue in forming process. Kimura et al. [182] evaluated component assembly based on shape error. In addition, metal flow imperfection related defects have attracted the attention of many researchers. Chan et al. [183] proposed a dynamic change of tooling geometry to control the most common flow-induced defect such as folding. Other defects such as die filling and barrel formation during the lateral extrusion process have been discussed by Tahir [184]. Similarly, Liu et al. [185] studied the under-filling problem in the rotary rolling of a flange. On the other hand, Narayanasamy et al. [186] studied the reaction of various metals to barreling during the cold upsetting process. In his study, un-lubricated truncated cone billets were used as a case study, and the relationship between the measured radius of curvature of the barrels and the stress ratio parameter was established. In addition, Baskaran and Narayanasamy [187] applied white grease as a lubricant to determine the dimensions such as height, contact, and bulge diameter at different stress-ratio parameters. Yilmaz et al. [188] conducted an experimental investigation of conventional closed-die forging to study the effect of aspect ratios and indentation to the forging load and die filling. In another work, Lu and Zhang [189] found that forging defects are caused by improper die dimension and an optimized die dimension was proposed. The study was carried out, taking into consideration the temperature dependency of the thermal and mechanical properties of materials. Song and Im [190] studied the effect of process design parameters to the formation of under-filling and folding defect during closed-die forging of bevel gears. In another study, Qamar investigated the effect of shape complexity and dead metal zone to the quality of cold extruded part [191]. In addition, Sheu and Yu introduced a new type of die design to solve the folding defect during the orbital forging process [192]. The new design influenced the flow of the preform, resulting in lower tool stresses and preventing the folding problem.

1.2. Forging defects

There is some confusion in the use of various terms associated with ductility. The following definitions will be used in this PhD thesis [193].

Ductility: the ability to deform plastically without fracture in a standard test, usually expressed by some measure of limiting strain.

Formability: the ability of a material to deform plastically without fracture in a forming process.

Workability: the ability of a material to deform without occurrence of any defect in a forming process.

Defect: the properties of a product that do not conform to the design specifications, which make the product less suitable or unsuitable for the purpose for which it has been designed [193].

Alternatively to the Devedzić classification, Arentoft and Wanheim [194] summarized the different defects observed in forging processes. They classified forging part defects into six groups: folds, shear defects, cracks, surface defects, form defects and structural defects. Each group can be divided into several sub-groups. A defect-matrix was then proposed to provide design reference for engineers. The matrix contained six defect groups, horizontally, and six groups, with possible causes for the defects, vertically. The possible causes for the defects were divided into six main groups (*i.e.* tribology, preform, tools, press, process and workpiece material), with several sub-groups.

A brief description of defects and their remedial methods is given below.

Surface and internal cracking

Cracking is also the defect that has been researched most extensively.

Surface cracking occurs when the surface of an extrusion splits, which is often caused by extrusion temperature, friction, or speed being too high. It can also happen at lower temperatures if the extruded product temporarily sticks to the die.

Internal cracking occurs when the centre of the extrusion develops cracks or voids. These cracks are attributed to a state of hydrostatic tensile stress at the center line in the deformation zone in the die.

The Okamoto et al. classification will be used as a guideline although it will be slightly modified sometimes [195].

Surface imperfections

Not much interest is being displayed in literature about surface imperfections. These defects are most times fairly easy to overcome by improving the lubrication. Friction and wear (defects) may be explained through several related mechanisms: tearing of weldments, plowing, a thin surface layer of severe plastic deformations and galling.

Plowing

The localized high pressures cause the asperities of the hard tool to penetrate into the deforming workpiece. With the relative motion of each asperity over the workpiece, a deeply plowed groove is created. These grooves expose fresh, uncontaminated surfaces, which produce a shiny appearance of the workpiece surface.

Tearing of weldments

The high pressures over the relatively small areas of actual contact may cause localized welding. The metals at the weld interface may form hard intermetallic compounds. As the weldments break loose, they cause damage to both tool and workpiece. Intermetallic fragmented particles may now move between the two mating surfaces and cause further damage. The particles may be pressed into the workpiece, become imbedded, and present hard cutting edges plowing into the hard die.

Galling

When there is a strong chemical affinity between the tool material and the workpiece, layers of the workpiece material adhere to the tool surface and may become immobilized. The difference between tearing of weldments and galling is that the galling material contains only workpiece material, whereas the torn of weldments contain tool material as well.

Surface layer of severe plastic flow

The description of plowing and tearing of weldments demonstrates that a thin layer in the surface of the workpiece is severely affected by friction between tool and workpiece. The amount of deformation is highest at the interface and diminishes further from the surface.

Surface roughening due to coarse grain size

The grain size is, as Dautzenberg and Kals state, one of the main causes for surface roughening. In agreement with the plasticity theory it can be assumed that the deformation takes place by shear in the planes of maximum shear stress. From a metallurgical point of view, this means that the nearest closed packed planes provide for shear by means of dislocation glide. Kudo [196] illustrates the effect of the grain size of the workpiece material on the rate of roughening of the free surface of a workpiece due to deformation.

Excessive lubrication of the tool-workpiece interface is another reason for surface roughening of the product [196].

Extreme roughening can be overcome by choosing a workpiece material with a small grain size or a careful heat treatment of the billet, preform or interstage in order to refine the structure.

Surface lines

These are the lines visible on the surface of the extruded profile. This depends heavily on the quality of the die production and how well the die is maintained, as some residues of the material extruded can stick to the die surface and produce the embossed lines.

Scale pits (Pits marks)

Scale pits are seen as irregular depositions on the surface of the forging that is caused primarily due to improper cleaning of the stock used for forging. The oxide and scale gets embedded into finish forging surface. When forging is cleaned by pickling, these are seen as depositions on the forging surface.

Flow imperfections

The flow imperfections represent a wide range of defects, including such defects as buckling, non-concentricity, folding and the occurrence of fins and flashes. Flow imperfections will be one of the most important defects in near-net-shape forging processes since in these processes as accurate as possible products and no material waste, subsequent machining or trimming are wanted.

Three kinds of flow imperfections can be distinguished:

- Dimensional inaccuracies: the inability to achieve the designed dimensions;
- Shape inaccuracies: the inability to meet the designed product shape;
- Positional error: the inability to align the several design features.

The factors and sources that result in these three kinds of flow imprecisions were listed by Kudo [196].

Cracking at the flash

This crack penetrates into the interior after flash is trimmed off.

Increasing flash thickness, relocating the flash to a less critical region of the forging, hot trimming and stress relieving are the ways to prevent flashes.

Cold shut (Fold)

Cold shut appears as small cracks at the die corners of the forged part. Two surface of metal fold against each other without welding completely. That is caused primarily due to very tight fillet radii that inhibit smooth material flow towards the corner of the die (i.e. sharp corner, excessive chilling, high friction). An increase fillet radius on the die can prevent that type of defect.

Unfilled section (Underfilling)

This defect refers to localized unfilled portion within the die cavity due to improper design of the forging die or inappropriate selection of the forging technique, less raw material and poor heating. Some section of die cavity is not completely filled by the flowing metal.

Proper die design, raw material and heating are the ways to prevent underfillings.

Flakes

These are basically internal ruptures caused by the improper cooling of the large forging. Rapid cooling causes the exterior to cool quickly causing internal fractures. This can be avoided by following proper cooling practices.

Die shift (Mismatch)

Die shift is caused by the misalignment of the top and the bottom dies making the two halves of the forging to be improper shape. The possible remedy of this dies mismatch is a proper alignment of die halves.

2. Plastic deformation structures

Advances in understanding deformation microstructures have been closely related to the development of automatic and semiautomatic techniques in the transmission electron microscopy (TEM), scanning electron microscopy (SEM) and x-ray diffraction. Microstructure and crystallographic texture represent the key material features used in the continuous endeavor to relate the processing of a metal with its final properties. Optical microscopy and macroetching are used to view the macroscale grain flow, size and pattern in a steel forging. Traditional grain and flow patterns remain in use today to assess die and forge process design, as well as for quality control of the homogeneity of the forging deformation. In addition, the trapped dislocations induce significant changes in mechanical properties that depend on their number and arrangement.

2.1. Recrystallization and grain-growth structures

Although there is a great deal of empirical knowledge of the microstructures that can be produced during current industrial processing, the ability to produce more nearly ideal microstructures for different applications is very limited. It is in order to gain improved control of recrystallization processing that increased scientific understanding is needed.

As steel is deformed, the internal energy increases through the storage of dislocations. This energy is released in three main processes, those of recovery, recrystallization, and grain coarsening. The usual definition of recrystallization [197] is the formation and migration of a new grain structure in a deformed material by the formation and migration of high angle grain boundaries (HABs) driven by the stored energy of dislocations. High angle grain boundaries are those with greater than a 10-15° misorientation. On this definition, recovery includes all processes releasing stored energy that do not require the movement of a high angle grain boundary. Typically, recovery processes involve the rearrangement of dislocations to lower their energy, for example by the formation of low-angle subgrain boundaries. Grain coarsening is the growth of the mean grain size driven by the reduction in grain boundary area. Coarsening can take place by either "normal" grain growth, whose main mechanism is the disappearance of the smallest grains in the distribution, or "abnormal" grain growth. The latter process involves the growth of a few grains which become much larger than the average.

During warm and hot deformation of steels various softening processes occur to reduce the internal energy of the deformed metal. When the internal energy reaches a threshold value, the deformed grains may be replaced by new strain-free grains via the recrystallization mechanism [198]. When recrystallization occurs concurrently with deformation, the process is called dynamic recrystallization (DRX) and when it occurs after deformation, it is termed static recrystallization (SRX). In some cases DRX may initiate through nucleation, but may not proceed to completion during deformation. In these cases, the recrystallization is completed after deformation by the growth of dynamically nucleated grains. This is known as metadynamic or post dynamic recrystallization (MDRX). The conditions under which SRX, DRX and MDRX occur are determined by the combination of processing parameters. In addition to strain hardening, precipitation of microalloying elements in steels may harden the austenite during hot deformation [199,200].

Extensive experimental primary recrystallization studies have been conducted for nearly one hundred years. Studies are summarized with eight laws of recrystallization [201]:

- A certain minimum amount of cold work or deformation and a certain minimum temperature are necessary to initiate recrystallization;
- The smaller the amount of deformation, the higher the temperature required to initiate recrystallization;
- Recrystallization is time-temperature dependent, and increased time decreases the temperature required for recrystallization;
- Final grain size is more dependent on the amount of deformation or cold work than either the temperature or the time of anneal;
- The larger the original grain size of the material, the greater the amount of cold work required to achieve an equivalent recrystallization for a given temperature and time;
- For a given amount of work hardening, an higher working temperature is accompanied by a coarser grain size and requires an higher temperature to cause recrystallization;

- New grains first originate at grain-boundary triple points and do not grow into deformed grains having identical or slightly deviated crystallographic orientations;
- Heating after the recrystallization process is complete causes grain growth to occur.

2.2. Conventional dynamic recrystallization (DRX)

Dynamic recrystallization (DRX) enables the desired microstructure to be obtained directly during metal working under appropriate conditions in various structural steels [202]. When this type of "annealing" process is taking place, both nucleation as well as growth (grain boundary migration) take place while the strain is being applied.

The mechanism for DRX involves a local migration (bulging) of grain boundaries leading to the formation of DRX nuclei, which grow out, consuming work-hardened surroundings during deformation at elevated temperatures. The process of nucleation and grain growth exhibits a cyclic behavior, and therefore this process is referred to as discontinuous DRX (dDRX) [203]. In particular, grain boundary bulging occurs repeatedly in previously grown and work-hardened grains during deformation.

Because DRX involves diffusion controlled grain boundary migration, an increase in the deformation temperature accelerates the recrystallization kinetics. Structural steels with a grain size well below 1 μm possess a beneficial combination of mechanical properties including high strength and sufficient ductility [204,205]. The mean grain size evolved by DRX can be substantially decreased by decreasing the deformation temperature [203]. Therefore, deformation under conditions of warm working is a very effective method for processing of ultrafine-grained metals and alloys [203,205-208]. However, in contrast to hot working, the mechanisms and regularities of microstructure evolution and DRX during warm deformation are still unclear. It is generally accepted that the new ultrafine grains result from a type of continuous reaction [203,207,208].

In particular, the structural changes are characterized by a gradual transformation of strain-induced sub-boundaries into grain boundaries when the sub-boundary misorientations increase to the values typical of conventional grain boundaries during deformation. This process is sometimes referred to as continuous DRX (cDRX) [203,209]. The deformation banding that rapidly introduces large misorientations in deformation substructures plays an important role in the development of strain-induced high-angle grain boundaries and new ultrafine-grained structures at low temperatures [203,210,211]. The density of the deformation bands continuously increases with straining, which leads to progress in cDRX. The kinetics of cDRX remains unclear and has attracted much interested. Apparent retardation of the new grain evolution due to decreasing the deformation temperature may be due to stunted dynamic recovery [206].

On the other hand, a model of grain fragmentation based on lattice curvature, which has been recently proposed by Toth et al. [212], suggests an acceleration of the development of high-angle strain-induced grain boundaries as the deformation temperature decreases. This ambiguity in the kinetics of cDRX is associated with a lack of experimental data and different approaches to their interpretation.

The following topics will now be considered in turn: selective growth, the role of twinning and texture development during DRX.

Selective growth

With regard to DRX, the results obtained to date indicate that selective growth plays a significant role in fcc metals, but not bcc metals. Whether or not a particular boundary class (or misorientation relationship) is associated with a mobility edge thus also appears to

depend on crystal structure, as well as on the dislocation densities and internal stresses generated in the grains (high in fcc, low in bcc).

This is a topic area where orientation imaging microscopy (OIM) can be very useful and where there is a need for both data and careful analysis.

There are two related types of boundaries that can participate in selective growth: PM (plane matching) boundaries were first described in detail by Watanabe [213] and are illustrated in Fig. 37a and coincident site lattice (CSL) boundaries are much better known than PM boundaries and can also participate in selective growth.

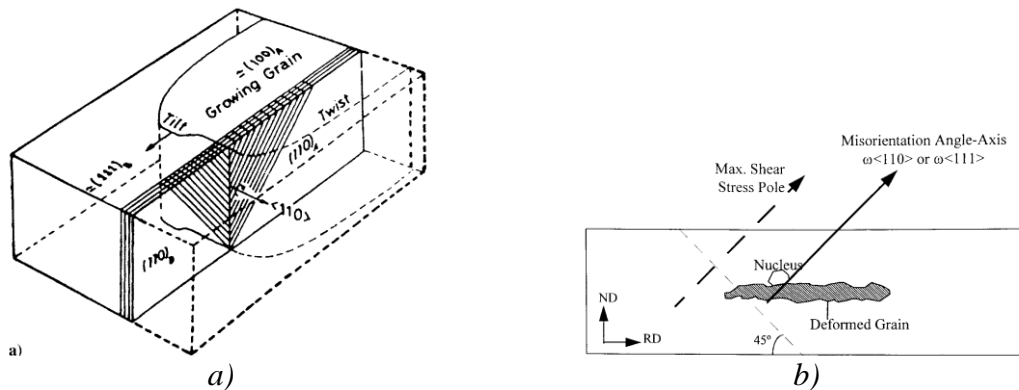


Fig. 37. a) Geometry of "plane matching" as it applies to deformed grain B (lower left) being consumed by new grain A (upper right). Note that the highlighted $\{110\}$ planes in grains A and B share a common $\langle 110 \rangle$ normal, which lies in the boundary. The angle of rotation about this z-axis required to bring the grains into correspondence is the angle of misorientation between the two grains [213]. (b) Schematic representation of one of the two maximum shear stress poles associated with rolling. Also shown is a $\langle 110 \rangle$ or $\langle 111 \rangle$ misorientation axis that is nearly parallel to the maximum shear stress pole. The former can be used to specify the angle of misorientation associated with a particular boundary; such boundaries frequently display high mobilities [214].

There is recent evidence [215] that selective growth, when it occurs, involves "variant selection"; that is, that not all geometrically equivalent boundaries participate in the recrystallization process. When selective growth by either the PM or the CSL mechanism is taking place, the replacement of a deformed grain by a new or recrystallized grain can be described in terms of a rotation about a $\langle 110 \rangle$ or $\langle 111 \rangle$ axis that is common to both grains. Although there are six crystallographically equivalent $\langle 110 \rangle$ axes (and four equivalent $\langle 111 \rangle$ axes), it appears that only the axes in the vicinity of the maximum shear stress poles are able to participate in the transformation. For the case of plane strain rolling, these poles are inclined at 45° to both the ND and RD directions (Fig. 37b). Similar axis selection has been reported to occur during torsion testing.

It has also been proposed that variant selection is essentially due to the internal stresses developed during deformation [216]. Although high internal stresses are produced in cold worked materials, as indicated above, much lower dislocation densities are generated during high temperature deformation, particularly in bcc metals. As a result, the high temperature internal stresses may be too low in these materials to produce variant selection. This may be why little evidence for selective growth has been observed in bcc metals to date; this is clearly a topic that needs to be followed.

Role of twinning

Single crystal studies have revealed that twinning plays an important role in DRX in these materials.

Successive generations of twins form (e.g. second, third, fourth, etc.), some of which will clearly have more growth potential (in their specific environments) than others. In a similar way, some grain orientations may be more susceptible to twinning than others. Thus, the process of twinning can contribute to selective growth. The picture is slightly different in polycrystalline materials because the presence of grain boundaries makes it somewhat easier for heterogeneous nucleation to take place. Nevertheless, even in these materials, twinning can play an important role in the propagation of DRX, particularly in low stacking fault energy alloys such as the 304 stainless steels. On the deformation of these materials to the vicinity of the peak strain, many fine grains form, bounded largely by first and second order twins [217]. As the strain is increased into the steady state region, the large initial grains are replaced by a fairly homogeneous microstructure (Fig. 38). Most of the boundaries displayed here are in motion, and it is of interest that the majority of the interfaces can be classified as first and second order twin boundaries.

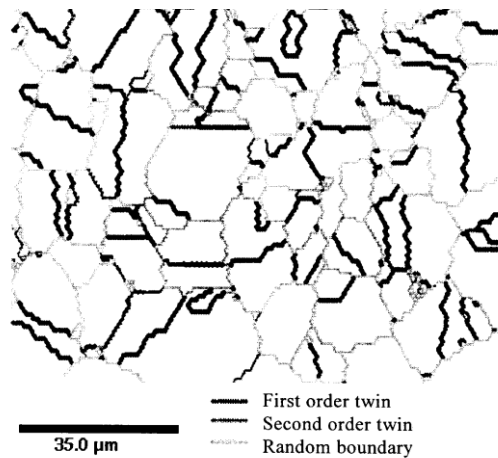


Fig. 38. Misorientation map of 304 stainless steel deformed in torsion at $\dot{\epsilon} = 1 \text{ s}^{-1}$ at 1050 °C. A strain of 2.2 was applied, which is within the steady state regime. Most of the boundaries can be classified as first order twins, some as second order twins and only a minority as random boundaries [217].

Texture development during DRX

When low stored energy nucleation is the most important DRX mechanism, the resulting texture will be dominated by the orientations of the low stored energy grains. Similar remarks apply to high stored energy nucleation or to recrystallization via twin formation. As indicated above, selective growth appears to be more important during the DRX of fcc as opposed to bcc metals. When this mechanism is operating, it leads to quite specific changes in texture, especially if variant selection (i.e. the choice of particular rotation axes) is involved (Fig. 39) [218]. Here the simulations were based on a low stored energy nucleation model together with $\langle 111 \rangle$ selective growth. It is, therefore, important to continue to search for evidence of selective growth and then to see if this can lead to industrial applications.

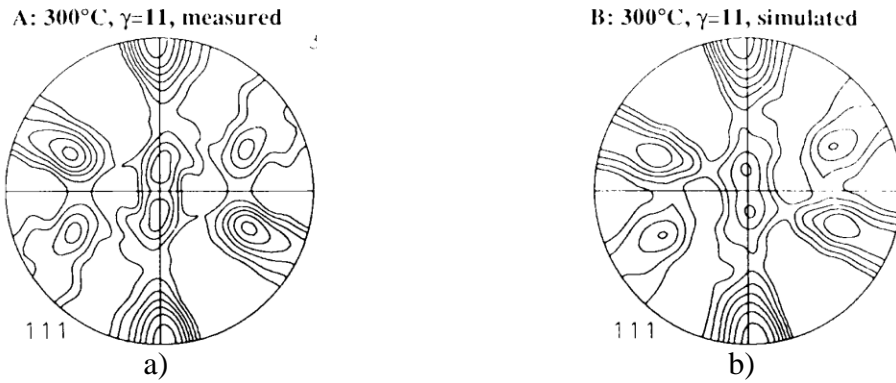


Fig. 39. a) Measured (111) pole figure of an OFHC copper sample twisted at 300 °C to $\gamma=11$. b) Simulated texture starting with the experimental initial texture using crystallographic slip and dynamic recrystallization. Isovalues on all diagrams: 0.8, 1.0, 1.3, 1.6, 2.0, 2.5, 3.2, 4.0, 5.0, 6.4 [218].

3. Electron backscatter diffraction (EBSD) technique

Electron BackScatter Diffraction (EBSD) is a scanning electron microscope (SEM) based electron diffraction technique allowing automated mapping of crystal orientations from bulk samples. Centimeter-sized samples with millimeter-sized grains, to metal thin films with nanograins may be analyzed. The nominal angular resolution limit is $\sim 0.5^\circ$ and the spatial resolution is related to the resolution of SEM, but for modern field emission gun SEMs (FEG-SEMs), 20 nm grains can be measured with reasonable accuracy. The macroscopic sample size is dependent on the ability of the SEM's stage and chamber to orient a sample at 70° tilt at an appropriate working distance, usually in the range 5 to 30 mm.

The technique is now widely used in materials characterization and reveals grain size, grain boundary character, grain orientation, texture and phase identity of the sample under the beam. Another potential use of EBSD is in quantifying plastic strain. This section reviews the current state of technology in terms of plastic strain analysis.

3.1. Plastic strain

It is well known that it is not easy to know the degree of plastic strain for materials in forged components. In many cases, hardness measurement and numerical stress analysis have been applied to estimate the plastic strain [219].

It is well known that the pattern quality of the EBSD deteriorates with increasing defect and dislocation density in materials caused by plastic strain. Measuring the deterioration by means of image analysis on patterns obtained from samples deformed to known strains, allows a calibration curve to be constructed and used to determine the plastic strain in samples of interest. With plastic strain, the distortions in the crystal lattice are relieved by the formation of dislocations in a material as shown in Fig. 40.

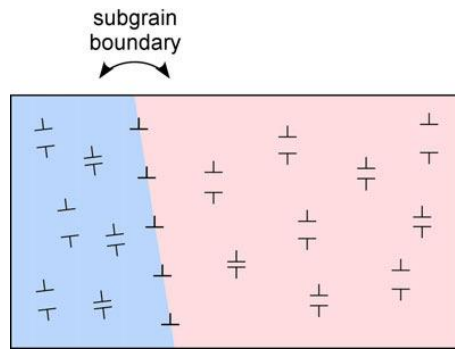


Fig. 40. Schematic representation of dislocations and subgrain boundary.

There are regions in the material with significant dislocation density with a net Burgers vector of zero. These are sometimes called "statistically stored dislocations" (SSDs). There are also areas with net non-zero Burgers vectors across which there is a change in crystallographic orientation or lattice curvature. These dislocations are often termed "geometrically necessary dislocations" (GNDs). Arrays of GNDs can form subgrain boundaries. If the diffraction volume is contained within a region of high dislocation density but with a net Burgers vector of zero, then the resulting pattern is degraded due to local perturbations of the diffracting lattice planes leading to incoherent scattering.

If the diffraction volume contains GNDs, then the pattern quality is degraded as the pattern is essentially a superposition of the patterns from each individual subgrain within the diffraction volume as shown schematically in Fig. 41. As the rotations associated with subgrain boundaries are small, the material within the diffraction volume will no longer meet a specific Bragg condition but rather a range of near Bragg conditions in three dimensions. This results in a diffraction pattern with degraded contrast. The degree of degradation is dependent on the amount of deformation within the interaction volume.

There are essentially two approaches to analyze plastic strain: the first based on the degradation of the diffraction patterns quality in deformed materials [220] and the second based on changes in local misorientation [221].

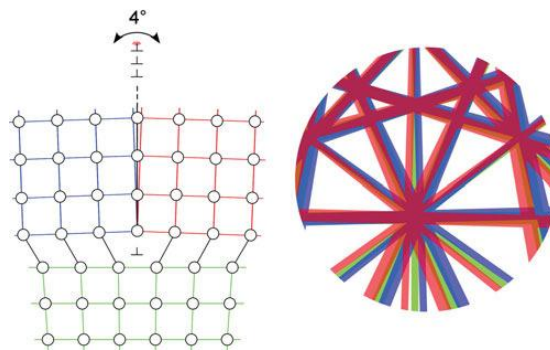


Fig. 41. Schematic showing the effect of a subgrain boundary on the EBSD pattern.

3.1.1. Image quality (IQ) approach

At each measurement point in an OIM scan, a parameter quantifying the quality of the corresponding diffraction pattern is recorded. Maps can be generated based on this image quality (IQ) parameter. In such maps, deformed areas appear darker than undeformed regions of the microstructure. As already expressed, the image quality is affected by residual strain in the diffracting volume. Thus, an indication of the distribution of strain in the material can be observed in an IQ map [222]. For a very large scan area on a bulk

sample, if the average IQ value is assumed to correspond to the overall strain measured mechanically, then the strain can be quantified by assuming a linear relationship between the IQ value and the local strain. Unfortunately, IQ is not solely dependent on strain; other factors affect image quality as well. Such factors include grain boundaries, surface topology, second phases, beam conditions, sample preparation and camera settings. Some of which can be observed in Fig. 42.

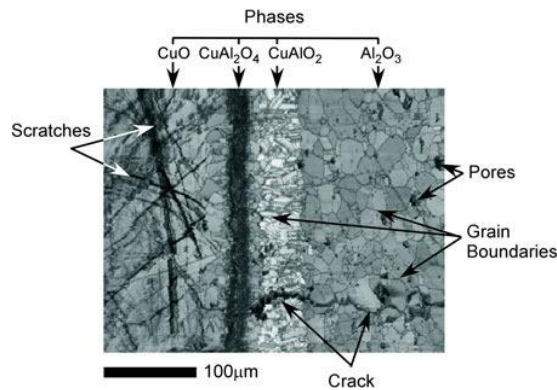


Fig. 42. IQ map showing the many factors influencing the IQ value, in a reaction zone between copper and aluminum [222].

The indexing success rate stated in the caption for an IQ map is defined as the percentage of points with confidence index values greater than 0.1 after standardizing the confidence index to the point in each grain with the highest confidence index. The percentage of points "cleaned up" are those points modified using a grain dilation post-processing routine divided by the total number of points in the scan. For the dilation routine, a grain tolerance angle of 5° and a minimum grain size of 3 pixels were used. The grain was also required to extend across at least two rows in the scan.

As was mentioned previously, the size of the diffraction volume will affect the results. Thus, we would expect the IQ effect to be more marked as the larger diffraction volume will be more likely to contain lattice imperfections.

3.1.2. Local misorientation approach

As dislocations form in the material, the residual strain is manifest as local variations in lattice orientation. This is evident on grain boundary maps of deformed materials. OIM measurements allow a user to define which kind of boundaries should be drawn in maps created in OIM data. For example, Fig. 43 shows low angle grain boundaries (2-15°) in red and high angle (>15°) boundaries in blue. Regions with high concentrations of low angle boundaries are indicative of areas of concentrated GND density.

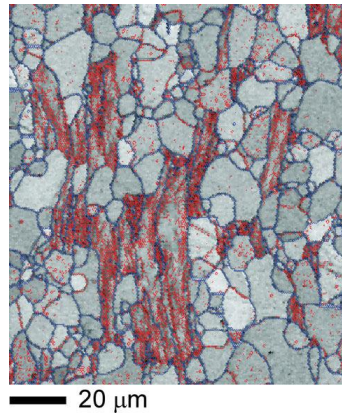


Fig. 43. Grain boundaries in 85% recrystallized low-carbon steel: red 2-15°, blue >15°.

As with the IQ, local misorientations provide an indication of the strain distribution in the material. Several useful methods for characterizing local misorientations have been proposed. The first two methods are "grain" based. The second three are based on individual measurement points. The last one is a hybrid of the two approaches. Most of the maps shown in the following figures were obtained from a partially recrystallized steel sample at two different magnifications.

1. The *grain orientation spread* (GOS) is the average deviation in orientation between each point in a grain and the average orientation of the grain. This approach leads to assigning the same value to every scan point contained within the grain. The average orientation of the grain is calculated using the methodology outline by Kunze et al. [223]. An example GOS map is shown in Fig. 44.
2. The *grain average misorientation* (GAM), which is the average misorientation between each neighboring pair of measurement points within the grain. In general, as the step size decreases, the misorientation between neighboring points on the scan grid will decrease as well. An example GAM map is shown in Fig. 44.
3. The *kernel orientation spread* (KOS) is similar to GOS but done within a kernel. A kernel is a set of points of prescribed size surrounding the scan point of interest. The size of the kernel is generally prescribed to the n^{th} nearest-neighbor (Fig. 45). The calculations performed on this kernel are performed with the kernel centered at each point in the scan and value obtained by the calculations assigned to the center point. If more than one grain is contained within the kernel, then multiple average orientations are calculated for the kernel. The value calculated for the kernel is assigned to the scan point at the center of the kernel.

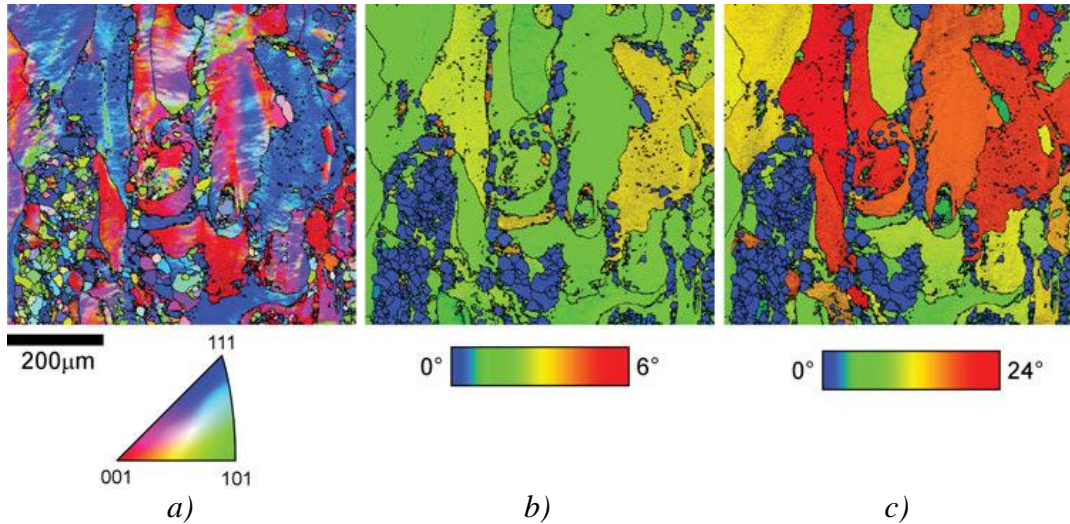


Fig. 44. OIM maps from a partially recrystallized steel sample. a) Color code orientation map, b) GAM map and c) GOS map. Grains are outlined with black boundaries.

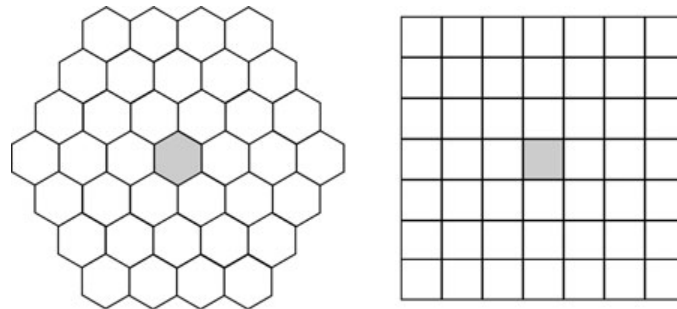


Fig. 45. 3rd nearest-neighbor kernels for a hexagonal and a square grid.

4. The *kernel average neighbor misorientation* (KANM) is similar to GAM but calculated within a kernel instead of a grain. That is, misorientations between all neighboring points within the kernel are averaged. Thus, to focus on local small rotations, the grain boundary effect is excluded by only including misorientations less than a specified tolerance value from the averaging calculation.
5. The *kernel average center misorientation* (KACM) is the average misorientation between a point on the measurement grid and its neighbors. For a hexagonal measurement grid, this is the average misorientation between the orientation of a given measurement point and the orientations of the six equidistant neighbors. As with KANM, the grain boundary effect is removed by only including points misoriented relative to the point at the center of the kernel within some prescribed value included in the averaging calculation. If the kernel is larger than the first nearest-neighbors, then KACM can be calculated in two different ways: a) the misorientation from each point in the kernel with respect to the center point of the kernel is calculated and averaged or b) only the points at the perimeter of the kernel are used in the calculation. If only the nearest-neighbors are used, then the variants are identical. Because this method focuses on the center point of the kernel, the boundary edges are well preserved as can be observed in Fig. 46.

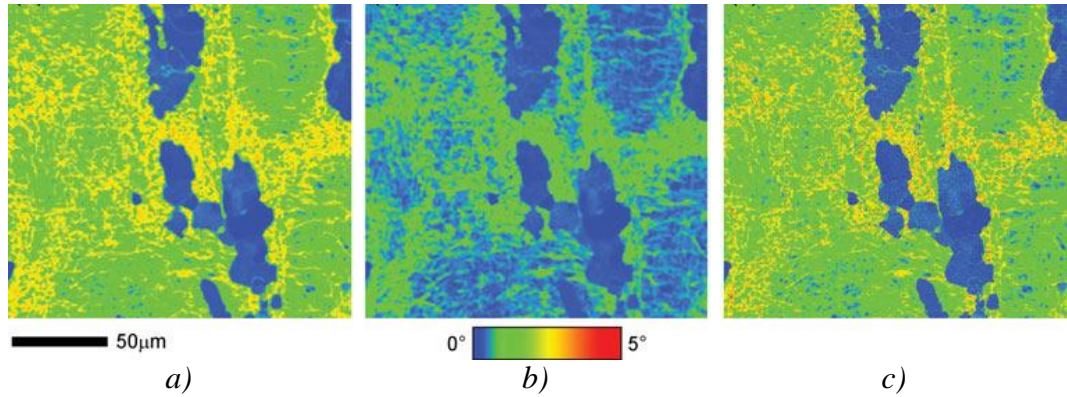


Fig. 46. a) KOS, b) KANM and c) KACM maps from a partially recrystallized steel sample-6th nearest-neighbor kernels.

- The *reference orientation deviation* (ROD) map shows the deviation in orientation of a measurement point from the average orientation of the grain to which the point belongs. Two approaches that have been reported are the use of the average orientation for a grain as the reference orientation and the point in the grain with the lowest kernel average misorientation.

3.1.3. Statistical correlation of EBSD strain indicators with crystal orientation

As previously described, various metrics such as IQ or local misorientation can be correlated to calibration curves to provide a somewhat quantitative measure of strain within the scan area. Two approaches can be taken. The first is to partition the data using one of the various measures of "strain", while the second is a more continuous approach termed "scalar texture".

Partitioning

Because of the discrete nature of OIM data, it is possible to correlate the strain measurements with specific orientations. Fig. 47 shows an example for a large combined beam and stage scan obtained on the partially recrystallized steel sample already described. The KAM distribution data were partitioned into two subsets: one containing all of the measurements with KAM values greater than 1.5° and another subset containing all of the orientation measurements with KAM values greater than 1.5°.

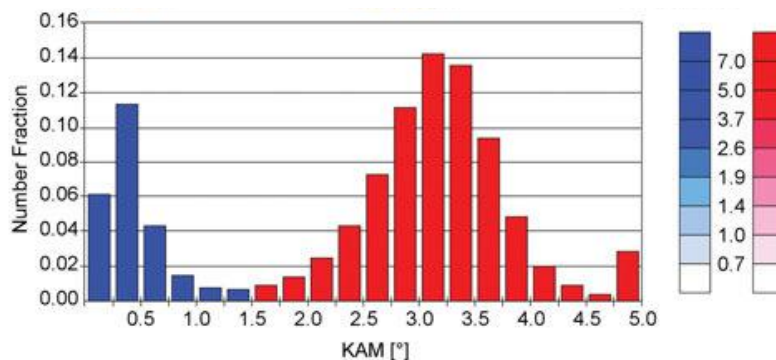


Fig. 47. 5th nearest-neighbor KAM distribution calculated for two subsets of the full dataset partitioned based on the KAM distribution for partially recrystallized steel.

Scalar textures

The correlation between any scalar parameter and crystallographic orientation can be characterized using an approach termed *scalar textures* [224]. In a scalar texture, orientation space is divided up into many bins. For each orientation measurement in the OIM scan, the bin corresponding to the measured orientation is incremented by the value of the scalar parameter in question. A second value is tracked for the bin, that is, the number of points contributing to the bin. Thus, an average value for the given scalar parameter can be calculated for each bin. *Pole figures* and *inverse pole figures* can be constructed showing the variation in the scalar parameter average value with crystallographic orientation. This technique works best when there are many random orientations. Using this approach any of the parameters described previously such as the IQ or the measures of local misorientation can be determined as a function of orientation. Fig. 48 shows the KAM scalar texture for the large dataset described in the previous section.

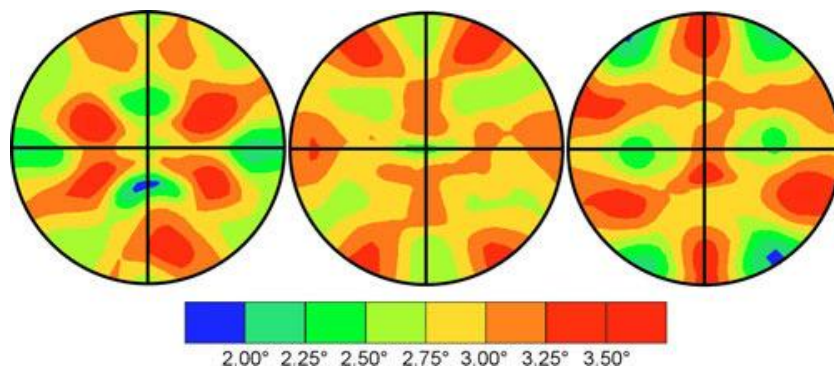


Fig. 48. (100), (110) and (100) pole figures showing the average KAM value as a function of pole orientation for a partially recrystallized steel.

3.2. Grain boundary

Typically, grain boundaries with misorientations between 2° and 10° are considered subgrain or low-angle grain boundaries (LABs) and given a specific color, such as silver, whereas boundaries with misorientations major than 10° are considered random high-angle grain boundaries (HABs) and are typically colored black. EBSD technique allow percentages of grain boundaries in each category to be compared and OIM maps possessing this component allow the concentration and distribution of low-angle grain boundaries to be determined. If the neighboring pixels are from different phases, phase boundaries may be displayed instead.

3.3. Special boundaries

Special boundaries (SB) are individual user-defined boundaries using an axis-angle definition to identify specific types of boundaries. For example, the $\Sigma 3$ CSL/twin may be described by a 60° rotation about $\langle 111 \rangle$ between neighboring crystallographic domains. EBSD tools are also available to determine the character, prevalence and distribution of special boundaries, where the axis/angle definition is not known for a material or processing method. Quantitative analysis of the information depicted in an EBSD map is also usually possible. For a map made of a mixture of pattern quality and grain size coloring components, histograms may be generated describing the overall frequency

distribution of the pattern quality parameter, as well as the grain size distribution within the area of analysis.

Numerous studies have shown that low- Σ coincidence site lattice (CSL) boundaries, usually taken as $\Sigma 3^n$ with $n=1, 2$ and 3 , possess good resistance to carbide precipitation [225]. Ductility is enhanced by the presence of low- Σ CSL boundaries, too. Additionally, low- Σ CSL boundaries have been found to offer strong resistance to weld decay by reducing intergranular precipitation [226].

While the resistance to carbide precipitation of CSL has been pointed out in a large number of studies, Singh et al. [227] have indicated that an increase in the frequency of CSL does not necessarily translate into a higher resistance to sensitisation.

Although positive reports on the low- Σ CSL boundaries are numerous, a recent study by Santos et al. [228] has reported unfavourably on the susceptibility of the $\Sigma 3$ (twins) boundary of a gas-nitrided AISI304L to corrosion-erosion damage. In actuality, the possibility of obtaining very favourable properties by the generation of high fractions of low- Σ CSLs in alloys was very early proposed as grain boundary design and control by Watanabe [229] in the 1980s. Methods for generating low- Σ CSL boundaries have been explored by a few groups [230,231] and these include thermomechanical treatments such as strain annealing [232] and strain recrystallisation [233].

The nature of recrystallisation has a direct impact on the resulting grain boundary characters. In a 304 stainless steel, Mishin et al. [234] have found that static recrystallisation promotes the formation of $\Sigma 3^n$ boundaries ($n = 1-3$), but dynamic recrystallisation promotes low-angle boundaries ($\Sigma 1$) with literally no twin boundaries, insofar as the dominant mechanism of microstructural change in dynamic recrystallisation is dislocation rearrangement. Surprisingly, in a recent study on 304, Wasnik et al. [235] have shown that when the amount of random grain boundaries exceeds a certain critical value, they can suppress intergranular corrosion. Besides the amounts of CSLs, their distribution has been found to be equally important. When the CSLs are uniformly distributed in 304 stainless steels, more significant enhancement of the resistance to intergranular corrosion can be attained because the network of susceptible random boundaries will be broken up.

It was mentioned at the beginning of this section that $\Sigma 3^n$ ($n = 1-3$) were typically regarded as being special. However, a study has shown that only coherent twins ($\Sigma 3$) are truly "special" [236].

4. Grain refinement on stainless steels

Traditionally plastic deformations have been used to increase the strength of stainless steels. Nevertheless, strengthening in this way leads to poor formability and ductility. In order to get around this problem, strengthening through grain refinement is commonly utilised. Besides strength and wear resistance [237], pitting resistance [238] and resistance to cavitation and cavitation-erosion [239] can also be improved by reducing grain size.

4.1. Heavy plastic deformation

A number of workers have focused on methods that may refine the grains throughout the bulk of metallic materials by utilising very severe plastic deformations with techniques like high-pressure, equal channel angular pressing, high-pressure torsion, accumulative roll-bending, mechanical milling, single and multiple forging.

While the microstructural evolutions of metallic materials after hot deformation have been well studied, the microstructural evolutions of metallic materials after "*warm deformation*"

(i.e. $0.25-0.65T_m$) were less studied until recently. A series of studies [240,241] devoted to this topic have shown that the evolution of grains after severe warm deformation is not related to discontinuous dynamic recrystallization. Rather, a strain-induced continuous recrystallisation is involved [242,243]. The strain-induced continuous recrystallisation leads to a large number of subboundaries with moderate to high misorientations at high strain levels and some of the boundaries look like conventional grain boundaries. The subgrains eventually develop an equiaxed, homogeneous, fine-grained microstructure with decreased densities of dislocations in their interiors.

The microstructural changes in materials deformed at temperatures below $0.65T_m$ has not been well documented. Recently, the microstructural evolutions of austenitic [244,245] and duplex stainless steels [246] during warm deformation ($0.25-0.65T_m$), the mechanisms for their subsequent grain refinements and the microstructural changes in the deformed stainless steels during annealing have been examined in detail by Belyakov et al. [246-249] in a series of studies.

For the 304 austenitic stainless steel used by Belyakov et al. [245,247,248], severe deformation was imparted to it through multiple compressions at about $600\text{ }^\circ\text{C}$ ($0.5T_m$), with a change in loading direction by 90° in each pass. The evolution of microstructure is as follows: in the early stage of deformation, high densities of dislocations form nearly homogeneously in parallel layers that are crossed by dislocation walls with low-to-medium misorientations. At moderate levels of strain, recognisable, more equiaxed subgrains containing high densities of dislocations in their interiors appear, with an attendant increase in the misorientations among their boundaries. During deformation, the grains are broken up by dense dislocation walls (called geometrically necessary boundaries, GNBs [249,250]) into domains/cell blocks, which possess different combinations of operative slip systems. At even higher strain levels, the high internal stresses may act as back stresses to hinder the movement of dislocations, thereby leading to a decreased number of dislocations in the interiors of the fine grains and a high hardening of the material. The strain-induced, fine grains containing reduced amounts of dislocations spread homogeneously over the bulk of the material.

Interestingly, the fine-grained microstructure with high-angle boundaries developed in this way, although being high in strain energy, has been found to be resistant to discontinuous (primary) recrystallisation and grain coarsening [245]. While primary recrystallisation occurs heterogeneously in materials that sustain low-to-medium levels of deformation (i.e., levels of deformation obtained by conventional deformation techniques), the recrystallisation in strain-induced fine-grained austenitic stainless steels, which sustain very large deformation, occurs homogeneously. This recrystallisation is called continuous recrystallisation [245] and the strain-induced fine grains themselves act as the recrystallisation nuclei. The evolution of microstructure in duplex stainless steels upon severe plastic deformation has also been studied by Belyakov et al. [251]. In duplex stainless steels, the austenite and ferrite phases have different deformation kinetics [246]. The austenite phase will attain an ultrafine-grained microstructure faster than will the ferrite phase because multiple twinning occurs readily in the former phase at the early stage of deformation [246].

5. Industrial case studies

Experiments of multi-stage cold forging of an AISI 1005 heat pipe fitting and of single-stage forging of an AISI 1005, AISI 304L and Duplex 2205 hex-head plug fitting were performed, in order to validate the proposed FE models. The process parameters were the same as those in the FE simulations and results detected in both components were in good

agreement with experimental results. The experimental tests were conducted at Zoppelletto S.p.A.

5.1. Evaluation of defects in multi-stage cold forged heat pipe fitting

Although many works have been carried out on forging defects (*cf. §1.1 of "Part 3"*), there is lack of extensive research on defects formation in multi-step forming of axisymmetrical components. *Article II and III* were aimed at supporting the research in this field by analyzing an industrial multi-stage cold forging process of an heat pipe fitting using a 3D rigid-plastic FE model (*cf. §7.1 of "Part 2"*). In particular, the formation mechanisms of surface defects in the optimized three-stage forging-sequence were studied through FEM simulations and the numerical model was then validated by means of experimental data coming from the real process (*cf. Article III*).

Article III describes the experimental forging test in detail. In particular, the AISI 1005 cylindrical billets (24 mm diameter, 91.4 mm height and 324 g weight) were coated using the experimental single bath lubrication system (*cf. §2.3.4 of "Part 1"*). Tool steels were heat treated (i.e. preheated, austenitized, quenched and tempered) to produce an hardness of 60-65 HRC and coated with a multilayer PVD coating, composed of an AlCrN layer and a TiN interlayer deposited upon the steel substrate (*cf. Article I*).

Underfilling and surface defects evaluation

By analyzing a series of workpieces coming from each forging stage, the reduction of underfilling areas was detected through regular visual inspections and stereoscopic observations. In addition, the FE results were finally compared with those obtained from the experimental investigations and a good agreement was observed (*cf. Article II and III*).

By using FEM simulation, it was found that defects occur in each stage of the optimized forming sequence (*cf. §7.1 of "Part 2"*). For more details on the description of the formation mechanisms of surface defects see *Article III*.

In this work, visual inspections coupled with microscopic investigations were performed to validate FE results. These analyses were based on the surface defects photographs and micrographs collected by light optical (LOM) and scanning electron (SEM) microscopy. The good correlation between virtual and experimental observations allowed to link the forging defects, detected on each forged part, to the evaluated conditions which could cause them (*see Table 2 of "Article II"*).

5.2. Dimensional inspection and microstructural characterization of the single-stage forged hex-head plug fitting

Conventional cold forging set-up

Starting from the FE simulations developed for each tested steel (*cf. §7.2 of "Part 2"*), a series of cold forged hex-head plug fittings were obtained from single-stage forming tests, in order to validate the proposed FE models and results.

Before experimental tests, 50 cylindrical billets (i.e. 22 mm diameter, 18 mm height and 51 g weight) were cut from the hot rolled bars for each material considered. AISI 304L and Duplex 2205 stainless steel bars were solution heat-treated at 1150 °C and 1050 °C respectively and water-quenched in order to avoid precipitation of carbides and secondary phases. Then steel billets were coated using the experimental single bath lubrication

system (cf. §2.3.4 of "Part 1"). Finally tool steels were heat treated and coated as reported in §5.1 of "Part 3".

For more details on process description see *Article IV*.

As the basis of tools design (i.e. dies and punches) and quality certification for forgings, the forging drawing of the low-carbon AISI 1005 component is illustrated in Fig. 49.

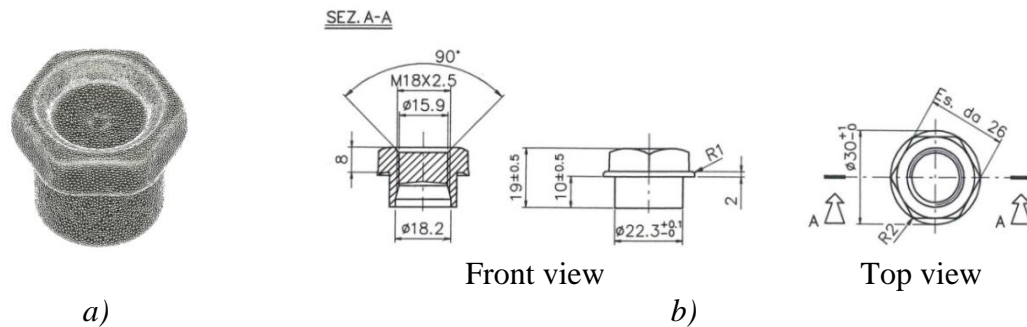


Fig. 49. a) The hex-head plug fitting CAD geometry, and b) front and top views. All dimensions are in mm.

By analyzing the simulated stainless steel forged components, some underfilling areas occurred close to the hex-head of the plug (cf. §7.2 of "Part 2"). Moreover, these forged parts did not meet the forging drawing tolerances established by Zoppelletto S.p.A.

Optimized cold forging set-up

The re-design of the conventional single-stage process for cold forging of stainless steels were performed by using finite element methods (cf. §7.2 of "Part 2"). Thus, for each steel considered, a series of cold forged plugs were formed from 50 optimized cylindrical billets (i.e. 22 mm diameter, 18.3 mm height and 55 g weight), cut from the same treated bars used for conventional tests. Then billet surfaces were lubricated (cf. §2.3.4 of "Part 1") and tool steels were heat-treated and coated (cf. §5.1 of "Part 3").

Compared to the conventional process, focusing on FE results reported (cf. §7.2 of "Part 2") and on regular visual inspections of forged parts, the underfilling areas were limited at the flange of the optimized plug fittings in both stainless steels considered (cf. *Article IV*).

Table 16 reports the dimensional tolerances revealed on the stainless steel components produced by optimized cold forging process and measured by a vernier caliper. As can be seen, the stainless steel forged parts slightly meet the drawing tolerances "A" and "B" established by the company for the AISI 1005 part (Fig. 49b). About 100 stainless steel forged parts (50 in AISI 304L and 50 in Duplex 2205) were submitted to dimensional inspections by vernier caliper measurements.

Forging tolerances [mm]	AISI 1005	AISI 304L	Duplex 2205
A	30 + 1.0	28.8	28.7
B	19 ± 0.5	18.5	18.4
C	10 ± 0.5	9.7	9.5

Tab. 16. Average values of tolerances revealed on the optimized stainless steel cold forged components.

Optimized warm forging set-up

In order to ensure a better filling at the die corners and meet the drawing tolerances reported in Fig. 49b, a series of warm forged stainless steel plug fittings were produced from the optimized billet geometry at the forging process conditions and parameters reported on section "*Optimized cold forging set-up*" of *Part 3*. Thus, the billets were subsequently preheated at 700, 600, 500 and 400 ±5 °C respectively using a muffle furnace before warm forging tests.

For more details on process description see [Article V](#).

About 400 near-net-shape components (50 for each stainless steel grade and forging temperature) were obtained from the forging tests.

Table 17 lists the dimensional tolerances obtained on the warm forged plug fittings and revealed by a vernier caliper at different forging temperatures. The stainless steel forged parts strictly meet the drawing tolerances of AISI 1005 plug.

Forging tolerances [mm]	AISI 1005	Temperature [°C]	AISI 304L	Duplex 2205
A	30 + 1.0	400	30.1	30.4
		500	31.1	30.5
		600	30.2	30.5
		700	30.3	30.6
B	19 ± 0.5	400	18.9	18.6
		500	19.0	19.0
		600	19.1	19.2
		700	19.5	19.4
C	10 ± 0.5	400	9.7	9.6
		500	9.9	9.8
		600	9.9	9.9
		700	10.0	10.0

Tab. 17. Average values of tolerances revealed on the optimized stainless steel warm forged components.

The temperature of 400 °C was then selected to guarantee the production of near-net-shape plug fittings resulting in energetic, economic and ecologic benefits to the company.

Microstructural characterization of optimized cold-warm forged parts

The effects of the optimized cold and warm forging on microstructural and local plastic strain evolution of α - and γ -phase on steels considered were also studied.

The investigation was performed by using EBSD techniques coupled with micro-hardness measurements, in order to detect local plastic strain, grain size, grain boundary character, grain orientation, texture and strain hardening rate of the undeformed and deformed samples.

The metallographic analyses were performed on the cylindrical billets and cold-warm forged samples sections parallel to the rolling direction (RD) and compression z -axis (CA) respectively (*cf. Article IV and V*). The focus was set on the microstructural analysis of areas corresponded to different levels of strain. For more details see [Article IV and V](#).

The main results found can be summarized as follows (*cf. Article IV and V*):

- The cold and warm forging processes cause a significant grain refinement in the deformed zones for each steel considered.
- Cold forged samples with the presence of ferrite (i.e. AISI 1005 and Duplex 2205) exhibit a preferential distribution of grain orientations in [100] direction on the 001 and 111 poles. Moreover, the α -grains in Duplex 2205 at the as-received state show a strong crystallographic orientation in all directions of observation ([010], [100], [001]) on the 001 pole. On the other hand, cold forged samples with the presence of austenite (i.e. AISI 304L and Duplex 2205) report a change of the crystallographic orientations, with a preferential distribution of grains in [100] direction on the 011 and 101 poles.
- The cold-worked α -phase in AISI 1005 steel has a lower tendency to harden compared to γ -phase of AISI 304L steel. Furthermore, γ -phase tends to harden easier on austenitic than on dual-phase stainless steel. This can be associated to the crossing of slip planes, different effect of twin boundary formation and the raise of the dislocation density in the deformed zones.
- In the cold-forged material, the estimated deformed volume fraction is higher in the γ -phase than in the α -one. The γ -phase grains deform more homogeneously than the initially large α -phase grains, in which a strong internal substructure builds up during deformation.
- Steels forged at room temperature result in the development of fine grained microstructures. Low-angle boundaries (LABs) increase and high-angle boundaries (HABs) decrease, as a direct consequence of the building up of dislocation microstructures.
- The microstructure of γ -phase develops from 400 to 500 °C is composed of fine grained microstructure at different strain levels. The fraction of special boundaries (SB) decrease rapidly from 400 to 500 °C on deformed zones of stainless steels analyzed. On the other hand the morphologies of γ -phase detect at higher forging temperatures (i.e. 600 and 700 °C) are almost fully composed of fine nearly-equiaxed and large-elongated grains, which are considered to be discontinuous dynamic recrystallized (DRX) grains. Similar values of LABs and HABs fractions and formation of annealing twins are observed on stainless steels forged parts.

CONCLUSIONS

Forging is one of the most economical and efficient method for producing simplex or complex steel components. The metal is plastically deformed and assumes the shape of the forging tools and the resulting components have refined grain structure and improved mechanical properties, such as strength, toughness, and ductility.

In particular cold and warm forging of low-carbon steels are economically attractive due to savings in material, dimensional accuracy and good surface finish.

Furthermore, there is still lack of extensive research on closed-die cold and warm forming of stainless steels, which require advanced tools for the design of forging operations and close control of the process variables.

In recent years numerical simulation techniques, mainly based on finite-element (FE) analysis, have been used to investigate metal forming processes, providing useful informations in the prediction of several process parameters. Furthermore, the correct design of the forging stages involves the use of numerical simulation, where a coupled thermo-mechanical model has to be implemented and calibrated.

In this PhD thesis a new approach has been presented, focused on testing and modelling to correctly analyze the different phenomena that affect material, process and product performance during and after the mechanical and microstructural events in cold and warm forging operations.

In particular, an experimental setup was designed and developed in order to determine the elasto-plastic properties of low-carbon and stainless steels at different strain rates and temperatures. Moreover, a new testing procedure for the evaluation of the friction conditions for the industrial forging processes analyzed was developed.

Numerical models able to performed coupled thermo-mechanical simulations of the industrial cold and warm forging processes were then implemented in the commercial FORGE2011[®]-3D software. The material rheology and friction conditions at the die-workpiece interface were evaluated by an inverse analysis approach, in order to properly calibrate such FE models. Numerical simulation demonstrated to be a useful tool to re-design and predict the formation mechanism of surface defects on a multi-stage cold forging process of a low-carbon steel; moreover it helped to calibrate an industrial single-stage cold forging process to form stainless steel forged parts starting from different forging temperatures. The temperature of 400 °C was then selected after several trial tests by using the FE code, in an attempt to guarantee the production of near-net-shape components resulting in energetic, economic and ecological benefits to the company.

Finally, the developed FE procedures were applied to industrial forging processes and a good agreement between numerical and experimental results was observed. Cold and warm forged parts, obtained from the optimized single-stage process, were then compared in order to investigate the microstructural evolution of α and γ -phase grains on each steel tested at different forging temperatures. The coupled effect of strain and temperature seems to great influence the α - and γ -grains orientation distribution and their morphology on both phases.

This confirms the "leading thread" of the thesis, which describes the relationships between the industrial case histories, numerical FE models and final forged components obtained.

REFERENCES

- [1] T. Altan, S.-I. Oh, H.L. Gegel, "Metal forming: Fundamentals and applications", ASM International, 1983.
- [2] H. Cather, R. Morris, M. Philip, C. Rose, "Design engineering", Butterworth Heinemann, Oxford, 2001.
- [3] Forming and Forging, Vol. 14, ASM Handbook, ASM International, 1988, p 6.
- [4] K. Lange et al., "Handbook of metal forming", McGraw-Hill, 1985, p 2.3, 9.19.
- [5] T. Altan, "Short course on near net shape cold, warm and hot forging without flash", Engineering Research Center for Net Shape Manufacturing, The Ohio State University, 2002.
- [6] S. Kalpakjian, S. Schmid, "Manufacturing engineering and technology", Prentice Hall, 2001.
- [7] "Tool and manufacturers engineering handbook", Desk Edition (1989), 4th ed., Society of Manufacturing Engineers, 1989, p 15-8.
- [8] H.D. Feldmann, "Cold forging of steel", Hutchinson and Company Ltd., London, 1961.
- [9] C.H. Wick, "Chipless machining", Industrial Press, New York, 1961.
- [10] J. Billigmann, H.D. Feldmann, "Upsetting and pressing", Carl Hansen Verlag, Munich, 1973 (in German).
- [11] M.T. Watkins, "Cold forging and extrusion of steel", Review 176, International Metallurgical Review, Vol 18, 1973 (Part I: Basic Principles, p 123; Part II: Properties and Tooling, p 147; Part III: Economics and Future Applications, p 162).
- [12] H.D. Feldmann, "Cold extrusion of steel", Merkblatt 201, prepared for Beratungsstelle fuer Stahlverwendung, Dusseldorf, 1977 (in German).
- [13] A.N. Bramley, D.J. Mynors, "The use of forging simulation tools", Mater. Des. 21 (2000) 279-286.
- [14] S.L. Semiatin, "Introduction to bulk-forming processes", ASM Handbook, Metalworking: Bulk Forming (#06957G), vol. 14A, 2005.
- [15] K. Serope, R. Steven Schmid, "Manufacturing engineering and technology", Prentice-Hall, Upper Saddle River, NJ, 2006.
- [16] ICFG, "Steels for cold forging: their behavior and selection", Document No. 11/01, International Cold Forging Group, 2001.
- [17] M. Hillert, "The formation of pearlite, in decomposition of austenite by diffusional processes", V.F. Zackay and H.I. Aaronson, Ed., Interscience, 1962, pp 197-247.
- [18] R.A. Lula, "Stainless steel", American Society for Metals, 1986.
- [19] J. Beddoes, J.G. Parr, "Introduction to stainless steels", 3rd edition, ASM International, Materials Park, OH, USA, 1999.
- [20] D. Peckner, I.M. Bernstein (Eds.), "Handbook of stainless steels", McGraw-Hill Inc., 1977.
- [21] Anonymous, "Advanced materials and processes", February, 2007, p 20.
- [22] www.worldstainless.org (website of International Iron and Steel Institute, accessed on 14 March 2008).
- [23] People's Daily Online, 13 February 2007.
- [24] B.F. Brown, "Stress corrosion cracking control measures", Monograph 156, National Bureau of Standards, U.S. Department of Commerce, June 1977.
- [25] S.W. Dean, "Review of recent studies on the mechanism of stress corrosion cracking in austenitic stainless steels", in Stress Corrosion-New Approaches, STP 610, H.L. Craig, Jr., Ed., American Society for Testing and Materials, 1976, pp 308-337.
- [26] G. Fontana, "Corrosion engineering", 3rd ed., McGraw-Hill, 1986.
- [27] M. Kobayashi, "Duplex statistics 2008", www.outokumpu.com.
- [28] J-C. Gagnepain, "Duplex stainless steels: success story and growth perspectives", Stainless Steel World America 2008 Conference & Expo.
- [29] K.H. Lo, C.H. Shek, J.K.L. Lai, "Recent developments in stainless steels", Materials Science and Engineering R 65 (2009), 39.
- [30] J. Charles, "Past, present and future of the duplex stainless steels", Proc. 7th Duplex2007 Int. Conf & Expo, Grado, Italy (2007).
- [31] R. Dakhalaoui, C. Braham, A. Baczmanski, S. Wronski, K. Wierbanoski, E.C. Oliver, "Analyze of phase's mechanical behaviour of duplex stainless steels by X-ray and neutron diffraction". Duplex, Grado, Italy (2007).
- [32] H.W. Hayedn and S. Floreen, Trans. ASM, 61 (1968) 474.
- [33] M. Jacobsson, "Fatigue testing of the duplex grades SAF 2304, SAF 2205 and SAF 2507", Internal Report no. 6060, Sandvik Steel, Sandviken, Sweden (1991).

- [34] J. Charles, "Duplex stainless steels, a review after DSS '07 held in Grado", *Rev. Met. Paris*, 3 (2008) 155-171.
- [35] H. Sieurin, "Fracture toughness properties of duplex stainless steels", Doctoral Thesis (2006).
- [36] J-B. Vogt, "Fatigue properties of high nitrogen steels", *Mater. Proc. Tech.*, 117 (2001) 364-369.
- [37] A. Mateo, L. Llanes, N. Akdut, M. Anglada, "High cycle fatigue behaviour of a standard duplex stainless steel plate and bar", *Mater. Sci. Eng. A*, 319-321 (2001) 516-520.
- [38] D.S. Bergstrom, "Benchmarking of duplex stainless steels versus conventional stainless steel grades", *Proc. 7th Duplex 2007 Int. Conf & Expo, Grado, Italy* (2007).
- [39] M. Holmquist, "Consider duplex stainless steels for corrosive exchangers' service", *Hydrocarbon Processing* (2001).
- [40] D. Zuili, *The Use of Duplex Stainless Steel in Oil & Gas Industry, Conf proc Duplex Stainless Steels* (2010).
- [41] M. Kobayashi, "Duplex statistics 2008", www.outokumpu.com.
- [42] P-J. Cunat, "Stainless steel properties for structural automotive applications", *Metal Bulletin International Automotive Materials Conference, Cologne, 21st to 23rd* (2000).
- [43] A. Geleji, "Forge equipment, rolling mills and accessories", (in English), *Akademiai Kiado, Budapest*, 1967.
- [44] E. Mueller, "Hydraulic forging presses", Springer Verlag, Berlin, 1969.
- [45] K.H. Peters, "Design features of the hydraulic press and its field of application", *Sheet Metal Ind.*, Vol 46, March 1969, pp 221-226.
- [46] H. Bohringer, K.H. Kilp, "Development of the direct-drive percussion press", *Sheet Metal Ind.*, Vol 43, Nov 1966, p 857.
- [47] Schuler, "Metal forging handbook", Springer, Goppingen, Germany, 1998.
- [48] L. Lazzarotto, L. Dubar, A. Dubois, P. Ravassard, J. Oudin, "Three selection criteria for the cold metal forming lubricating oils containing extreme pressure agents", *J. Mater. Process. Technol.* 80-81 (1998) 245-250.
- [49] N. Bay, "The state of the art in cold forging lubrication", *Journal of Materials Processing Technology* 46 (1994) 19-40.
- [50] ICFG Doc. 8/91: "Lubrication aspects in cold forging of carbon steels and low alloy steels". The Int. Cold Forging Group, 1991.
- [51] ICFG Doc. 10/95: "Lubrication aspects in cold forging of aluminium and aluminium alloys". The Int. Cold Forging Group, 1991.
- [52] N. Bay (1994), "The state of the art in cold forging lubrication", in: Invited paper at the 2nd International Cold & Warm Forging Conference, Columbus, Ohio, September 27-29, *Journal of Materials Processing Technology* 46: 19-40.
- [53] N. Bay (1995), "Aspects of lubrication in cold forging of aluminium and steel". Keynote paper. *Proceedings of International Cold Forging Congress, Solihull, England*, 135-146.
- [54] R. Geiger (1983), "Surface treatment for the cold forging of steel: Part I". *Wire* 33(1):11-13. and vol. 33 no. 3: 75-78.
- [55] H.J. Haupt (1979), "Oberflächenvorbehandlung für das Kaltmassivumformen". *wt-Z ind Fertig* 69: 555-558.
- [56] H.Y. Oei (1988), "Einflüsse auf werkstück und verfahren beim phosphatieren von teilen für das kaltumformen". *Maschinenmarkt* 94(7): 24-28.
- [57] D.H. Jang, T.K. Ryou, D.Y. Yoon, B.B. Hwang, "The process sequence design of a power-assisted steering part", *J. Mater. Process. Technol.* 113 (1-3) (2001): 87-92.
- [58] J. Monaghan, M. O' Reilly, "Influence of lubrication on the surface finish of cold forged components", *J. Mater. Process. Technol.* 56 (1996): 678-690.
- [59] J. Donofrio, "Zinc phosphating", *Metal Finish.* 98 (6) (2000): 57-73.
- [60] J.A. Schey, "Tribology in metalworking: friction, lubrication and wear", *American Society for Metals- (ASM), Metal Park, Ohio*, 1984.
- [61] W. Rausch, "The phosphating of metals", *Finishing Publications Ltd., London*, 1990.
- [62] P. Hivart, J. Bricout, J. Oudin, "New real-time test for prediction of zinc phosphate-stearate coatings breakdown: optimal stearate settlings parameters for steel billets in cold forging", *Tribology International* 25 (1) (1992): 45-51.
- [63] B. Bhushan, B.K. Gupta, "Handbook of tribology: materials, coatings, and surface trea[t]ments", *McGraw-Hill, New York*, 1997.
- [64] N. Bay, "State of the art in cold forging lubrication", *Journal of Materials Processing Technology* 46 (1-2) (1994): 19-40.
- [65] N. Bay (1994), "The state of the art in cold forging lubrication". *Journal of Materials Processing and Technology* 46: 19-40.

- [66] ICFG Doc. 8/91 (1991), "Lubrication aspects in cold forging of carbon steels and low alloy steels". The International Cold Forging Group.
- [67] L. Dubar, J.P. Bricout, C. Wierre, P. Meignan (1998), "New surface processes for cold forging of steels". *Surface and Coatings Technology* 102: 159-167.
- [68] M. Geiger (1995), "Towards clean forming technologies". *Annals of the CIRP* 44(2):581-592.
- [69] T. Nakamura, I. Ishibashi (2004), "Environmentally friendly lubrication system for forging". English translation of Report from JSTP's Sub-Committee on Process-Tribology.
- [70] D. Schmoeckel, M. Rupp (1997), "More environment friendly cold massive forming-production of steel without zinc phosphate layer". *Proceed. Neuere Entwicklunde der Massivumformung, Stuttgart*, 183-200. (in German).
- [71] S. Shida (2002), "Environmentally friendly lubricants for cold forging". *Proceed. 215th Symp. of JSTP*, 215, 33-39. (in Japanese).
- [72] N. Yamamoto (2002), "Tribology in forging". *Tribologist* 47-6: 451-456. (in Japanese).
- [73] S. Komatsuzaki, T. Uematsu, T. Narahara (1998), "Effects of extreme pressure additives in forward extrusion". *Journal of the JSTP* 29-330: 748-754. (in Japanese).
- [74] S. Komatsuzaki (1986), "Extreme pressure additives for cold forging lubricant". *Journal of the Japan Society of Lubrication Engineers* 31(6): 381-386. (in Japanese).
- [75] T. Ohmori, N. Kitamura, A. Danno, M. Kawamura (1991), "A cold forging oil containing phosphorus type EP additives". *Tribology Transactions* 34-3: 458-464.
- [76] T. Ohmori, N. Kitamura, A. Danno, M. Kawamura (1991), "Lubricity of lubricants added phosphate extreme pressure additives for cold forging". *Tribologist* 36(6): 452-458. (in Japanese).
- [77] N. Asaba (2001), "Non-conversion coating lubricants for cold forging". *Anticorrosion Management* 45(87): 426-429. (in Japanese).
- [78] T. Horita (2001), "Non-chlorinated lubricants for cold forging". *Technical Review by Forging Technology Institute of Japan* 26(87): 59-62. (in Japanese).
- [79] M. Yoshida (2001), "Characteristics and application of recent lubricants for cold forging". *Technical Review by Forging Technology Institute of Japan* 26(87): 53-58. (in Japanese).
- [80] G. Cortellaro, E. Bucci, P. Anelli, M. Yoshida (2004), "E-Phos1 technology for wire drawing". *Wire Journal International* 37(6): 67-69.
- [81] N. Kobatashi, A. Moriyama, M. Yoshida (2005), "Electrolytical phosphating process for steel wire drawing". *Nihon Parkerizing, Technical report No. 17*.
- [82] K.D. Nittel (2008), "Neue beschichtungen und trends beim kaltfliesspressen und kaltstauchen". *Proceed. 23th Jahrestreffung der Kaltmassivumformer, Düsseldorf, VDI*. (in German).
- [83] N.J. Bjerrum, E. Christensen, T. Steenberg (1996/2002), "Method for electrochemical phosphating of metal surfaces", Danish patent, No. 0910/96/US patent, US 6,346,186 B1.
- [84] P.T. Olesen, T. Steenberg, E. Christensen, N.J. Bjerrum (1998), "Electrolytic depositions of amorphous and crystalline Zn/Ca-phosphates on stainless steel". *Journal of the Materials Science* 33: 3059-3063.
- [85] O. Wibom (1998), "Tribology in cold forging of stainless steel". Ph.D. Thesis, Technical Univ. of Denmark. (in Danish).
- [86] <http://www.coldforming.chemetall.com>.
- [87] H. Utsunomiya, S. Kawajiri, N. Takahira, J. Miyamoto, T. Sakai, T. Tanaka (2007), "Porosification of steel surface-new lubrication system for cold forging". In Azushima A, (Ed.) *Proceed. 3rd Int. Conf. on Tribology in Manuf. Process., ICTMP* 363-72.
- [88] M. Arentoft, N. Bay, T. Tang, J.D. Jensen (2009), "A new lubricant carrier for metal forming". *Annals of the CIRP* 58(1): 243-246.
- [89] P.T. Tang, M. Arentoft, N. Bay, M. Borrild, I. Mizushima, J.D. Jensen, N.A. Paldan (2008), "A microporous layer for lowering friction in metal forming processes", Patent PCT/DK2008/000233.
- [90] T. Nakamura, Y. Sumioka, Y. Sagisaka, I. Ishibashi, M. Sekizawa (2008), "Lubrication performance of environmentally friendly lubricants for forging", 1st Report. *Proceed. 59th Japanese Joint Conference for the Technology of Plasticity*, 579-580.
- [91] T. Nakamura, Y. Sumioka, K. Sakoda, S. Miyano, Y. Ishiizumi, I. Ishibashi, M. Sekizawa (2008), "Lubrication performance of environmentally friendly lubricants for forging". 2nd Report. *Proceed. of the 59th Japanese Joint Conference for the Technology of Plasticity*, 333-334.
- [92] L. Lazzarotto, L. Dubar, A. Dubois, P. Ravassard, J. Oudin (1998), "Three selection criteria for the cold metal forming lubricating oils containing extreme pressure agents". *Journal of Material Processing Technology* 80-81: 245-250.
- [93] T. Nakamura, I. Ishibashi (2004), "Environmentally friendly lubrication system for forging". English translation of Report from JSTP's Sub-Committee on Process-Tribology.

- [94] N. Kashimura, M. Takeuchi, F. Oda, F. Kawahara, H. Ojima, M. Tomono (2000), "Development of environmentally friendly lubricant for cold forging with high performance and simple treatment". *Journal of the JSTP* 41(469): 109-114. (in Japanese).
- [95] K. Morishita (2001), "Trends of environmentally friendly lubricants for cold forging". *Technical Review by Forging Technology Institute of Japan* 26(87): 12-18. (in Japanese).
- [96] M. Takeuchi, F. Ikesue, N. Kashimura (1999), "Development of environmentally friendly lubricant with high performance and simple treatment for cold forging". In Geiger M, (Ed.) *Advanced Technology of Plasticity. Proc. 6th ICTP* 383-389.
- [97] A. Uno, S. Shida, M. Tomono, T. Shimizu, T. Sano (2002), "Development of waste free water-system lubricant for cold forging". In Kiuchi M, (Ed.) *Advanced Technology of Plasticity. Proc. 7th ICTP* 1669-1673.
- [98] Anon, "Replaceable lubricants to phosphate/soap treatment", *Technical Bulletin of Daido Chemical Industry Co.*
- [99] M. Gariety, G. Ngaile, T. Altan (2007), "Evaluation of new cold forging lubricants without zinc phosphate precoat". *International Journal of Machine Tools and Manufacture* 47: 673-681.
- [100] K. Hirai (1984), "Lubricants for deformation processes". *Journal of JSTP* 25(285): 878-885. (in Japanese).
- [101] M. Morishita (2007), "Tribology in manufacturing processes of automobiles at Toyota". In Azushima A, (Ed.) *Proceed. 3rd Int. Conf. on Tribology in Manufacturing Processes, ICTMP* 31-9.
- [102] T. Nakamura (1993), "Counter measures for seizure phenomena in deformation processes". *Journal of the JSTP* 34(393): 1082-1090. (in Japanese).
- [103] C. McCormack, J. Monaghan. Failure analysis of cold forging dies using FEA [J]. *J Mater Process Technol*, 2001, 117: 209-215.
- [104] T. Nakamura, I. Ishibashi (2004), "Environmentally friendly lubrication system for forging". English translation of Report from JSTP's Sub-Committee on Process-Tribology.
- [105] J. Bolton, "Modern developments in sintered high speed steels". *Met Powder Rep* 1996; 51: 30-8.
- [106] G. Hoyle, "High speed steels". London: Butterworths; 1988. p. 222.
- [107] *Steel Products Manual, "Tool Steels"*, Iron and Steel Society, 1988.
- [108] "Tool steels, heat treater's guide: practices and procedures for irons and steels", H. Chandler, Ed., ASM International, 1995, pp. 517-669.
- [109] J.G. Gensure, D.L. Potts, "International metallic materials cross-reference", 3rd ed., Genium Publishing, 1988.
- [110] M. Boccalini, H. Goldenstein, "Solidification of high speed steels". *International Materials Review*, 2001, 46: 92.
- [111] "Tool steels, heat treater's guide: practices and procedures for irons and steels", H. Chandler, Ed. ASM International, 1995, pp. 517-669.
- [112] E.S. Lee, W.J. Park, K.H. Baik, S. Ahn, "Solidification microstructure and M₂C carbide decomposition in a spray-formed high-speed steel". *Scripta Materialia*, 1998, 39: 1395.
- [113] C. Rodenburg, W.M. Rainforth, "A quantitative analysis of the influence of carbides size distributions on wear behaviour of high-speed steel in dry rolling/sliding contact". *Acta Materialia*, 2007, 55: 2443.
- [114] H. Takigawa, H. Manto, N. Kawai, K. Homma, *Powder Metall.* 24 (4) (1981) 196.
- [115] P. Matteazzi, F. Wolf, *Mater. Sci. Eng. A* 248 (1998) 19.
- [116] D. Jakubeczyova, J. Blach, M. Fáberová, *Kovove Mater.* 39 (2001) 278. (in Slovak).
- [117] E. Pippel, J. Woltersdorf, G. Pöckl, G. Lichtenegger, *Mater. Characterisation* 43 (1999) 41.
- [118] F. Preisser, *Proceedings of 18th National Conference on Heat Treatment with International Participation, Brno, Czech Republic, 28-30 November, Asociace pro tepelné zpracování kovů, Praha, 2002, p. 189.*
- [119] S. Kheirandish, Y.H.K. Kharrazi, S. Mirdamadi, *ISIJ Int.* 37 (7) (1997) 721.
- [120] O. Sandberg (2008), "Advanced low-friction tool steel for metal processing: properties and industrial experiences". *International Journal of Microstructure and Materials Properties* 3(2-3): 391-400.
- [121] O. Sandberg, B. Högman, B. Johansson, A. Thuvander (2008), "New tool concept for stamping of HSS and AHSS sheet". *Proceed. Int. Conf. on Deep Drawing, IDDRG, Olofström, Sweden, 591-602.*
- [122] Anon (2003), "Development of replacements for phosphating used in forging", *Extrusion and Metal Forming Processes. National Center for Manufacturing Sciences, Ann Arbor, MI, USA.*
- [123] S.G. Harris, E.D. Doyle, A.C. Vlasveld, J. Audy, J.M. Long, D. Quick, "Influence of chromium content on the dry machining performance of cathodic arc evaporated TiAlN coatings", *Wear* 254 (1-2) (2003) 185-194.
- [124] F. Klocke, M. Massmann, K. Gerschwiler (2005), "Combination of PVD tool coatings and biodegradable lubricants in metal forming and machining". *Wear* 259: 1197-1206.

- [125] Ngaile, G., and Altan, T., "Simulations of Manufacturing Processes: Past, Present and Future," Proceedings of the Seventh ICTP, Oct 2002, Japan, p. 271.
- [126] Kobayashi, S., Oh, S.I., Altan, T., 1989. Metal Forming and the Finite Element Method. Oxford University Press.
- [127] Lee, C.H., Kobayashi, S., 1973. New solutions to rigid-plastic deformation problems using a matrix method. Trans. ASME J. Eng. Ind. 95, 865-873.
- [128] Oh, S.I., 1982. Finite element analysis of metal forming processes with arbitrarily shaped dies. Int. J. Mech. Sci. 24, 479-493.
- [129] Park, J.J., Kobayashi, S., 1984. Three-dimensional finite element analysis of block compression. Int. J. Mech. Sci. 26, 165-176.
- [130] Mori, K., Osakada, K., 1990. Finite element simulation of three dimensional deformation in shape rolling. Int. J. Numer. Methods Eng. 30, 1431-1440.
- [131] Im, Y.T., Kang, S.H., Cheon, J.S., Kim, S.Y., 2003. Finite element investigation of tip test with an aluminum alloy. JSME Int. J. Ser. A Mech. Mater. Eng. 46, 224-229.
- [132] Vasquez, V., Walters, J., and Altan, T., "Forging Process Simulation-State of the Art in USA," Proceedings of the Conference on New Developments in Forging Technology, Stuttgart, Germany, May 19-20, 1999.
- [133] Howson, T.E., and Delgado, H.E., "Computer Modeling Metal Flow in Forging," JOM, Feb. 1989, pp. 32-34.
- [134] Oh, S.I., "Finite Element Analysis of Metal Forming Problem with Arbitrarily Shaped Dies," Int. J. Mech. Science, Vol. 24 (No. 4) 1982, p. 479.
- [135] Sellars, C.M., "Modeling Microstructural Development during Hot Rolling," Materials Science and Technology, Vol. 6, 1990, p. 1072.
- [136] Shen, G., "Microstructure Modeling of Forged Components of Ingot Metallurgy Nickel Based Superalloys," Advanced Technologies for Superalloy Affordability, K.M. Chang, S.K. Srivastava, D.U. Furrer, and K.R. Bain, Ed., TMS, 2000, pp. 223-231.
- [137] A. Erman Tekkaya, A guide for validation of FE simulations in bulk metal forming. The Arabian Journal for Science and Engineering, Vol 30, 2005, pp. 113-136.
- [138] FORGE2 Technical Documentation, Transvalor SA, 2000.
- [139] Shen, G., Denkenberger, R., Furrer, D., "Aerospace Forging-Process and Modeling", Materials Design Approaches and Experiences, J.C. Zhao, M. Fahrman, and T.M. Pollock, Ed., TMS, 2001, pp. 347-357.
- [140] Wu, W.T., Li, G.J., Arvind, A., Tang, G.P., "Development of a Three Dimensional Finite Element Based Process Simulation Tool for the Metal Forming Industry," Proceedings of the Third Biennial Joint Conference on Engineering Systems Design and Analysis, Montpellier, France, 1996.
- [141] P.F. Bariani, T. D. Negro, and S. Bruschi, "Testing and Modelling of Material Response to Deformation in Bulk Metal Forming," Annals of the CIRP Vol. 53/2/2004 573-598.
- [142] J.C. Fisher and J. H. Hollomon, "Dislocation glide as an aid to precipitation at low temperatures", Acta metallurgica, vol. 3/6: 608, 1955.
- [143] E. Voce, "A practical strain-hardening function", Acta metallurgica, vol. 51, pp. 219-226, 1948.
- [144] D. Lorenz and K. Roll, "Simulation of Hot Stamping and Quenching of Boron alloyed Steel", presented at 7th Int. ESAFORM Conf. on Mat. Forming, Trondheim, Norway, 2004.
- [145] Czichos H. Tribology - a system approach to the science and technology of friction, lubrication and wear. Amsterdam: Elsevier Scientific Publishing Company, 1978.
- [146] Schey JA. Tribology in metalworking: friction, lubrication and wear. Metals Park (OH): American Society For Metals, 1983.
- [147] Bay N. Friction and adhesion in metal forming and cold welding. D. Sc. thesis (MM.85.43), Institute of Manufacturing Engineering, Technical University of Denmark, 1985.
- [148] Kalpakjian S. Recent progress in metal forming tribology. Ann. CIRP 1985; 34(2): 585-92.
- [149] Lenard JG. Tribology in metal rolling: keynote paper. Ann. CIRP 2000; 49(2): 567-90.
- [150] Von Karman Th. On the theory of rolling. Z. angew. Math. Mech. 1925; 5: 139-41.
- [151] Siebel E. Resistance and deformation and the flow material during rolling. Stahl und Eisen 1930; 50: 1769-75.
- [152] Wanheim T. Friction at high normal pressures. Wear 1973; 25: 225-44.
- [153] Wanheim T., Bay N., Petersen A.S., "A Theoretically Determined Model for Friction in Metal Working Processes", Wear, 28 (1974), pp. 251-258.
- [154] Wanheim T, Bay N. A model for friction in metal forming processes. Ann. CIRP 1978; 27(1): 189-94.
- [155] Tan X. "Comparisons of Friction Models in Bulk Metal Forming", Tribology International, v.35, pp. 385-393, 2002.

- [156] V.K. Jain, B.J. Foster. Investigation of friction behaviour during non-isothermal deformation-processing, ASME Paper PED 54, Atlanta, 1991, S187-S201.
- [157] Hansen B.G., Bay N. Two new methods for testing lubricants for cold forging. *J. Mech. Work. Technol.* 13, 1986, 189-204.
- [158] Groche P., Kappes B. Tribologie der Massivumformung-Modellprüfstände der Tribologie. In: Bartz, W.J. (Ed.), *Tribologie und Schmierung bei der Massivumformung*, vol. 13. Expert Verlag, Renningen-Malmsheim, Germany, 2004, pp. 1-14.
- [159] Doege E., Alasti M., Schmidt-Jürgensen, 2002b. An innovative procedure for the numerical identification of accurate friction and heat transfer laws for precision forging processes. In: *Proceedings of the Ninth ISPE International Conference on Concurrent Engineering: Research and Application-Advances in Concurrent Engineering*, pp. 199-207.
- [160] Ngaile G., Saiki H., Ruan L., Marumo Y., 2007. A tribo-testing method for high performance cold forging lubricants. *Wear* 262, 684-692.
- [161] Daouben E., Dubar L., Dubar M., Deltombe R., Dubois A., Truong-Dinh N., Lazzarotto L., 2007. Friction and wear in hot forging of steels. In: *Proceedings of the 10th ESAFORM Conference on Material Forming*, pp. 505-508.
- [162] Kunogi M., 1954. On plastic deformation of hollow cylinder under axial compression. *Rep. Scient. Res. Inst.* 30, pp. 63-92.
- [163] Male A.T., Cockcroft M.G., 1965. A method for determination of the coefficient of friction of metals under conditions of bulk plastic deformation. *J. Inst. Metals* 93, pp. 38-46.
- [164] Sofuoğlu H., Gedikli H., Rasty J. Determination of Friction Coefficient by Employing the Ring Compression Test, *Transactions of ASME, Journal of Engineering Materials and Technology*, Vol. 123, 2001, pp. 338-348.
- [165] Rao KP, Sivaram K. A review of ring-compression testing and applicability of the calibration curves. *J Mater Process Technol* 1993; 37: 295-318.
- [166] Sofuoglu H, Rasty J. On the measurement of friction coefficient utilizing the ring compression test. *Tribol Int* 1999; 32: 327-35.
- [167] Sofuoglu H, Gedikli H. Determination of friction coefficient encountered in large deformation processes. *Tribol Int* 2002; 35: 27-34.
- [168] Joun MS, Moon HG, Choi IS, Lee MC, Jun BY. Effects of friction laws on metal forming processes. *Tribol Int* 2009; 42: 311-9.
- [169] Geiger R., 1976. Metal flow in combined can extrusion. In: *Berichte aus dem Institut für Umformtechnik, Universität Stuttgart*, No. 36. Verlag Giradet, Essen, Germany. (in German).
- [170] Buschhausen A., Lee J.Y., Weinmann K., Altan T., 1992. Evaluation of lubrication and friction in cold forging using a double backward extrusion process. *J. Mater. Process. Technol.* 33, pp. 95-108.
- [171] Arentoft M., Vigsø C., Lindegren M., Bay N., 1996. A study of the double cup extrusion process as a friction test. In: *Proceedings of the Advanced Technology of Plasticity*, vol. I, 5th ICTP, pp. 243-250.
- [172] Kim H., Padwad S., Altan T., 2004. Evaluation of new lubricants for cold forging without zinc phosphate coating. In: *Proceedings of the 37th Plenary Meeting of the International Cold Forging Group*.
- [173] Forcelllese A., Gabrielli A., Barcellona A., Micari A., "Evaluation of Friction in Cold Metal Forming", *Journal of Materials Processing Technology*, 45(1994), pp. 619-624.
- [174] Schrader T., Shirgaokar M., Altan T., 2007. A critical evaluation of the double cup extrusion test for selection of cold forging lubricants. *J. Mater. Process. Technol.* 189, 36-44.
- [175] Sheljaskow S., 2001. Tool lubricating systems in warm forging. *J. Mater. Process. Technol.* 113, 16-21.
- [176] A. Tarantola, *Inverse problem theory*: Elsevier, 1987.
- [177] J.D. Coolins, G. C. Hart, T. K. Hassleman and B. Kennedy, "Statistical identification of structures," *AAIA Journal*, vol. 12, pp. 185-190, 1974.
- [178] J.V. Beck and K.J. Arnold. *Parameter estimation in Engineering and Science*: John Wiley & Sons, 1986.
- [179] A. Badrinarayanan, A. Constantinescu and N. Zabras, "Preform in metal forming", presented at *Proceedings of the 1995 Numiform Conference (Balkema)*.
- [180] D.S. Schnur and N. Zabras, "An inverse method for determining elastic material properties and a material interface", *International Journal for Numerical Methods in Engineering*, vol. 33, pp. 2039-2057, 1992.
- [181] D.M. Bates and D. G. Watts, *Nonlinear regression Analysis and its Application*, 1988.
- [182] Kimura F., Suzuki H., Takahashi K. Product design evaluation based on effect of shape errors for part assembly. *CIRP Annals: Manufacturing Technology* 1992; 41(1): 193-6.

- [183] Chan WL, Fu MW, Lu J, Chan LC. Simulation-enabled study of folding defect formation and avoidance in axisymmetrical flanged components. *Journal of Materials Processing Technology* 2009; 209(11): 5077-86.
- [184] Tahir A., 2007. A study of barreling profile and effect of aspect ratio on material flow in lateral extrusion of gear-like forms, *Ind. J. Eng. Mater. Sci.* 14 (3), 184-192.
- [185] Liu G, Zhang LB, Hu XL, Wang ZR, Wang RW, Huang SD, et al. Applications of numerical simulation to the analysis of bulk-forming processes-case studies. *Journal of Materials Processing Technology* 2004; 150(1-2): 56-61.
- [186] Narayanasamy R., Thaheer A.S.A., Baskaran K., 2006. Comparison of barreling unlubricated truncated cone billets during cold upsetting forging of various metals, *Indian Journal of Engineering and Materials Science* 13 (3): 202-208.
- [187] Baskaran K., Narayanasamy R., 2006. Effects of various stress ratio parameters on cold upset forging of irregular shaped billets using white grease as lubricant, *Indian Journal of Engineering and Materials Science* 13 (4): 281-292.
- [188] Yilmaz C, Tahir AM, Erol AH. An investigation on forging loads and metal flow in conventional closed-die forging of preforms obtained by open-die indentation. *Indian Journal of Engineering and Materials Science* 2004; 11(6): 487-92.
- [189] Lu C., Zhang L.W., 2006. Numerical simulation on forging process of TC4 alloy mounting parts, *Transactions of Nonferrous Metals Society of China* 16 (6), 1386-1390.
- [190] Song J.H., Im Y.T., 2007. Process design for closed-die forging of bevel gear by finite element analyses, *J. Mater. Process. Technol.* 192, 1-7.
- [191] Qamar S.Z., 2010. Shape complexity, metal flow, and dead metal zone in cold extrusion, *Materials and Manufacturing Processes* 25, 1454-1461.
- [192] Sheu J.J., Yu C.H., 2008. The die failure prediction and prevention of the orbital forging process, *J. Mater. Process. Technol.* 201 (1-3), 9-13.
- [193] Vries M. de. Inclusion of defect avoidance in expert systems for cold forging, Reading University, RUEL Report No. 101/92, 1992, pp. 1-30.
- [194] Arentoft M., Wanheim T., 1997. The basis for a design support system to prevent defects in forging, *J. Mater. Process. Technol.* 69, 227-232.
- [195] Okamoto T., T. Fukuda and H. Hagita. Material fracture in cold forging Systematic classification of working methods and types of cracking in cold forging. *The Sumitomo Search No.9*, May 1973, pp. 46-56.
- [196] Kudo H. Towards net-shape forming, *Journal of Materials Processing Technology.* 22, 1990, pp. 307-342.
- [197] R.D. Doherty, G. Gottstein, J.R. Hirsch, W.B. Hutcheon, K. Lucke, E. Nes, P.J. Wilbrandt, in: J.S. Kallend, G. Gottstein (Eds.), *Panel Discussion on Recrystallization Texture*, ICOTOM 8, TMS, Warrendale, PA, 1988, p. 369.
- [198] F.J. Humphreys and M. Hatherly, *Recrystallization and Related Annealing Phenomena*, 2nd ed., Pergamon, Oxford, 2004.
- [199] S.F. Medina and A. Quispe. Improved Model for Static Recrystallization Kinetics of Hot Deformed Austenite in Low Alloy and Nb/V Microalloyed Steels, *ISIJ Int.*, 2001, 41(7), p. 774-781 (in English).
- [200] R. Abad, A.I. Fernandez, B. Lopez and J.M. Rodriguez. Interaction Between Recrystallization and Precipitation During Multipass Rolling in a Low Carbon Niobium Microalloyed Steel. *ISIJ Int.*, 2001, 41(7), p. 1373-1382 (in English).
- [201] J.E. Burke and D. Turnbull, *Prog. Met. Phys.* Vol. 3, 1952, p. 200.
- [202] H. Beladi, P. Cizek, P.D. Hodgson, *Metall. Mater. Trans. A* 40A (2009) 1175.
- [203] T. Sakai, A. Belyakov, R. Kaibyshev, H. Miura, J.J. Jonas, *Prog. Mater. Sci.* 60 (2014) 130-207.
- [204] R.Z. Valiev, T.G. Langdon, *Adv. Eng. Mater.* 12 (2010) 677-691.
- [205] Y. Estrin, A. Vinogradov, *Acta Mater.* 61 (2013) 782-817.
- [206] C. Kobayashi, T. Sakai, A. Belyakov, H. Miura, *Philos. Mag. Lett.* 87 (2007) 751-766.
- [207] A. Belyakov, T. Sakai, H. Miura, K. Tsuzaki, *Philos. Mag. A* 81 (2001) 2629-2643.
- [208] N. Dudova, A. Belyakov, T. Sakai, R. Kaibyshev, *Acta Mater.* 58 (2010) 3624-3632.
- [209] T. Sakai, J.J. Jonas, in: K.H. Buschow, R.W. Cahn, M.C. Flemings, B. Ilshner, E.J. Kramer, S. Mahajan (Eds.), *Encyclopedia of materials: science and technology*, vol. 7, Elsevier, Oxford, 2001.
- [210] Y. Huang, J.D. Robson, P.B. Prangnell, *Acta Mater.* 58 (2010) 1643-1657.
- [211] R. Kaibyshev, S. Malopheyev, V. Kulitskiy, M. Gazizov, *Mater. Sci. Forum* 783-786 (2014) 2641-2646.
- [212] L.S. Toth, Y. Estrin, R. Lapovok, C. Gu, *Acta Mater.* 58 (2010) 1782-1794.
- [213] T. Watanabe, *Mater. Sci. Forum* 94-96 (1992) 209.
- [214] L. Kestens, J.J. Jonas, *Metall. Mater. Trans.* 27A (1996) 155.

- [215] T. Urabe, J.J. Jonas, *ISIJ Int.* 34 (1994) 435.
- [216] Y.B. Park, D.N. Lee, G. Gottstein, Proc. 11th Int. Conf. on Textures of Materials ICOTOM-11, Nonferrous Metals Society of China, Beijing, 1996, p. 531.
- [217] Ph. Bocher, Ph.D. Thesis, McGill University, Montreal, Canada, 1997.
- [218] L.S. Tóth, J.J. Jonas, *Scr. Metall. Mater.* 27 (1992) 359.
- [219] Okamura T., Sakashita A., Fukuda T., Yamashita H., Futami T., 2003. Latest SCC issues of core shroud and recirculation piping in Japanese BWRs. Transactions of 17th International Conference on Structural Mechanics in Reactor Technology (SMiRT 17), Prague, WG01-1.
- [220] Krieger Lassen N.C., Juul Jensen D., Conradsen K. (1994). Automatic recognition of deformed and recrystallized regions in partly recrystallized samples using electron backscattering patterns. *Mater. Sci. Forum* 157-162, 149-158.
- [221] Field D.P. (1995). Quantification of partially recrystallized polycrystals using electron backscatter diffraction. *Mater. Sci. Eng. A* 190, 241-246.
- [222] Wardle S.T., Lin L.S., Cetel A.D., Adams B.L. (1994). Orientation imaging microscopy: Monitoring residual stress profiles in single crystals using and imaging quality parameter. IQ. In Proceedings of the 52nd Annual Meeting of the Microscopy Society of America, Bailey G.W., Garratt-Reed A.J. (Eds.), pp. 680-681. San Francisco CA: San Francisco Press.
- [223] Kunze K., Wright S.I., Adams B.L., Dingley D.J. (1993). Advances in automatic EBSD single orientation measurements. *Text. Microstruc.* 20(1-4), 41-54.
- [224] Nowell M.M., Wright S.I. (2005). Orientation effects on indexing of electron backscatter diffraction patterns. *Ultramicroscopy* 103(1), 41-58.
- [225] Y. Zhou, K.T. Aust, U. Erb, G. Palumbo, *Scripta Materialia* 45 (2001) 49.
- [226] H. Kokawa, *Journal of Materials Science* 40 (2005) 927.
- [227] R. Singh, S.G. Choedhury, B.R. Kumar, S.K. Das, P.K. De, I. Chattoraj, *Scripta Materialia* 57 (2007) 185.
- [228] J.F. dos Santos, C.M. Garzon, A.P. Tschiptschin, *Materials Science and Engineering A* 382 (2004) 378.
- [229] T. Watanabe, *Materials Forum* 11 (1988) 284.
- [230] A.H. Advani, R.J. Romero, L.E. Murr, D.J. Matlock, W.W. Fisher, P.M. Tarin, C.M. Cedillo, J.M. Maldonado, R.C. Miller, E.A. Trillo, *Scripta Metallurgica et Materialia* 27 (1992) 1759.
- [231] J. Mizera, A. Garbacz, K.J. Kurzydowski, *Scripta Metallurgica et Materialia* 33 (1995) 515.
- [232] A.J. Schwartz, W.E. King, *JOM* 50 (1998) 50.
- [233] E.M. Lechockey, G. Palumbo, P. Lin, *Metallurgical and Materials Transactions A* 29 (1998) 3069.
- [234] O.V. Mishin, V.Y. Gertsman, I.V. Alexandrov, R.Z. Valiev, *Materials Science and Engineering A* 212 (1996) 281.
- [235] D.N. Wasnik, V. Kain, I. Samajdar, B. Verlinden, P.K. De, *Acta Materialia* 50 (2002) 4587.
- [236] E.A. Trillo, L.E. Murr, *Acta Materialia* 47 (1999) 235.
- [237] L. Valentini, A. Di Schino, J.M. Kenny, Y. Gerbig, H. Haefke, *Wear* 253 (2002) 458.
- [238] A. Di Schino, J.M. Kenny, *Journal of Materials Science Letters* 21 (2002) 1969.
- [239] G. Bregliozzi, A. Di Schino, S.I.-U. Ahmed, J.M. Kenny, H. Haefke, *Wear* 258 (2005) 503.
- [240] M. Richert, Q. Liu, N. Hansen, *Materials Science and Engineering A* 260 (1999) 275.
- [241] A. Belyakov, T. Sakai, H. Miura, K. Tsuzaki, *Philosophical Magazine A* 81 (2001) 2629.
- [242] A. Belyakov, W. Gao, H. Miura, T. Sakai, *Metallurgical and Materials Transactions A* 29 (1998) 2957.
- [243] Y. Iwahashi, Z. Horita, M. Nemoto, T.G. Langdon, *Acta Materialia* 45 (1997) 4733.
- [244] I.A. Yakubtsov, A. Ariapour, D.D. Perovic, *Acta Materialia* 47 (1999) 1271.
- [245] A. Belyakov, T. Sakai, H. Miura, R. Kaibyshev, K. Tsuzaki, *Acta Materialia* 50 (2002) 1547.
- [246] A. Belyakov, Y. Kimura, K. Tsuzaki, *Acta Materialia* 54 (2006) 2521.
- [247] A. Belyakov, T. Sakai, H. Miura, R. Kaibyshev, *Philosophical Magazine Letters* 80 (2000) 711.
- [248] A. Belyakov, T. Sakai, H. Miura, R. Kaibyshev, *ISIJ International* 39 (1999) 592.
- [249] A. Belyakov, Y. Kimura, K. Tsuzaki, *Materials Science and Engineering A* 403 (2005) 249.
- [250] D.A. Hughes, N. Hansen, *Acta Materialia* 45 (1997) 3871.
- [251] A. Belyakov, K. Tsuzaki, Y. Kimura, Y. Kimura, Y. Mishima, *Materials Science and Engineering A* 456 (2007) 323.

ACKNOWLEDGEMENTS

This PhD work has been financially supported by the “Zoppelletto S.p.A.” which is gratefully acknowledged.

Special thanks are also due to Cogne Acciai Speciali S.p.A., Oerlikon Balzers Coating Italy S.p.A. and Henkel Italy S.p.A. for supplying materials and some equipments to support the experimental tests. I also wish to thank the following persons:

- My supervisors Professor Paolo Ferro and Professor Franco Bonollo, who made it possible for me to write this thesis. I wish to express my sincere gratitude for sharing their vast experience and for their excellent guidance. Thank you for showing me the way.
- Eng. Luca Zoppelletto for his useful advices and for introducing me to industrial cold forging processes and for his patient and precious technical support in forging tests.
- My colleagues and technicians at the Department of Management and Engineering at the University of Padua - Vicenza: Giacomo Mazzacavallo, for his patient technical support and for his valuable all-embracing assistance, Giulio Timelli and Alberto Fabrizi for their precious help in the experimental approach and discussions, Stefano Ferraro, Elena Fiorese, Stefano Capuzzi, Daniele Caliarì, Eleonora Battaglia and Giorgio Kral for help, enjoying lunches and discussions.
- Professor Alberto Tiziani for his experience, useful advices and enjoying discussions.
- My girlfriend and future wife Martina: thanks for still being at my side and for brought me up during this last year. You give me moral support every time I have needed it. You are my life and I will always love you.
- My family deserves special thanks. Dad, mommy, and grandmothers: I hope you are satisfied with this work because it was you who made it possible.
- My friend Alberto for always keeping me up and gave me funny moments.

PAPERS

ARTICLE I

ADVANCED MICROSTRUCTURAL CHARACTERIZATION OF TOOL STEELS AND COATINGS FOR COLD FORGING OF STEELS

F. Bassan, P. Ferro, F. Bonollo*

**University of Padua, Department of Management and Engineering,
Stradella S. Nicola, 3 I-36100 Vicenza, Italy*

Proc. of 24th AIM National Conference on Heat Treatments, 17-18th October 2013,
Piacenza, Italy.

ABSTRACT

Surface treatments of tool steels have the main purpose of improving the wear and fatigue resistance. Cold deformation and shearing require protection of forging and cutting tools, against severe abrasive wear. This goal is achieved through an accurate surface finishing of tools and the deposition of coatings at low friction coefficient, that allow to considerably increase tools life in many applications.

In this work, the surface morphology, microstructure and element composition of different PVD deposited single- and multi-layer coatings, applied on conventional and powder metallurgy (PM) cold work tool steels, were investigated by using a Field-Emission Gun Environmental Scanning Electron Microscope (FEG-ESEM, model QUANTA 250 FEI[®]) equipped with an Energy Dispersive X-ray Spectroscopy (EDS, EDAX[®]) system. EDS analyses also permitted to identify the presence of complex carbides composed by the main alloying elements on tool steels analyzed, after heat treatment.

KEYWORDS

Cold forging, Tool steels, PVD coatings, Hard coatings, Complex carbides.

1. INTRODUCTION

In recent years, production techniques are remarkably improved, due to the increasing demand of accuracy and high productivity by the companies. Especially tool material selection, design and manufacture are important factors to reduce long process development time and high production costs.

To achieve these targets, it is also required to well know the selection criteria of the tool steel grades, specially in severe working applications.

In particular, the performances of a cold work tool steel are affected by many factors (Fig. 1) and are mostly evaluated by examining the quality of the forged parts.

In most applications, a remarkable increase in dimensional accuracy and surface finish is required and a wear or damage tool raises the rate of waste material. Therefore, it must be retreated or replaced.

The steel selected has notable influence on failure mechanisms of the most common cold work tools, such as abrasive and adhesive wear, bonding, chipping and cracks.

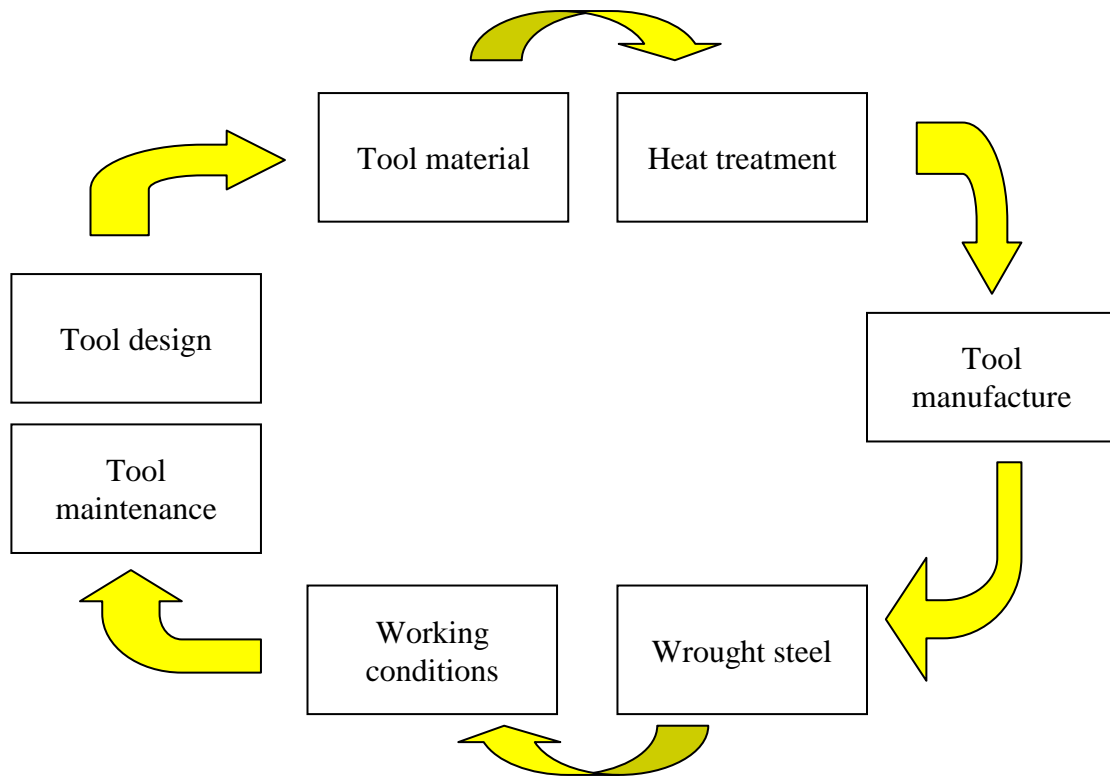


Fig. 1. Factors affecting tool performances.

Nowadays high-speed steels (HS or HSS) are the mostly used materials to design tools for cold forging operations (e.g. shearing, deep extrusion, etc.).

The main properties of cold work tools, after heat treatment, can be summarized as follows:

- Hardness values reached in the range of 56-62 HRC [1-5];
- High resistance to wear and to repeated impacts;
- High toughness (i.e. the best compromise between higher hardness and lower embrittlement);
- Good fatigue resistance, which strictly depends on the geometry and finishing state of the tool as well as its hardness and metallographic structure;
- Thermal fatigue and shock resistance, which are essential due to the high localized temperatures that are generated during forging.

Nevertheless, the mechanical properties of these steels are largely determined by the chemical composition and the manufacture method used.

In recent years, the need to provide high performance tool steels has intensified drastically and this demand has been satisfied thanks to the introduction of powder metallurgy (PM) steels. PM tool steels improve resistance to wear and heat, hardness, toughness and dimensional stability as compared to the conventional HSS steels. It is also possible to produce tools with complex geometry and restricted tolerances at a low cost [6-7]. This is possible due to the reduction of macro-segregations that allows the production of steels with a complex multi-component alloying system [6-7].

In addition small carbides, with high hardness, usually have a more homogeneous distribution in the matrix after conventional heat treatment. This give the possibility to produce an isotropic steel almost avoid of inclusions and with a uniform microstructure [1,2,8,9,10,11].

Furthermore, cold forming processes require a protection of the forging tools, in an attempt to control the severe wear developed on them during forging. This phenomenon can be minimized by using a particular management of surface finish and the deposition of hard coatings, characterized by low friction coefficients and high hardness. In this way, it is possible to greatly improve the process conditions and the forging tools life in many applications.

The request for strict dimensional tolerances and reduced coating thicknesses of cold work tool steels, makes the physical vapor deposition (PVD) technique suitable for this purpose [12,13]. Settings on the deposition technique and the number of coating layers can be useful in order to improve the coating performances. Moreover, the study of the best combinations between the steel substrate and coating may offers advantages.

In industrial practice, the results are not always based solely on the mechanical properties of the coating and such gaps between predictions and reality can be justified considering the fact that the forging tools are complex parts, mechanically and thermally stressed unevenly.

It follows that the coating selection requires a prior characterization about wear and corrosion, but also experimental tests that simulate as much as possible the working conditions of the tool.

In this work, starting from these assumptions, the surface morphology of different PVD hard coatings deposited on conventional and PM cold work tool steels samples were characterized by using a Field-Emission Gun Environmental Scanning Electron Microscope (FEG-ESEM, model QUANTA 250 FEI[®]) equipped with an Energy Dispersive X-ray Spectroscopy (EDS, EDAX[®]) system. The complex carbides composed by the main alloying elements, after heat treatment, were also investigated in term of type, chemical composition, size, morphology and distribution on the steel matrix.

2. EXPERIMENTAL PROCEDURE

The materials used in this work were a conventional (i.e. commercially named HPS) and a powder metallurgy (PM) HS 6-5-3C high-speed steel. Their corresponding chemical compositions are reported in Table 1.

Steel	Fe	C	Si	Mn	Cr	Mo	V	W
HPS	Bal.	1.00	1.00	0.40	7.00	1.40	2.00	0.80
HS 6-5-3C	Bal.	1.28	0.5	0.3	4.20	5.00	3.10	6.40

Tab. 1. Chemical composition of the steels examined in this study (wt. %).

Five cylindrical specimens (18 mm diameter and 4 mm thick) were drawn from the as-received hot rolled round bars and then heat-treated in a vacuum furnace with inert gas. The vacuum heat treatment cycle consisted of four stages (Fig. 2):

- preheating
- austenitizing
- quenching
- tempering

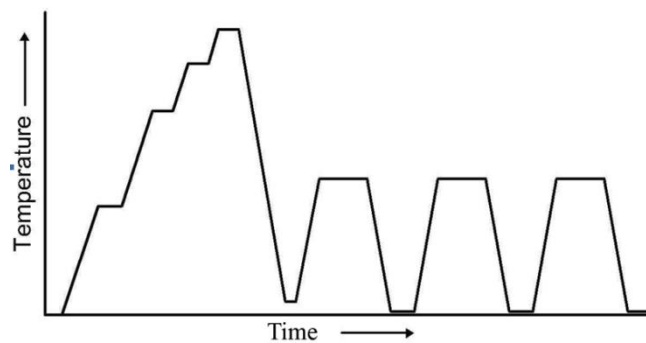


Fig. 2. A typical heat treatment cycle of tool steel.

The preheating stage involved a uniform heating of the samples through three preheat steps in order to guarantee the homogeneity of the core and surface temperatures.

The austenitizing procedure is the key factor of the entire heat-treatment cycle as it drives the grain size of austenitic phase and, consequently, controlled the toughness and the wear resistance of the materials. After the austenitizing, the specimens were rapidly quenched to achieve a desired martensitic microstructure and maximize the hardness.

After quenching, the specimens of both materials were subjected to repeated multi-tempering cycles to relieve the stress on the brittle martensite and reduce the amount of retained austenite (Table 2).

Steel	Temperature [°C]							
	Preheating			Austenitizing	Tempering			
I°	II°	III°	I°		II°	III°	IV°	
HPS	850	900	1050	1100	540	540	540	-
HS 6-5-3C	850	900	1050	1120	540	540	540	550

Tab. 2. Temperatures selected during heat treatment cycle.

After the heat treatment, the hardness of HPS alloy and HS steel grade increased up to 60 and 65 HRC, respectively.

Some specimens were then polished to mirror-like finish, cleaned in ethanol and coated by using Physical Vapour Deposition (PVD) techniques.

More specifically, different PVD deposition routes were used (Table 3):

- Sample A and B: single-layer TiN coating, deposited at 420 °C;
- Sample C and D: double-layer TiN/AlCrN coating, deposited at 450 °C;
- Sample E: duplex treatment, consisting of plasma nitriding and subsequent multi-layer TiAlCN coating, deposited at 550 °C.

For sample E, plasma nitriding and PVD coating were done inside the same chamber, by changing the processing parameters used for each of the diffusion and coating treatments steps. When duplex treatment was performed in a hybrid reactor, contact of the specimen's surface with air between the treatments was avoided and no cleaning or activating of the pre-nitrided surface was needed. Plasma nitriding was carried out in conditions where no white layer can be formed. After plasma nitriding, PVD coating was carried out, by depositing a thin multi-layer TiAlCN film. The resultant coating showed an high hardness (i.e. 2000-4000 HV), with good physical and mechanical properties such as a good wear and corrosion resistance, low friction coefficients and low thermal conductivity. Moreover, such surface treatment produced a hardness-gradient layer between the coating and substrate which improves the final wear resistance and induces a high resistance to compression tests. In fact the incremental hardness value of the inter-layer associated to its chemical modulation, increases the coating adhesion to the substrate and reduces the fracture risks of thin film under high concentrated compressive loads.

Sample	Steel	First layer	Second layer	Multi-layer film	Coating thickness [μm]
A	HPS	TiN	-	-	5
B	HS 6-5-3C	TiN	-	-	5
C	HPS	TiN	AlCrN	-	10
D	HS 6-5-3C	TiN	AlCrN	-	10
E	HS 6-5-3C	-	-	Ion nitriding + TiAlCN	3

Tab. 3. PVD coatings analyzed.

3. RESULTS AND DISCUSSION

3.1. Structural and chemical characterization of PVD coatings

The EDS line scans, showing the main alloying elements of the PVD coatings, are reported in Figs. 3-7. Fig. 3 and 4 exhibit the deposition of a TiN layer of about 10 μm, while Figs. 5 and 6 show the deposition of a first TiN layer on steel substrates and then a second AlCrN film. Fig. 7 displays the EDS spectrum of duplex multi-layer coating deposited onto PM HS 6-5-3C tool steel.

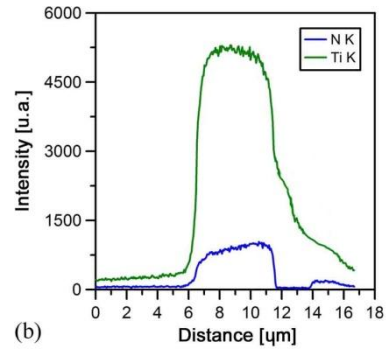
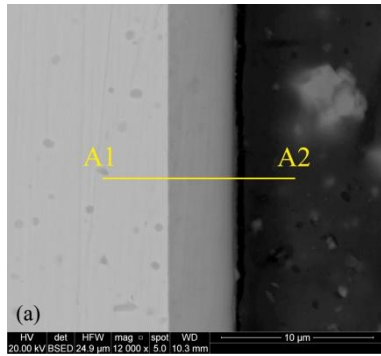


Fig. 3. a) SEM micrograph and b) EDS line scan on sample A.

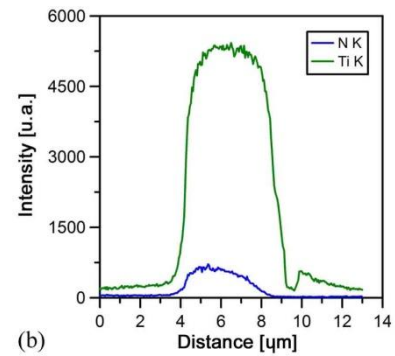
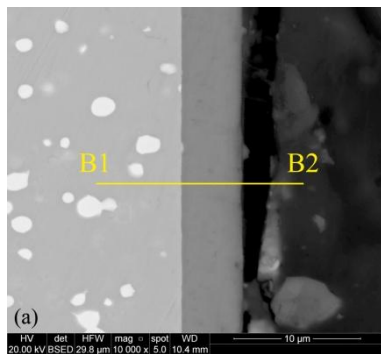


Fig. 4. a) SEM micrograph and b) EDS line scan on sample B.

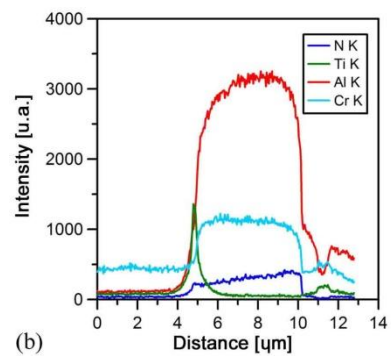
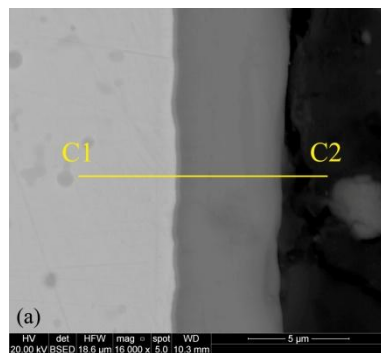


Fig. 5. a) SEM micrograph and b) EDS line scan on sample C.

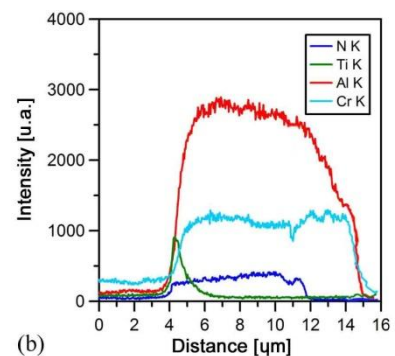
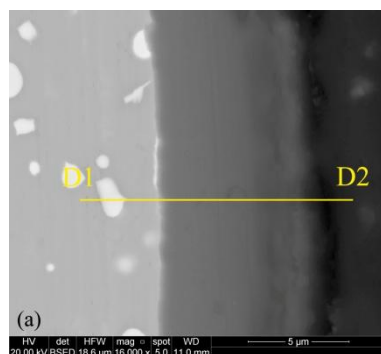


Fig. 6. a) SEM micrograph and b) EDS line scan on sample D.

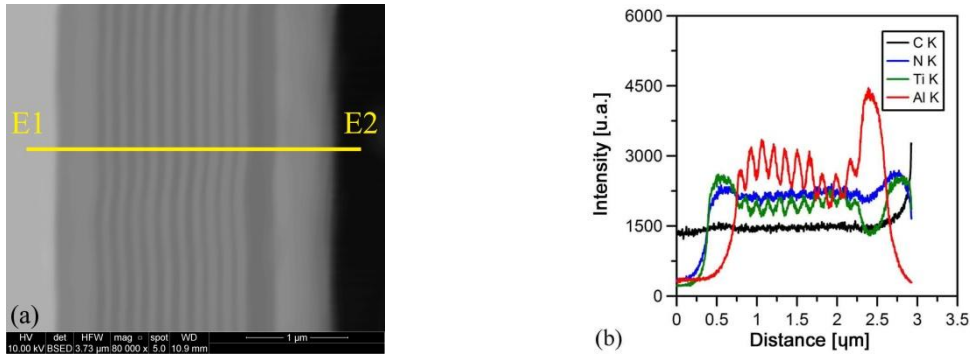


Fig. 7. a) SEM micrograph and b) EDS line scan on sample E.

3.2. Chemical characterization and morphology of carbides

The carbides morphology, identified in both tool steels after heat treatment, was analyzed by using a field-emission gun environmental scanning electron microscope equipped with an EDS system for chemistry analysis.

Starting from PM tool steel, it is well known from the literature that this kind of alloys contain primary carbides rich in V-W-Mo. These precipitates play a key role in the mechanical properties of these steels, increasing hardness, wear and heat resistance [14]. The powder consists predominantly of austenite, a small amount of martensite, as well as MC-carbides.

Typically M_6C -carbides (rich in W) and MC-carbides (rich in V) are also known, although is still unclear if the latter have actually VC stoichiometric composition [15].

Q.L. Yong et al. reported that VC-carbides are often detected in the form of V_8C_7 or V_6C_5 on PM tool steels [16]. Other researches by transmission electron microscopy (TEM) identified these precipitates as V-rich carbides (i.e. V_6C_5) [17].

Fig. 8a shows the typical microstructure of the heat-treated PM HS 6-5-3C tool steel (i.e. sample B, D and E). The white particles detected at the grain boundaries are W-Mo rich carbides (Fig. 8b) and, on the other hand, darker particles within the grain are V-W-Mo rich carbides (Fig. 8c). These precipitates are homogeneously distributed in the matrix.

Fig. 9 presents the EDS maps showing the presence of different types of carbides within the matrix. The presence of Mn-sulphides can be detected by both the EDS spectrum (Fig. 8d) and the EDS map (Fig. 9e), where the Mn-concentration in these particles is greater than the rest of the matrix.

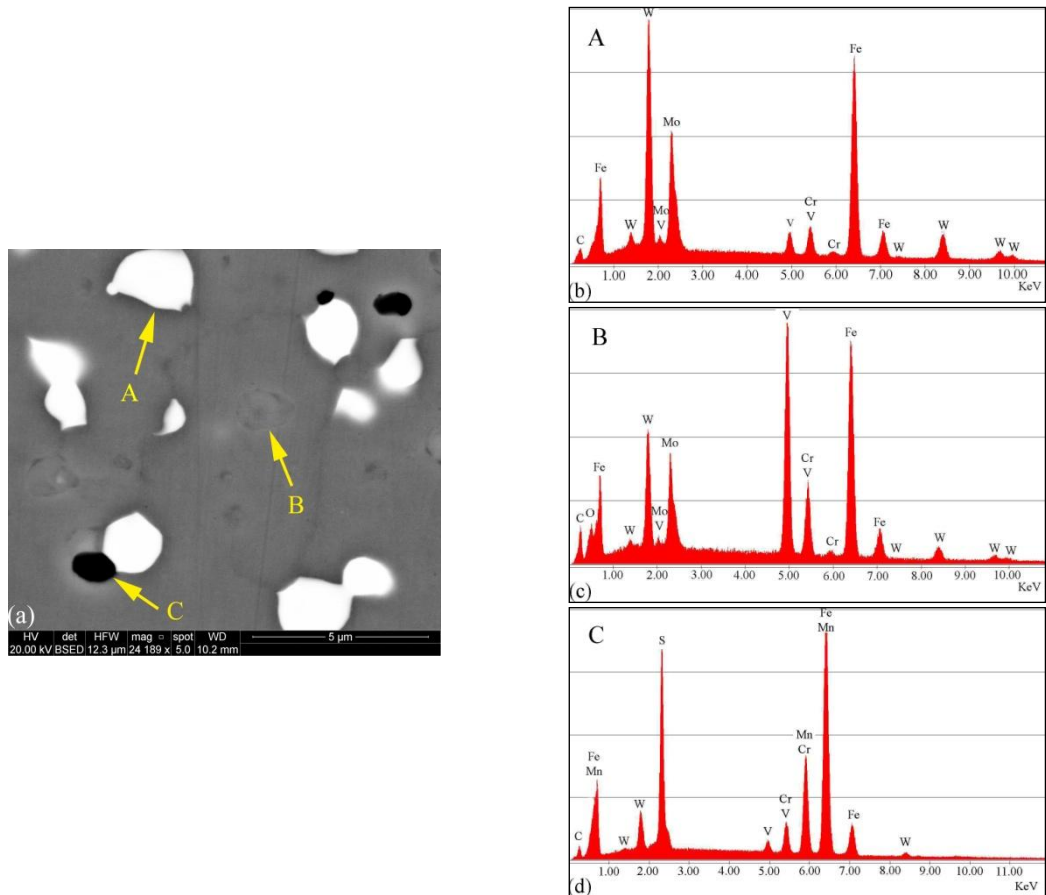


Fig. 8. a) SEM micrograph of carbides and EDS spectra of b) W-Mo rich, c) V-W-Mo rich carbides and d) Mn-sulphides.

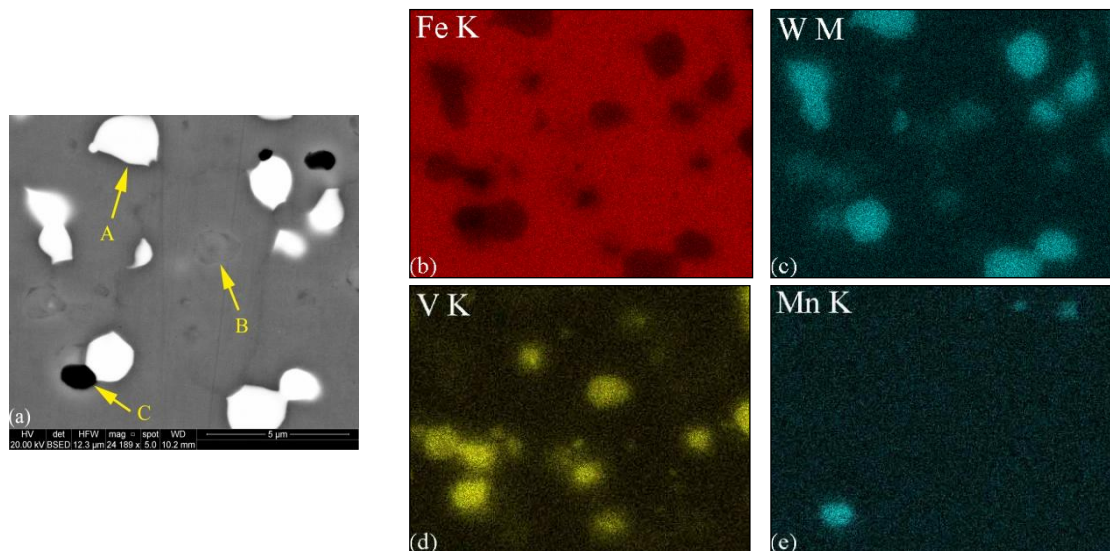


Fig. 9. a) SEM micrograph of carbides and b,c,d,e) EDS maps of the main alloying elements.

The conventional heat-treated HPS steel (i.e. samples A and C) contains several carbides forming elements, such as W, Mo, Cr, and V, which form coarse primary carbides during the solidification process [18-19]. Normally, three types of primary carbides M_6C , MC and M_2C occur during the solidification process [20]. Fig. 10a shows a SEM micrograph that

highlights the presence of carbides with uneven morphology and size, after heat treatment. The EDS spectrum of the darker particles (marked with "A") shows the presence of V-rich carbides (Fig. 10b). The clearer spheroidal shape particles (marked with "B") are identified as V-Cr rich carbides (Fig. 10c).

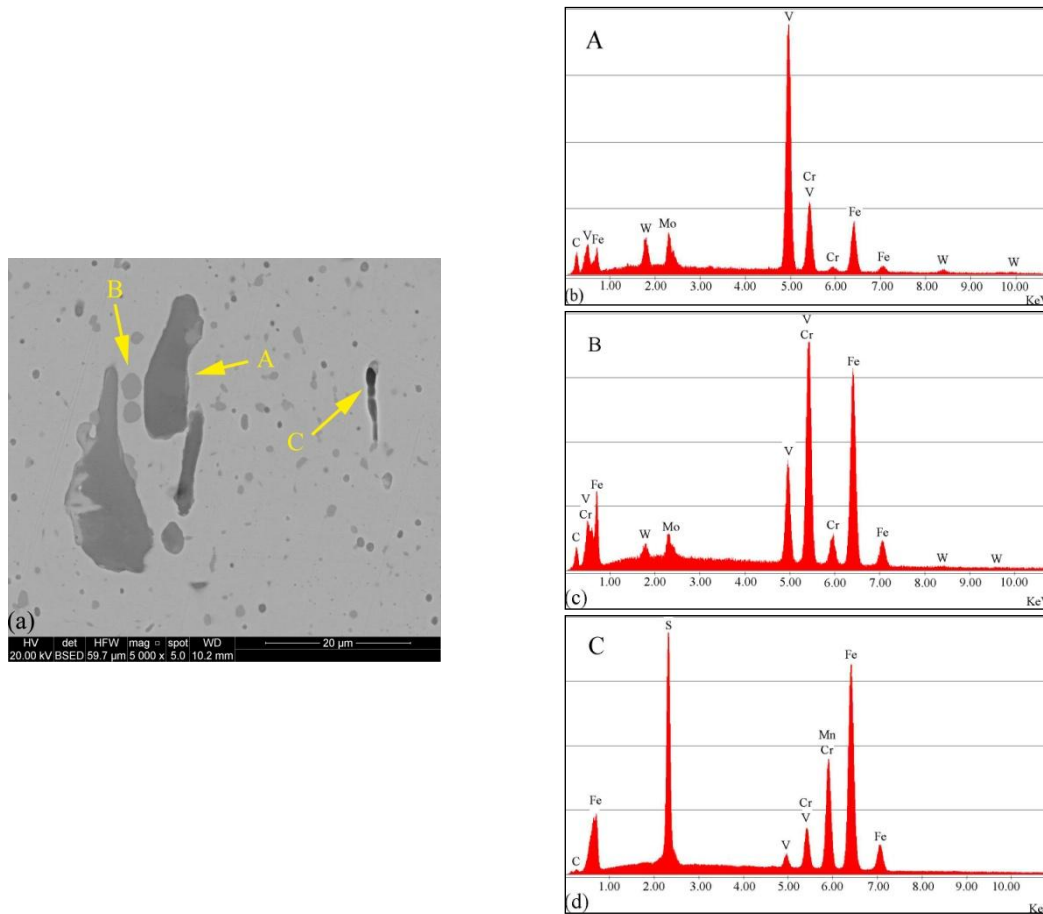


Fig. 10 a) SEM micrograph of carbides and EDS spectra of b) V-rich, c) V-Cr rich carbides and d) Mn-sulphides.

Fig. 11 reports the SEM micrograph of the heat-treated HPS alloy and the EDS maps of the main alloying elements. It can be noted the presence of Mn-sulphides as detected by the EDS spectrum in Fig. 10d and the EDS map in Fig. 11f.

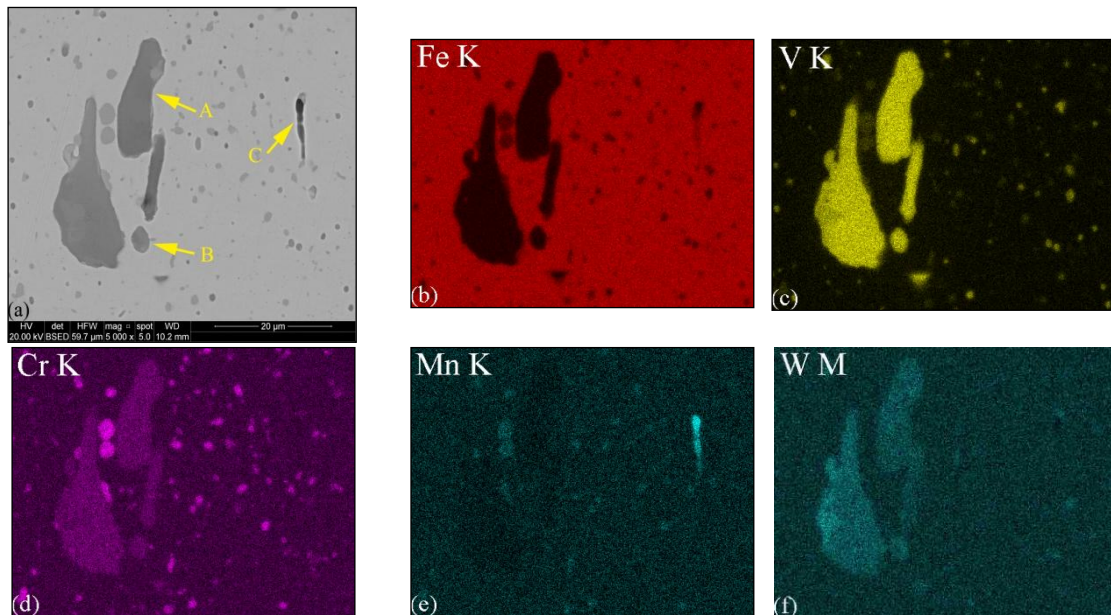


Fig. 11. a) SEM micrograph of carbides and b,c,d,e,f) EDS maps of the main alloying elements.

4. CONCLUSIONS

In the present study, the surface morphology, microstructure and element composition of different PVD deposited single- and multi-layer coatings, applied on conventional and powder metallurgy (PM) cold work tool steels, were investigated.

The characterizations were performed by using a Field-Emission Gun Environmental Scanning Electron Microscope (FEG-ESEM, model QUANTA 250 FEI[®]) equipped with an Energy Dispersive X-ray Spectroscopy (EDS, EDAX[®]) system.

Based on the results obtained, the following conclusions can be drawn:

- PVD single-layer, double-layer and duplex multi-layer coatings have a thickness of 5, 10 and 3 μm respectively. The combined coatings lead to higher surface microhardness (i.e. 3200 HV) as compared to the TiN coating (i.e. 2300 HV). This makes them more suitable to be used in cold forging processes.
- On samples B, D and E is highlight the presence of W-Mo and V-W-Mo rich carbides, and Mn-sulphides homogeneously distributed on the matrix. Meanwhile on samples A and C are detected V-rich and V-Cr rich carbides. Even in this case Mn-sulphides particles are revealed.

ACKNOWLEDGEMENTS

The authors would like to thank Zoppelletto S.p.A. and in particular Eng. L. Zoppelletto and P.I. P. Dal Maso for having supplied the material and for their availability in the realization of samples, heat-treated and coated by different PVD coatings.

REFERENCES

- [1] S. Gimenez, C. Zubizarreta, V. Trabadelo, I. Iturriza, *Materials Science and Engineering A*, vol. 480 (2008), p. 130.
- [2] V. Trabadelo, S. Gimenez, I. Iturriza, *Materials Science and Engineering A*, vol. 499, (2009), p. 360.
- [3] V. Trabadelo, S. Gimenez, I. Iturriza, *Journal of Material Processing Technology*, vol. 202, (2008), p. 521.
- [4] T. M. Torralba, J. M. Ruiz-Roman, L. E. G. Cambroner, J. M. Ruiz-Prieto, M. Gutierrez-Stampa, *Journal of Material Processing Technology*, vol. 64, (1997), p. 387.
- [5] Liu ZY, Loh NH, Khor KA, Tor SB. *Material Science and Engineering A*, vol. 293, (2000), p. 46.
- [6] O. Grindler, *Metal Powder Report*, vol. 62, (2007), p. 16.
- [7] Z. Y. Liu, N. H. Loh, K. A. Khor, S. B. Tor, *Materials Letters*, vol. 45, (2000), p. 32.
- [8] J. M. Ruiz-Roman, J. M. Torralba, L. E. G. Cambroner et al., *Advances in Powder Metallurgy and Particulate Materials*, MPIF, NJ, USA, Part 19, (1996), p. 97.
- [9] H. Takigawa, H. Manto, N. Kawai, K. Homma, *Powder Metallurgy*, vol. 24, (1981), p. 196.
- [10] P. Matteazzi, F. Wolf, *Materials Science and Engineering A*, vol. 248, (1998), p. 19.
- [11] G. Hoyle, *High Speed Steels*, Ed. Butterworths, Borough Green, Sevenoaks Kent, 1988.
- [12] F. Klocke, H.-W. Raedt, J. Grams, *Conference Proceedings 13th International Tribology Colloquium*, TAE, Esslingen, (2002), p. 1811.
- [13] E. Lugscheider, K. Bobzin, S. Bärwulf, S. Kienitz, F. Klocke, H.-W. Raedt, *Report and Conference Proceedings of the GfT-Conference*, Göttingen, Germany, (2000), p. 23/1-22.
- [14] M. Godec, B. Šetina Batič, D. Mandrino, A. Nagode, V. Leskovšek, S. D. Škapin, M. Jenko, *Materials Characterization*, vol. 61 (2010), p. 452.
- [15] Neumeyer TA, Kasak A. *Metallurgical and Materials Transactions B*, vol. 3, (1972), p. 2281.
- [16] Yong QL, Yan SG, Pei HZ, Tian JG, Yang WY. *Journal of Iron and Steel Research*, vol. 10, (1998), p. 63.
- [17] Yan F, Xu Z, Shi H, Fan J., *Materials Characterization*, vol. 59, (2009), p. 592.
- [18] Goiczewski J., Fischmeister H. F., *Steel Research*, vol. 63, (1992), p. 354.
- [19] Li Y.J., Jiang Q.C., Zhao Y.G., et al., *Scripta Materialia*, vol. 37, (1997), p. 173.
- [20] Pan F.S., Wang W., Tang A., Wu L., Liu T., Cheng R., *Progress in Natural Science: Materials International*, vol. 21, (2011), p. 180.

ARTICLE II

PREDICTION OF DEFECTS IN MULTI-STAGE COLD FORGING BY USING FINITE ELEMENT METHOD

F. Bassan, P. Ferro, F. Bonollo*

**University of Padua, Department of Management and Engineering,
Stradella S. Nicola, 3 I-36100 Vicenza, Italy*

Published in "Key Engineering Materials", 2014, vols. 622-623, pp. 659-663.

ABSTRACT

In this work, the formation mechanisms of surface defects in multi-stage cold forging of axisymmetrical parts have been studied through FEM simulations. As case history, the industrial production of an heating pipe fitting by cold forging has been analyzed. Based on simulated flow behaviour of material, several types of surface defects are identified and attributed to plastic instability of the work-material, inappropriate axial/radial flow ratio, excessive forming-pressure and uncorrect tooling design. The results of the FE model are finally compared with those obtained from real forging process and good agreement is observed.

KEYWORDS

Finite element method, Defects prediction, Multi-stage cold forging, Heating pipe fitting.

1. INTRODUCTION

In the last few decades, near-net-shape or net-shape manufacturing is becoming a useful practice in metal forming, resulting in saving material and energy. Cold forging, one of the net-shape manufacturing processes, is governed by many factors such as friction, geometry of the part, tooling design, and temperature setting of the tools and workpieces [1]. Hence, this process has a high tendency to form defects and thus it is essential to detect and prevent them during the production process.

In the past, defects related to metal flow imperfections have attracted the attention of many researchers. Arentoft and Wanheim paid attention to this issue and summarized the different defects in forging processes. A defect-matrix was then proposed to provide design reference for engineers [1]. Giuliano studied the compound cold extrusion process to avoid the flow-induced defects [2]. Lu and Zhang found that forging defects are caused by improper die dimension [3]. Song and Im studied the effect of process design parameters to the formation of under-filling and folding defects during closed-die forging of bevel-gears [4]. In another study, Qamar investigated the effect of shape complexity and dead metal zone to the quality of cold extruded part [5]. Although many researches have carried out studies about defect formation in cold forging processes, there is still lack of extensive research on defects formation in multi-step forming of axisymmetrical components. This work is aimed to support the research in this field by analyzing an industrial multi-stage cold forging process of an heating pipe fitting, having floating dies, by using a rigid-plastic FEM model. Based on the simulated material flow behavior, the defects formation mechanisms are revealed through each forging-stage and a good agreement between FE analysis and real forged components is observed.

2. FINITE ELEMENT SIMULATION OF MULTI-STAGE COLD FORGING PROCESS

2.1. Process description

Fig. 1 shows the sequence of the analyzed three-step axisymmetric cold forging process (preforming, calibration and double deep backward extrusion). A 6300 kN (~642 ton) multiple-station mechanical knuckle-joint press with 21 spm and automatic workpiece transfer between stations is used. Bottom punches are fixed during the forming cycle and act as workpiece ejectors at the end of it. Top punches and dies are driven by press cinematism; moreover top dies in each forming stage and bottom dies in the first and third operation are floating tools. They are connected with an hydraulic circuit and driven by the contact stresses exerted on their interface between the dies and the material during the forging process.

The initial cylindrical billet, lubricated with zinc phosphate/stearate coating, is compressed into a preform in the first forging-step and calibrated in the second one. With these two operations, an axisymmetric T-shape part is obtained, which is similar to the final shape of the component. Finally, in the third stage, the lower and upper part of the workpiece is backward extruded.

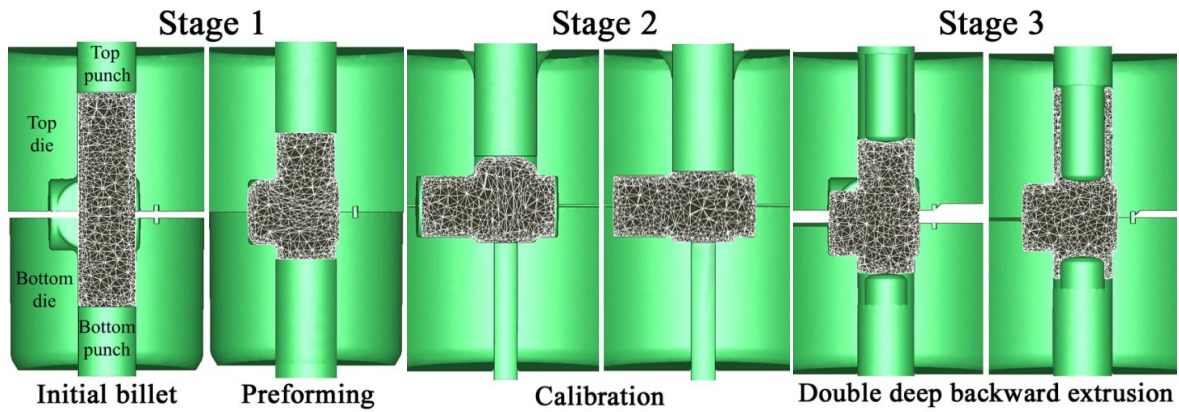


Fig. 1. Multi-stage forging of heating pipe fitting.

As can be seen from the load-stroke curves (Fig. 2a), in stage 1 the top punch load increases rapidly after the top and bottom dies end their strokes and reaches its maximum value at the end of the forging process. In the third operation, a large deformation also occurs in the workpiece near to the walls of the punches and dies. As shown in Fig. 2c, the load applied to the dies increases steadily as the top punch moves forward; by approaching the end of the forging operation, this load becomes almost constant, as expected. On the other hand, the maximum loads on tools are reached during the second operation (calibration).

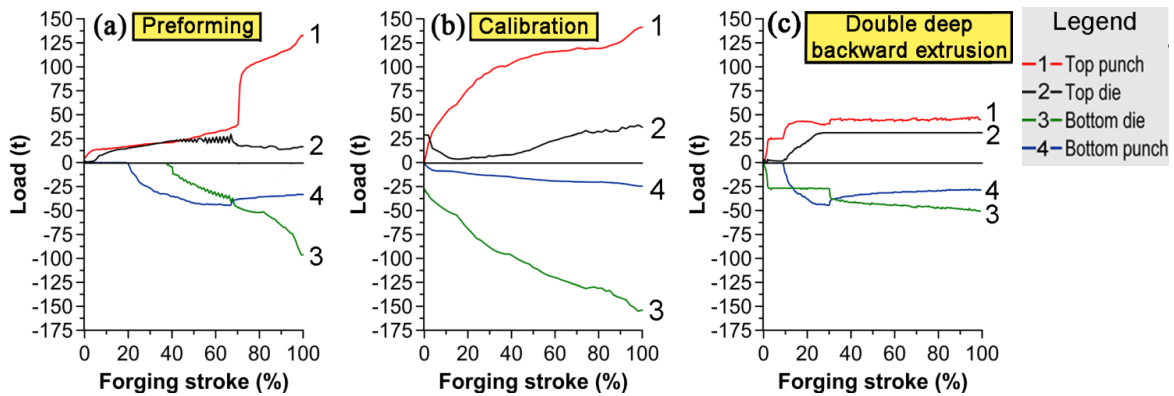


Fig. 2. Load-stroke relationships for the three-operation process.

2.2. Numerical model

A 3D rigid-plastic FEM model is considered more suitable for this process, due to its major computational efficiency compared to the others numerical methods. The initial billet is modeled with 25958 tetrahedral elements. Remeshing is automatically calculated when element distortion becomes excessive and the volume compensation is considered during the forming process. The material used for the billet is a steel, whose chemical composition is listed in Table 1.

C	Si	Mn	Cr	Cu	Others	Fe
0.05	0.07	0.30	0.06	0.08	<0.03	bal.

Tab. 1. Chemical composition of the SAE 1005 alloy used in the present work (wt.%).

The initial temperature of the billet and tools is 20 °C and tools are considered as rigid bodies. It is well known that friction conditions prevailing at the tool-workpiece interface have a deep effect on material deformation, forming load, surface finish, internal structure of the component, as well as die wear characteristics in metal forming processes. In order to accurately predict metal flow, in this work the forging process-sequence is assumed to have a Coulomb friction law with a friction coefficient (μ) equal to 0.2 and a shear friction coefficient (m) equal to 0.4.

3. RESULTS AND DISCUSSION

3.1. Underfilling defects formation

During the preforming stage, the billet deforms asymmetrically and underfilling occurs (Fig. 3). This defect is attributed to the small radii at the die corners and insufficient forming-pressure at the final stage of the forming operation. As a matter of fact, by approaching to the end of forging stroke, the friction resistance of the die surfaces to the material flow is almost fully established; a further material deformation, to enable dies-filling, would be very difficult. Fig. 3 represents the reduction of the underfilling blue areas at the die corners from stage 1 to 3 and a good agreement between numerical and experimental results is observed.

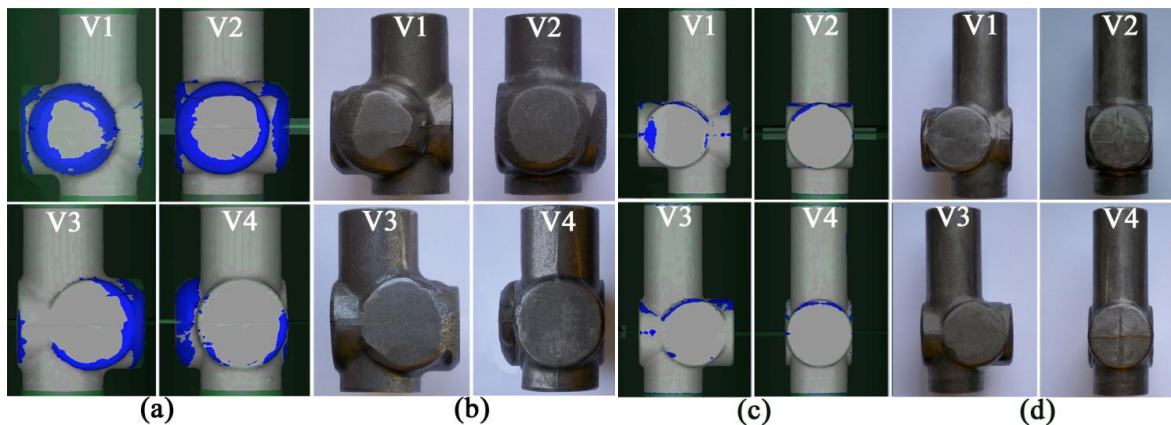


Fig. 3. Comparison between (a,c) analytical and (b,d) experimental evaluation of underfilling on stage 1 and 3 at final forging stroke. All front views are reported (V1-V2-V3-V4).

3.2. Surface defects evaluation

Stage 1

In order to investigate the beginning of defect formation mechanisms in stage 1, effective strain and strain rate maps are plotted in Fig. 4 and 5 at two instants of the forming process. The metal flow velocity fields are represented by colors and line segments with arrows; colors stand for flow velocity and arrows direction depicts the direction of metal flow. At 89% forging stroke, when top and bottom dies end their stroke and only the top punch moves downwards compressing the billet, the surface area marked with A in Fig. 4, experiences high effective strain (~ 2.34) and different directions of strain rate vectors, reaching a flow velocity of 170 mm/s. This area can be thus considered a critical zone for

the formation of surface micro-pockets. As a matter of fact, those defects are observed in that zone of the real forged part as shown in Fig. 4c.

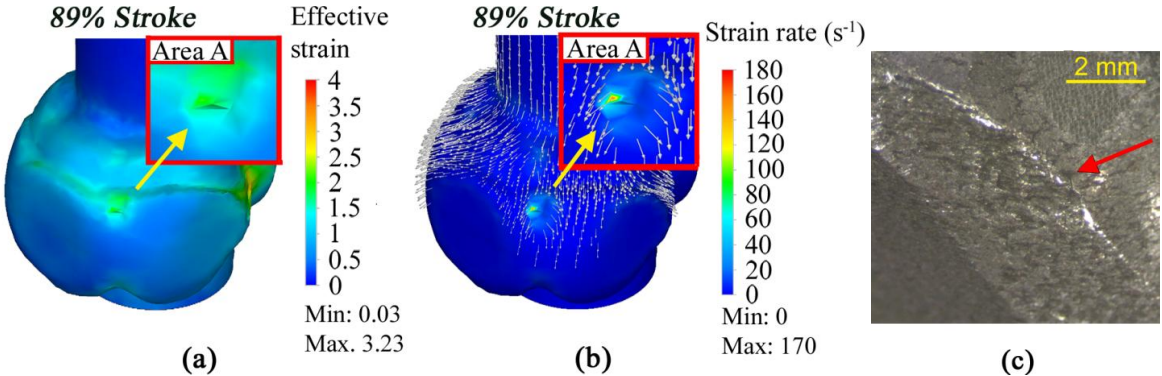


Fig. 4. a) Plastic strain and b) strain rate plots (with superimposed nodal velocity vectors) at 89% forging stroke. c) Stereo micrograph of the analyzed area.

At 92% forging stroke, the asymmetrical deformation of the billet appears to create a "dead zone" in the material. The FE model shows that the onset of the fold is a consequence of the material expansion, which flows onto that dead zone. The velocity vectors plotted confirm that the folding defect is the result of two sliding material flows which occurred from 92% to 100% forging stroke (Fig. 5a). The SEM micrograph on the real part confirms the presence of that defect on the investigated region (Fig. 5b).

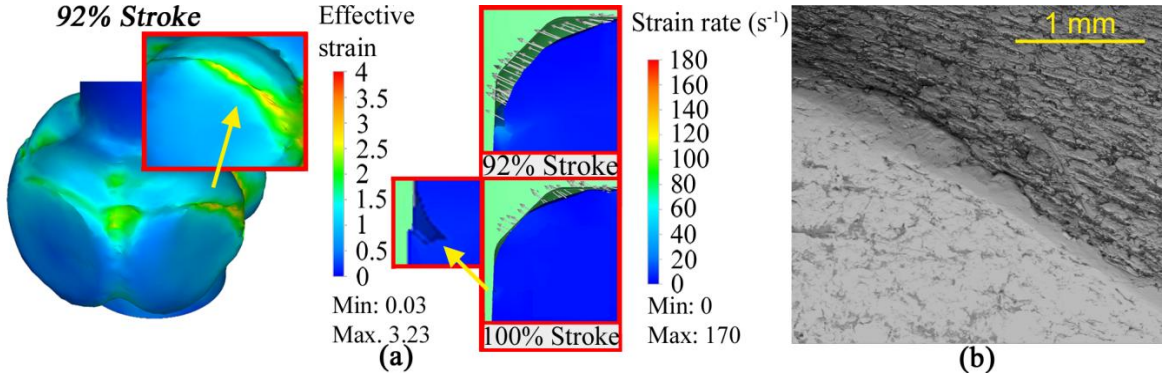


Fig. 5. a) Plastic strain and superimposed nodal velocity plot showing the mechanism of defect formation; b) SEM micrograph of the fold revealed on the investigated zone.

Stage 2

At the end of stage 1, the top punch and die are moved upwards allowing the workpiece to establish the equilibrium of residual stresses induced by the first plastic deformation. Fig. 6a shows that the location of the maximum effective strain areas at the beginning of deformation on stage 2, coincides with those revealed at the previous stage. At 100% forging stroke, due to an excessive top punch stroke and a non-optimized design of top die geometry with an unnecessary chamfer angle, a great amount of material flows to fill the area between the top punch and die (Fig. 6b). The photograph of the real part produced after the calibration operation validates the FE results obtained (Fig. 6c).

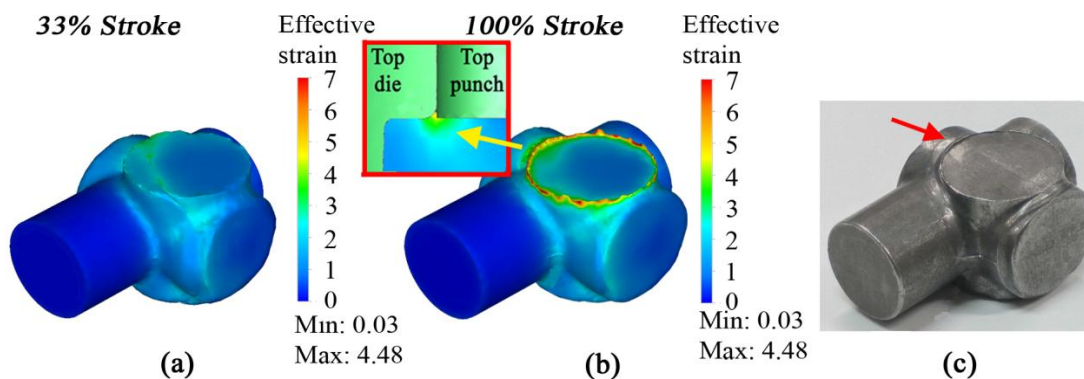


Fig. 6. Mechanism of defects formation on second stage at different forging times with plastic strain and reported a) Stroke 33% and b) Stroke 100%. c) Photograph of real part showing circular fold.

Stage 3

As mentioned above, the surface defects formed during the previous forming stages are reported on stage 3, as revealed by high plastic strain values obtained by FE analysis (Fig. 7a) and confirmed by the photograph of the final product (Fig. 7c). At 11% forging stroke, when the top punch starts the backward extrusion operation and bottom die has just ended its stroke, the top die comes into contact with the material developing a circular fold as shown in Fig. 7a. In Fig. 7 the presence of this defect is individuated by high values of effective strain revealed from the beginning (i.e. 11% forging stroke) to the end of its formation (i.e. 100% forming stroke). Photograph of the final forged part confirms the presence of that folding defect, as underlined by ellipse in Fig. 7c.

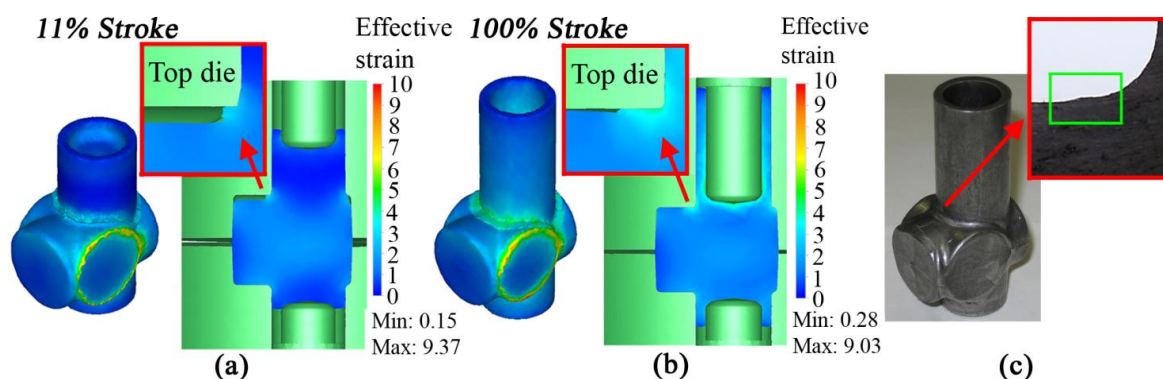


Fig. 7. Formation mechanism of circular folding defect on third forging stage, from (a) the beginning to (b) the end. (c) Photograph of final forged part with defect underlined.

3.3. Defect-Matrix of multi-stage cold forging process

In order to summarize the results obtained, Table 2 is proposed which links the forging defects previously analyzed, investigated through FEM analysis and experimental observation on each single-stage forged part, to the evaluated conditions which can cause them.

Legend		Possible causes						
		Tools			Process parameters			
		Geometry			Geometrical		Flow related	
Stage 1: S1		Too small fillet radius	Inconvenient and insufficient geometry	Too small die angle	Too long punch stroke	Too high strain rate	Inconvenient material flow	Inhomogeneous deformation
Stage 2: S2								
Stage 3: S3								
effects	Folds	S3					S3	
	Surface def.	Pockets				S1	S1	S1
		Small ext. defects		S2		S2		
Form def.	Incomplete filling	S1		S1				

Tab. 2. A part of Defect-Matrix, linking classification of defects in forging to the possible causes of them, in accordance to Ref. [2].

4. CONCLUSIONS

In this work, a 3D rigid-plastic FE model of an industrial multistage cold forging process for the production of an heating pipe fitting has been carried out by using Forge[®] numerical code. A systematic approach to predict surface defects, based on numerical simulation, has been proposed which shows good agreement between numerical and experimental observations. The approach adopted is considered useful for calibrating multistage forging process applied to different material categories with different operation sequences, in order to produce defect-free parts. The simulation-enabled approach shifts the design paradigm from experience-based try-and-error to scientific-based calculation and analysis, reducing the time required to set up new forging cycles at about 40%.

REFERENCES

- [1] J.H. Lee, B.S. Kang, J.H. Lee, J. Mater. Process. Technol. 58 (1996) 174-183.
- [2] M. Arentoft, T. Wanheim, J. Mater. Process. Technol. 69 (1997) 227-232.
- [3] G. Giuliano, Mater. Des. 28 (2007) 726-729.
- [4] C. Lu, L.W. Zhang, Trans. Nonferr. Met. Soc. China 16 (2006) 1386-1390.
- [5] J.H. Song, Y.T. Im, J. Mater. Process. Technol. 192-193 (2007) 1-7.
- [6] S.Z. Qamar, Mater. Manuf. Process. 25 (2010) 1454-1461.

ARTICLE III

SIMULATING MULTI-STAGE COLD FORGING TO REDUCE TIME-TO-MARKET AND PRODUCTION COSTS

F. Bassan*, L. Zoppelletto**, M. Gabrielli***

**University of Padua, Department of Management and Engineering,
Stradella S. Nicola, 3 I-36100 Vicenza, Italy*

***Zoppelletto S.p.A., Via Camisana, 278 I-36040 Torri di Quartesolo (Vicenza), Italy*

****Enginsoft S.p.A., Via della Stazione, 27 I-38123 Trento, Italy*

Published in "Forging", September/October, 2014, pp. 18-22.

ABSTRACT

Cold forging process design presents a process layout problem. Due to the variety of working procedures and the complexity of the workpiece, it is very difficult to design a cold forging process without the designer's knowledge and experience. The case study presented here involves finite-element analysis of a multi-stage cold forging process for a heat pipe fitting made by Zoppelletto S.p.A., an Italian company operating in the cold forged components market for more than 50 years. Cold forging is the company's core business and in the past 30 years Zoppelletto has evolved from a craft manufacturer into an advanced industrial enterprise, able to produce millions of specialty components and guaranteeing timely production for delivery.

Production focuses on five principal sectors: thermo hydraulic, oil-pressure hydraulic, automotive, office furniture, and hardware for bolts, hinges, etc. Zoppelletto's technical department has at its disposal the latest CAD-CAM capabilities for manufacturing production equipment and forging tools, engineered and produced in-house. For mass production of small or medium-sized components, multi-station automatic cold forging presses are used. In cold forging, initial materials are formed progressively to final shapes by automatic and synchronized operations, including shearing, upsetting, forward and/or backward extrusion and piercing. The development of forging simulation software presented the challenge of how best to introduce its use into forging companies. Its effective introduction has required advances in the user-friendliness of the simulation software and its application to a wide range of problems.

KEYWORDS

Finite element method, Process description, Multi-stage cold forging, Heating pipe fitting.

1. PLANNING A PRODUCTION PROCESS

Because the choice of a process plan affects the design, manufacture, and maintenance of the dies, cold forging research emphasizes improvement of process planning. The design of a multi-stage forging process sequence involves determining the number of preforms along with their shapes and dimensions. The best designs for preforming operations can be identified by their ability to achieve adequate material distribution; this is one of the most important aspects in the cold forging processes. Traditionally, forging-sequence design is carried out using mainly empirical guidelines, experience, and trial-and-error, which results in a long process development time, and high production costs. Using computer-aided simulation techniques in metal forming before physical tests may reduce the cost and time of the process design. Many computer-aided approaches based on approximate analysis and empirically established design rules have been published. These techniques do not always provide detailed information concerning the mechanics of the process. However, the finite element method has been shown to provide more accurate and detailed information, and thus has been widely adopted for simulating and analyzing various metalforming processes. Finite-element analysis (FEA) has become one of the most widely used engineering tools and has been adopted in practically all fields of industry due to advances in both software capabilities and the availability of more powerful computers. In addition, since FEA can simultaneously predict all the necessary stress-strain states in both die and workpiece, extensive applications of this method have been reported for large-scale deformation forging processes. Many researchers have focused on the effective strain, damage and flow patterns within the workpiece during cold forging processes. However, up to now, work on the process planning of cold forging has concentrated on rotationally symmetric parts. Work on non-axisymmetric parts has not been so actively pursued, due to difficulties of shape cognition and expression, calculations of the process variables such as forming load, effective strain, effective stress, and so on. In this study, numerical simulations were carried out for the design of a cold-forged heat pipe fitting used in thermo-hydraulic applications. The simulation was performed using the Transvalor FORGE2011[®]-3D software. A forging experiment of the heat pipe fitting also was carried out using the designed tool set. From a comparison of the results between the simulation and the experiment, it was found that the simulation showed good agreement with the experimental result.

2. PROCESS DESCRIPTION AND MODELLING

Fig. 1 shows the sequence of the analyzed multi-stage, non-axisymmetric cold forging process. The cold forging process-sequence to form the heat pipe fitting consists of four operations: preforming, first and second calibration, and double deep backward extrusion.

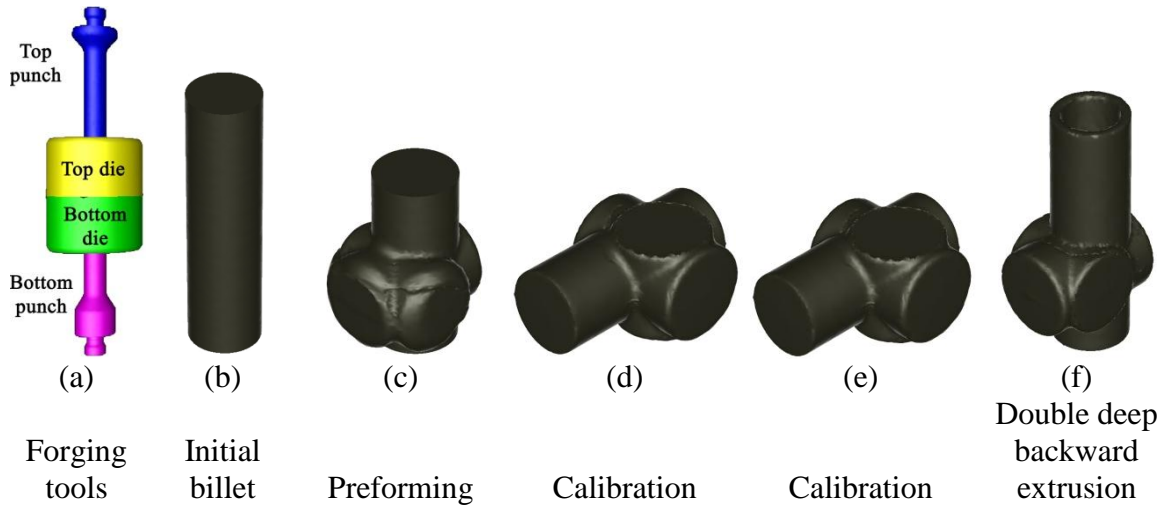


Fig. 1. a) Forging tools used and b-c-d-e-f) sequence of the four-stage cold forging process of heating pipe fitting

A 6300 kN, multi-station general-purpose mechanical knuckle press and automatic workpiece transfer between stations is used. The cooling time for the workpiece was 2.86 sec., which for each stage was calculated from the end of one forging operation to the beginning of the next one. The top dies in each forming stage and the bottom dies in the first and third operation are floating, and driven by the contact forces exerted during the forging process. Bottom punches are fixed during the forging process and act as workpiece extractors. The material used for the workpiece is a low-carbon alloy steel, whose chemical composition is listed in Table 1. Tools are assumed to be rigid with an infinite elasticity modulus and a constant temperature of 20 °C. The heat-transfer coefficient is taken as 20 kW/m². The die-workpiece interface is characterized by the constant factor friction law usually used for bulk metal-forming problems, $\tau = mk$. Here, τ is the frictional shear stress, m is the friction factor, and k is the shear flow stress. The shear friction coefficient (m) was set to 0.4.

C	Si	Mn	Cr	Cu	Others	Fe
0.05	0.07	0.30	0.06	0.08	<0.03	bal.

Tab. 1. Chemical composition of C4C alloy used (wt.%).

3. PROCESS SEQUENCE OPTIMIZATION

The main objective of the process sequence design in this study is to obtain intermediate preforms that will produce a near-net-shape product. Also, design constraints, such as the limit of the press capacity and the avoidance of surface defects, should be satisfied. As can be seen in the load-forming time relationship (Fig. 2a), the top punch load is almost constant at the beginning of the operation. However, immediately after the top die touches the bottom die, the punch load suddenly increases and reaches its maximum value at the end of the process. The maximum load in this process is 133 metric tons, which is less than the limit of the available press capacity of 642 metric tons. In the fourth operation, shown in Fig. 2d, a large deformation also occurs in the workpiece near to the walls of the punches and dies. From the load-forming time relationship (Fig. 2d), it is noted that the load applied to the dies increases steadily as the top punch moves forward. As expected,

approaching the end of the operation this load becomes almost constant. In this stage, the maximum punch load is estimated to be 50 metric tons, which can be identified as the minimum value of the current four-stage process. On the other hand, the maximum load on the top punch and the bottom die during the second calibration is 142 and 155 metric tons, respectively (Fig. 2b). During the third stage (the second calibration operation) the top punch doesn't contact the workpiece, and therefore the maximum load revealed is zero (Fig. 2c). Moreover, due to the lower forging loads reached by the other tools in this third forging stage, the elimination of this operation is suggested. This gives a shorter development lead time, lower cost production, savings in tool material costs, and the development of a higher precision part.

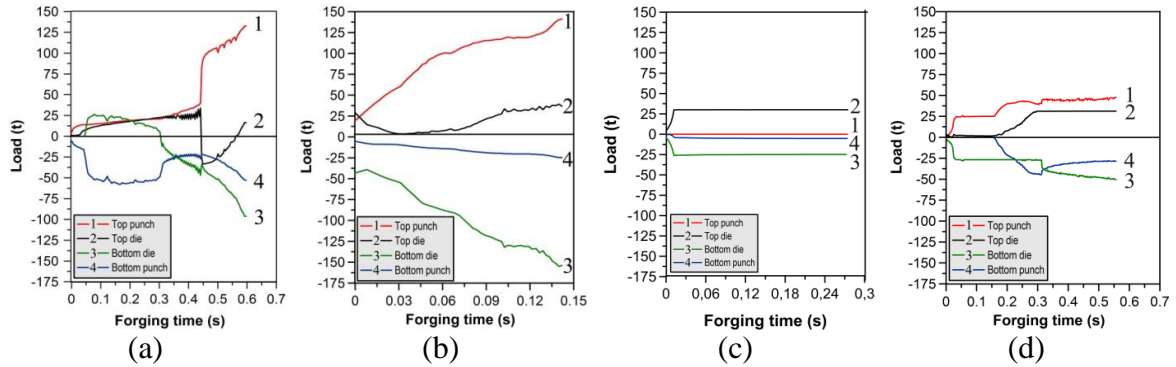


Fig. 2. Load - forging time curves of tools for the four-operation process: a) preforming; b) first and c) second calibration; d) double deep backward extrusion.

4. DEFECTS EVALUATION

During the preforming operation, the billet deforms asymmetrically and underfilling occurs. Underfilling problems are limited by the use of multiple forming stages. Fig. 3 shows the reduction of the underfilling areas (in blue) at the die corners obtained by the FE analysis, which is consistent with the experimental observation.

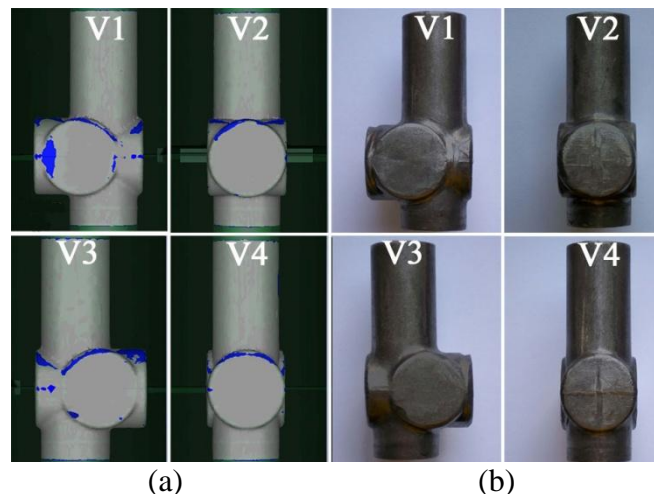


Fig. 3. Comparison between (a) analytical and (b) experimental evaluation of underfilling on stage 4 at final forming stroke. All front views are reported.

By using FEM simulation, it was found that defects occur in each stage of the forming sequence. The numerical results coming from each forging stage are validated by means of experimental observations. In particular, during the second-stage operation (calibration), a great amount of material flows to fill the area between the top punch and die, due to an excessive top punch stroke (Fig. 4).

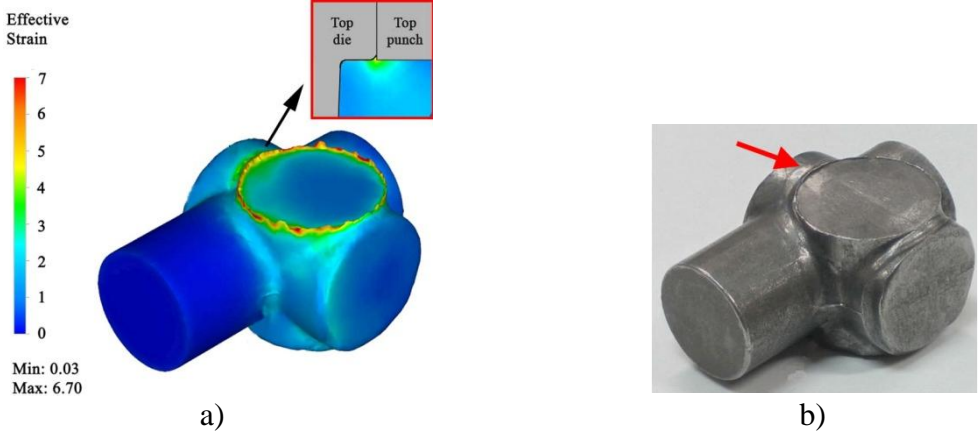


Fig. 4. Defects evaluation on stage 2 at the end of the forging stroke with (a) simulated FE model of the workpiece and (b) photograph of real part.

5. BENEFITS OF FE METHOD

In the “forming” process chain, the simulation of the forming process offers substantial opportunities for improvement: for example optimizing the component and tools may provide opportunities to enhance process reliability. The numerical simulation carried out by using Transvalor Forge software could be extended in various directions in order to accommodate such new requirements. In metal forming, as mentioned above, process simulation is used to predict metal flow, strain, temperature distribution, stresses, tool forces, and potential sources of defects and failures. In some cases, it is even possible to predict product microstructure and properties as well as elastic recovery and residual stresses. The main reasons for simulation are reducing time-to-market, reducing tool development costs, predicting the influence of process parameters, reducing production cost, increasing product quality, improving the understanding of material behavior, and reducing material waste. These things are achieved by accurately predicting the material flow, determining the filling of the die, accurately assessing net shape, predicting if folds or other defects exist, determining the stresses, temperatures, and residual stresses in the workpiece, and determining the optimal shape of the preform. Also, as simulation allows us to capture behavior that cannot be readily measured, it provides deeper insights into the manufacturing process. There are several principal steps involved in integrated product and process design for metal forming. The geometry (shape, size, surface finishes, and tolerances) and the material are selected for a part depending on the functional requirements. The design activity represents only a small proportion (5 to 15 percent) of the total production costs of a part. However, decisions made at the design stage determine the overall manufacturing, maintenance and support costs associated with the specific product. Once the part is designed for a specific process, the steps outlined in Table 2, lead to a rational process design.

Applying the FE method in this complex cold forging process of a heat pipe fitting involves:

- The conversion of the assembly-ready part geometry into a formable geometry;
- The preliminary design of tools/dies necessary to perform the operations used for forming the parts;
- The analysis and optimization of each forming operation and associated tool design, to reduce process development time and trial-and-error;
- Manufacturing of tools and dies by CNC milling, or by EDM or another similar technology.

Ascertaining process-specific factors in production engineering by means of process simulation promotes efficient manufacturing of products of specified properties. Three objectives are emphasized:

- Review of the feasibility of an existing concept for manufacturing of a product;
- Assessment of product characteristic;
- Enhanced understanding as to what really occurs in a process, for the purpose of optimizing the manufacturing technique. To achieve these goals, however, it only makes sense to use process simulation if this is more economical in the long run than experimental repetition of the actual process. Focusing on a new product development chain of a company's multi-stage cold-forged component (Table 2), the actual time-to-market revealed is more than four months. Moreover, due to the company's costly trial-and-error method, this time-to-market can increase exponentially (see red lines arrows on Table 2).

	Operation time [man-hours]
1) Project planning and analysis	80
↓	
2) CAD design of tools	120
↓	
3) Evaluation of uncertain parameters	240
↓	
4) Trial tools production	800
↓	
5) Real trial-and-error on press machine	40
↓	
6) Final set-up on press machine	8
↓	
7) Production	8

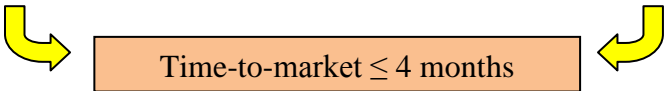
Tab. 2. New product development of a multistage cold forged component using traditional method (five-stage forging process).

Using the FE method, the company’s estimated time-to-market expected is less than four months (Table 3). In this case the traditional time-consuming and costly trial-and-error method has been replaced with a simulation-based approach using Transvalor FORGE2011®-3D, which now can address the whole manufacturing process.

The two approaches may seem similar if we look at the use of CAD/CAE design of tools instead of real trial-and-error on the press machine, but it’s important to highlight that normally this trial-and-error step is the most time- and cost-consuming part of the traditional method of designing a new component. The number of “red” iterations needed to arrive at a good process can be very high if unexpected problems occur, and this can have a great impact on the total time-to-market. As more simulation skill is developed in the organization, the difference between the traditional approach and the FEM approach increases. This looks not only at man hours, but also more deeply at other aspects of the cost of a new component.

Completely removing the trial-and-error iterations saves the costs of trial tool production, so the time to recover the entire software and training investment decreases dramatically to some months (less than one year), depending on how widely this approach is adopted. Moreover, it is important to notice that one hours’ loss of production, due to a traditional time-consuming trial-and-error step, costs about €180.00-230.00 (est. \$230.00-\$290.00). For this reason, Zoppelletto S.p.A. has decided to break with the traditional method of new product development and has committed to using Transvalor FORGE2011®-3D software to support its development process.

	Operation time [man-hours]
1) Project planning and analysis ↓	80
2) CAD design of tools ↓	160
3) Evaluation of uncertain parameters ↓	240
4) Tools production ↓	800
5) Final set-up on press machine ↓	8
6) Production	8



Time-to-market ≤ 4 months

Tab. 3. New product development of a multistage cold forged component using finite element method (five-stage forging process).

6. CONCLUSIONS

Using finite-element methods as tools results in cost reduction, time savings, and improvements in product quality for Zoppelletto S.p.A.. The design of the deformation sequence and forging tools can be modeled before, and also during, production. This allows the engineer to identify process deficiencies easily, leading to cost and time savings. Such modeling efforts can be very valuable in identifying inhomogeneous deformations, such as folds that could not easily be detected through regular visual inspection. Moreover, based on industrial experience, this approach is estimated to reduce the time required to set up new forging cycles by about 40%.

ACKNOWLEDGEMENTS

The author expresses his gratitude to Zoppelletto S.p.A., in particular to Eng. Luca Zoppelletto, for providing information about the multi-stage cold forging process used to support this analysis. Thanks are extended as well to Eng. Marcello Gabrielli, EnginSoft S.p.A., for his interest in the work and helpful discussions, advice, and suggestions.

ARTICLE IV

NUMERICAL PROCESS SIMULATION AND MICROSTRUCTURAL EVOLUTION OF CARBON AND STAINLESS STEEL FORGED COMPONENTS

F. Bassan, P. Ferro, F. Bonollo*

**University of Padua, Department of Management and Engineering,
Stradella S. Nicola, 3 I-36100 Vicenza, Italy*

Accepted for publication in "La Metallurgia Italiana", 2015.

ABSTRACT

The environment concerning the recent forging industry has been changed rapidly. Decreasing experienced designer and declining the technical quality of process designer have been important issue recently. Moreover, the customer's needs have been more difficult to be satisfied with. Making higher quality product within shorter development time and lower cost is the lowest level that must be cleared. The designers should be in correspondence with such needs by considering new materials and advanced processes as soon as possible. The importance of Computer Aided Engineering (CAE) in the forging process design has been raised remarkably to overcome the difficulties in the recent design environment.

In this work, a 3D rigid-plastic FE model of an industrial single-stage cold forging process for the production of a low-carbon component has been carried out by using FORGE2011[®] numerical code. The approach adopted is considered useful for calibrating the forging cycle applied to different stainless steel grades. The conventional process to form an AISI 1005 hex-head plug fitting used in thermo-hydraulic applications is investigated and the variations of process parameters for forging an AISI 304L and Duplex 2205 stainless steel are picked out.

Metallographic investigations have been carried out by using an optical microscope (OM) and a Field-Emission Gun Environmental Scanning Electron Microscope (FEG-ESEM) equipped with an Electron Back-Scattered Diffraction (EBSD) technique in order to investigate the microstructural evolution on steels before and after deformation.

Simulation and experimental results obtained provide a basis for the new product development of a stainless steel component.

KEYWORDS

Cold forging, Numerical simulation, FEM method, Stainless steel, Microstructure.

1. INTRODUCTION

Dealing with highly competitive markets is a constant battle. Being successful as a supplier often depends on the cost of production, delivered quality, time-to-market and sometimes also on product and/or process innovation. In this context, the challenge lies in the design phase and its crucial role in evaluating possible product and process solutions before the equipment and parameters are defined.

In the last years, the environment concerning the forging industry has been changed rapidly [1]. Forging is one of the most economical and efficient methods for fabricating complex metal components.

In the last decades, near-net-shape or net-shape manufacturing is become a trend in metal forming, especially in cold forging, resulting in savings in material and energy [2]. In this process, billets are usually deformed to large strains using high compression loads, generally applied by single- or multi-stage hydraulic or knuckle-joint press, and following one or more subsequent deformation cycles [3]. The resulting components have refined grain structure and improved mechanical properties, such as strength [4-6].

However cold forging is governed by many factors, such as friction at the tool-workpiece interface, part geometry and tools shape. Hence, this process has a high tendency to form defects and thus it is essential to detect and prevent them during the production process. In the past, many researchers have discussed about types and formation mechanisms of forging defects [7-15].

To avoid this, the selection of appropriate process parameters and the proper design of the forging tools becomes crucial.

In recent years, computer-aided simulation techniques in metal forming have proved to be a powerful tool to predict and analyze the material deformation during a forging operation. Metal forming processes represent an interest field of application for recent CAE (Computer Aided Analysis) techniques for the theoretical complexity of the processes and the influence of various parameters. In practice, cold forging requires several preforming operations to transform an initial simple billet into a final complex product without defects. The design of a forging-process sequence involves the determination of the number of preforms, and the determination of the shapes and preform dimensions. Traditionally, forging-sequence is carried out using mainly empirical guidelines, experience and trial-and-error, which results in a long cost of the products. A FEM (Finite Element Method) approach is therefore the best suited to study the cold forging process in detail [16-18].

Aim of the work is to analyze the conventional cold forging process of a low-carbon component. The forged part examined is an hex-head plug fitting used in thermo-hydraulic applications. Using FEM method, the re-design of the conventional single-stage cold forging process to form stainless steel components (i.e. AISI 304L and Duplex 2205) is carried out. It has been also considered the variation of process parameters applied on the optimized forging operation utilize to produce stainless steel parts, by using a virtual optimization approach.

The project is aimed to control the material flow, the loads and stresses exerted on tools and to prevent the formation of defects during the forging process. The stainless steel forged components obtained slightly meet the drawing tolerances established by the company for the AISI 1005 part, ensuring the development of a new components with better mechanical properties.

Finally, metallographic investigations are carried out by using an optical microscope (OM) and a Field-Emission Gun Environmental Scanning Electron Microscope (FEG-ESEM) equipped with an Electron Back-Scattered Diffraction (EBSD) technique in order to

evaluate and compare the microstructural evolution on steels before and after deformation, focusing attention on certain deformed areas of the component.

2. THE CONVENTIONAL COLD FORGING PROCESS

The forged component analyzed is an hex-head plug fitting used in the thermo-hydraulic applications, which CAD geometry is shown in Fig. 1. It is traditionally an AISI 1005 low-carbon steel component (Wr. N. 1.0303).

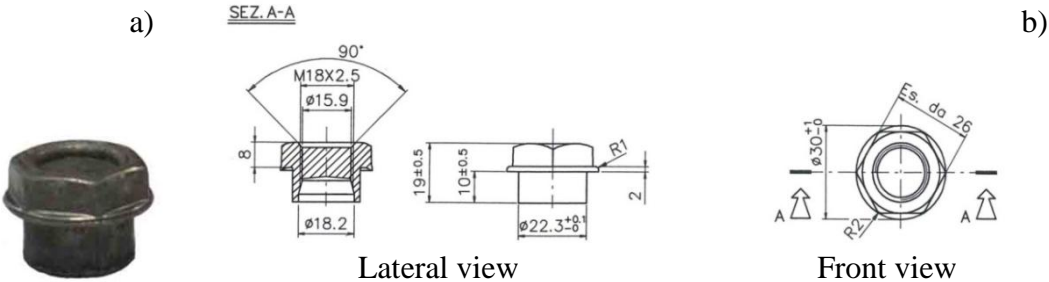


Fig. 1. a) AISI 1005 hex-head plug fitting and b) front and top views. All dimension are in mm.

Thanks to its excellent cold formability and plastic properties, this type of steel is widely used, from several decades, for the production of small components and quite complex geometries by using single- or multi-stage forging processes. Fig. 2 shows the traditional single-stage cold forging process analyzed.

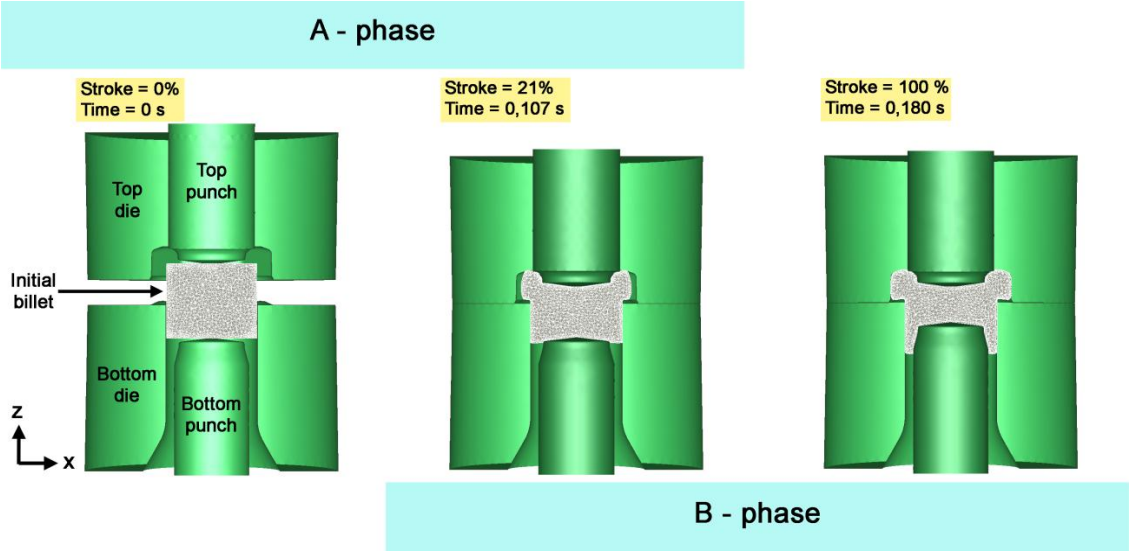


Fig. 2. Forming process of the single-stage forged plug fitting.

The industrial process analyzed is one-stage forging operation, which consists of two phases: a first compression to create the hex-head of the plug fitting (named "A-phase") and a second deep backward extrusion operation to form the "neck" of the plug fitting (named "B-phase"). The cylindrical AISI 1005 steel billet (22 mm diameter, 18 mm height and 51 g weight) was coated using a single layer coating, in order to reduce friction at die-workpiece interface. The forging stage is obtained by the action of a single-station

mechanical knuckle-joint press, which has a nominal power of 250 tons, a forging-stroke of 400 mm and a velocity of 50 spm.

During the initial deformation step (Step A in Fig. 2), the billet is initially compressed between the two punches (top punch and bottom punch respectively) under the action of the mechanical press. In this way, the material fills the top die shape, creating the hex-head of the plug.

Bottom punch is fixed during the forming cycle. Top punch and die is driven by press kinematism. Moreover bottom die is floating and driven by the contact forces exerted during the whole process. The phase B (Fig. 2) begins when the top die comes into contact with the bottom one. In this case the billet, partially deformed, is backward extruded leading to the formation of the "neck" of the plug. This operation is made possible, because bottom die is floating and driven by the contact forces exerted during the whole process. Moreover the formation of the hex-head of the plug, already started in phase A, is completed in phase B.

3. STUDY OF THE CONVENTIONAL FORGING PROCESS BY USING FEM METHOD

The analysis of the conventional process, carried out on the AISI 1005 cold forged component and later extended to the AISI 304L (Wr. N. 1.4307) and Duplex 2205 (Wr. N. 1.4462) stainless steel, was performed by means of FORGE2011[®]-3D software. The numerical code allowed to define process parameters and then was able to predict their influences on the process itself. The chemical composition and supply condition of the alloys analyzed are listed in Table 1 and 2.

Computer-aided simulation analysis was used to model the traditional single-stage forging process, starting from a cylindrical billet (i.e. 22 mm diameter, 18 mm height and 51 g weight). In FEM code was then predicted the material flow, the loads and stresses exerted on tools during forging.

Steel	C	Si	Mn	Cr	Mo	Ni	Cu	Co	N	Others	Fe
AISI 1005	0.05	0.07	0.30	0.11	0.02	0.13	0.17	0.01	0.01	<0.07	Bal.
AISI 304L	0.02	0.35	1.32	18.66	0.40	8.11	0.49	0.12	0.09	<0.06	Bal.
Duplex 2205	0.02	0.52	1.28	22.30	3.13	5.68	0.19	0.07	0.18	<0.05	Bal.

Tab. 1. Chemical compositions of the materials analyzed (wt.%).

Steel	Type of product	Diameter [mm]	Heat Treatment
AISI 1005	Round bar	22	-
AISI 304L	Round bar	22	Solubilization at 1150 °C + water-quenched
Duplex 2205	Round bar	22	Solubilization at 1050 °C + water-quenched

Tab. 2. As-received conditions of the materials analyzed.

The forging process analyzed is considered complex to be modeled, due to the "floating-die" kinematic and non-linearity of the contact conditions to be implemented on the numerical code. Due to these problems and for the sake of decreasing computer CPU time, forging tools are assumed to be rigid body with an infinite elasticity modulus and a constant temperature of 20 °C. The initial billet is discretized with tetra elements with four

nodes into 167235 elements and 29942 nodes; these numbers are sufficient to ensure accuracy and convergence [19].

3.1. Material

The numerical simulation of a forging process consists primarily of thermo-mechanical analysis of the plastic deformation. To obtain results with a high degree of confidence, the simulation calculation must be based on real accurate data.

The most important data used in FE computations is the material rheology [20,21]. The material model for the current work was developed through tensile tests and data was used to produce the material flow curve.

For this purpose, a series of round tensile specimens were drawn from the steel bars, at the as-received conditions reported in Table 2. Tensile tests were performed with a MTS 810 hydraulic materials testing machine, 250 kN in capacity, with a crosshead speed of 2 mm/min.

The experimental data obtained from the tests were used to derive the true stress and strain curves ($\sigma_{true}-\epsilon_{true}$) for the different steels considered. In literature, there are several constitutive equations that describe the material flow behavior. Hansell-Spittel's law is used in the numerical model of this work [22,23] (Eq. (1)):

$$\sigma_f = A \cdot e^{m_1 T} \cdot \epsilon^{m_2} \cdot \dot{\epsilon}^{m_3} \cdot e^{m_4/\epsilon} \cdot (1 + \epsilon)^{m_5 T} \cdot e^{m_7 \epsilon} \cdot \dot{\epsilon}^{m_8 T} \cdot T^{m_9} \quad (1)$$

where A, m_1 , m_2 , m_3 , m_4 , m_5 , m_7 , m_8 , m_9 are the regression coefficients.

The determined regression coefficients are given in Table 3. As only room temperature testing was considered the temperature related terms were ignored. These coefficients derived from Eq. (1) using the strain values from the experimental data. This was achieved through a number of iterations using FEM code.

Steel	Regression coefficients								
	A	m_1	m_2	m_3	m_4	m_5	m_7	m_8	m_9
AISI 1005	863.63114	-0.00138	0.30842	0.02031	-0.01149	0	0	0	0
AISI 304L	1551.20326	-0.00148	0.71957	0.01014	0.00372	0	0	0	0
Duplex 2205	1600.10251	-0.00103	0.98337	0.00302	0.00001	0	0	0	0

Tab. 3. Estimated regression coefficients of Hansell-Spittel's law.

Fig. 3 shows the average $\sigma_{true}-\epsilon_{true}$ curves obtained for each material analyzed. They were derived from the engineering stress and engineering strain measurements, and were calculated using the following formulas (Eq. (2,3)):

$$\epsilon_{reale} = \ln(1 + l) \quad (2)$$

$$\sigma_{reale} = \sigma_{nom} \times (1 + l) \quad (3)$$

where l is the elongation, computed as $(L-L_0)/L_0$, with L and L_0 being current and initial gauge lengths respectively.

The experimental and the numerical flow curves for each material tested are shown in Fig. 3. As can be seen, the difference between the curves is less than $\pm 6\%$ and $\pm 7\%$ for AISI 304L and Duplex 2205 stainless steel respectively, whereas it is lower by about $\pm 3\%$ for AISI 1005 material grade. This suggest that there is a good correlation between the model and measurements.

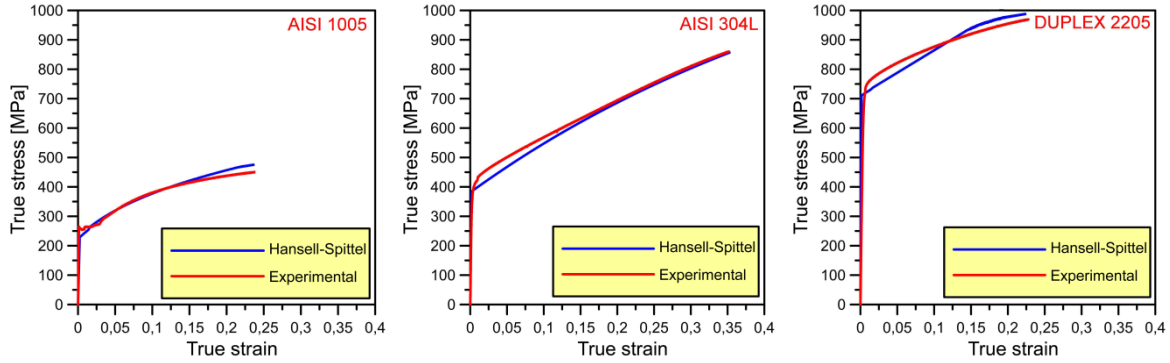


Fig. 3. Experimental (i.e. average engineering σ - ϵ curves) and calculated (i.e. Hansell-Spittel's law) flow curves for the materials tested.

In order to ensure the repeatability and accuracy of the results obtained, also the average values of the mechanical parameters, such as the yield strength ($YS_{0,2\%}$), the tension strength (UTS) and the Young's modulus (E) were considered (Table 4). The mechanical properties, reported in Table 4, associated with the constitutive equations determined for each steel considered, were subsequently implemented as input data into the FEM model of the process, for the definition of the rheological behavior of the material.

Steel	Mechanical parameters		
	$YS_{0,2\%}$ (MPa)	UTS (MPa)	E (GPa)
AISI 1005	260 (0.3)	366 (1.8)	212 (0.4)
AISI 304L	443 (0.5)	641 (0.2)	188 (0.3)
Duplex 2205	761 (1.1)	808 (0.9)	186 (0.1)

Tab. 4. Average $YS_{0,2\%}$, UTS and E for the different steels analyzed (standard deviations in parentheses).

3.2. Friction conditions

It is well known that friction conditions prevailing at the tool-workpiece interface have a deep effect on material deformation, forming load, surface finish, internal structure of the component, as well as die wear characteristics in metal forming processes [24,25].

To avoid the appearance of excessive friction, it is indispensable to use lubricants with efficient intrinsic low-friction properties in cold forming.

Before forging tests, the billets were coated using a single layer coating, in order to reduce friction at tool-workpiece interface. After sandblasting and hot water rising, the billets were dipped in an aqueous bath containing 70% of Bonderlube FL 744 lubricant and subsequently dried in a muffle furnace. The cleaning operations were designed to remove fine scale and grease from the billet surface. The sandblasting even provided a porous structure on it that is beneficial for entrapment of liquid lubricant.

The Bonderlube FL 744 lubricant was a water-based compound, which generic chemical composition were: sodium nitrite 0.1-1%, dipotassium tetraborate tetrahydrate 5-10% and

water 89-94.9%. The sandblasting operation consisted of a mechanical-centrifugal process, where in a specific blasting the piece was hit by jets of abrasive material obtained through the use of centrifugal turbines.

In addition, it is essential to evaluate a friction condition as close as possible to those that occur at the tool-workpiece, in order to accurately predict the material flow during deformation.

In literature, there are two friction laws which are widely applied to calculate the tangential stress between specimen and tool in metal forming processes. In commercial FEM packages (e.g. FORGE2011[®]-3D), Amontons-Coulomb and constant friction models are normally applied.

The Coulomb law, uses a friction coefficient μ to quantify the interface friction, and is expressed as follows (Eq. (4)):

$$\tau = \mu p \quad (4)$$

where τ is the friction stress and p is the normal pressure. This law is valid for forming process with either low contact pressure or low friction stress. The Coulomb expression does not limit the shear stress. Because the friction stress cannot exceed the shear strength of the material, the shear friction law (constant friction or Tresca law) is developed as (Eq. (5)):

$$\tau = \frac{m}{\sqrt{3}} \bar{\sigma} \quad (5)$$

where m is the friction factor and $\bar{\sigma}$ is the flow stress of the deformed material.

In this paper, these two friction laws were used in order to obtain the friction coefficient μ and factor m , in an according manner with the real industrial process.

To make this possible, a series of T-shape compression tests at room temperature coupled with FEM simulations of the test were performed, in order to evaluate friction conditions at tool-workpiece interface for each material subject to forging tests.

Unlike other experimental tests reported in literature [26-31], the test consists on the compression of cylindrical specimens into a V-groove shape die (Fig. 4). The steel specimens 6.85 mm diameter and 7 mm long, were used for performing the T-shape compression tests. They were machined directly from drawn bar at as-received conditions previously reported. For each steel considered, three specimens were tested and mechanical parameters were obtained from the average of three experimental tests. The loading speed of testing was 0.03 mm/s and the maximum stroke was 4.5 mm.

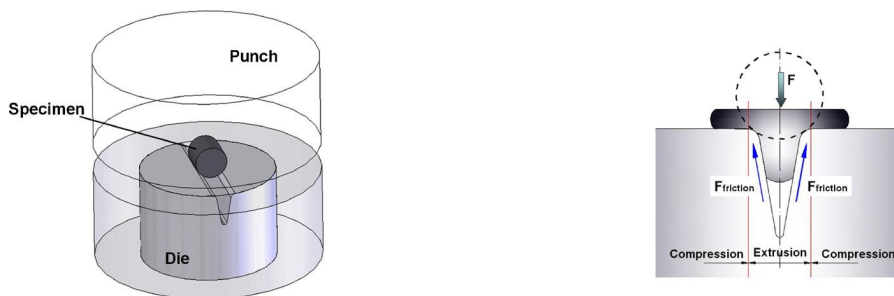


Fig. 4. The principle of T-shape compression test performed for the three types of steel analyzed.

From experimental tests, the load curves along z -axis were obtained. The values of the friction coefficient μ and factor m were then obtained by using FE model of T-shape compression test and the inverse FE analysis. In order to estimate the values of the friction coefficient μ and factor m , the experimental and simulated load curves are plotted in Fig. 5. It shows that the simulated and experimental results are in good agreement. In addition, it means that the T-shape compression test is a good method for determination of friction condition.

For sake of simplicity, Fig. 5 shows the comparison between experimental and simulated load curves for Duplex 2205 steel. Table 5 reports the friction coefficient μ and factor m for the steels considered. A good correlation between the experimental and numerical data is observed (Fig. 5b).

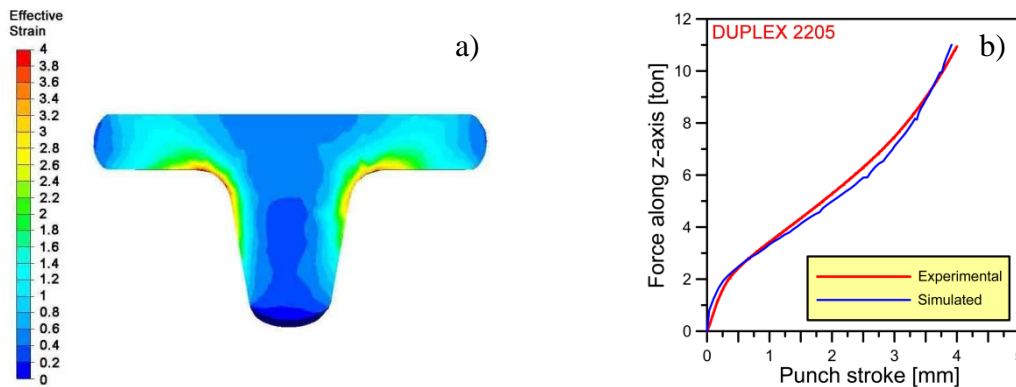


Fig. 5. a) Effective strain distribution on the cross section of Duplex 2205 specimen and b) comparison between the average experimental and simulated load curves.

Steel	Friction conditions	
	μ	m
AISI 1005	0.11	0.83
AISI 304L	0.03	0.86
Duplex 2205	0.05	0.91

Tab. 5. Estimated values of friction factor m and friction coefficient μ .

3.3. Results and discussion

The results obtained from the FE model for the conventional forging process of AISI 1005 steel were subsequently compared with the real forged component, validating the process parameters selected. The final shape of the simulated and experimental part seems to be identical. Analyzing the FE results obtained for stainless steel parts (Fig. 6), there were underfilling areas at the hex-head of the plug fitting and an height H of 9.1 and 8.8 mm was reached for AISI 304L and Duplex 2205 stainless steel respectively. These values were lower than the drawing tolerances established by the company (i.e. 10 ± 0.5 mm).

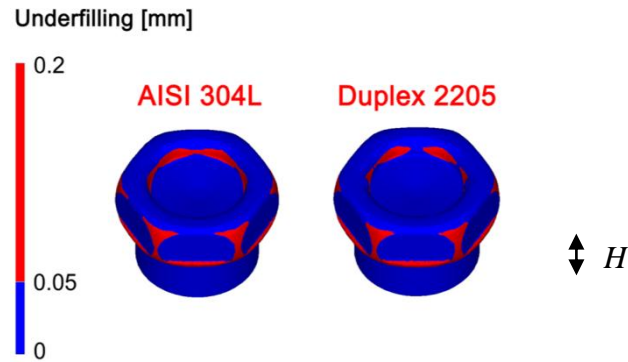


Fig. 6. Underfilling red areas on virtual conventional cold forged parts.

4. OPTIMIZATION OF THE CONVENTIONAL COLD FORGING PROCESS BY USING FEM METHOD

The analysis of the forging process continued, in the attempt to eliminate or reduce the underfilling areas at the hex-head of stainless steel plugs and form forged components that strictly meet the drawing tolerances established by the company. The variations of process parameters are shown in Table 6.

Initial billet mass		Kinematic	
Conventional process	Optimized process	Optimized process	
Diameter: 22 mm Weigth: 0,051 kg	Diameter: 22 mm Weigth: 0,055 kg		

Tab. 6. Variations of process parameters for cold forging conventional cycle.

Other process parameters, such as the material rheology and the friction conditions at the tool-workpiece interface, have not changed in this optimization phase and have been implemented within FE code using the same procedure adopted in the traditional cold forging cycle.

4.1. Results and discussion

By analyzing FE results obtained on the optimized process of the AISI 304L and Duplex 2205 forged components, a reduction of the underfilling red area at the flange of the plug fitting on both materials analyzed is observed (Fig. 7).

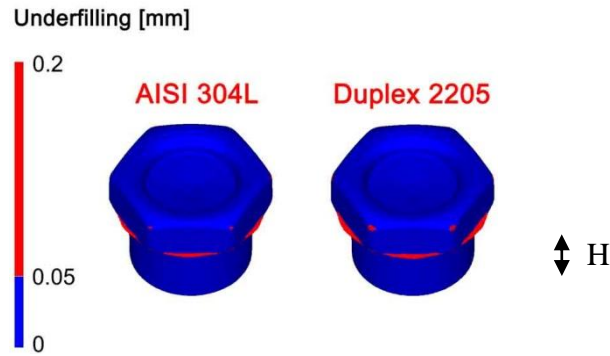


Fig. 7. Underfilling red areas on virtual optimized cold forged parts.

This material flow imperfection does not affect the functionality of the component, which maintained the established drawing tolerance (i.e. 31 mm). A slight underfilling at the hex-head (i.e. less than 0.2 mm on the top die) was detected on Duplex 2205 plug fitting. Finally, looking at the "neck" of the part, the height H reached by the FE optimized component was 9.7 and 9.5 mm for AISI 304L and Duplex 2205 steel plug fitting respectively. These drawing quotes were slightly greater than the tolerances established in the design phase (i.e. 10 ± 0.5 mm). In both processes, the actual forging time calculated using FEM analysis was 0.18 s, in good agreement with the measurements performed on the industrial conventional and optimized forging cycle.

Fig. 8 shows the load-forming time relationship exerted on dies for each steel considered during both forging processes. By analyzing the conventional forging cycle (Fig. 8a), it can be seen that the maximum forces detected are 50 tons on each steel considered, which is less than the limit of the available press capacity of 250 tons. Due to higher forging loads require in forging of stainless steels, the maximum values of force detected in these latter are slightly higher than in the low-carbon steel. In the optimized cold forging process of these steels, the maximum force detected reaches values lower than 50 tons in both stainless steels, ensuring an energy saving as compared to the conventional process.

In Fig. 8a is observed that the phase of formation of the hex-head of the plug ends at the peak force at 0.11 s revealed for both the dies.

Due to the variations of process parameters on the optimized process, the top die comes into contact with the lower one with a certain delay. Consequently, the forging phase A has a longer duration on the optimized process compared to the conventional cycle; This is confirmed by the value of force detects at 0.14 s as compared to 0.11 s of the conventional process.

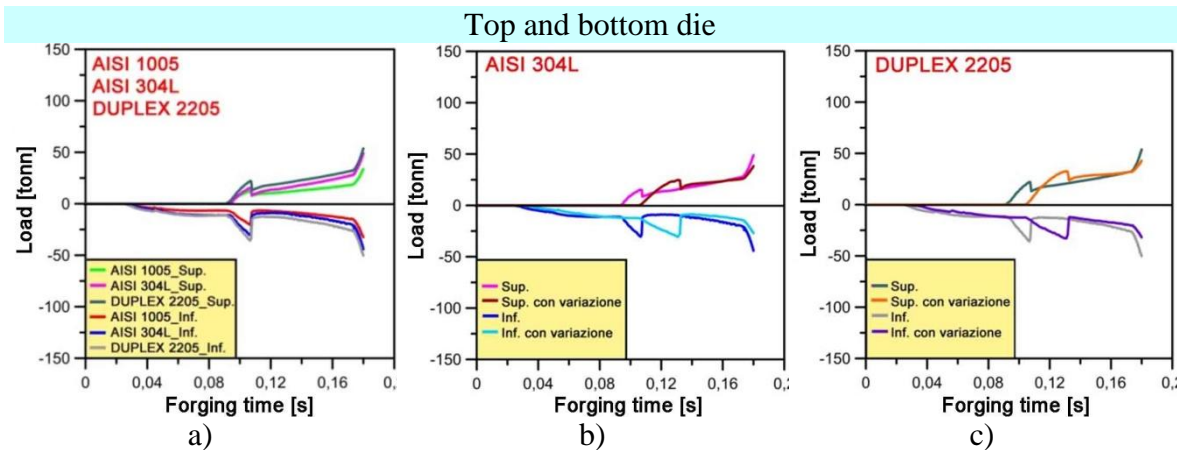


Fig. 8. a) Loads exerted during the conventional process on top and on bottom die for the tested steels and b-c) comparison between the forces exerted on dies during the conventional (i.e. top die - Sup. and bottom die - Inf.) and optimized cycle (i.e. top die - Sup. with variation and bottom die - Inf. with variation) for AISI 304L and Duplex 2205 steel respectively.

Fig. 9 shows the load-forming time relationship exerted on punches during both forging processes for each steel considered.

In this case, by analyzing the conventional forging cycle (Fig. 9a), it can be seen that the maximum forces revealed on punches are higher as compared to the loads exerted on dies (Fig. 8a). In fact they are of 125 tons and 75 tons on forging of stainless and low-carbon steel components respectively.

This can be related to the fact that, having a smaller contact area with the workpiece as compared to the dies, higher states of stress are concentrated further in terms of compression stress along z -axis.

Moreover, punches are most stressed during the cold forging of AISI 304L and Duplex 2205 parts (Fig. 9a), as a consequence of the higher mechanical properties of such materials as compared to AISI 1005 steel (Table 4).

In Fig. 9 it may be observed that the limit of the available press capacity of 250 tons is not exceeded and the maximum loads exerted on punches are lower in the optimized than conventional forging cycle (Fig. 9b-c).

The optimized process records a decrease of the press load as compared to conventional one, leading to energetic, economic and ecological benefits.

In Fig. 9 it is detected a peak of load on top punch, which corresponds to the last step of formation of the hex-head of the plug, for all steel grades and forging processes analyzed. This is due to the fact that stresses are more concentrated on this tool, which pushes the material to fill the gaps between deformed part and top die during the last stage of the process. In this case it is detected a greater durability of this phase on the optimized forging process (Fig. 9b-c), due to the variations of process parameters previously applied, with the maximum peak force identified at 0.14 s as compared to 0.11 s of the conventional cycle.

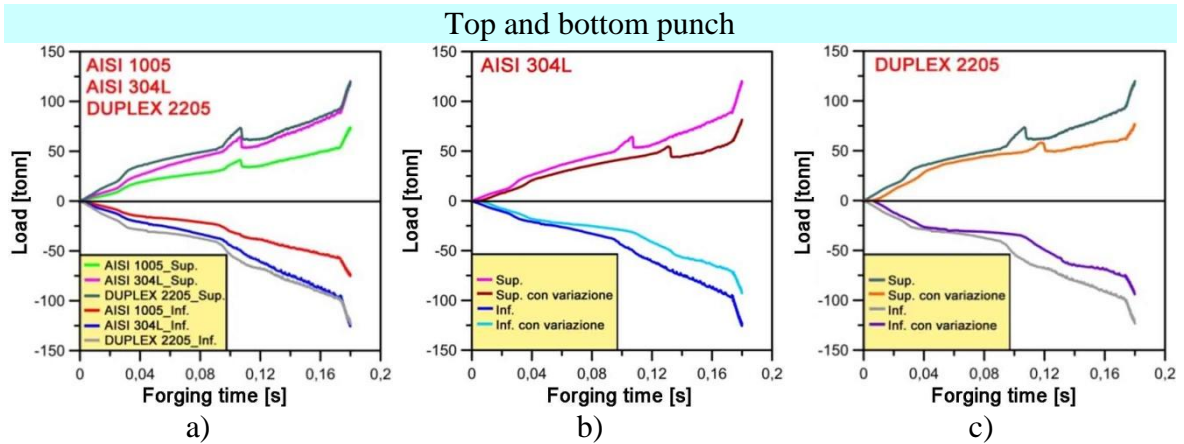


Fig. 9. a) Loads exerted during the conventional process on top and on bottom punch for the tested steels and b-c) comparison between the forces exerted on punches during the conventional (i.e. top die - Sup. and bottom die - Inf.) and optimized cycle (i.e. top die - Sup. with variation and bottom die - Inf. with variation) for AISI 304L and Duplex 2205 steel respectively.

5. EXPERIMENTAL INVESTIGATIONS

AISI 1005 forged components, produced by means of the conventional forging process, and stainless steel plugs obtained through the optimized process were then macro- and microstructurally investigated, in the attempt to verify the presence of surface or internal defects and characterize the microstructure.

The hex-head plug fittings were therefore checked through visual inspection by using a vernier calliper (i.e. approximation degree of 0.02 mm).

For a detailed understanding of the effects caused by the optimized cold forging process, metallographic longitudinal sections parallel to the rolling direction (RD) and the compression z -axis were then drawn from the as-received and forged samples, as indicated in Fig. 10.

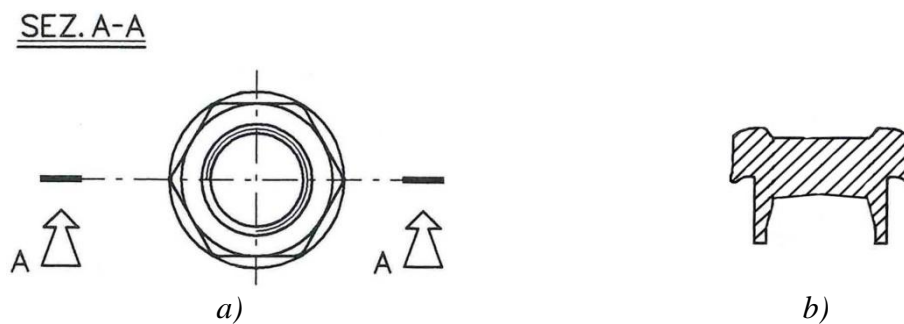


Fig. 10. a) Top view of the hex-head plug fitting CAD geometry and b) side view showing the investigated zone.

Microstructural analysis was carried out using an optical microscope (OM) and a Field-Emission Gun Environmental Scanning Electron Microscope (FEG-ESEM, model QUANTA 250 FEI[®]), operated at an accelerated voltage of 20 kV and equipped with an Electron Back-Scattered Diffraction (EBSD) analyser incorporating an orientation imaging microscopy (OIM) system (EDAX TSL software, version 5) for crystal orientation mapping. The OIM images were then subjected to clean-up procedures, setting a minimal

confident index of 0.1, in order to compare size and crystal grains orientation before and after deformation on each steel considered.

5.1. Results and discussion

5.1.1. Underfilling defects evaluation

The presence of surface cracks or flashes were not detected on the 150 components analyzed (i.e. fifty for each steel grade). The visual inspection techniques, by means of a vernier calliper, allowed to verify full compliance with the drawing tolerances established during the design phase of the AISI 1005 plug fitting and reported in Fig. 1.

For stainless steel components, an underfilling area was detected at the flange of the parts, as shown from numerical results. In 100 forged parts checked, the average diameter of the plug fitting's flange was 28.8 mm and strictly met the drawing tolerance established by the company (Fig. 1).

5.1.2. Microstructural characterization

Microstructural analyses were carried out on a series of hex-head plug fittings for each steel grade and allowed to identify the flow lines of the materials examined (see the real sections in Fig. 11). For optical investigations, AISI 1005 samples were etched with 4% HNO₃ in ethanolic solution; AISI 304L with a reagent for electrolytic etching (i.e. a mixture of 60% HNO₃ and 40% distilled water) and Duplex 2205 specimens with Beraha etching solution (i.e. 10 ml HCl, 40 ml distilled water, 1 g K₂S₂O₅).

The optical observations highlighted the total absence of internal micro-cracks and the highly deformed areas; the latter were also detected by the simulated equivalent strain maps (Fig. 11).

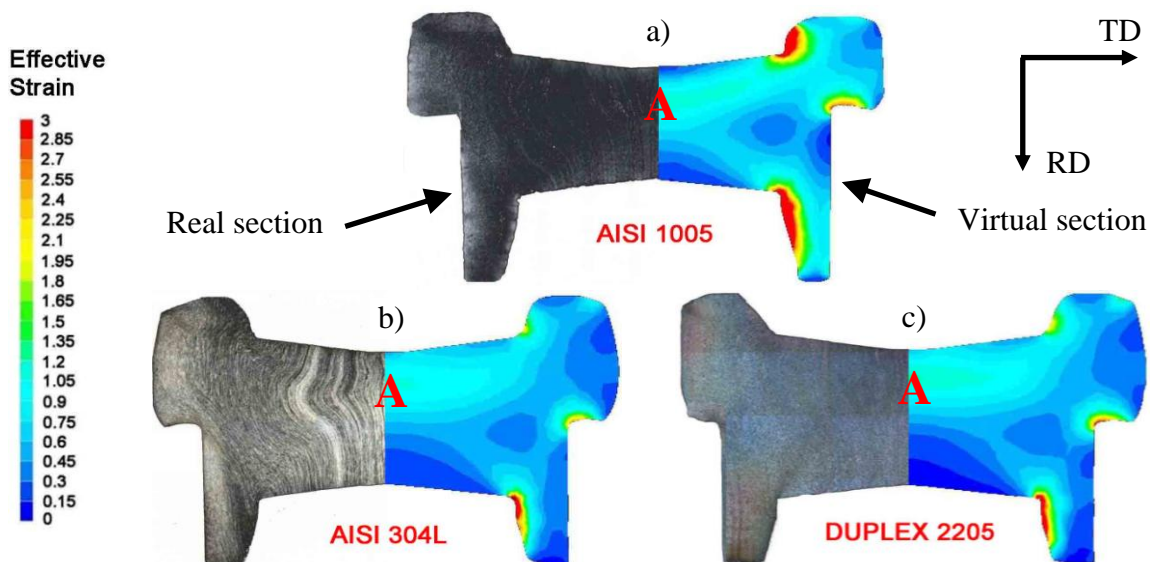


Fig. 11. Flow lines (real section) and effective strain maps (virtual section) revealed on a) AISI 1005, b) AISI 304L and c) Duplex 2205 samples.

For a complete microstructural characterization of forged components, the Zone A of each sample was investigated (Fig. 11). This area is subject to more stresses in operating conditions and presents medium-high values of strain. The EBSD technique was used to

compare undeformed zones (i.e. steels in the "as-received" conditions) and deformed zones, in order to analyze crystal orientation and grain size evolution during the transition between pre and post-deformation.

Considering the rolling direction (RD) of the samples coincident with the direction of the press-load, the EBSD maps were carried out by selecting a suitable scanning area along the RD-TD plane (Fig. 11). The selected area was $100 \times 150 \mu\text{m}^2$ for Duplex 2205 and $200 \times 300 \mu\text{m}^2$ for AISI 1005 and 304L grade.

For the correct data analysis, the OIM images were then subjected to clean-up procedures, setting a minimal confident index (CI) of 0.1 for a correct data analysis [32].

It is well known that AISI 1005 reveals a predominantly ferritic microstructure (i.e. α -phase), whereas AISI 304L has an austenitic structure (γ -phase). Moreover Duplex 2205 presents a dual-phase structure with a very good balance between ferrite and austenite.

Fig. 12 shows the EBSD images of the constituent phases of each steel at the "as-received" state. The estimated average grain sizes are shown in Table 7.

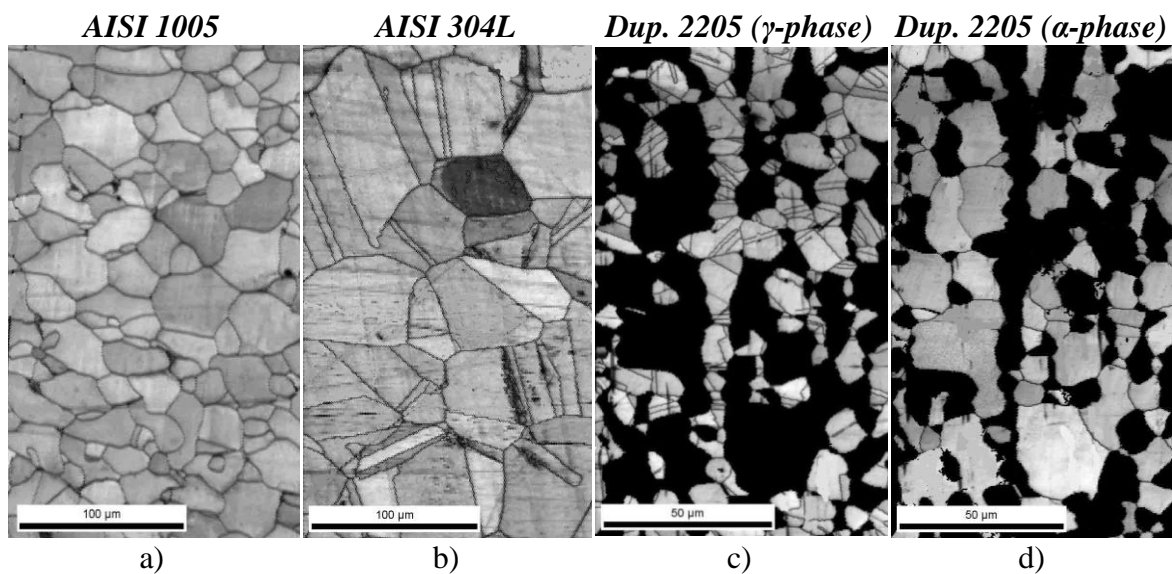


Fig. 12. EBSD images of steels at as-received state: a) α -phase of AISI 1005, b) γ -phase of AISI 304L, and c) γ -phase and d) α -phase of Duplex 2205.

Steel	Phase	
	Ferrite	Austenite
AISI 1005	22 (8)	-
AISI 304L	-	40 (9)
Duplex 2205	9 (4)	6 (3)

Tab. 7. Average grain sizes (μm) revealed on each steel at as-received state (standard deviation in parentheses).

Fig. 13 shows EBSD analyses carried out on AISI 1005 samples at "as-received" and deformed state.

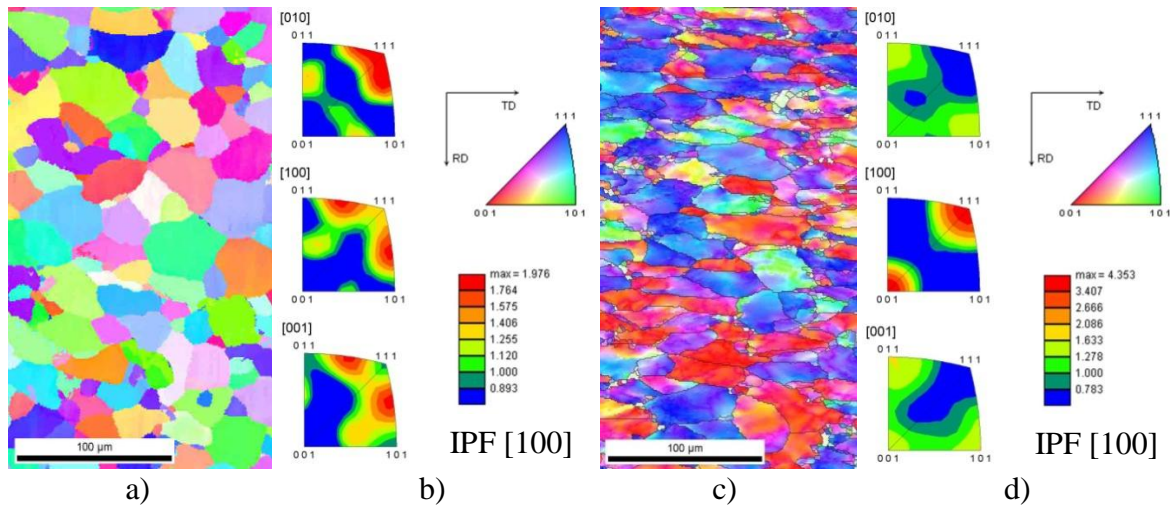


Fig. 13. Electron backscatter diffraction (EBSD) analysis of AISI 1005 steel: orientation imaging microscopy micrographs of α -phase at a) as-received and c) deformed state and inverse pole figures of α -phase at b) as-received and d) deformed state.

Fig. 13 shows the samples at as-received and deformed state (i.e. the zone A shown in Fig. 11), bringing their crystallographic orientation (OIM) maps and texture evolution during the transition between pre- and post-deformation (Fig. 13b-d).

On the deformed sample, the formation of a great amount of subgrains boundaries and grains, due to the cold forging process, increases the hardness in the affected zone. This is also due to the low-angle grain boundaries (i.e. Low Angle Boundaries, LABs) detected on the area.

A comparison of the inverse pole figures, which are given in Fig. 13b and d, reflect the calculated texture and the distribution of crystallographic planes and directions.

The texture shows a faint maxima (red color - maximum intensity = 2.0) in all directions of observation ([010], [100], [001]) in the undeformed state, with a maximum of intensity in [010] direction on the 111 pole. Due to the forging process, the texture changes significantly in Fig. 13d. Whereas the as-received material shows a random distribution of the crystal orientations, a strong maximum of intensity of 4.4 has been observed in [100] direction on the pole 001 and 111 in deformed state (Fig. 13d).

The change of the grain orientations strongly relates to the increase of low (LABs) and high (HABs) angle grain boundaries, which leads to a formation of a fine grained microstructure. An increase of the misorientations and further a decrease of the mean value of the confidence index (CI) from 0.4 (undeformed) to 0.2 (deformed) also points out grain refinement, which leads to higher hardness and toughness [33-36].

EBSD analysis continued on AISI 304L steel and OIM maps are shown in Fig. 14.

In this case, the texture on sample at as-received state presents a faint maxima in all directions of observation, with grains that tend to be orientated toward the direction [100] on the 111 pole (Fig. 14b). Moreover OIM images point out a strong change of the crystallographic orientations due to the deformation.

The most significant changes in the texture have been identified in the [100] orientation, where the intensity increases from ~2.5 on the 111 pole (i.e. undeformed condition) to ~4.9 on the poles 011/101 (Fig. 14d).

Furthermore, it is noted a strong grain refinement with grain size values comprise between 2 and 20 μm .

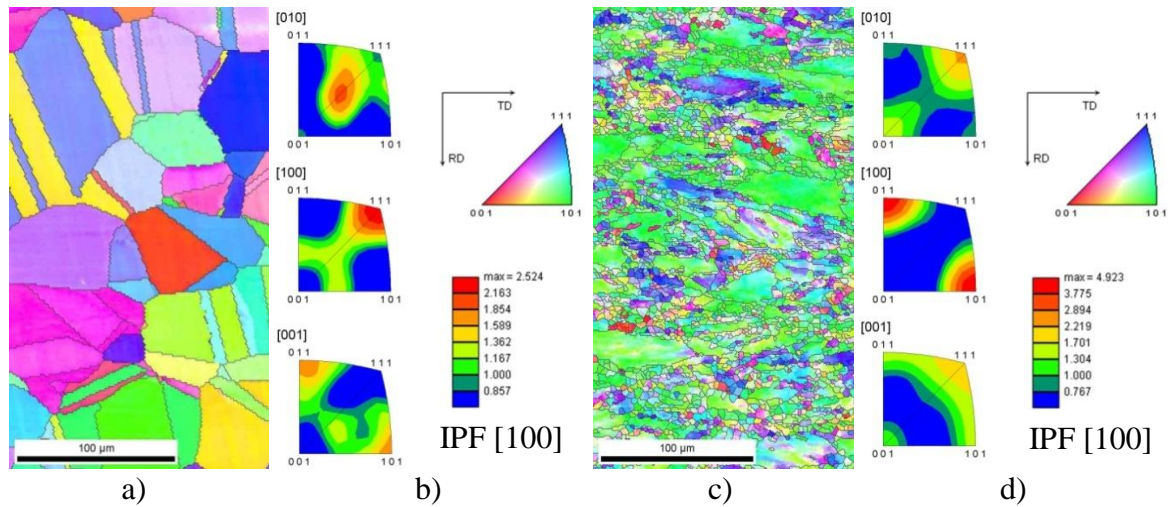


Fig. 14. Electron backscatter diffraction (EBSD) analysis of AISI 304L steel: orientation imaging microscopy micrographs of γ -phase at a) as-received and c) deformed state and inverse pole figures of γ -phase at b) as-received and d) deformed state.

Finally, the behaviour of ferrite and austenite during plastic deformation of Duplex 2205 samples were analyzed (Fig. 15).

By comparing the as-received Duplex 2205 and AISI 304L sample, it can be seen that austenite on Duplex 2205 exhibits a more or less random distribution of grain orientations. The texture shows a slight maxima (red color - maximum intensity = 1.9) in [100] direction on the 001 pole as compared to the maximum intensity of ~ 2.5 that occurs on the 111 pole in the same direction of observation for AISI 304L sample.

On the other hand, deformed γ -grains point out a preferential orientation in [100] direction on the poles 011 and 101; this confirms the considerations made for 304L steel grade.

The α -phase on Duplex 2205 shows a strong maximum of intensity (i.e. ~ 7.5) in all direction of observation on the 001 pole at the as-received state. On the contrary, in case of the ferritic AISI 1005 steel, the investigations highlighted a more or less random distribution of grain orientations in all directions of observation.

On forged Duplex 2205 specimen, the α -phase confirms the crystallographic orientation found on deformed low-carbon sample, with higher intensities achieved on [100] direction on 001 and 111 poles.

The grain refinement phenomenon on both phases is less evident than on the other steel grades analyzed. The average values of the grain size detected on the deformed zone are included between 2 and 5 μm , starting from 6 μm for the γ -phase and 9 μm for the α -phase found on sample at the as-received state.

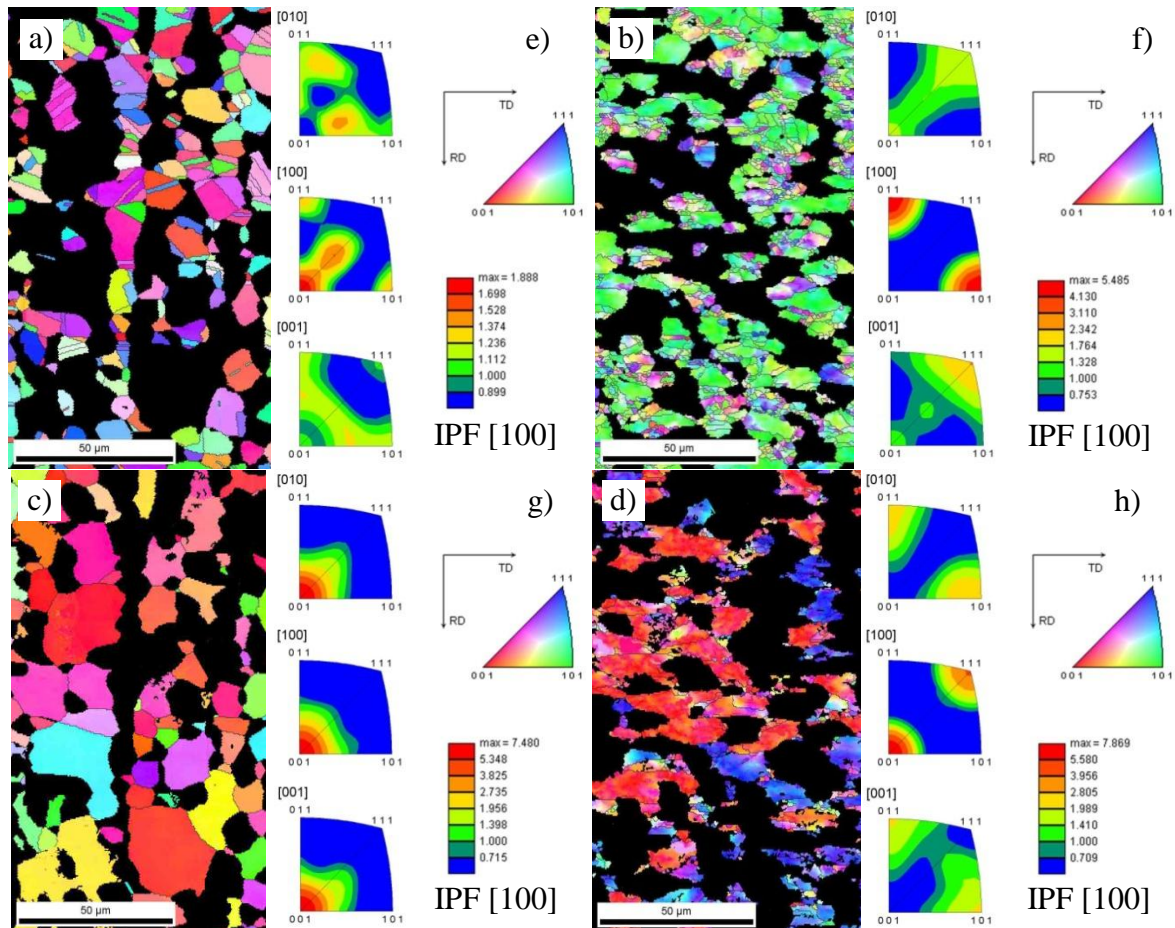


Fig. 15. Electron backscatter diffraction (EBSD) analysis of Duplex 2205 steel: orientation imaging microscopy micrographs of a) γ -phase and c) α -phase at as-received state and of b) γ -phase and d) α -phase at deformed state and inverse pole figures of e) γ -phase and g) α -phase at as-received state and of f) γ -phase and h) α -phase at deformed state.

6. CONCLUSIONS

The design of a conventional cold forging process to form an AISI 1005 hex-head plug fitting used in thermo-hydraulic applications has been investigated. A new optimized cold forming cycle has been proposed in order to produce AISI 304L and Duplex 2205 stainless steel parts. The optimized forged components produced at different steel grade were finally characterized from a microstructural point of view. Numerical simulation was used throughout the work. The following conclusions can be drawn:

- Numerical simulation of the conventional forging process and its optimization constitute valid approaches that allow to give solutions in the process in question, getting over the simple designers experience and allowing to adapt the conventional forging deformation cycle to new materials.
- The virtual optimization reduces long new product development lead-time and time-to-market, ensuring the production of defect-free and near-net-shape components.
- The optimized cycle allows to limit loads and stresses exerted during forging, leading to a reduction of onerousness on the process management with energetic, economic and ecological benefits.

- Cold forged samples with the presence of ferrite (i.e. AISI 1005 and Duplex 2205) exhibit a preferential distribution of grain orientations in [100] direction on the 001 and 111 poles. Moreover, the α -grains in Duplex 2205 at the as-received state show a strong crystallographic orientation in all directions of observation on the 001 pole.
- Cold forged samples with the presence of austenite (i.e. AISI 304L and Duplex 2205) report a change of the crystallographic orientations, with a preferential distribution of grains in [100] direction on the 011 and 101 poles.

ACKNOWLEDGMENTS

The authors wish to thank Zoppelletto S.p.A. (Torri di Quartesolo, Vicenza, Italy) and in particular Eng. Luca Zoppelletto for the availability of the material and the support in the forging tests.

REFERENCES

- [1] S.Y. KIM, S. KUBOTA, M. YAMANAKA, *J. of Mater. Process. Technol.*, Vol. 201 (2008), page 25.
- [2] F. BASSAN, P. FERRO, F. BONOLLO, *Key Eng. Mater.*, Vol. 622-623 (2014), page 659.
- [3] R. DI LORENZO, F. MICARI, *CIRP Annals: Manufact. Technol.*, Vol. 47-1 (1998), page 189.
- [4] A.N. BRAMLEY, D.J. MYNORS, *Mater. Des.*, Vol. 21 (2000), page 279.
- [5] *ASM Handbook - Vol. 14A: Metalworking: Bulk Forming*, ASM International, Materials Park, Ohio, (2005).
- [6] S. KALPAKJIAN, S.R. SCHIMD, *Manufacturing Engineering and Technology*, Pearson Prentice Hall, Upper Saddle River, New Jersey, U.S.A., (2006).
- [7] M. ARENTOFT, T. WANHEIM, *J. of Mater. Process. Technol.*, Vol. 69 (1997), page 227.
- [8] F. KIMURA, H. SUZUKI, K. TAKAHASHI, *CIRP Annals: Manufact. Technol.*, Vol. 41-1 (1992), page 193.
- [9] F.C. LIN, S.Y. LIN, *Finite Elem. in Anal. and Des.*, Vol. 39 (2003), page 325.
- [10] W.L. CHAN, M.W. FU, J. LU, L.C. CHAN, *J. of Mater. Process. Technol.*, Vol. 209 (2009), page 5077.
- [11] R. NARAYANASAMY, A. THAHEER, K. BASKARAN, *Ind. J. of Eng. and Mater. Sci.*, Vol 13 (2006), page 202.
- [12] C. YILMAZ, A.M. TAHIR, A.H. EROL, *Ind. J. of Eng. and Mater. Sci.*, Vol. 11 (2004), page 487.
- [13] C. LU, L.W. ZHANG, *Trans. of Nonferr. Met. Soc. of China*, Vol. 16 (2006), page 1386.
- [14] J.H. SONG, Y.T. IM, *J. Mater. Process. Technol.*, Vol. 1-7 (2007), page 192.
- [15] S.Z. QAMAR, *Mater. and Manufact. Proc.*, Vol. 25 (2010), page 1454.
- [16] Y. HAMMI, *Simulation numérique de l'endommagement dans les procédés de mise en forme*, Ph.D. thesis, University of Technology of Troyes (UTC), April 2000.
- [17] A. TEKKAYA, *Proc. 6th Int. Conference on Numerical Methods in Industrial Forming Processes, NUMIFORM '98*, Enschede, Netherlands, 22-25 June 1998, page 529.
- [18] Z. XU, W. YUANPING, C. JUN, Z. LINGSHOU, R. XUEYU, *J. Mater. Process. Technol.*, Vol. 91 (1999), page 191.

- [19] X. DENG, L. HUA, X. HAN, Y. SONG, *Mater. and Des.*, Vol. 32 (2011), page 1376.
- [20] A. GAVRUS, ET AL., *J. Mater. Process. Technol.*, Vol. 60 (1996), page 447.
- [21] A. BEHRENS, ET AL., *Proc. 8th Int. Conference Metal Forming 2000*, Kraków, Poland, 3-7 September, Ed. A.A. Balkema Publishers, 2000, page 245.
- [22] FORGE2 Technical Documentation, Ed. Transvalor SA, France, 2000.
- [23] I. PILINGER, P. HARTLEY, ET AL., *Proc. 8th Int. Conference Metal Forming 2000*, Kraków, Poland, 3-7 September, Ed. A.A. Balkema Publishers, 2000, page 203.
- [24] R. KOPP, R. BÜNTEN, K. KARHAUSEN, F.D. PHILIPP, R. SCHNEIDERS, *Umformtechnik*, Vol. 26-5 (1992), page 318.
- [25] E. DOEGE, M. ALASTI, R. SCHMIDT-JÜRGENSEN, *J. of Mater. Process. Technol.*, Vol. 150 (2004), page 92.
- [26] A.T. MALE, M.G. COCKCROFT, *J. Inst. Metals*, Vol. 93 (1964), page 38.
- [27] R. GEIGER, *Metal flow in combined can extrusion*, Ed. Verlag W. Girardet, Essen, Germany, Vol. 36 (1976), page 197.
- [28] A. BUSCHHAUSEN, J.Y. LEE, K. WEINMANN, T. ALTAN, *J. Mater. Process. Technol.*, Vol. 33 (1992), page 95.
- [29] M. ARENTOFT, C. VIGSØ, M. LINDEGREN, N. BAY, *Advanced Technology of Plasticity 1996*, *Proc. of 5th ICTP*, Ohio, U.S.A., 7-10 October 1996, Ed. T. Altan, Vol. 1 (1996), page 243.
- [30] L. LAZZAROTTO, L. DUBAR, A. DUBOIS, P. RAVASSARD, J. OUDIN, *Wear*, Vol. 211 (1997), page 54.
- [31] L. LAZZAROTTO, A. DUBOIS, L. DUBAR, A. VERLEENE, J. OUDIN, *Surf. Eng.*, Vol. 14 (1998), page 335.
- [32] M. TIKHONOVA, A. BELYAKOV, R. KAIBYSHEV, *Mater. Sci. Eng. A*, Vol. 564 (2013), page 413.
- [33] W. BERGMANN, *Werkstofftechnik 1: Struktureller Aufbau von Werkstoffen - Metallische Werkstoffe - Polymerwerkstoffe - Nichtmetallisch-anorganische Werkstoffe*, Ed. Carl Hanser Verlag, Munich, Germany, (2008).
- [34] S.L. KAKANI, A. KAKANI, *Material science*, Ed. New Age International, New Delhi, India, (2004).
- [35] E. HORNBOGEN, *Werkstoffe - Aufbau und Eigenschaften von Keramik, Metall, Polymer und Verbundwerkstoffen*, Ed. Springer Berlin, Germany, (2006).
- [36] H.J. BARGEL, H. SCHULZE, *Werkstoffkunde*, Ed. Springer Berlin, Germany, (2008).

ARTICLE V

**MICROSTRUCTURAL AND LOCAL PLASTIC
STRAIN EVOLUTION IN COLD-WARM
FORGED COMPONENTS STUDIED
BY MEANS OF EBSD TECHNIQUE**

F. Bassan, P. Ferro, F. Bonollo*

**University of Padua, Department of Management and Engineering,
Stradella S. Nicola, 3 I-36100 Vicenza, Italy*

Submitted to "Materials Characterization", 2015.

ABSTRACT

Strain hardening is a common technique to exploit the full potential of materials in different applications. In this work Electron BackScatter Diffraction (EBSD), in conjunction with Field-Emission Environmental Scanning Electron Microscopy (FEG-ESEM), is used to evaluate the microstructural and local plastic strain evolution in different alloys (AISI 1005, AISI 304L and Duplex 2205) deformed by a single-stage cold and warm forging process. The main purpose is to describe, qualitatively and quantitatively, the austenite and ferrite different behavior during plastic deformation at different forging temperatures (i.e. from ambient temperature to 700 °C). Several topological EBSD maps are measured on the deformed and undeformed state and image quality factor, distributions of grain size and misorientation are analyzed in detail.

KEYWORDS

Low-carbon steel, Stainless steel, EBSD, Cold and warm forging, Twinning.

1. INTRODUCTION

Properties of metallic materials depend significantly on their microstructures. Two of the most important structural parameters affecting mechanical behaviour of various metals and alloys is the grain size and strain hardening.

During forging processes interconnected variables, such as strain, strain rate, strain distributions and temperature control how the microstructure evolves. Altan et al. [1] indicated the importance of deformation temperature by stating that above the recrystallization temperature of a formed metal, strain rate is the significant processing parameter, while below the recrystallization temperature, strain is the processing parameter of primary significance. Herzberg [2] defined metal deformation above the recrystallization temperature as hot-working. McQueen [3] revealed that for many metals there is also a transitional region of forming temperatures between hot working and cold working within which both strain and strain rate, as well as deformation temperature, interact to affect the resulting microstructure and mechanical properties. This intermediate temperature range is often called warm working range.

Recently, forging producers are increasingly using precision forging in which complicated parts can be formed directly in net shape or near-net shape in order to reduce cost. Particularly, in cold forging, materials with high formability are required and low carbon steels are widely used, since they can reduce the formation of cracks on forged parts [4].

In this scenario, stainless steels are an important class of alloys. Their importance is manifested in the plenitude of applications that rely on their use. The application of austenitic stainless steels in food, petrochemical and nuclear industries is due to their combination of good conformability, mechanical and corrosion resistance. In particular, AISI 304L steel is widely used, not only for its high corrosion resistance but also for its excellent formability and mechanical behavior. Many researchers have studied the changes in 304L stainless steel material behavior and microstructure under different conditions; its plastic deformation and corresponding microstructural evolution was found obviously different from static or dynamic loading conditions at high strain rate [5-9]. Another steel grade of great interest in forging industry is the Duplex Stainless Steel (DSS). DSS is a two-phase alloy (ferrite/austenite) which combine the properties of austenitic and ferritic stainless steels. The good combination of its mechanical properties and corrosion resistance makes it of great interest for a wide range of applications especially in the oil, chemical and power industry [10]. During the last years, in views of the great interest of forging industries on these materials, several studies on their formability were conducted. It is noted that its properties strongly depend on the microstructure and substructural changes of α and γ -phase during deformation under low and high strain rate conditions [11,12].

Grain boundary characters also play a key role in the plastic deformation of polycrystalline materials and a beneficial combination of mechanical properties can be attained by grain refinement. In particular, the mechanical properties of carbon and stainless steels can be improved by extensive fine-grained structures [13-16]. Such materials do not undergo phase transformations within a wide temperature range and small grain sizes can be produced by dynamic recrystallization (DRX) under warm or cold forging conditions [17,18]. Since the dynamic grain size sensitively depends on processing temperature, the fine-grained microstructures can be developed under warm deformation conditions, i.e. during plastic working at relatively low temperature from about 0.5 to 0.7 of melting point ($0.5-0.7T_m$) [19]. Recently, two main DRX mechanisms were found to operate in metallic materials with low stacking fault energy (SFE): discontinuous DRX (DDRX) and continuous DRX (CDRX). In the DDRX mechanism, the formation of a new grain

structure results from the operation of a grain boundary bulging, namely grain boundary serration and migration consuming the strain hardened substructures [20]. The recrystallized structure can be achieved by using conventional metal working techniques and consists of recrystallized and work hardened component [15,21,22].

The other type is the continuous DRX which operate mainly under conditions of warm working [23]. The new grains develop as a result of the gradual increase in the misorientations between the subgrains that are caused by the plastic deformation; thus, fine-grained materials cannot be produced by standard thermomechanical processing [17,19,20].

The present work is first aimed to describe, qualitatively and quantitatively, the differences in the plastic behavior of ferrite and austenite, during one-stage cold forging process to form an hex-head plug fitting used in thermo-hydraulic applications. The strain heterogeneities and microstructural evolution of γ -phase in AISI 304L and Duplex 2205 stainless steel during warm forging process at different temperatures (i.e. 400, 500, 600 and 700 °C) are also investigated. Finally, the strain hardening behavior of the steels at cold and warm working conditions is analyzed.

2. MATERIALS AND EXPERIMENTAL PROCEDURES

The chemical composition of the alloys analyzed (AISI 1005 (Wr. N. 1.0303), AISI 304L (Wr. N. 1.4307), Duplex 2205 (Wr. N. 1.4462)) are listed in Table 1.

In the as-received conditions the materials were obtained by continuous casting and then hot rolled down to a final bar diameter of 22 mm. AISI 304L and Duplex 2205 steel bars were solution heat-treated at 1150 °C and 1050 °C, respectively, and water-quenched in order to avoid precipitation of secondary phases.

Steel	C	Si	Mn	Cr	Mo	Ni	Cu	Co	N	Others	Fe
AISI 1005	0.051	0.07	0.30	0.11	0.02	0.13	0.17	0.01	0.01	<0.07	bal.
AISI 304L	0.031	0.35	1.32	18.66	0.40	8.11	0.49	0.12	0.09	<0.06	bal.
Duplex 2205	0.022	0.52	1.28	22.30	3.13	5.68	0.19	0.07	0.18	<0.05	bal.

Tab. 1. Chemical compositions of the materials analyzed (wt.%).

Fig. 1 shows the step-sequence of the analyzed one-stage forging process at different strokes. The process consisted of two forging phases: a first compression to create the hex-head (named "A-phase") and a second deep backward extrusion operation to form the "neck" of the plug fitting (named "B-phase"). Bottom punch was fixed during the forming cycle. Top punch and die were driven by press mechanism. Moreover bottom die was floating and driven by the contact forces.

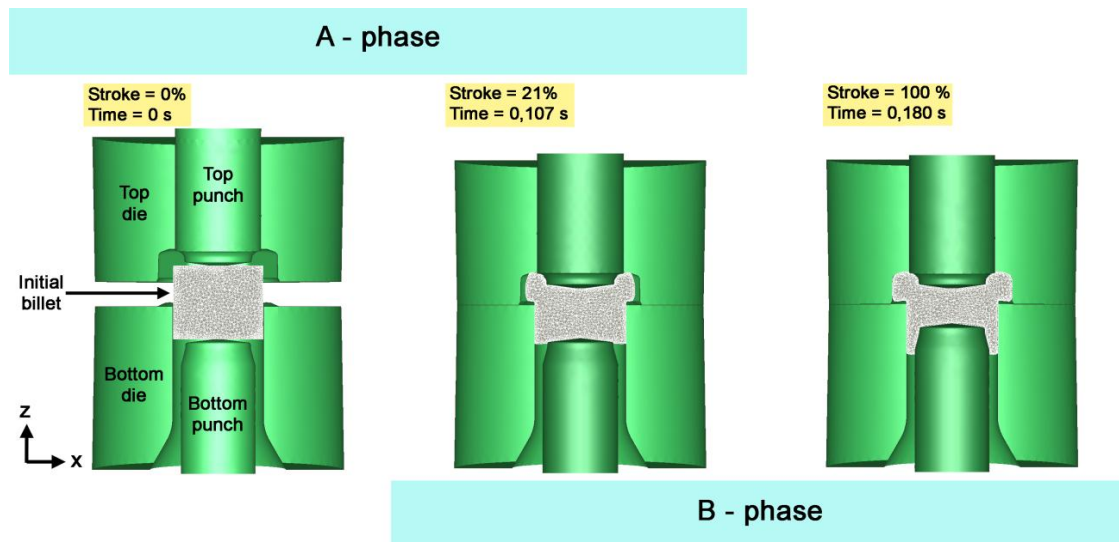


Fig. 1. Set-up of the single-stage forging test.

3D solid modeling of the workpiece (i.e. cylindrical billet, 18.3 mm height and 55 g weight) and tools were carried out by Pro/E[®] software and then imported into FORGE2011[®] numerical code.

Details about the numerical model such as materials rheology and friction conditions can be found in previous works [24,25]. 550 cylindrical billets (50 in AISI 1005, 250 in AISI 304L and 250 in Duplex 2205) were used for cold and warm forging experimental tests. Samples were forged by using a 2453 kN single-station general-purpose mechanical knuckle press with 50 spm.

2.1. Microstructural analysis

For a detailed understanding of the effects caused by cold and warm forging processes, metallographic longitudinal sections parallel to the compression z -axis (CA) were drawn from the cylindrical billets and forged samples at different temperatures (Fig. 2). The focus was set on the microstructural analysis of three areas corresponding to different strain levels, named *zone A* (no deformation), *zone B* (intermediate level of strain) and *zone C* (high strain level). Height reductions h (Fig. 2d) for each alloy at different forging temperatures are reported in Table 2.

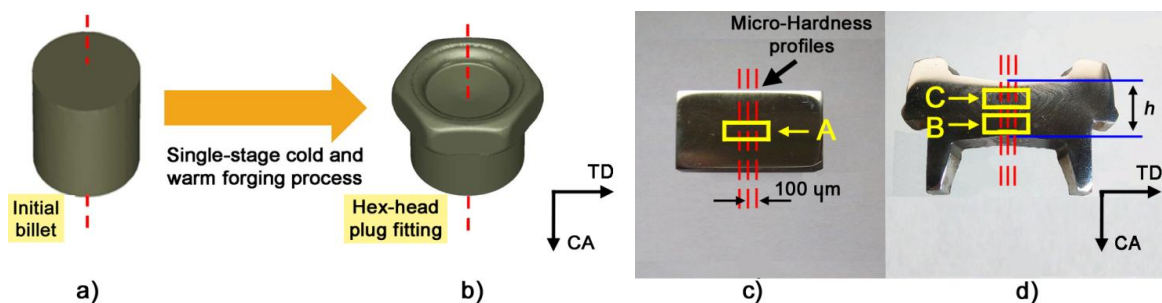


Fig. 2. CAD geometry of initial billet a) and hex-head plug b), longitudinal sections of real billet c) and forged component d).

Steel	Height reduction h [%]				
	20 °C	400 °C	500 °C	600 °C	700 °C
AISI 1005	96.1	-	-	-	-
AISI 304L	54.0	56.5	57.4	60.9	64.5
Duplex 2205	49.7	53.2	54.1	57.9	61.0

Tab. 2. Height reductions h at various forging temperatures.

For optical investigations and micro-hardness measurements, AISI 1005 specimens were etched with 4% HNO₃ in ethanolic solution; AISI 304L was etched with a reagent for electrolytic etching (a mixture of 60% HNO₃ and 40% distilled water) and Duplex 2205 samples were etched with Beraha etching solution (10 ml HCl, 40 ml distilled water, 1 g K₂S₂O₅). The micro-hardness tester Vickers Leitz Wetzlar D-35578 was used to perform three micro-hardness profiles, as shown in Fig. 2c-d. Measurements were carried out according to Standards ASTM E92-82 by using a load of 100 g. Microstructural investigation was also carried out by using a FEI Quanta 250 scanning electron microscope equipped with an electron back scattering diffraction (EBSD) analyzer incorporating an orientation imaging microscopy (OIM) system (EDAX TSL software, version 5). The surfaces of the undeformed and cold-warm forged specimens were prepared by using a polishing solution of 0.05 μm colloidal silica suspension and then electropolished in an electrolytic etching solution (60 ml HClO₄, 40 ml distilled water) at 20 °C to ensure the highest surface quality. Samples were placed in FEG-ESEM microscope immediately after preparation. In order to compare the strain levels of *zone A* and *B*, step and area size used in the EBSD scans were 50 nm and 300 x 300 μm² respectively; on the other hand, the comparison between *zone A* and *B* was made by using a step and area size of 70 nm and 150 x 150 μm², respectively. The OIM images were subjected to clean-up procedures by setting a minimal confident index of 0.1.

3. RESULTS AND DISCUSSION

3.1. Optical microscope observations at forging temperature of 20 °C

Fig. 3 shows the alloys microstructures before and after the cold forging test. In the as-received state (Fig. 3a - *zone A*) AISI 1005 is characterized by a ferritic microstructure with a low amount of pearlite and an average grain size of 21 μm; its hardness value was found to be equal to 128 ±3 HV_{0.1}. AISI 304L (Fig. 3b - *zone A*) shows the typical austenitic microstructure with twin boundaries; initial values of average grain size and hardness were found to be 42 μm and 207 ±4 HV_{0.1}, respectively.

Finally, the grain size and hardness of the ferritic-austenitic stainless steel (DDS 2205, Fig. 3c - *zone A*) were 9 μm and 245 ±6 HV_{0.1}, respectively. In the as-received state, a balanced amount of austenite to ferrite is observed.

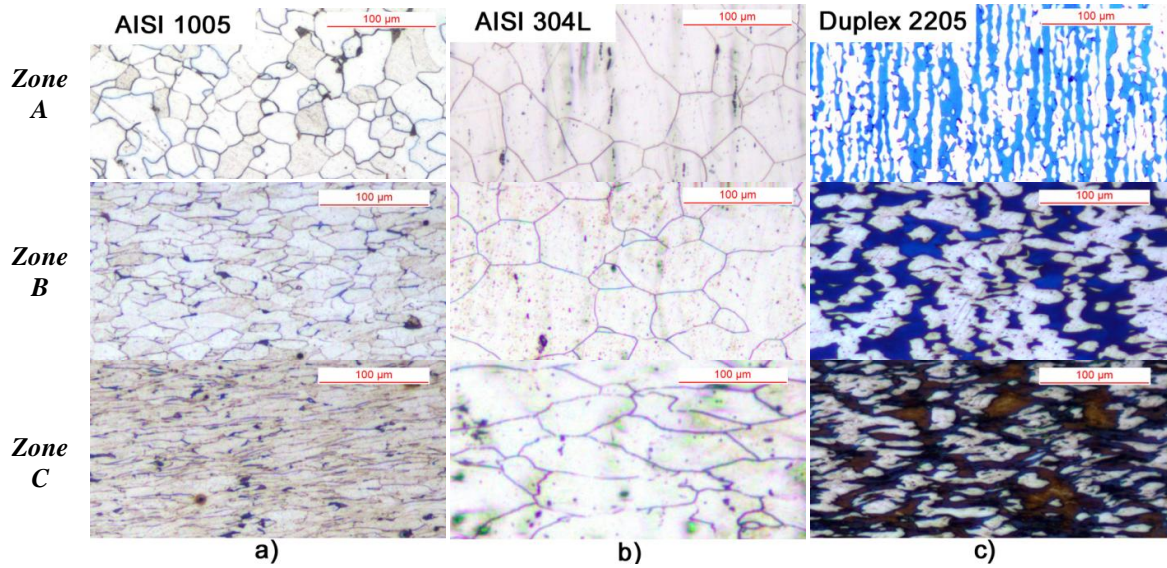


Fig. 3. Microstructure of a) AISI 1005, b) AISI 304L and c) DDS 2205 as a function of the analyzed zone (Figs. 2c and 2d).

3.2. Micro-hardness evolution at forging temperature of 20 °C

Micro-hardness profiles reveal different hardening intensities for cold forged tested steels (Fig. 4a). AISI 1005, due to the almost fully presence of α -phase, shows a nearly homogeneous hardening behavior. The highest mean values of hardness are observed on the area close to the contact surface between the top punch and the workpiece (Fig. 4a). This can be related to the combination of the material elastic-plastic properties (low strain hardening coefficient) and the forging technique used.

The cold forged stainless steel samples show an inhomogeneous hardening behavior with a hardness increase in zone C (Fig. 4a). For AISI 304L, the hardness values vary from 356 to 257 $HV_{0.1}$; while, they are in the range of 399 to 282 $HV_{0.1}$ in DSS. The highest hardness properties of the ferritic-austenitic stainless steel is mainly associated to the higher mean values of hardness reached on the as-received state ($\sim 245 \pm 6 HV_{0.1}$). Furthermore, due to the higher strain hardening coefficients of stainless steels compared to low carbon steel the deformation tends to localize in zone C forming a sort of barrier that prevents the flow to extend into other zones of the mold (Fig. 5). This is also confirmed by the distribution of the micro-hardness increase ($\overline{HV}_{0.1}[\%]$) (Fig. 4b) defined as:

$$\overline{HV}_{0.1}[\%] = \frac{\overline{HV}_{0.1}(\text{deformed}) - \overline{HV}_{0.1}(\text{as-received})}{\overline{HV}_{0.1}(\text{as-received})} \quad (1)$$

where $\overline{HV}_{0.1}(\text{deformed})$ and $\overline{HV}_{0.1}(\text{as-received})$ are the mean values of micro-hardness derived from the three profiles reported in Fig. 2c and 2d respectively, calculated at the same distance along the compression axis (CA). It easy to show that stainless steels are characterized by a rapid hardness increase from zone B to zone C. Even if DSS is characterized by a higher hardness value in the as-received conditions, which makes it more difficult to forge, it has a lower tendency to harden than AISI 304L steel (Fig. 4b). The highest strain hardening effect of the fully austenitic stainless steel is associated to the crossing of slip planes [27], twin boundaries formation [26], the increase of dislocation and stacking fault density in the deformed regions [28-29].

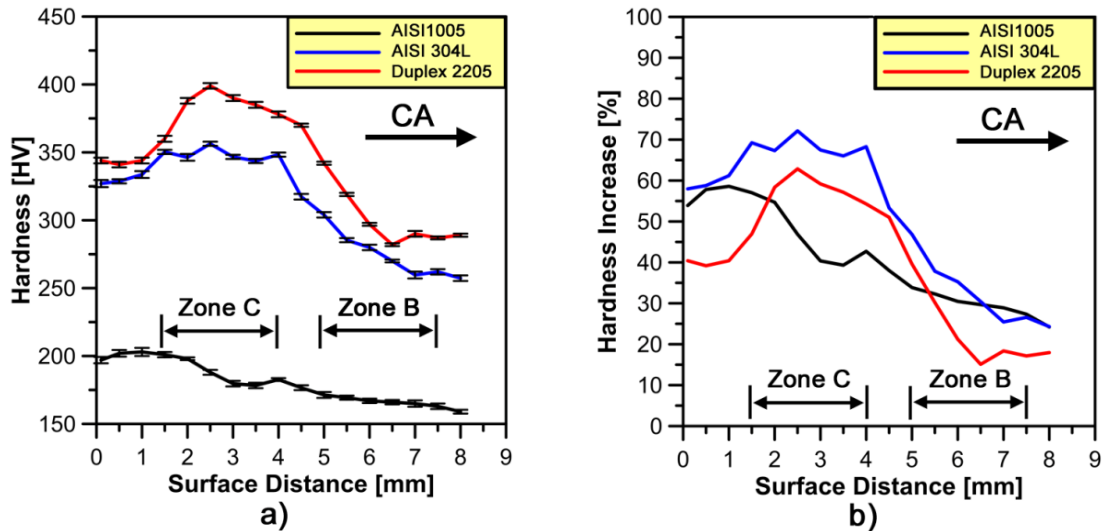


Fig. 4. Average a) micro-hardness profiles and b) trends of micro-hardness increase rate as a function of distance along the compression axis (CA). Data refer to the investigated steels.

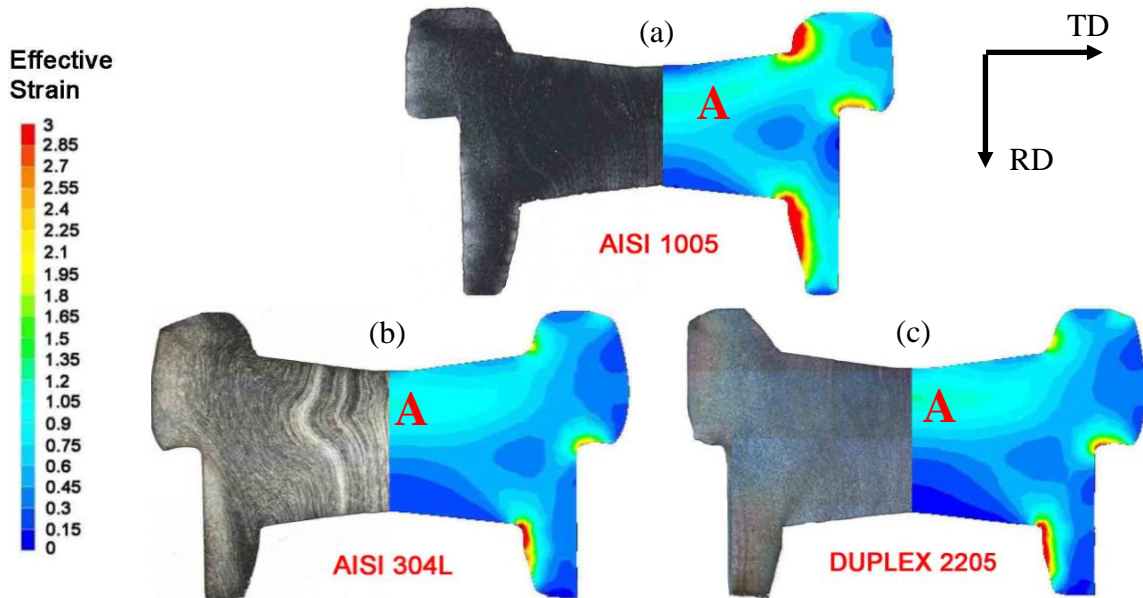


Fig. 5. Effective strain obtained by FE analysis.

3.3. Electron backscatter diffraction analysis at forging temperature of 20 °C

Several statistical analyses were performed on the EBSD data from each scanned area (zone A, B and C) in order to compare local plastic strain and grain evolution behavior of α - and γ -phase on the as-received and deformed steels considered.

3.3.1. Image quality (IQ) factor

At each measurement point in an OIM scan, a parameter quantifying the quality of the corresponding diffraction pattern is recorded. It is well known [30] that the image quality (IQ) is affected by residual strain in the diffracting volume. Thus, an indication of the distribution of strain in the material can be observed with an IQ map. For a large scanned

area on a bulk sample, if the average IQ value is assumed to correspond to the overall strain measured mechanically, then the local strain can be quantified by assuming a linear relationship between the IQ value and the local plastic strain. In this work, the quantitative evaluation method of the local plastic strain rate is based on the concept proposed by Tarasiuk et al. [31] by using IQ factor distributions. The idea is reported in Fig. 6. In each graph, two normalized IQ distributions are plotted which correspond to the undeformed and deformed sample. The total area under each distribution curve is equal to one since it includes all the points within the area under investigation used to estimate deformed and undeformed material volume fractions. By superposing these two plots, two areas are detected: *region X*, which corresponds to all the points deformed without ambiguity, and *region Y*, which corresponds to the still unreformed points (Fig. 6). The area of *region X* is used to estimate the minimal deformed volume fraction ($V_{f\ min}$) as (Eq. (2)):

$$V_{f\ min} = \int_{x:p(x)>q(x)} [p(x) - q(x)]dx \quad (2)$$

where $p(x)$ and $q(x)$ are the normalized IQ distributions for deformed and undeformed samples respectively.

Fig. 6 shows the IQ normalized distributions as a function of phase (ferrite, austenite) corresponding to the as-received (*zone A*) and cold forged (i.e. *zone C*) materials (the IQ distributions measured in *zone B* are directly used in the subsequent calculations of $V_{f\ min}$ fraction). In both phases, plastic strain leads to a shift of the normalized IQ distribution peak to lower values.

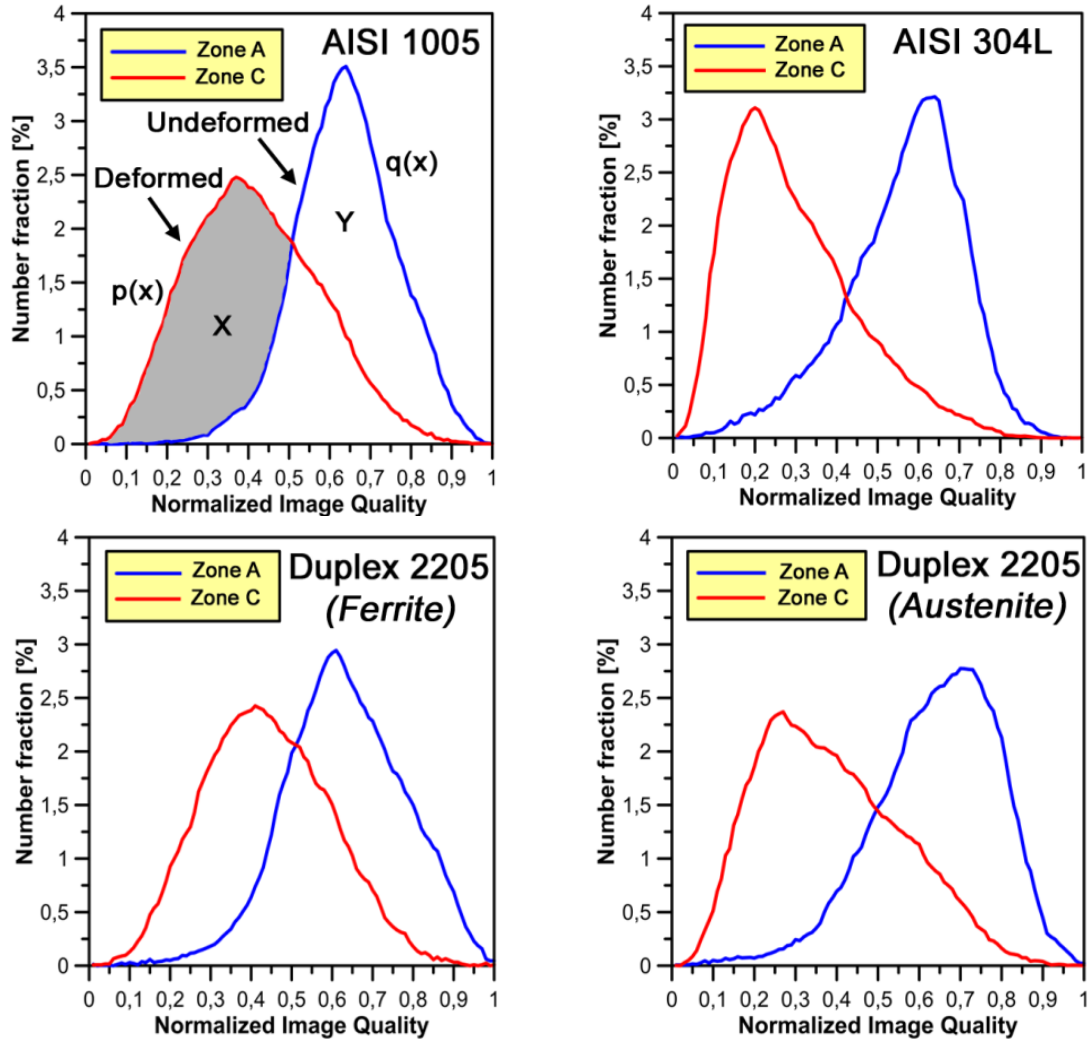


Fig. 6. Normalized IQ distribution for various degrees of strain at 20 °C for the two phases on the different steels investigated.

In Table 3 the $V_{f\min}$ fraction is estimated (Eq. (2)) by assuming that the as-received state of steels is deformation free ($V_{f\min} = 0\%$).

Investigated area	$V_{f\min}$ fraction [%]			
	α -phase [%]		γ -phase [%]	
	AISI 1005	Duplex 2205	AISI 304L	Duplex 2205
Zone B	12.3	24.7	14.3	25.8
Zone C	55.8	63.4	64.7	71.3

Tab. 3. $V_{f\min}$ fractions estimated in α and γ -phase after different strain levels.

From Table 3 it can be noted that the highest values of $V_{f\min}$ fraction are reached on γ -phase. This is confirmed by the average misorientation angles determined by EBSD that has been observed (in the present work and in a previous study [32]) to increase faster in γ -phase than in α -phase.

Variations of 44 to 39% in α -phase for AISI 1005 and Duplex 2205 steel and of 50 to 46% in γ -phase for AISI 304L and DDS 2205 are respectively observed; the difference is

attributed to the slightly higher tendency to work-harden of single-phase steels (AISI 304L) as mentioned above. Moreover, DDS 2205 shows the highest values of V_{fmin} fraction for both phases in *zone C*. This may be due to the highest micro-hardness values previously measured on that area.

3.3.2. Microstructural evolution at forging temperature of 20 °C

A detailed analysis of the misorientation angle distributions by EBSD for estimating the amount of low-angle boundaries (LABs) ($\theta = 2^\circ \div 5^\circ$) and high-angle boundaries (HABs) ($\theta > 15^\circ$) has been carried out. Fig. 7 and 8 show the histograms of LABs and HABs volume fractions as a function of the analyzed zone.

It is noted that the volume fraction of LABs increases and HABs decreases after a cold forging cycle in both phases. This can be attributed to the development of a sub-grains microstructure, characterized by dislocation walls, which forms during plastic deformation. With the exception of AISI 1005, an higher amount of LABs is revealed in the α -phase compared to γ -phase in the as-received state. This upholds the hypothesis of incomplete recrystallization of α -phase. On the other hand, HABs prevail in γ -phase. They form through the fragmentation of elongated grains, as provided after complete recrystallization.

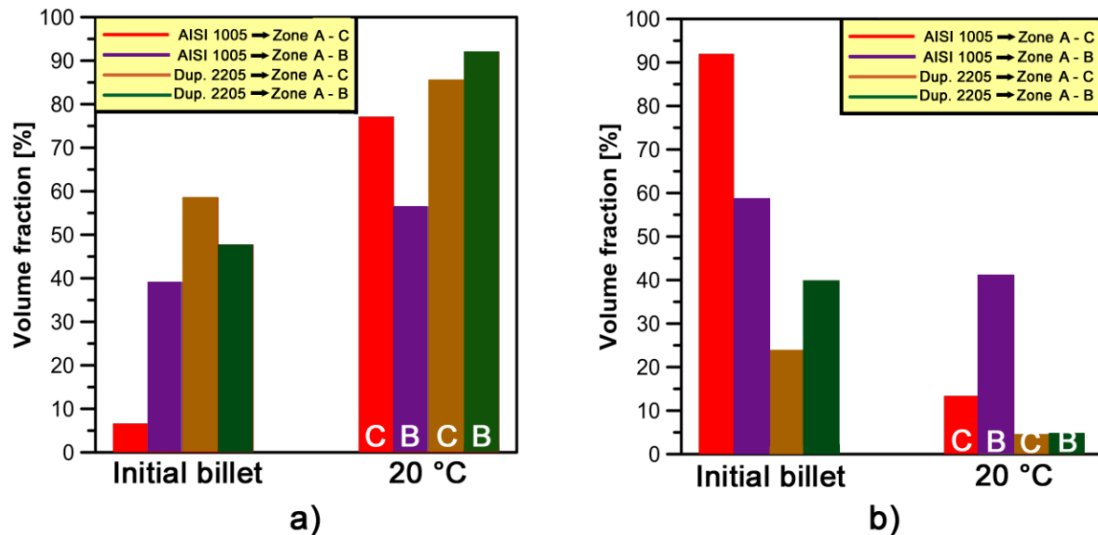


Fig. 7. Volume fractions of a) LABs and b) HABs developed in α -phase for AISI 1005 and DDS 2205 samples at 20 °C and different strain levels.

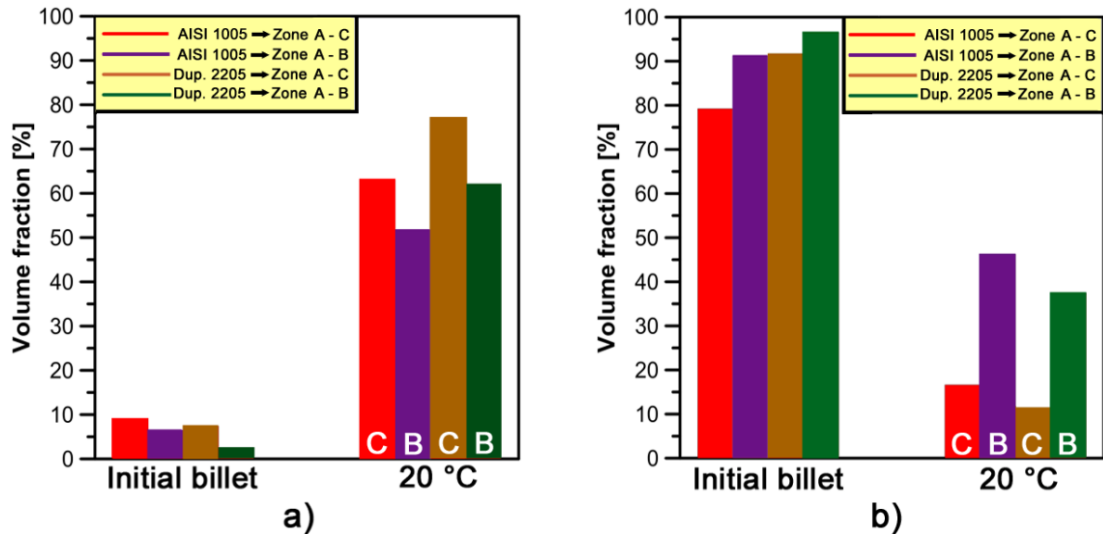


Fig. 8. Volume fractions of a) LABs and b) HABs developed in γ -phase for AISI 304L and DDS 2205 samples at 20 °C and different strain levels.

The variation of LAB and HAB fraction within a phase may depend on different parameters. In Fig. 9 the LABs increase of and HABs decrease is calculated as difference between the associated deformed (*zone B* and *C*) and undeformed (i.e. *zone A*) values reported in Fig. 7 and 8.

It can be observed in Fig. 8a that the highest increase of LABs volume fractions has been found on the α -phase of low carbon steel (*zone C*). This is due to the higher formability properties of this material compared to the stainless steels analyzed. It is also in good agreement with the high $V_{f\min}$ increase estimated on that phase for AISI 1005 (Table 3). On the other hand, the LABs fraction increase in *zone B* is higher for DDS 2205 compared to AISI 1005 steel as a consequence of the higher $V_{f\min}$ fraction value reached in that zone.

The increase of LABs volume fractions in γ -phase, on both deformed zones (~ 20 -25%), is higher in DSS 2205 than AISI 304L. This is due to the building up of higher amount of dislocation microstructure composed by sub-grains induced by the higher levels of strain ($V_{f\min}$ fraction) observed on γ -phase of DDS 2205 compared to AISI 304L. Moreover, the highest increase of LABs volume fractions noted on *zone C* (high strain area) for the stainless steels is directly related to their high strain-hardening behavior (Fig. 4b). A very similar histogram is observed for the HABs volume fractions decrease (Fig. 8b).

A detailed statistical analysis of the misorientation distribution angles across the so-called special γ -grain boundaries, i.e. those having dense Coincident Site Lattice (CSL), was also carried out. By using EBSD analysis, the CSL numbers (Σ) were measured by means of the following equation:

$$\Sigma = \frac{\text{number of coincidence sites } \varepsilon \text{ an elementary cell}}{\text{total number of all lattice sites } \varepsilon \text{ an elementary cell}} \quad (3)$$

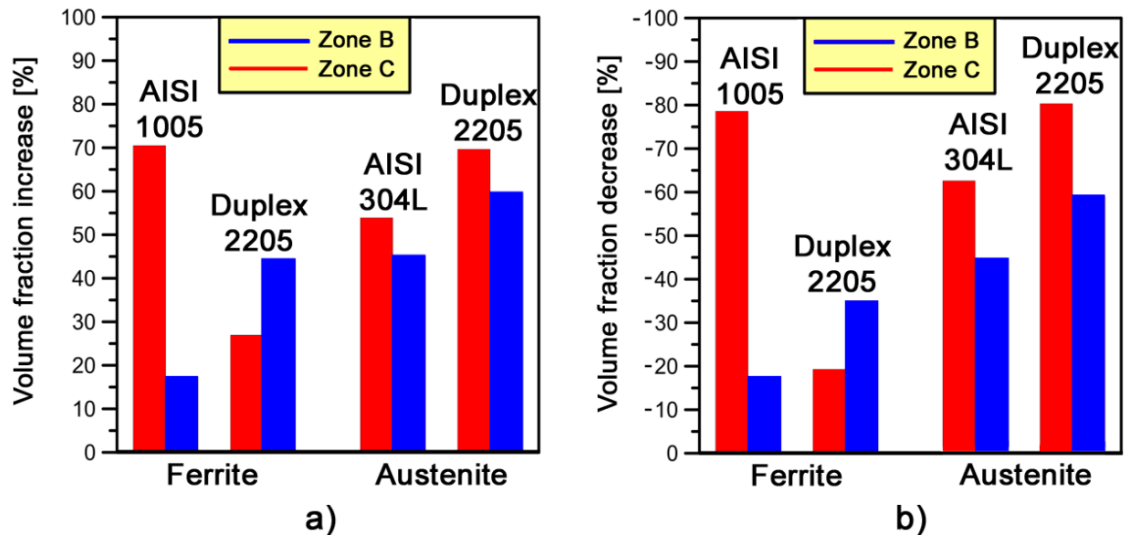


Fig. 9. a) LABs volume fractions increase and b) HABs volume fractions decrease on zones B and C for both phases.

In face centered cubic metals and alloys with low stacking fault energy (SFE), most of these special boundaries are $\Sigma 3$ or $\Sigma 3^n$ CSL boundaries related to twin boundaries. On *zone A*, about 59.2% and 65.9% of the HABs on AISI 304L and DSS 2205, respectively, display the first-order twin CSL orientation relationship $\Sigma 3$ (within a deviation of 2°) characterized by 60° rotation about $\langle 111 \rangle$ axis. About 3.2% of boundaries in AISI 304L and 3.0% of boundaries in DDS 2205 appear to correspond to the second-order twins represented by $\Sigma 9$ ($38.9^\circ/\langle 011 \rangle$) CSL orientation relationship.

On *zone B*, the γ -phase islands become slightly more elongated and locally fragmented compared to *zone A*. They show a tendency to become preferentially aligned at determined angles. The originally sharp peak in the γ -phase misorientation distribution centered on the ideal $\Sigma 3$ CSL orientation relationship becomes broader and the portion of first-order twin boundaries among the HABs decrease to about 55.8% and 64.7% on AISI 304L and Duplex 2205 steel, respectively.

As the plastic strain increases (i.e. *zone C*), the austenite islands become more elongated. The broadening of the original $\Sigma 3$ peak in the γ -phase misorientation distribution becomes more pronounced; the portion of the first-order twin boundaries among the HABs further decreases to about 14.3% and 12.3% on fully austenitic stainless steel and DDS 2205, respectively. The observed presence of second-order twin boundaries in the misorientation spectra is about 1.1% for AISI 304L and 2.0% for the duplex stainless steel. Table 4 summarizes the main fraction of CSL boundaries examined in the γ -phase; α -phase is practically free of them.

The present results show that pre-existing annealing twin regions within the austenite display a tendency to progressively rotate away from the ideal CSL orientation relationship during straining.

Thus, the corresponding originally straight coherent twin boundaries become gradually converted to general HABs during the deformation process. Similar results showing that such rotations appear to occur very early in the deformation process and might reach values of several tens of degrees at large strains have been reported by Cizek et al. [33].

Investigated area	CSL boundaries volume fraction [%]			
	AISI 304L		Duplex 2205	
	$\Sigma 3$	Total: $\Sigma 3 - \Sigma 49$	$\Sigma 3$	Total: $\Sigma 3 - \Sigma 49$
Zone A	59.2	68.1	65.9	73.7
Zone B	14.3	25.8	12.3	24.7
Zone C	55.8	63.4	64.7	71.3

Tab. 4. CSL boundary fractions parameter in the γ -phase.

4. EFFECT OF TEMPERATURE ON THE MICROSTRUCTURAL EVOLUTION OF γ -PHASE

4.1. Micro-hardness evolution on zones B and C at different warm forging temperatures

Fig. 10a-b show micro-hardness profiles on stainless steel samples forged at different temperatures. The effect of increasing temperature tends to continuously decrease the micro-hardness profiles on each type of steel (Fig. 10a-b). This behaviour is mainly associated with the lower presence of dislocation boundaries and densities at higher forging temperatures [22]. All micro-hardness profiles confirm the presence of the high strain-hardened area around *zone C* under the forging impact at different temperatures. This effect is less pronounced at higher forging temperatures tests.

In Fig. 11a-b, a comparison between micro-hardness profiles obtained at 20 °C and at different forging temperatures has been made on each stainless steel, in terms of the rate of decrease of micro-hardness measurements ($\overline{HV}_{0.1}$ [%]) estimated by Eq. (1).

As shown in Fig. 11b, Duplex 2205 has a lower tendency to decrease micro-hardness values at different forging temperatures than AISI 304L; moreover, the increase of temperature seems to drastically decrease the strain hardening effect on *zone C*. This behaviour is not clear on AISI 304L samples forged at 400 and 500 °C respectively, due to lower temperatures and similar micro-hardness profiles as compared to cold forged one.

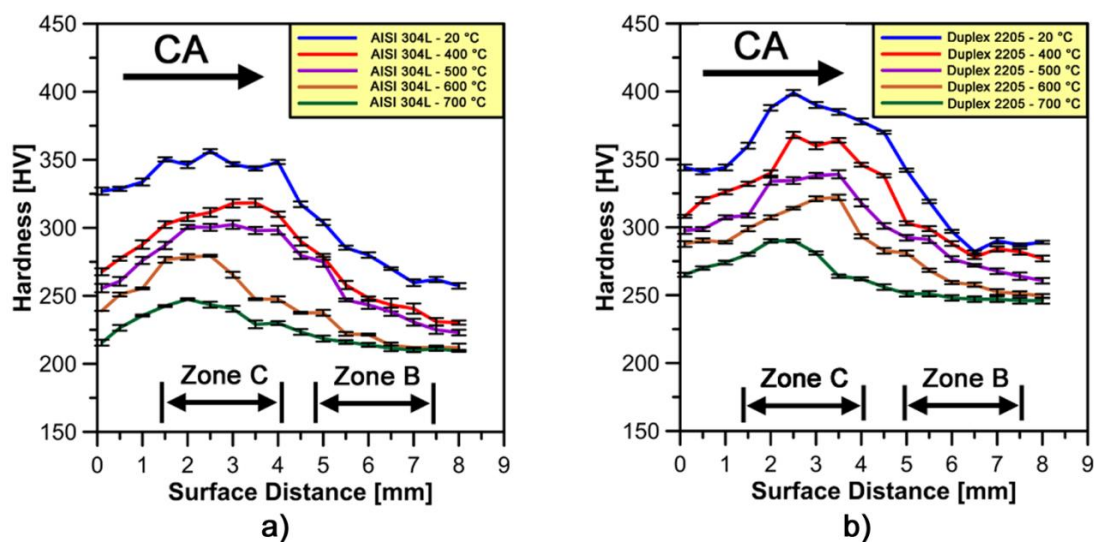


Fig. 10. Average micro-hardness profiles as a function of distance along the compression axis (CA) for a) AISI 304L and b) Duplex 2205 stainless steel.

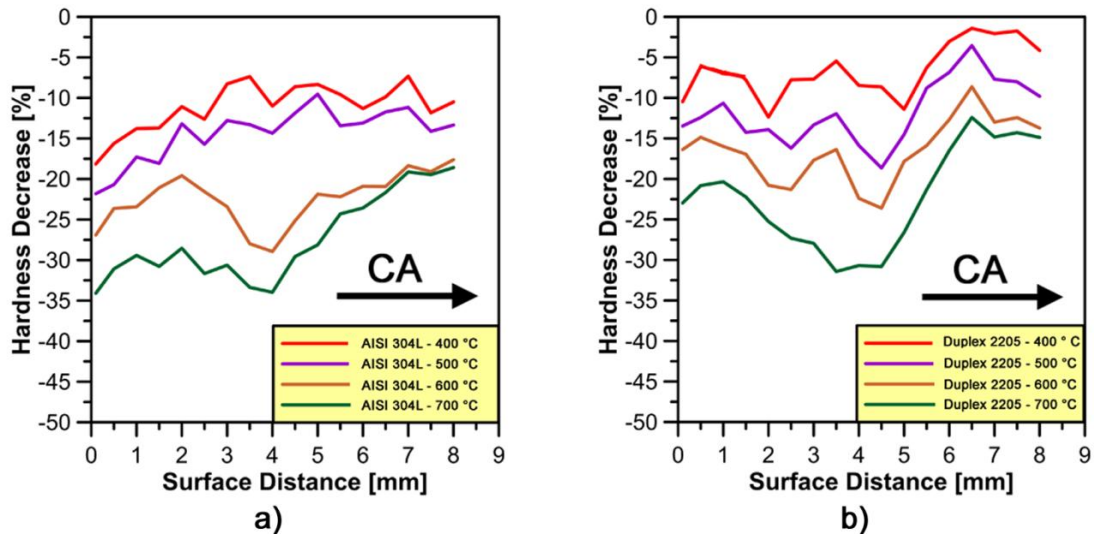


Fig. 11. Average trends of micro-hardness decreases as a function of distance along the compression axis (CA) for a) AISI 304L and b) Duplex 2205 stainless steel.

4.2. Electron backscatter diffraction analysis of zones B and C at different warm forging temperatures

4.2.1. Image quality (IQ) factor

Fig. 12 shows the trends of the $V_{f\ min}$ fractions for AISI 304L and Duplex 2205 stainless steel at different forging temperatures.

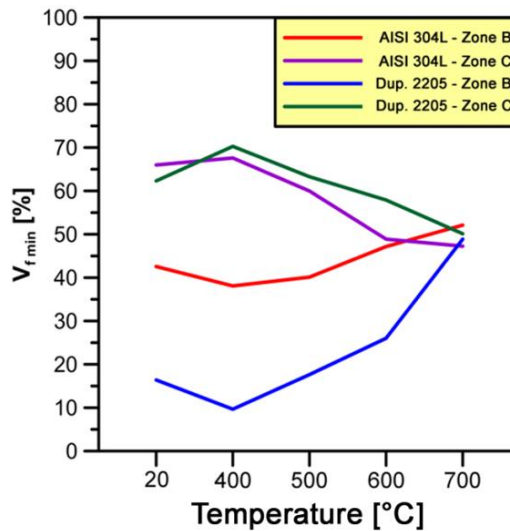


Fig. 12. Relationships between the minimum deformed volume fractions ($V_{f\ min}$) and forging temperatures evolved under cold-to-warm deformation of γ -phase in AISI 304L and Duplex 2205 stainless steel.

As can be seen in Fig. 12, the $V_{f\ min}$ fractions are almost constant with an increase in forging temperature from 20 to 400 °C on zone C in both steels analyzed; they slightly decrease on zone B. The warm-working temperature of 400 °C gives not enough relevant alteration and evolution on γ -grains and sub-grains structures at different levels of strain (i.e. zone B and C). In zone B, with an increase in temperature from 400 to 700 °C, the $V_{f\ min}$ fractions are in the range of 38 to 52% and from 10 to 49% in AISI 304L and Duplex

2205 steel respectively. On the other hand, in the same range of temperatures, the $V_{f\ min}$ fractions vary from 68 to 47% and from 70 to 50% in the austenitic and dual-phase stainless steel respectively. If this range of temperatures is considered, variations of 14 and 39% in $V_{f\ min}$ fractions are observed in *zone B* for AISI 304L and Duplex 2205 respectively. On the other hand, the raising of $V_{f\ min}$ fractions are almost constant and set at about 20% on *zone C* for both steels; it means that the γ -phase presents the same formability properties at different temperatures in both steels, for this metal working technique. In *zone B*, the different increase of $V_{f\ min}$ fractions on the two steels analyzed is a direct consequence of the forging process used. *Zone B* is the last zone of the workpiece to be deform and the lowest formability properties of Duplex 2205 steel involve lower $V_{f\ min}$ fractions at low temperatures as compared to AISI 304L steel. Through the effect of temperature increase, a reduction of $V_{f\ min}$ fractions gap between the steels analyzed is revealed and the formability properties of Duplex 2205 are greatly improved. As a matter of fact in Fig. 12, it is noted that γ -phase reaches almost similar $V_{f\ min}$ fractions at 700 °C in both steels considered.

4.2.2. Microstructural evolution of γ -phase on zones B and C at different warm forging temperatures

The deformation microstructures developed after one-stage forging process at temperatures of 20 °C, 400 °C, 500 °C, 600 °C and 700 °C are shown in Fig. 13.

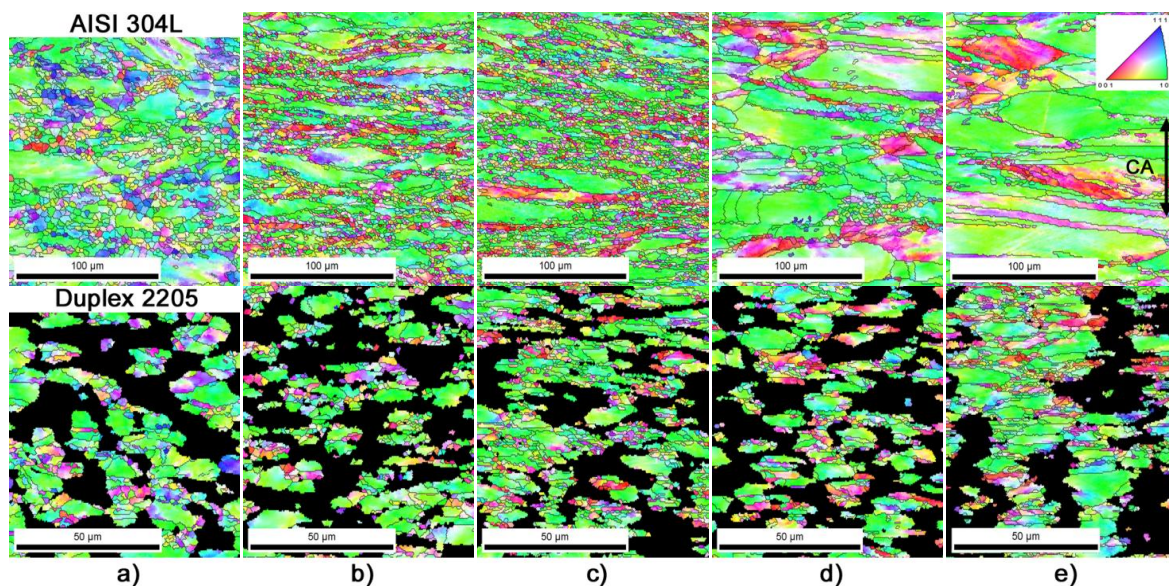


Fig. 13. OIM micrographs on *zone C* for deformed γ -phase microstructure evolved in the AISI 304L and Duplex 2205 steel processed by one-stage forging process at a) 20 °C, b) 400 °C, c) 500 °C, d) 600 °C and e) 700 °C. The inverse pole figure is shown for the compression z -axis (CA). The black lines indicate high-angle boundaries (HABs).

The single-stage warm forging process at all studied zones (i.e. *zone B* and *C*) and temperatures results in slight γ -grain refinement from 20 to 500 °C for each stainless steel considered. A non-uniform fine grained structure evolves in the samples processed at these temperatures in *zone B* and *C* analyzed, as reported in Fig. 14. The γ -grains, from 20 to 500 °C, are in the range of 3671 to 2285 μm^2 and from 267 to 77 μm^2 for AISI 304L steel in *zone B* and *C* respectively. At the same time, the average size of the γ -grains on Duplex 2205 steel changes from 116 to 58 μm^2 in *zone B* and from 25 to 12 μm^2 in *zone C*. The

microstructure at these temperatures is characterized by some heterogeneities. In addition to the equiaxed fine dynamic recrystallized (DRX) grains, these microstructures contain a low amount of large-elongated γ -grains with irregular boundaries, which are the remainders of the original grains.

At 600 °C and 700 °C, the microstructures are almost fully composed of fine nearly-equiaxed and large-elongated γ -grains, which are considered to be DRX grains. This is clearly shown in both deformed zones of the austenitic stainless steel analyzed. For Duplex 2205 stainless steel, the presence of minor unrecrystallized areas at 600 and 700 °C as compared to AISI 304L steel, involve rather homogeneous γ -grain size distributions on the deformed zones through different forging temperatures, as shown in Fig. 14b.

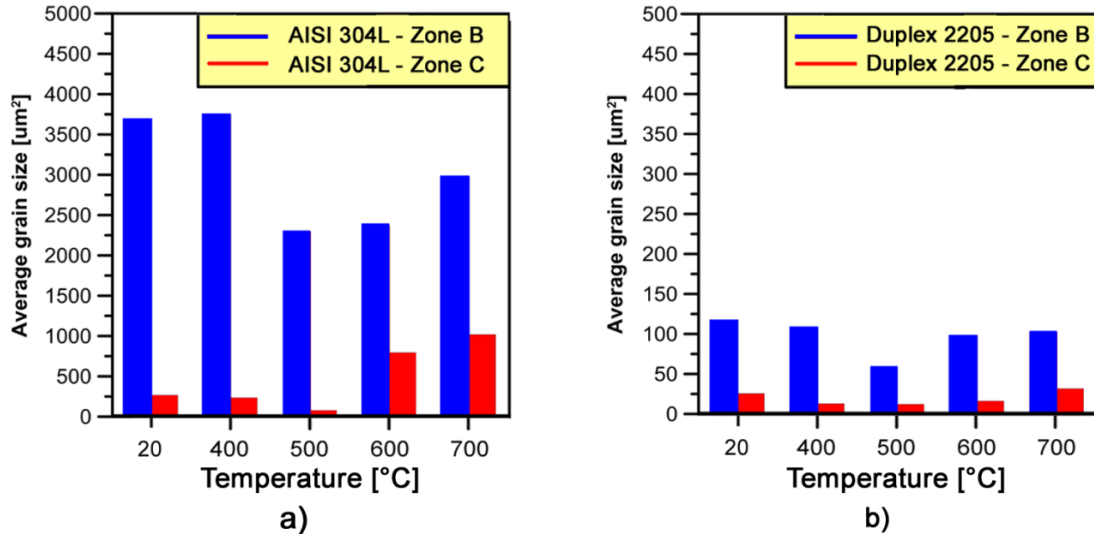


Fig. 14. Average γ -grain size distributions evolved in the a) AISI 304L and b) Duplex 2205 stainless steel after forming process on zone B and C at different forging temperatures.

Fig. 15 reports an examination of the boundary and sub-boundary misorientation distribution during deformation process at different forging temperatures, which shows that the fractions of LABs (i.e. $2 \leq \theta \leq 5^\circ$) and HABs (i.e. $15^\circ \leq \theta \leq 90^\circ$) tend to become almost similar at higher temperatures (i.e. 600 and 700 °C) for both deformed zones and stainless steels considered. The originally large differences between fractions of LABs on both deformed zones at 20 °C (i.e. ~12% for AISI 304L and 15% for Duplex 2205), decrease remarkably to about 6 and 2% on single-phase and dual-phase steel respectively at 700 °C. At this temperature the fractions of LABs vary slightly from 66 to 72% (Fig. 15a). On the other hand, in Fig. 15b, a very closed behaviour of HABs fractions are also revealed at different forging temperatures. At 20 °C the differences between fractions of HABs on both deformed zones are 30% for AISI 304L steel and 26% for Duplex 2205 steel, which decrease drastically to 1 and 5% on single-phase and dual-phase steel respectively at 700 °C.

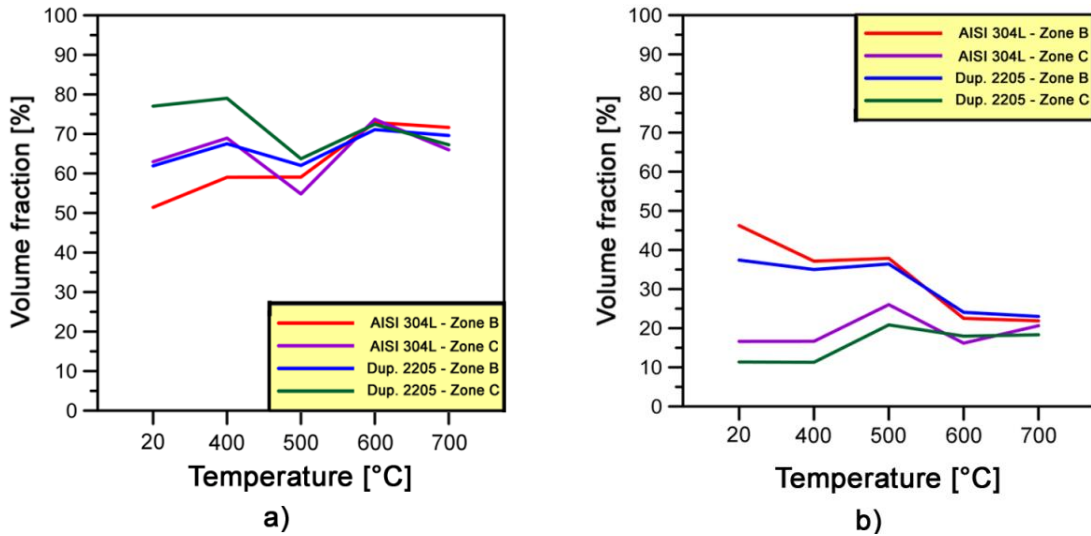


Fig. 15. Fractions of a) LABs and b) HABs estimated in both stainless steels at different forging temperatures.

As regards the specific misorientations which might be present within the stainless steels considered, the fraction of CSL boundaries has also been examined in the γ -phase. Resulting values are presented in Fig. 16. At lower temperatures (i.e. from 20 to 500 °C), the fraction of CSL boundaries decreases in both deformed zones and stainless steels analyzed. On *zone B*, $\Sigma 3$ boundaries fraction decreases from 56 to 45% for AISI 304L and from 68 to 59% for Duplex 2205 steel. Moreover it decreases from 14 to 9% and from 25 to 21% for austenitic and dual-phase stainless steel respectively on *zone C*. At the same time the percentage of total CSL boundaries decreases simultaneously on both deformed zones and stainless steel considered. On the other hand, the fractions of CSL boundaries at 600 and 700 °C increase as a consequence of the new grains nucleate as a result of local bulging of grain boundaries during the dynamic recrystallization (DRX) mechanism [34,35].

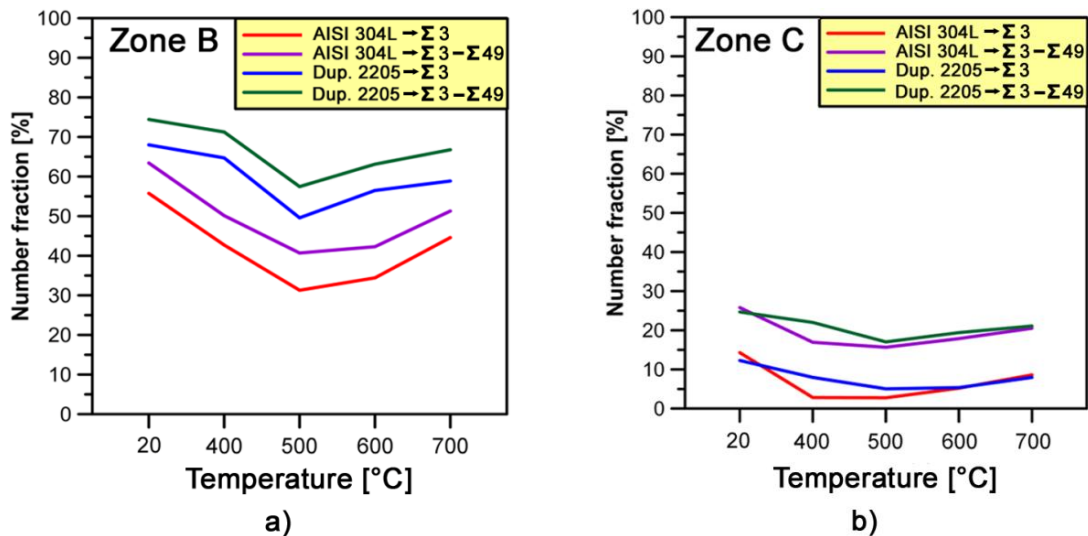


Fig. 16. Fractions of CSL boundaries in γ -phase estimated for both stainless steels at different forging temperatures.

5. CONCLUSIONS

The microstructural and local plastic strain evolution of α - and γ -phase in AISI 1005 low carbon steel, AISI 304L and DDS 2205 during single-stage cold forging test was investigated. Microstructural characterizations were carried out on samples both cold and warm forged with temperatures ranging from 400 °C to 700 °C.

The main results can be summarized as follows:

- The α -phase in AISI 1005 steel has a lower tendency to harden compared to γ -phase of AISI 304L steel. On the other hand, γ -phase tends to harden easier on austenitic than on duplex stainless steel. The highest strain hardening effect of γ -phase is associated to the crossing of slip planes, twin boundaries formation, the increase of dislocation and stacking fault density in the deformed regions.
- During the cold forging process, the estimated deformed volume fraction is higher in the γ -phase compared to the α -phase. Furthermore, the γ -phase grains deform more homogeneously than the initially large α -phase grains.
- Samples forged at 20 °C result in the development of fine grained microstructures. Low-angle boundaries (LABs) increase and high-angle boundaries (HABs) decrease, as a direct consequence of the dislocation microstructures formation.
- The γ -phase microstructure which develops during single-stage forging from 400 to 500 °C is characterized by fine grained microstructure at different strain levels. The fraction of special boundaries decrease rapidly from 400 to 500 °C for both stainless steel analyzed. On the other hand the microstructures of γ -phase detect at higher forging temperatures (i.e. 600 and 700 °C) are almost fully composed of large-elongated and fine nearly-equiaxed grains, which are considered to be discontinuous dynamic recrystallized (DRX) grains. Similar values of LABs and HABs fractions and annealing twins formation are observed on stainless steels investigated.

ACKNOWLEDGMENTS

The authors gratefully acknowledge Zoppelletto S.p.A. (Torri di Quartesolo, Vicenza, Italy) for the materials supply and assistance with experimental tests.

REFERENCES

- [1] Altan T, Boulger FW, Becker JR, Akgerman N, Henning HJ. Forging equipment, materials and practices. Batelle, Columbus, OH, USA, 1973.
- [2] Hertzberg RW. Deformation and fracture mechanics of engineering materials, fourth edition. John Wiley & Sons, Inc., New York, NY, USA, 1996.
- [3] McQueen HJ. The production and utility of recovered dislocation substructures. Metall Trans A 1977; 8A: 807-823.
- [4] Marchand A, Duffy J. An experimental study of the formation process of adiabatic shear bands in a structural steel. J Mech Phys Solids 1988; 36: 251-283.
- [5] Mataya MC, Brown EL, Riendeau MP. Effect of hot working on structure and strength of type 304L austenitic stainless steel. Metall Trans A 1990; 21(7): 1969-1987.
- [6] Harvey DP, Terrell JB, Sudarshan TS, Louthan MR. Participation of hydrogen in the impact behavior of 304L stainless steel. J Eng Fract Mech 1993; 46(3): 455-465.

- [7] Lee WS, Lam HF. The deformation behaviour and microstructure evolution of high-strength alloy steel at high rate of strain. *J Mater Proc Technol* 1996, 57: 233-240.
- [8] Lee WS, Lin CF. High-temperature deformation behaviour of Ti6Al4V alloy evaluated by high strain-rate compression tests. *J Mater Proc Technol* 1998, 75(1-3): 127-136.
- [9] Meyers MA, Chen YJ, Marquis FDS, Kim DS. High-strain, high-strain rate behaviour of tantalum. *Metall Mater Trans A* 1995; 26: 2493-2501.
- [10] Cabrera JM, Mateo A, Llanes L, Prado JM, Anglada M. Hot deformation of duplex stainless steels. *J Mater Process Technol* 2003; 143-144: 321-325.
- [11] Llanes L, Mateo A, Iturgoyen L, Anglada M. Aging effects on the cyclic deformation mechanisms of a duplex stainless steel. *Acta Mater* 1996; 44: 3967-3978.
- [12] Mateo A, Llanes L, Akdut N, Anglada M. High cycle fatigue behaviour of a standard duplex stainless steel plate and bar. *Mater Sci Eng A* 2001; 319-321: 516-520.
- [13] Valiev RZ. Nanomaterial advantage. *Nature* 2002; 419: 887-889.
- [14] Nakao Y, Miura H. Nano-grain evolution in austenitic stainless steel during multi-directional forging. *Mater Sci Eng A* 2011; 528: 1310-1317.
- [15] Yanushkevich Z, Mogucheva A, Tikhonova M, Belyakov A, Kaibyshev R. Structural strengthening of an austenitic stainless steel subjected to warm-to-hot working. *Mater Charact* 2011; 62(4): 432-437.
- [16] Andrievski RA, Glezer AM. Strength of nanostructures. *Phys-Usp* 2009; 52(4): 315-334.
- [17] Belyakov A, Sakai T., Miura H., Tsuzaki K. Grain refinement in copper under large strain deformation. *Phil Mag A* 2001; 81: 2629-2643.
- [18] Valiev RZ, Langdon TG. Principles of equal channel angular pressing as a processing tool for grain refinement. *Progr Mater Sci* 2006; 51: 881-981.
- [19] Dudova N, Belyakov A, Sakai T, Kaibyshev R. Dynamic recrystallization mechanisms operating in a Ni-20%Cr alloy under hot-to-warm working. *Acta Mater* 2010; 58: 3624-3632.
- [20] Humphreys FJ, Hatherly M. Recrystallisation and related annealing phenomena. Pergamon press, Oxford, 2004.
- [21] Yanushkevich Z, Belyakov A, Kaibyshev R. Structural changes in a 304-type austenitic stainless steel processed by multiple hot rolling. *Adv Mater Res* 2012; 409: 730-735.
- [22] Tikhonova M, Dudko V, Belyakov A, Kaibyshev R. The formation of fine-grained structure in S304H-type austenitic stainless steel during hot-to-warm working. *Mater Sci Forum* 2012; 715-716: 380-385.
- [23] Belyakov A, Tsuzaki K, Miura H, Sakai T. Effect of initial microstructures on grain refinement in a stainless steel by large strain deformation. *Acta Mater* 2003; 51(3): 847-861.
- [24] Bassan F, Ferro P, Bonollo F. Numerical process simulation and microstructural evolution of carbon and stainless steels forged components. Proc. of the 35th AIM National Conference, 2014, paper 114.
- [25] Bassan F. Optimization of industrial processes for forging of carbon and stainless steels. PhD Thesis; University of Padua, 2015 (In press).
- [26] Kocks UF, Mecking H. Physics and phenomenology of strain hardening: the FCC case. *Progr Mater Sci* 2003; 48: 171-273.
- [27] Neuhäuser H. Dislocations in solids. Amsterdam: North-Holland, 1983.
- [28] Mecking H, Kocks UF. Kinetics of flow and strain-hardening. *Acta Metall* 1981; 29: 1865-1875.

- [29] Sato S, Kwon EP, Imafuku M, Wagatsuma K, Suzuki S. Microstructural characterization of high-manganese austenitic steels with different stacking fault energies. *Mater Charact* 2011; 62: 781-788.
- [30] Wardle S.T., Lin L.S., Cetel A.D. & Adams B.L. Orientation imaging microscopy: monitoring residual stress profiles in single crystals using an imaging quality parameter, IQ. *Proc of the 52nd Annual Meeting of the Microscopy Society of America*, Bailey, G.W. & Garratt-Reed, A.J. (Eds.), San Francisco, CA: San Francisco Press, pp. 680-681.
- [31] Tarasiuk J, Ph Gerber, Bacroix B. Estimation of recrystallized volume fraction from EBSD data. *Acta Mater* 2002; 50: 1467-1477.
- [32] Badji R, Bacroix B, Bouabdallah M. Texture, microstructure and anisotropic properties in annealed 2205 duplex stainless steel welds. *Mater Charact* 2011; 62: 833-843.
- [33] Cizek P, Whiteman JA, Rainforth WM, Beynon JH. EBSD and TEM investigation of the hot deformation substructure characteristics of a type 316L austenitic stainless steel. *J Microsc* 2004; 213: 285-295.
- [34] McQueen HJ, Jonas JJ. Recovery and recrystallization during high temperature deformation. In: Arsenault RJ, editor. *Treatise on Materials Science and Technology*, Vol. 6. New York: Academic Press; 1975. p. 394-490.
- [35] Belyakov A, Sakai T, Miura H, Kaibyshev R. Grain refinement under multiple warm deformation in 304 type austenitic stainless steel. *Iron Steel Inst Jpn Int* 1999; 39: 592-599.

OTHER ACTIVITIES

ARTICLE VI

**INNOVATIVE RHEOCASTING PROCESSES
IN MG FOUNDRY**

expanded version of the paper:

**MICROSTRUCTURAL AND MECHANICAL
CHARACTERIZATION OF AM60B ALLOY
CAST BY RSF PROCESS**

F. Bassan, G. Timelli, F. Bonollo*

**University of Padua, Department of Management and Engineering,
Stradella S. Nicola, 3 I-36100 Vicenza, Italy*

Published in "Interall S.r.l.", 2013, pp. 58-67.

ABSTRACT

In the present work, the effects of different microstructural features on the mechanical properties of a traditional and semi-solid gravity sand cast AM60B alloy are investigated. The Rapid Slurry Forming (RSFTM) technology and a step casting geometry, with a range of thickness from 5 to 20 mm, have been used.

The results show that the microstructure of traditionally gravity cast step castings consist of primary α -Mg dendrites, while those cast at semi-solid state show the presence of quasi-globular α -Mg phase. Partially divorced α -Mg/ β -Mg₁₇Al₁₂ eutectic and fine intermetallic Al-Mn compounds, distributed among the interdendritic regions and along grain boundaries, are also revealed. Due to low solidification rate, discontinuous precipitations of Mg₁₇Al₁₂ into α -Mg grains take also place. The few micrometers size range of α -Mg grains, and the blocky morphology of α/β eutectic and Al-Mn compounds increase the mechanical properties of semi-solid alloy. Furthermore, lower fraction of α/β eutectic in the semi-solid castings tend to increase the mechanical properties.

KEYWORDS

Cast magnesium alloys, Semi-solid, Microstructure.

1. INTRODUCTION

Magnesium alloys are usually processed through different foundry processes due to their low formability near room temperature. Actually, the applicable methods are high-pressure die-casting and all kinds of gravity casting such as sand, permanent and semi-permanent mould casting. Other relevant production technologies are squeezing casting and semi-solid casting [1,2].

The High Pressure Die Casting (HPDC) has been the overall dominating technology for manufacturing Mg alloy components. However, improving the integrity of final products has been a continuous target by many researchers and companies for many years. Several solutions have been proposed and one of the most promising is to use semi-solid metal forming (SSM) processes.

Technologies for semi-solid processing can generally be divided into two basic routes: rheoforming and thixoforming [3].

In order to exploit the benefits of magnesium alloy, it is necessary to develop alternative processing that can effectively produce complex, high-precision casting with good mechanical properties at low expense. One of the latest technical developments in SSM technologies is the Rapid Slurry Forming (RSFTM) process [4], where high quality Mg slurry can easily produced in very short time.

Nowadays, semi-solid metal forming is mostly applied with high pressure [5,6]. In contrast, gravity sand casting has not been commonly used even though it has several advantages in small lots, complex parts or big parts [7].

The AM series alloys are among the most widely used magnesium alloys because of their excellent combination of ductility and strength. In these alloys, aluminium (Al) and manganese (Mn) are two primary alloying elements. Aluminium improves strength and hardness, and lowers the melting point for easy casting, and Manganese is mainly for improving the seawater corrosion resistance, by removing iron and possibly other heavy metal elements into relatively harmless intermetallic compounds [8]. However, the effects of Al and Mn contents on the microstructure and mechanical properties of SSM processed alloys is not completely clear. Moreover, no research focusing on the semi-solid gravity sand casting with AM60B has been reported even though this alloy has a good fluidity and castability, resistance to hot cracking and low solidification shrinkage [8].

This work aims to study the feasibility of semi-solid gravity sand casting with an AM60B alloy by the RSF technology and to understand the effects of the semi solid casting on the mechanical properties.

2. EXPERIMENTAL PROCEDURE

2.1. Alloy and traditional gravity casting

An AM60B magnesium alloy was studied in this paper. The chemical composition of the alloy, as obtained by an atomic emission spectrometer on separately poured samples is given in Table 1.

Alloy	Al	Mn	Si	Zn	Fe	Cu	Others	Mg
AM60B	5.75	0.27	0.031	0.039	0.001	0.003	<0.003	bal.

Tab. 1. Chemical composition of the alloy used in the present work (wt.%).

The geometry of the casting, with the front and the side views, is shown in Fig. 1. The step casting presented a range of thickness going from 5 to 20 mm and it was gated from the side of the riser, which also ensured a good feeding during the solidification.

This configuration allows to obtained a range of solidification rates and consequently different microstructures in the casting [9].

The weight of the casting is 0.492 kg, including the riser and the chamber.

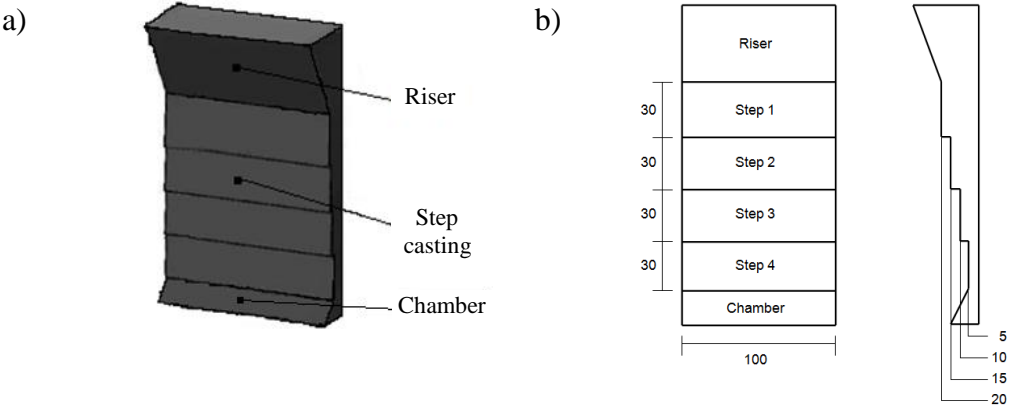


Fig. 1. (a) The step casting CAD geometry with (b) front and side views. All the measures are in mm.

The step castings were obtained by sand moulds, whose total dimensions were 230 x 190 x 125 mm³.

Two foundry technologies were used, that is the traditional gravity sand casting and RSF technology. In the first one, the AM60B alloy was first melted in a graphite crucible using an electric crucible furnace set at 750 °C, under a cover gas. About 4.5 kg of material was melted. The cover gas was moisture mixture of 50% CO₂ + 0.2% SF₆ + 49.8% Air.

Before pouring, the sand moulds were preheated up to ~100 °C. When the melt temperature was steady at 750 °C, a certain amount of liquid alloy (~1.5 kg) was gently taken using a preheated boron nitride coated steel ladle and poured to fill a series of 3 tilt-poured sand moulds, placed with an inclination angle of 60° to the horizontal as shown in Fig. 2. The castings were then allowed to cool up to room temperature inside the sand mould.



Fig. 2. Sand mould tilted 60° from horizontal.

2.2. Rapid Slurry Forming (RSFTM) process

In order to better explore the potential of the RSF technology, a series of semi-solid gravity sand step castings were obtained.

The RSF process is an innovative and cost effective way of forming semi-solid metal slurries to be used in casting processes for manufacturing high quality Mg components. The RSF is based on the enthalpy control instead of the temperature control for the production of the desired solid fraction in the metal slurry production. Two masses of the same alloy with different enthalpy are mixed together. While one mass is low superheated (high enthalpy), the other acts as a cold solid stirring material (low enthalpy). The solid stirring material is generally named Enthalpy Exchange Material (EEM) [4].

The three steps of the process for the slurry production by using the RSF are shown in Fig. 3 [10].

In the semi-solid gravity sand casting, the AM60B alloy was melted and used to produce the EEMs. The produced EEMs had a conical shape with a constant weight of 0.225 kg, in accordance with Ref. [11]. The rotation speed of EEM was set at 1200 rpm.

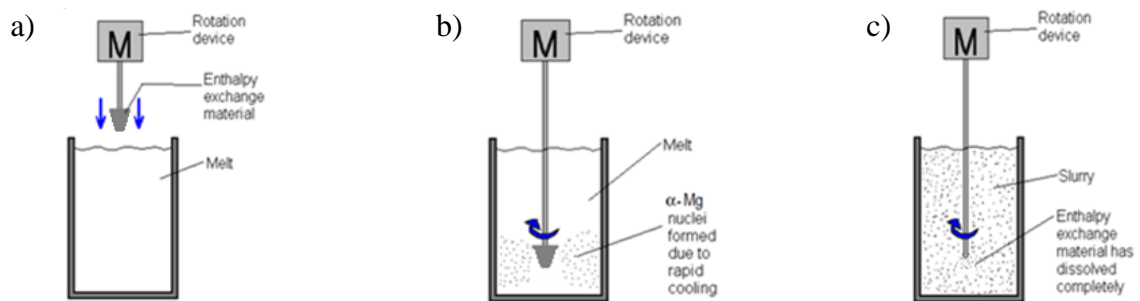


Fig. 3. The three process steps of the RSF process: (a) the solid EEM is submerged into the melt, (b) the EEM is stirred in the melt, causing formation of solid nuclei, (c) complete dissolution of EEM has occurred and slurry is formed.

The melt was prepared in a graphite crucible using an electric furnace set at 750 °C, under a cover gas and sand molds were preheated up to ~100 °C. The temperature of molten bath was then decreased and stabilized at 640 °C. The EEM was submerged into the melt and the stirring started and continued for 15-20 s until all the EEM had melted away. Thus, an homogeneous AM60B slurry had formed and steady at a temperature of 613 ± 1 °C. During slurry making, a K-type thermocouple was submerged into the bath to control the thermal history.

When the temperature of the slurry was at 613 °C, a similar pouring technique and cooling method were used.

2.3. Metallographic observation and mechanical testing

Traditional and semi-solid gravity sand castings were then sectioned and samples were drawn from the each step for metallographic investigations.

Flat tensile specimens with rectangular cross section have been obtained from the middle and external zone of the castings as indicated in Fig. 4. In this way it was possible to study the effect of the local temperature and the heat transfer on the solidification rate and, thus, on the microstructure and mechanical properties. The tensile specimens had a length of 100 mm and thickness of 3 mm, while the gauge length was 30 mm and the width was 10 mm. The tensile tests were done on a MTS 810 computer-controlled tensile testing machine.

The crosshead speed used was 2 mm/min (strain rate $\sim 10^{-3} \text{ s}^{-1}$). The strain was measured using a 25-mm extensometer.

For the analysis reported in this paper, at least ten specimens were tested for each zone of the casting. The best values in terms of Quality Index [12], were selected in an attempt to minimise any effects arising from casting defects on the fracture data and mechanism [13,16], and to maximize the chance of isolating the effects of microstructural components.

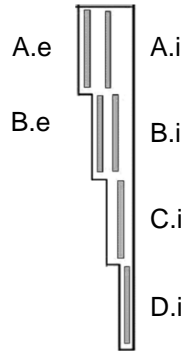


Fig. 4. Side view of the step casting showing sectioning scheme.

The microstructure of samples was studied and analyzed using optical microscopy (OM) and scanning electron microscopy (SEM) equipped with energy dispersive X-ray spectroscopy (EDS).

Samples were drawn from the cross section of the gauge length and mechanically prepared by grinding with SiC abrasive paper and polishing with a commercial fine silica slurry for metallographic investigations. Microstructural analysis was carried out using a LEICA DM2500M optical microscope and quantitatively analyzed using a LEICA LAS image analyzer. All samples were etched for a few seconds in a solution of 50 mL ethanol, 1 mL nitric acid and 0.7 mL phosphoric acid.

To analyse and quantify the microstructural features, the image analysis was focused on the area fraction and aspect ratio of the secondary phases and intermetallic particles (*i.e.* α -Mg/ β -Mg₁₇Al₁₂ eutectic and Al-Mn intermetallic compounds) and on size of the crystal grains. Size is defined as the equivalent circle diameter (d); the aspect ratio (α) is the ratio of the maximum to the minimum Ferets. The grain size was measured using the intercept method, according to the ASTM-E112 specification.

3. RESULTS AND DISCUSSION

3.1. Microstructural observations

The microstructure of traditionally gravity castings consists of primary α -Mg dendrites nucleate inside the undercooled liquid, with Al cored to the interdendritic regions. Equiaxed α -Mg grains with a rosette-like globular morphology were formed with the enrichment of Al content in solid solution between the dendrite arms, due to low solidification rate (Fig. 5a). The castings produced at semi-solid state show the presence of primary quasi-globular α -Mg phase formed inside the crucible during the RSF (Fig. 5b).

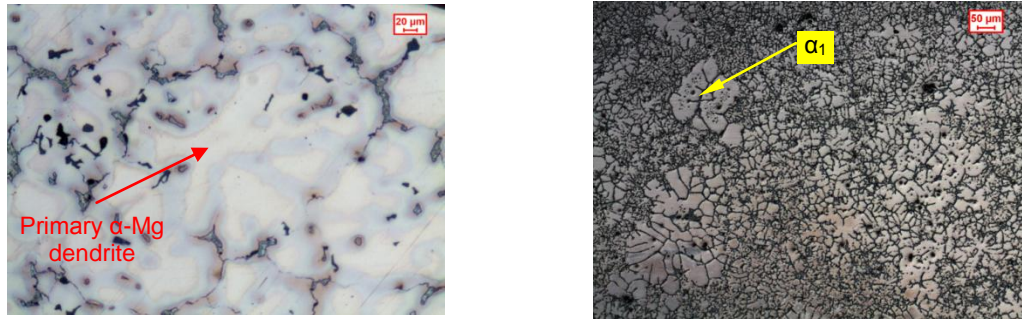


Fig. 5. Typical microstructure of (a) traditional gravity cast and (b) semisolid cast AM60B alloy; the different size and shape of primary α -Mg phase is evidenced.

It was found that the solid fraction, mainly composed by primary α -Mg phase (Fig. 5b), was about 36%, in accordance with the literature [17,18]. The addition of small amount of alloying elements such as Mn has a little effect on the nucleation of the primary α -Mg crystals since this element mostly segregates to form secondary phases [19]. A general coarsening of microstructure occurs by increasing the step thickness, as the result of the increased solidification time. For every section thickness, the microstructure were finer in the samples drawn from the external section than the specimens from the inner one.

Fig. 6a shows the secondary phases and intermetallic particles observed in the casting processed with both technologies. The EDS analysis confirmed that the structure with a sponge-like appearance is a partially divorced α -Mg/ β -Mg₁₇Al₁₂ eutectic, while the blocky intermetallics (Fig. 6b) and the particles with a lamellar morphology (Fig. 6c) are Al-Mn compounds and discontinuous Mg₁₇Al₁₂ precipitates respectively.

Due to the low diffusion rate of Al atoms into the α -Mg matrix and the middle cooling rate, the solidification of the AM60B alloy proceeded under non-equilibrium conditions, and a certain amount of non-equilibrium eutectic was detected. The eutectic exhibits a wide range of morphologies in hypoeutectic Mg-Al alloys depending on composition and cooling rate [19,20]. In this work, a partially divorced α -Mg/ β -Mg₁₇Al₁₂ eutectic morphology was observed, characterized by islands of eutectic α -Mg within the β -Mg₁₇Al₁₂ phase; while the bulk of the α -Mg is still outside the Mg₁₇Al₁₂ particles, *i.e.* the volume fraction of α -Mg within the Mg₁₇Al₁₂ particle is much lower than the proportion predicted by the equilibrium phase diagram.

A large number of fine intermetallic Al-Mn compounds distributed among the interdendritic regions and along grain boundaries, probably due to the presence of small amounts of Mn, were also revealed. These particles have been observed in AM series alloys by several researchers, but their identification is still uncertain. Sohn *et al.* [21] simply state that this is an intermetallic compound containing Al and Mn, whereas Wang *et al.* [22] identify the phase as Al₈Mn₅.

Completion of eutectic solidification does not mark the end of phase transformations in AM60B alloy investigated. The solidification rate is sufficiently slow (typical of sand-casting) and precipitation occur in the supersaturated areas of the α -Mg crystals. This precipitation may take two forms, continuous and discontinuous. In the present work, the precipitation shows a discontinuous form (Figg. 6a,d). This involves the growth of lamellar Mg₁₇Al₁₂ precipitates into α -Mg grains with a similar mechanism of pearlite into austenite grains during the cooling of steel. The Al partitions to the Mg₁₇Al₁₂ lamellae as they grow, leaving the α -Mg between the lamellae much leaner in Al than before discontinuous precipitation commenced. The discontinuous precipitation appears to grow from near the eutectic β -Mg₁₇Al₁₂ into the α -Mg grains, but whether the precipitates actually have the same orientation as the Mg₁₇Al₁₂ phase, or whether they nucleate separately in the

supersaturated α -Mg phase (e.g. on dislocation) has not been confirmed. Discontinuous precipitation occurs mostly in the α -Mg regions near the β -Mg₁₇Al₁₂ phase, since these regions have higher Al contents (approx. 10-13 wt.% Al) than the centre of the primary α -Mg dendrites, where the Al concentrations may be as low as 2 wt.% Al [23].

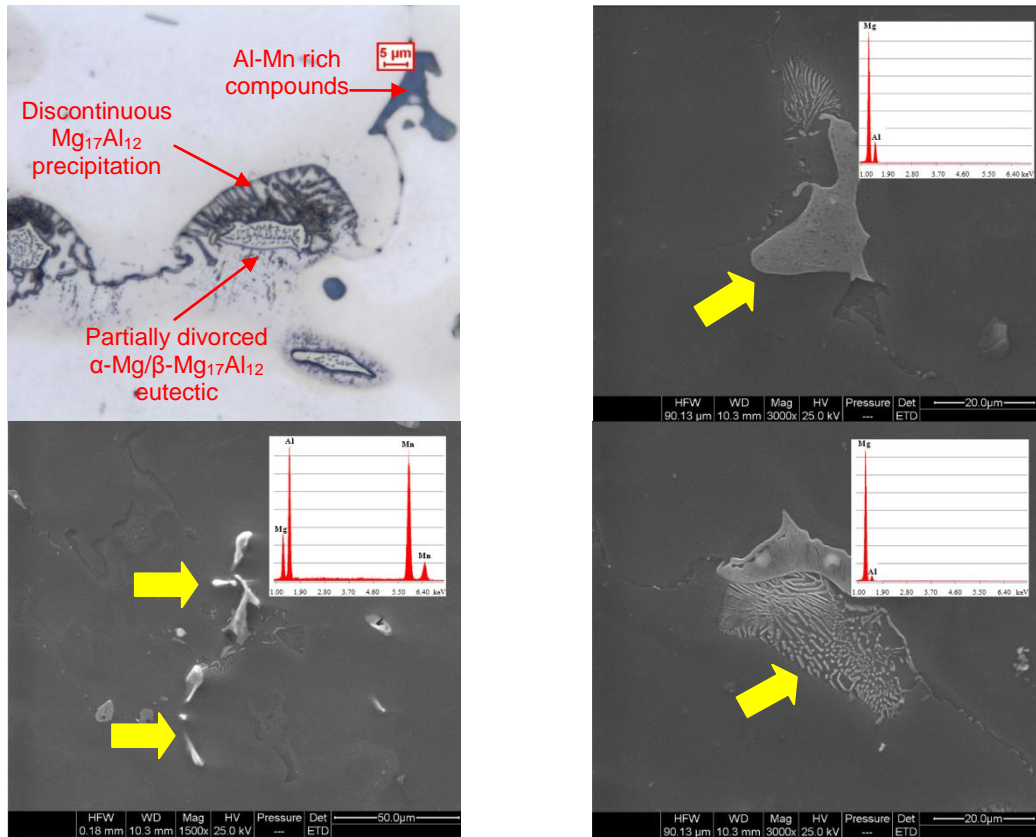


Fig. 6. (a) Secondary phases and intermetallic particles observed in the step castings; SEM micrographs with corresponding EDS spectra of (b) α/β eutectic, (c) intermetallic Al-Mn compounds and (d) discontinuous precipitates of Mg₁₇Al₁₂.

3.2. Tensile testing

The mean values and the standard deviation of yield stress (YS, actually 0.2% proof stress), ultimate tensile strength (UTS) and elongation to fracture (s_f) are summarized in Table 2. The low values of standard deviation confirm the presence of a low amount of casting defects, which can affect the mechanical properties [24].

Section	Conventional casting		Semi-solid casting	
	UTS [MPa]	s_f [%]	UTS [MPa]	s_f [%]
A.i	161 (8)	4.45 (0.52)	180 (13)	4.92 (0.72)
A.e	154 (10)	5.08 (0.87)	181 (10)	5.26 (0.83)
B.i	172 (11)	5.39 (0.86)	190 (12)	6.16 (1.44)
B.e	165 (13)	5.87 (0.68)	175 (9)	6.13 (1.36)
C.i	178 (12)	5.47 (0.97)	190 (14)	6.98 (1.47)
D.i	170 (9)	4.92 (0.62)	187 (15)	4.75 (0.69)

Tab. 2. Average mechanical properties obtained from different sections of the step castings (standard deviation in parentheses). Data refer to traditional and semi-solid gravity cast step castings.

If different sections are considered and compared, a reduction of 14 and 8% in UTS and 25 and 32% in elongation to fracture is observed for the traditional and semi-solid alloy respectively, as a consequence of the different microstructural scale. In the traditional gravity castings, the UTS varies from 154 to 178 MPa and the elongation to fracture from 4.5 to 5.9%, while the change is in the range of 175 to 190 MPa for UTS and from 4.8 to 7.0% for elongation to fracture, in the semi-solid gravity castings. On the other hand, different solidification times seem to not affect the YS of the alloy. In semi-solid castings, the mean YS is about 83 MPa independently from the step thickness, while in traditional castings the mean YS is 81 MPa, except for the outer zone of the castings where the presence of higher amount of brittle α -Mg/ β -Mg₁₇Al₁₂ eutectic and microdefects, induce even lower values of YS.

To relate the microstructural features with the mechanical behavior of AM60B alloy, the grain size can be firstly considered. It is well recognized how finer grains are beneficial in terms of mechanical properties for a material [25]. Consequently, it is not difficult to understand that the few micrometers size range of α -Mg grains observed in semi-solid castings generally increases the final mechanical properties, as reported in Fig. 7.

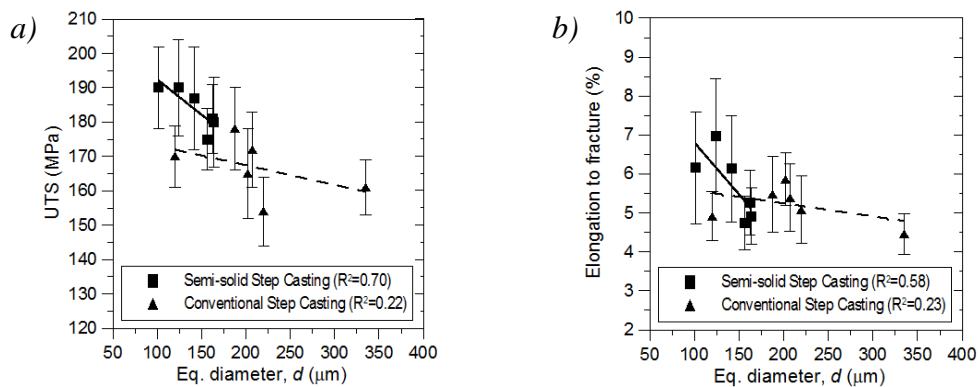


Fig. 7. Average (a) UTS and (b) elongation to fracture as a function of equivalent diameter of grains. Data refer to traditional and semi-solid gravity cast step castings.

4. CONCLUSIONS

In the present work, the potential and the feasibility of an innovative rheocasting process in Mg foundry is examined. In particular, the effects on microstructure and mechanical properties of a traditional and semi-solid gravity sand cast AM60B alloy have been investigated. Based on the results obtained in the present study, the following conclusions can be drawn.

- Nearly defect-free castings can be produced using RSF technology.
- The microstructure of traditionally gravity cast step castings consist of primary α -Mg dendrites, while those cast at semi-solid state show the presence of quasi-globular α -Mg phase. Partially divorced α/β eutectic and fine intermetallic Al-Mn compounds, distributed among the interdendritic regions and along grain boundaries, are also revealed.
- The few micrometers size range of α -Mg grains increase the mechanical properties of semi-solid alloy, in terms of UTS and elongation to fracture.

ACKNOWLEDGEMENTS

This work was developed with the financial support of Fondazione CARIPLO within the Project “Rivestimenti a base di polimeri conduttori e silani per la protezione di leghe leggere” (grant n° 2010.0458 CUP G41J11000150003).

REFERENCES

- [1] H.E. Friedrich, B.L. Mordike, “Magn. Tech.”, Springer, Germany, (2005).
- [2] S. Kleiner, O. Beffort, A. Wahlen, P.J. Uggowitzer, “J. Light Met.”, 2 (4), pp. 277-280, (2002).
- [3] A. Fadavi Boostani, S. Tahamtan, “J. Alloys Compd.”, 481, pp. 220-227, (2009).
- [4] M. Wessén, H. Cao, “Metall. Sci. Tech.”, vol. 25, No. 1, pp. 22-28, (2007).
- [5] S. Ji, Z. Fan, M.J. Bevis, “Mat. Sci. Eng.”, A299, pp. 210-217, (2001).
- [6] Guo Hong-min, Yang Xiang-jie, Wang Jia-xuan, “J. Alloys Compd.”, 485, pp. 812-816, (2009).
- [7] Kirkwood David H., Suery Michel, Kapranos Plato, Atkinson Helen V. and Young, Kenneth P, “Semi-solid Processing of Alloys”, Springer Series in Materials Science, 124, pp. 48-56, London, (2009).
- [8] M.M. Avedessian, H. Baker, “Magnesium and Magnesium Alloys”, ASM International, Materials Park, OH, 14-16, pp. 90-92, (1999).
- [9] F. Grosselle, G. Timelli, F. Bonollo, A. Tiziani, E. Della Corte, “Metall. Ital.”, 6, pp. 25-32, (2009).
- [10] H. Cao, M. Wessén, “International patent application”, No. PCT/SE2005/001889.
- [11] M. Wessén, H. Cao, “Proceedings of 3rd International Conference High Tech Die Casting”, AIM, Vicenza (2006).
- [12] M. Drouzy, S. Jacob, M. Richard, “AFS Int. Cast Met. J.”, 5, pp. 43-50, (1980).
- [13] A. John, G.M. Francis, Delphine Cantin, “Mat. Sci. Eng.”, A407, pp. 322-329, (2005).
- [14] B. Zhang, S.L. Cockcroft, D.M. Maijer, J.D. Zhu, A.B. Phillion, “JOM”, pp. 36-43, (2005).
- [15] T. Kobayashi, “Mat. Sci. Eng.”, A286, pp. 333-341, (2000).
- [16] C.H. Caceres, B.I. Selling, “Mat. Sci. Eng.”, A220, pp. 109-116, (1996).
- [17] M. C. Flemings, “Proceedings of 6th International Conference on Semi-solid Processing of Alloys and Composites”, G. L. Chiarmetta and M. Rosso Eds., pp. 11-14, Turin (2000).
- [18] Y. W. Riddle, L.P. Barber, M.M. Makhlof, “Mag. Tech.”, pp. 203-208, (2004).
- [19] M.D. Nave, A.K. Dahle, D.H. StJohn in: “Magnesium Technology”, H.I. Kaplan, J.N. Hryn, B.B. Clow Eds., TMS, pp. 243-250, Warrendale, PA, USA (2000).
- [20] M.D. Nave, A.K. Dahle, D.H. StJohn in: “Magnesium Technology”, H.I. Kaplan, J.N. Hryn, B.B. Clow Eds., TMS, pp. 233-242, Warrendale, PA, USA (2000).
- [21] K. Y. Sohn, J. W. Jones, J. A. Allison in: “Magnesium Technology, Proc. Symp. 2000 TMS Annual Meeting”, Nashville, TN, 2000, H. I. Kaplan, J. Hyrn, and B. Clow Eds., pp. 271-278, TMS, Warrendale, PA, USA (2000).
- [22] A. Luo, in: “Third International Magnesium Conference”, G. W. Lorimer Ed., pp. 449-464, Manchester (1996).
- [23] Y. W. Riddle, L.P. Barber, M.M. Makhlof, “Mag. Tech.”, pp. 203-208, (2004).
- [24] G. Timelli, “Metal. Sci. Tech.”, 28, pp. 9-17, (2010).
- [25] R.E. Smallman, R.J. Bishop, “Metals and Materials: Science, Processes and Application”, Butterworth-Heinemann Ltd., pp. 228-229, Oxford (1995).

ARTICLE VII

MICROSTRUCTURAL AND MECHANICAL CHARACTERIZATION OF AM60B ALLOY CAST BY RSF PROCESS

F. Bassan, G. Timelli*

**University of Padua, Department of Management and Engineering,
Stradella S. Nicola, 3 I-36100 Vicenza, Italy*

Published in "Materials Science Forum", 2013, vol. 765, pp. 296-300.

ABSTRACT

The effects of different microstructural features on the mechanical properties of a conventional and semi-solid gravity sand cast AM60B alloy are investigated. The Rapid Slurry Forming (RSFTM) technology and a step casting geometry, with a range of thickness from 5 to 20 mm, have been used. Tensile specimens have been drawn from the middle and external regions of the casting. The results show that the microstructure of conventionally gravity cast step castings consist of primary α -Mg dendrites, while those cast from the semi-solid state show the presence of globular and rosette-like α -Mg phase. Partially divorced Mg-Mg₁₇Al₁₂ eutectic and fine intermetallic Al_xMn_y compounds, distributed among the interdendritic channels and along grain boundaries, are also revealed. Due to low solidification rate, discontinuous precipitation of Mg₁₇Al₁₂ also takes place. The presence of primary blocky α -Mg phase and lower eutectic fraction tend to increase the mechanical properties of semi-solid cast Mg alloy.

KEYWORDS

Cast magnesium alloys, Gravity casting, Semi-solid, Microstructure, Mechanical properties, Rapid slurry forming (RSFTM).

1. INTRODUCTION

High-pressure die-casting is the overall dominating technology for manufacturing Mg alloy components. Improving the integrity of final products has been a continuous target by many researchers and companies for many years. Several solutions have been proposed and one of the most promising is actually the use of semi-solid metal (SSM) casting processes. One of the latest technical developments in SSM is the Rapid Slurry Forming (RSFTM) process, where high quality Mg slurry can be easily produced in very short time at low expense [1]. Nowadays, semi-solid metal forming is mostly applied with high pressure. In contrast, gravity sand casting has not been commonly used even though it has several advantages in small batch processing, complex or big parts [2].

The AM series alloys are among the most widely used Mg alloys because of their excellent combination of ductility and strength. In these alloys, aluminium and manganese are the primary alloying elements. Aluminium improves strength and hardness, and lowers the melting point, while Manganese is mainly added for improving seawater corrosion resistance, by removing iron and possibly other heavy metal elements into relatively harmless intermetallic compounds [3]. However, the effects of Al and Mn content on the microstructure and mechanical properties of a SSM processed alloy is not completely understood. Moreover, no research focusing on semi-solid gravity sand casting with AM60B has been reported even though this alloy has a good castability, resistance to hot cracking and low solidification shrinkage [3].

This work aims to study the influence of different microstructural features on the mechanical properties of conventional and semi-solid gravity sand cast AM60B alloy. The experimental work considered a step casting with a thickness ranging from 5 to 20 mm.

2. EXPERIMENTAL PROCEDURE

2.1. Alloy and gravity sand casting

An AM60B magnesium alloy was studied in this work. The chemical composition of the alloy is given in Table 1.

Al	Mn	Si	Zn	Fe	Cu	Others	Mg
5.75	0.27	0.031	0.039	0.001	0.003	<0.003	bal.

Tab. 1. Chemical composition of the AM60B alloy used in the present work (wt.%).

The step casting, obtained by sand mould and shown in Fig. 1, presented a range of thickness going from 5 to 20 mm and it was gated from the side of the riser. This configuration allows to obtain a wide range of solidification rates and consequently different microstructural scales [4].

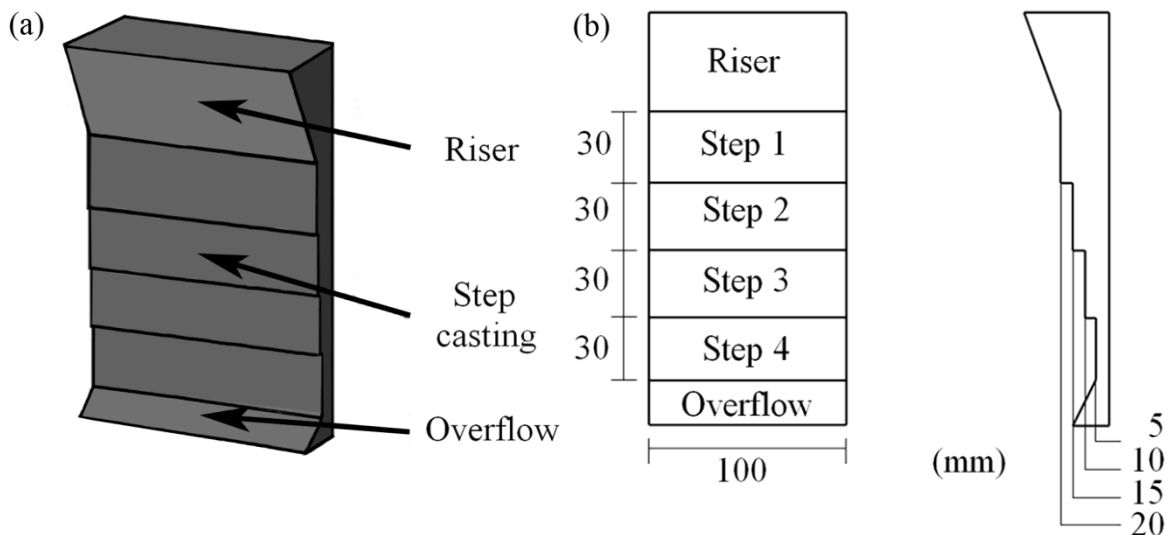


Fig. 1. a) The step casting CAD geometry with b) front and side views.

Two foundry technologies were used, that is traditional gravity sand casting and RSFTM technology. In the first one, the AM60B alloy was first melted in a graphite crucible using an electric crucible furnace set at 750 ± 5 °C, under a cover gas consisting of a mixture of 50% CO₂ + 0.2% SF₆ + remaining dry air. Before pouring, the sand moulds were preheated at ~ 100 °C. An amount of ~ 1.5 kg was gently taken from the molten bath using a preheated boron nitride coated steel ladle and poured to fill a series of three tilt-poured sand moulds, placed with an inclination angle of 60° to the horizontal. The castings were then allowed to cool down to room temperature inside the sand mould.

2.2. Rapid Slurry Forming (RSFTM) process

A series of semi-solid gravity sand castings were also obtained. Two masses of AM60B alloy with different enthalpy are mixed together. While one mass has low superheat (*high enthalpy*), the other acts as a cold solid stirring material (*low enthalpy*). The solid stirring material is generally named *Enthalpy Exchange Material* (EEM) [1]. The EEMs used in the present work had a conical shape with a constant weight of 0.225 kg, in accordance with Ref. [1]. The rotational speed was set at 1200 rpm and the sand moulds were preheated to ~ 100 °C. The EEM was submerged when the temperature of the molten metal was 640 ± 2 °C and the stirring extended for 20s. During the slurry making, a K-type thermocouple was submerged into the bath to control the thermal history. When the temperature of the slurry was stable at 613 ± 1 °C, the casting operations took place. The final temperature of the slurry was defined in order to obtain a viscosity and a solid fraction that could ensure a complete filling of the mould cavity, which was not guaranteed at lower temperatures through the gravity sand casting processing.

2.3. Metallography and mechanical testing

The sand castings were sectioned and samples were drawn from the each step for metallographic investigations. Flat tensile specimens with rectangular cross section were drawn from the middle of each step. The tensile specimens were 100 mm long and 3 mm thick, with a gauge length of 30 mm and a width of 10 mm. The best values in terms of *Quality index* [5] were selected, in an attempt to minimize any effects arising from casting defects on the fracture data and mechanism. Microstructural analysis was carried out using

an optical microscope and a scanning electron microscope (SEM) equipped with an energy-dispersive spectrometer (EDS), and quantitatively analysed using an image analyser.

3. RESULTS AND DISCUSSION

3.1. Microstructural observations

The microstructure of conventional gravity castings consisted of primary α -Mg dendrites with Al cored to the interdendritic regions (Fig. 2).

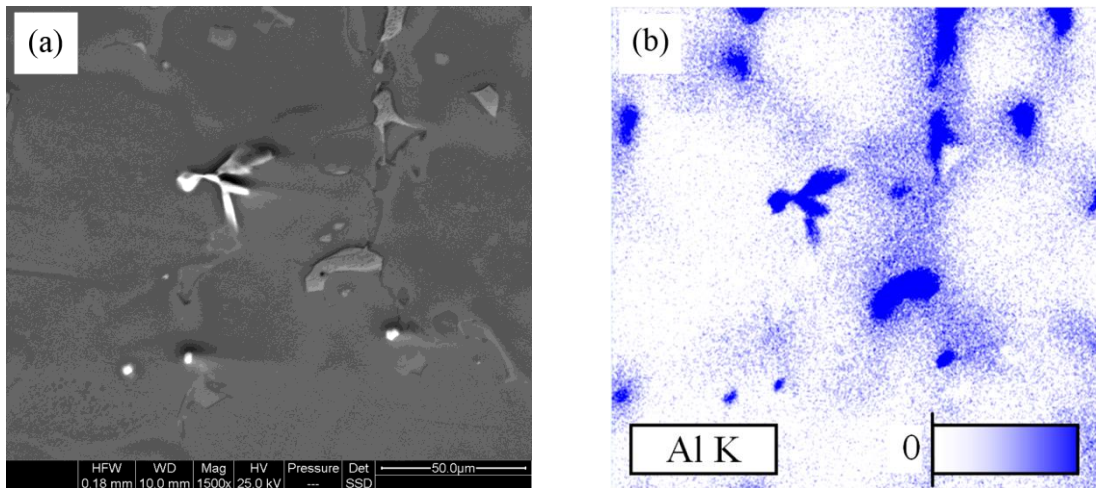


Fig. 2. a) SEM micrograph, and b) corresponding EDS map showing Al cored to interdendritic regions in conventional gravity sand castings. (Pictures refer to the 20 mm step).

Due to the low solidification rate, equiaxed α -Mg grains with a coarse dendritic morphology form (Fig. 3a). The semi-solid castings showed the presence of coarse primary α -Mg phase, with both rosette-like and spheroidal shape, which is mainly formed with the primary solidification during the RSF process, and finer secondary α -Mg dendrites nucleated and grown during the secondary solidification inside the mould cavity (Fig. 3b).

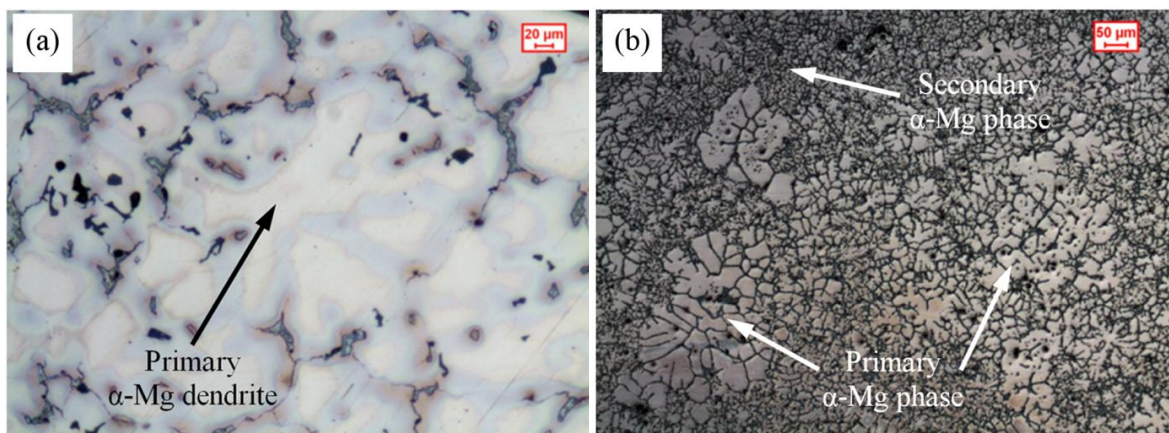


Fig. 3. Typical microstructures of a) conventional gravity cast, and b) semi-solid cast AM60B alloy observed in the 10 mm step; the different size and shape of primary α -Mg phase is evident.

The volume fraction of primary α -Mg phase, i.e. the solid fraction formed by RSF at 613 °C, was estimated by optical microscopy to be ~36%: this result is in accordance with Ref. [6]. In every step, the microstructure was finer close to the casting surface than in the centre of the casting. Due to the low diffusion rate of Al atoms into the α -Mg matrix and the moderate solidification rate, a non-equilibrium α -Mg + β -Mg₁₇Al₁₂ eutectic structure forms. In this work, a partially divorced α - β eutectic morphology was observed (Fig. 4a), characterised by islands of eutectic α -Mg within the β -Mg₁₇Al₁₂ phase. A great amount of fine Al-Mn intermetallic compounds distributed among the interdendritic regions and along grain boundaries was also revealed (Fig. 4). These particles have been analysed in AM series alloys by several researchers, but their identification is still uncertain. Luo [7] has identified this compound as Al₈Mn₅ phase, which forms on cooling inside the mould cavity.

The eutectic solidification does not mark the end of the phase transformations in the investigated alloy. The solidification rate is sufficiently slow (typical of sand-casting) to induce further precipitation of β -Mg₁₇Al₁₂ from the supersaturated regions of α -Mg crystals. This precipitation shows here a discontinuous form (Fig. 4a), which involves the growth of lamellar Mg₁₇Al₁₂ precipitates into α -Mg grains with a similar mechanism of pearlite into austenite grains during the cooling of steel [8]. The Al partitions to the Mg₁₇Al₁₂ lamellae as they grow, leaving the α -Mg between the lamellae much leaner in Al than before discontinuous precipitation began.

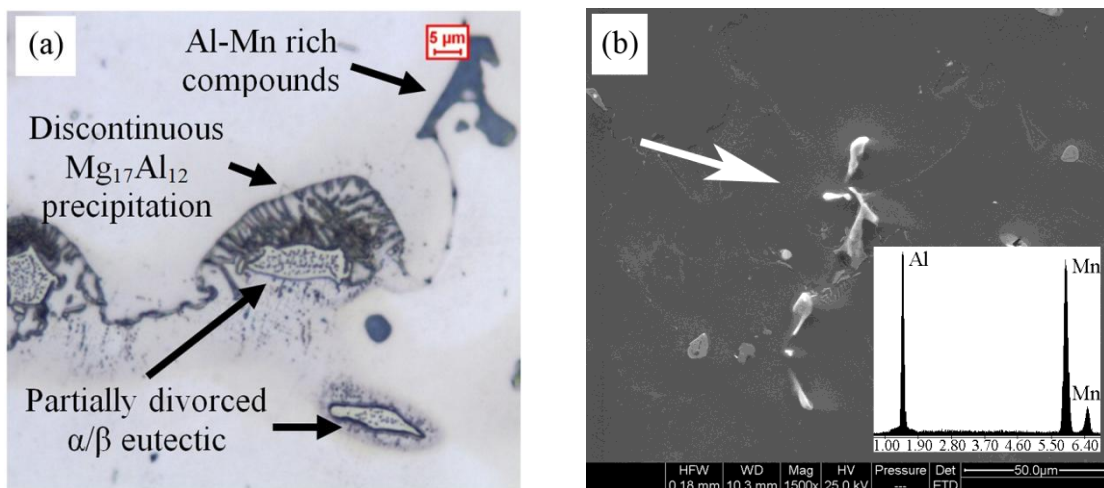


Fig. 4. a) Different intermetallic compounds observed in the 10 mm step of the castings and b) SEM micrograph with corresponding EDS spectra of Al-Mn intermetallics.

The eutectic variations of as-cast samples produced with conventional and semi solid foundry technologies were studied over the central cross section of each step (Table 2). The eutectic fraction varies in the range of 1.6% to 2.2% for conventional sand castings, while it varies between 0.6% and 1.2% for semi-solid castings. Lower eutectic fraction in the semi-solid castings can be related to the decrease of volume fraction of the liquid phase at the eutectic temperature and the increase of the volume fraction of primary α -Mg crystals [8].

Step thickness [mm]	Conventional gravity casting	Semi-solid casting
20	2.2 (0.59)	1.2 (0.48)
15	1.4 (0.57)	1.2 (0.42)
10	1.1 (0.36)	0.6 (0.32)
5	1.6 (0.54)	0.6 (0.29)

Tab. 2. Average Mg-Mg₁₇Al₁₂ eutectic fraction (%) in each section of the step castings (standard deviation in parentheses). Data refer to conventional and semi-solid castings.

3.2. Tensile testing

The mean values and the standard deviation of ultimate tensile strength (UTS) and elongation to fracture (s_f) are reported in Fig. 5. The low standard deviation confirms the presence of low content of casting defects in the investigated tensile specimens.

If the different steps are considered and compared, variations of 11 and 9% in UTS and 22 and 33% in elongation to fracture are observed for the conventional and semi-solid castings respectively, as a consequence of the different microstructural scale. In the conventional gravity castings, the UTS varies from 163 to 178 MPa and the s_f from 4.6 to 5.6%, but, the UTS and the s_f are in the range of 178 to 197 MPa and from 4.9 to 7.3% respectively in the semi-solid castings. On the other hand, the different cooling rates, in the range of step thickness analysed, seem to not affect the YS of the alloy. The highest mechanical properties of the semi-solid alloy are mainly associated with the presence of primary α -Mg phase formed with the primary solidification during the RSF process and a lower amount of brittle Mg-Mg₁₇Al₁₂ eutectic islands. The lower mechanical properties observed in step 4 can be related to the filling technique used in the present work. In conventional gravity as well as in the semi-solid casting, the liquid phase, eventually separated from the primary solid during filling, can generate a turbulent flow and produce oxide and air/gas entrapment in the last 5mm step. Therefore, the overflow connected to this step is revealed to be sub-sized. On the other side, the 20mm step for both the casting processes shows a higher Mg-Mg₁₇Al₁₂ eutectic fraction and a coarser microstructure, such as secondary α -Mg crystals, than steps 2 and 3 respectively.

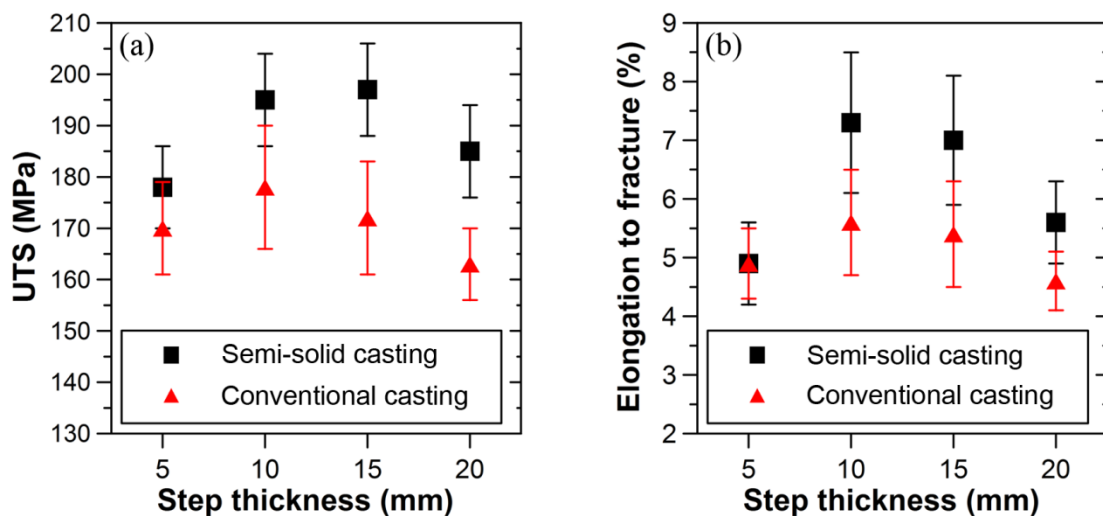


Fig. 5. Average a) UTS and b) elongation to fracture as a function of step thickness. Data refer to conventional and semi-solid castings.

4. CONCLUSIONS

In the present study the influence of different microstructural features on mechanical properties of conventional and semi-solid gravity sand cast AM60B alloy has been investigated.

Nearly defect-free castings have been produced using RSF technology. The conventional gravity castings show primary α -Mg dendrites, while those cast at semi-solid state show the presence of globular and rosette-like α -Mg phase. Partially divorced α - β eutectic, fine intermetallic Al_xMn_y compounds and discontinuous $Mg_{17}Al_{12}$ precipitation are also revealed. The presence of primary blocky α -Mg phase and lower amount of brittle eutectic islands tend to increase the mechanical properties of semi-solid cast Mg alloy.

REFERENCES

- [1] H. Cao, M. Wessen, O. Granath, Processing effects on the morphology of semi solid Mg alloy slurry produced by the RSF process, in: AIM (Ed.), Proceedings of the Third International Conference High Tech Die Casting, Vicenza, Italy, 2006, pp. 1-9.
- [2] A.K. Dahle, D.H. StJohn, G.L. Dunlop, Developments and challenges in the utilization of magnesium alloys, Mater. Forum 24 (2000) 167-182.
- [3] M.M. Avedessian, H. Baker, Magnesium and Magnesium alloys, first ed., ASM International, Materials Park, Ohio, USA, 1999.
- [4] F. Grosselle, G. Timelli, F. Bonollo, DOE applied to microstructural and mechanical properties of Al-Si-Cu-Mg casting alloys for automotive applications, Mat. Sci. Eng. A527 (2010) 3536-3545.
- [5] M. Drouzy, S. Jacob, M. Richard, Interpretation of tensile results by means of quality index and probable yield strength, AFS Int. Cast Met. J. 5 (1980) 43-50.
- [6] Q. Han, E.A. Kenik, S.R. Agnew, S. Viswanathan, Solidification behaviour of commercial magnesium alloys, in: J. Hryn (Ed.), Magnesium Technology 2001, Warrendale, PA, 2001, pp. 81-86.
- [7] A. Luo, Understanding the solidification of magnesium alloys, in: G.W. Lorimer (Ed.), Proceedings of the Third International Magnesium Conference, UK, 1996, pp. 449-464.
- [8] A.K. Dahle, Y.C. Lee, M.D. Nave, P.L. Schaffer, D.H. StJohn, Development of the as-cast microstructure in magnesium-aluminium alloys, J. Light Met. 1 (2001) 61-72.